Imaging the Main Frontal Thrust in Southern Bhutan using high-resolution near-surface geophysical techniques : implications for tectonic geomorphology and seismic hazard assessment

Dowchu Drukpa

UNIVERSITÉ DE MONTPELLIER

ECOLE DOCTORALE SIBAGHE

THESIS

To obtain the title of

PhD of Science of the University of Montpellier

Speciality: Geophysics, Seismology and Geology

IMAGING THE MAIN FRONTAL THRUST IN SOUTHERN BHUTAN USING HIGH-RESOLUTION NEAR-SURFACE GEOPHYSICAL TECHNIQUES: IMPLICATIONS FOR TECTONIC GEOMORPHOLOGY AND SEISMIC HAZARD ASSESSMENT

Defended by :

Dowchu DRUKPA

Thesis defense committtee members

CATTIN Rodolphe	Geosciences Montpellier	Directeur de thèse
GAUTIER Stéphanie	Geosciences Montpellier	Directeur de thèse
GIRARD Jean-Francois	EOST-Univ. Strasbourg	Président
HETÉNYI György	Univ. Lausanne	Rapporteur
BOLLINGER Laurent	CEA	Examinateur
BODET Ludovic	McF METIS-Univ. Paris 6	Examinateur

November 23, 2017

Abstract

Recent studies in southern-central Bhutan have proposed a Holocene slip rate of 20.8±8.8 mm/year. This overthrusting slip rate is estimated based on a mean vertical uplift rate of 8.8±2.1 mm/year and assuming a constant frontal thrust dip angle of 25°±5° extrapolated from structural measurements. Since geometry of the fault is a key parameter for discerning the slip rate and its associated seismic hazard assessment, we employed near-surface geophysical approach to accurately constrain the Topographic Frontal Thrust (TFT) geometry at shallow depth. Based on proven effectiveness of near-surface geophysical techniques for studying active faults, we adopted gravity, seismic and electrical resistivity tomography.

We deployed geophysical profiles at three key sites along the southern frontal areas of the Bhutan Himalayas. The first study area is in Sarpang, a small town located in southern-central Bhutan where we performed all three geophysical methods adopted. The second site is located in Phuentsholing in the south-western Bhutan, where we performed gravity and electrical resistivity survey. The third site is located between Sarpang and Phuentsholing, in the sub-district of Lhamoizingkha under Dagana district. A stochastic inversion approach was adopted to perform analysis of geophysical data collected from the above sites expect for Lhamoizingkha area. Unlike commonly used approaches based on search for the simplest model, the main advantages of this approach include its ability (1) to assess the fault geometry because no smoothing is applied, (2) to provide a measurement of the uncertainties on the obtained dip angle and (3) to allow trade-off analysis between geometric and either electrical resistivity, velocity or density properties.

The stochastic inversion results from Sarpang site show a TFT that is characterized by a flat and listric-ramp geometry with a north dipping dip angle of ca. 20°-30° at the upper depth of 0-5 m, steeply dipping angle of 70° in the middle 5-40 m depth and flattening with a dip angle of 20° at deeper depths. These new results allow us to estimate a minimum overthrusting slip rate of 10±2 mm/year on the TFT, which is about 60% of the far-field GPS convergence rate of ca. 17 mm/year. Based on these constraints we propose that, in Sarpang site, significant deformation partitioning on different faults including the TFT, the Main Boundary Thrust (MBT) and the Frontal Back Thrust (FBT) cannot be ruled out. More importantly, assuming a constant slip rate, the dip angle variations constrained from the present study correspond to variations in the deduced uplift rate with distance from the TFT. This, therefore, emphasizes the drawbacks in assuming constant dip angle measured

from surface observations and uplift rate estimates based on terrace dating only at the front, which may significantly bias the slip rate estimation.

Unlike in Sarpang, the TFT corresponds to the Main Frontal Thrust (MFT) in Phuentsholing. At this site a preliminary study suggests a MFT characterized by a flat and listric-ramp geometry. With additional terrace dating information, slip rate for the Phuentsholing area will be performed in a near future. Overall based on the stochastic inversion results, we propose a MFT geometry similar to that observed in Sarpang but with possible lateral variations in terms of deformation partitioning. In Lhamoizingkha area, the exact location of the MFT is not known. Our preliminary results suggest a complex fault trace and indicate that the MFT is located further north of the current resistivity line deployed in this area. Similar to Phuentsholing site (but contrary to Sarpang), we observed that the MFT is the most frontal structure and therefore most of the convergence in the area could be accommodated by the MFT, which is also in agreement with GPS observations.

Résumé

Des études récentes menées dans la région de Sarpang au sud du centre du Bhoutan estiment un taux de glissement Holocène de 20,8 $\pm$ 8,8 mm/an sur le «chevauchement frontal himalayen» est utilisé pour le MFT, pas le TFT.Que diriezvous de «chevauchement au front topographique »? Plus bas : effacer l'espace entre «au-del » et «à». Cette valeur est basée sur un taux de surrection moyen mesuré de 8,8 $\pm$ 2,1 mm/an et en supposant pour ce chevauchement un pendage constant de 25° $\pm$ 5°. La géométrie des failles est un paramètre clé dans l'estimation de la vitesse de glissement et donc dans l'évaluation de l'aléa sismique. Dans le cadre de ce travail, nous avons utilisé une approche géophysique de proche surface afin d'estimer précisément la géométrie de ce chevauchement.

Nous avons déployé des profils géophysiques dans trois sites clés le long de la frontiére sud du Bhoutan. La première zone d'étude se trouve à Sarpang, une petite ville située au centre du Bhoutan où nous avons effectué des mesures gravimétriques, sismiques et électriques. Le deuxième site est situé à Phuentsholing dans le sud-ouest du Bhoutan, où nous avons effectué des mesures gravimétriques et de résistivité électrique. Le troisième site est situé entre Sarpang et Phuentsholing, à Lhamoizingkha dans le district de Dagana.

Excepté pour la région de Lhamoizingkha, une approche d'inversion stochastique a été adoptée pour analyser des données géophysiques collectées. Contrairement aux approches couramment utilisées basées sur la recherche du modéle le plus simple, les principaux avantages de cette approche sont sa capacité (1) à mieux estimer la géométrie des zones de discontinuité car aucun lissage n'est appliqué, (2) à fournir une mesure des incertitudes sur le pendage obtenu et (3) à permettre une analyse des relations possibles entre les propriétés géométriques et celles du milieu (résistivité électrique, vitesse ou densité).

Les résultats d'inversion stochastique du site de Sarpang montrent un TFT qui se caractérise par une géométrie en plat-rampe-plat avec un pendage vers le nord d'environ 20°-30° dans la partie la plus superficielle (profondeur $<$ 5 m), un pendage fort de 70° entre 5 m et 40 m de profondeur et un l'aplatissement avec un pendage de 20° au-del à de 40 m. Ces nouveaux résultats nous permettent d'estimer un taux minimal de glissement de 10 $\pm$ 2 mm/an sur le TFT, soit environ 60% des 17 mm/an associés au taux de convergence GPS moyen obtenu en champ lointain. Sur la base de ces contraintes, il apparait donc qu'on ne puisse pas exclure la possibilité que la déformation soit distribuée sur plusieurs failles, comprenant le TFT, mais également d'autres chevauchements comme le MBT (au nord) ou

le FBT (au sud). De plus, en supposant un taux de glissement constant, les variations de pendage obtenues induisent des variations du taux de surrection en fonction de la distance au TFT. Cela souligne les faiblesses des hypothèses couramment faites pour estimer les taux de glissement Holocène sur les failles sismogènes : (1) pendage constant estimé uniquement à partir des observations de surface et (2) estimations du taux de surrection en supposant une surrection identique pour une terrasse fluviale donnée.

Contrairement à Sarpang, à Phuentsholing le TFT correspond au chevauchement frontal himalayen (MFT). Sur ce site, l'étude préliminaire que nous avons menée suggère un MFT ayant une gèomètrie de faille listrique. Des mesures de datations doivent maintenant être effectuées pour estimer le taux de glissement sur le MFT dans cette zone. Dans la région de Lhamoizingkha, l'emplacement exact du MFT n'est pas connu. Nos résultats préliminaires suggèrent une géométrie complexe de la trace de la faille en surface et indiquent que le MFT est situé plus au nord de la ligne de résistivité déployée dans cette zone. À l'instar du site de Phuentsholing (mais contrairement à Sarpang), nous avons observé que le MFT était la structure la plus frontale et que l'essentiel de la convergence dans cette zone pouvait être accommodé par le MFT, comme semble le suggérer les observations GPS.

Acknowledgments

Every pursuit to accomplish important milestones in life become possible when the processes to realize the end goal is supported and driven by great mind with ultimate objective to advance knowledge for the betterment of the society that we live in. Nothing more and nothing less!

My scientific curiosity and professional interest takes me to the University of Montpellier (France) to pursue Doctor of Philosophy in Geosciences at the beginning of 2015. The idea of doing a PhD was conceived when I met Rodolphe Cattin in 2010 while conducting gravity study in Bhutan as part of cooperation research project between the Department of Geology and Mines, Geosciences Montpellier (University of Montpellier) and ETH Zurich. In the years that ensued, we jointly developed a project proposal on **"Seismic coupling and megaquake along the Himalayan arc"**. Unfortunately, the proposal didn't get approved until mid-2014 after three successive resubmissions. Immediately upon approval of the project by the **French Agence Nationale de la Recherche (ANR)**, Rodolphe informed me about the good news and also reminded me about the prospect of starting my PhD. I was overjoyed and at the same time intimated by the enormity of commitment required to accomplish such a major undertaking in my life. I immediately replied to Rodolphe asking for some time to discuss with my family and get back to him with a decision. It was indeed a tough decision for me, especially realizing full well that pursuing a PhD would require me to be away from my family for a longer period of time. But in the end with full support my family and out of my own interest, I decided to undertake PhD study knowing full well, the challenges and commitment that I have to endure over the next three years.

Three years have now gone by and I have sacrificed a good amount of my time and energy in what I believe will make an important contribution in understanding the science and in enhancing my capacity as an individual. In this context, I must first of all sincerely thank Professor **Rodolphe Cattin** for giving me this unforgettable opportunity, and more importantly, for believing in me and rendering your unfailing support throughout the last three years. I am highly indebted to you and I shall never forget your kindness and for being always there when ever I needed your help. My sincere thanks to **Stéphanie Gautier** for your amazing support and I was indeed fortunate to have you as my co-supervisor. Your words of encouragement and critical comments helped me a great deal to complete this thesis. Thanks again for everything to both Rodolphe and Stéphanie!

My sincere thanks to comity members **Ludovic Bodet** and **Marguerite Godard** and thesis defense committee members:**Rodolphe Cattin, Stéphanie Gautier, Jean-Francois Girard, György Hetényi, Laurent Bollinger and Ludovic Bodic** for sparing their time and providing insightful comments. I must particularly thank **György** for thorough review of the draft thesis and providing invaluable comments, which greatly improved this manuscript.

My thanks also goes to amazing friends at Geosciences Montpellier including **Jeff Ritz, Matthieu Ferry, Romain Le Roux-Mallouf and Stéphane Mazzotti** with whom I had great opportunity to associate with both in Montpellier and during the field works in Bhutan. I will cherish the good moments we had together. Thanks also to **Theo Berthet** for permitting me to use his LaTeX code, which really helped me in writing and compilation of this thesis. I must also sincerely acknowledge my colleagues in DGM who helped us in deployment of geophysical investigation in southern Bhutan. Without their help, it would have been extremely difficult to accomplish the data acquisition task.

Last but not the least, I sincerely thank my beautiful and loving wife, **Tshering Denka** for her understanding and taking good care of our most adorable son, **Jigmi Namgyel Yoezer**. Without my wife's understanding and support, I will not have been able to complete my PhD. I owe you a lot now and forever!

This research thesis was funded by **French Agence Nationale de la Recherche (ANR-13-BS06-006-01)**.

LIST OF FIGURES

2.1 Cartoon depicting the Tethys sea that separates India from Eurasia during pre-Valanginian time, gradual subduction of the Tethys along the southern margin of Asia and collision of the two continents leading to formation of the great Himalayas (After Avouac, 2008). 8

2.2 (a) Simplified geological map of the Himalayan arc, (b) Cross-section along AA' in (a) along the longitude of Katmandu.Thick black line represents the MHT which expresses at the the surface as MFT at the front of the Siwalik Formation (Modified after Avouac, 2008). 10

2.3 Wide-angle seismic data showing variation in the depth of reflections coming from Moho underneath the Higher Himalayas and south of Yarlung Tsangpo (After Hirn et al, 1984) 13

2.4 Reflections from the INDEPTH deep seismic profile and corresponding interpreted major tectonic features MHT, STD and Moho (After Zhao et al, 1993). 14

2.5 Interpretative cross-section of India-Eurasia collision zone. The Indian lithosphere underplates the Himalaya and Tibetan plateau upto ∼450 km from the MFT (After Hetényi, 2007). 15

2.6 Arc-Parallel Gravity Anomaly. Red and blue values represent higher and lower values of gravity, resepectively, compared to the average profile perpendicular to the Himalayan arc. Yellow lines show change in arc-parallel gravity anomaly and highlight segments (After Hétenyi et al., 2016). 17

2.7 Coupling model and fit to the horizontal GPS data. Interseismic area is shown as shades of red. A coupling value of 1 means fully locked and 0 means fully creeping. The green and black arrows show the continuous and campaign gps velocities with their error bars, respectively. The blue arrows shows the modeled velocities which fit with the coupling. The dashed-line shows separation of region within which the long term velocity for that region is calculated show by large red arrow (After Stevens and Avouac, 2015). 18

2.8 Mid-crustal microseismicity from 1996-2008 superimposed on shear stress accumulation rate on MHT, deduced from coupling pattern. The red line shows the 3500 m elevation beyond which the seismicity seems to drop (After Ader et al., 2012). 19

2.9 Interseismic coupling of the MHT in the Bhutan Himalayas. Rectangles show interseismic coupling for different fault segments. The hatched segment represents flat part of the MHT. Colored base map represents coupling as shown in Figure 2.7. Dashed blue line shows the possible limits of the fully coupled zone.Green triangles show GPS station and black triangles represents GPS stations used in Stevens and Avouac, 2015 (After Marechal et al., 2016). 20

2.10 (a) Seismicity of the Himalayan region showing location of events that occurred between 1961-1981. Large, medium and small circles show very good, good and fair quality of epicenter location on basis of station locations and travel time residuals. Most of the epicenters lie along a relatively narrow belt of about 50 km between MCT and MBT. Seismicity within the triangles (A, B, C, D, E) are projected linearly on the center line of each triangle. (b) Fault plane solutions of historical events showing mostly compressional regime (After Ni and Barazangi, 1984). 21

2.11 Observations and model results related to the 1714 earthquake in the Bhutan Himalayas. Grey star and circle indicate, respectively, the location and intensity of earthquake as reported by Ambraseys and Jackson[2003] Abbreviations: WP-Wangdue Phodrang, Ga-Gangteng Monastery, Sa-Sarpang, Ge-Gelephu, Ba-Bahgara, Ch-Charaideo Hill, Ti-Tinkhong, pOF-proposed Oldham Fault, DF-Dauki Fault. Cities: Th-Thimphu, Da-Darjeeling, Gu-Guwahati, Te-Tezpur, Sh-Shillong, Jo-Jorhat (After Hetényi et al., 2016). 24

2.12 Great earthquakes along the Himalayan arc since 1500 AD (After Hetényi et al. 2016). 25

2.13 Synthesis of paleoseismic records along the Himalayas (a). Synoptic calender and locations of great/large earthquakes along the Himalayan front. Grey bars indicate minimum source lengths with or without observed surface rupture. Vertical orange bars show radio-carbon model constrains on the timing of different events. Vertical orange bars show the $\sim$ 3500 year long record deduced from Piping area (Le Roux-Mallouf et al., submitted). 26

3.1 Common geometric configurations used in electrical resistivity survey 37

3.2 The resistivity of rocks, soils and minerals (After Loke, 2015) 40

3.3 Flow chart to characterize fault activity in Quaternary settings for engineering applications (After Suzuki et al. 2000). 42

3.4 Relationship between angle of incidence(i) and angle of refraction (r) in layers with velocity V_1 and V_2 where $V_2 > V_1$. 43

3.5 Travel-time curves for the direct wave and head wave from a single refractor. 45

3.6 Travel-time curves for the head wave arrivals from a dipping interface in forward and reserve directions along a refraction profile (top); Ray-path geometry (Modified after Kearey, 2013) 46

3.7 Schematic diagram showing the relationship between model and data 53

3.8 A 2D best fit model obtained by comparing the synthetically computed data with the observed data and applying stochastic inversion processes. 58

4.1 Map of Sarpang area showing the major geological and tectonic units (Abbreviation in the map: Qt-River terraces; Qu-Unconsolidated sediments deposited in braided stream;Tsl-Lower member Siwalik Group; Tsm-Middle member Siwalik Group; Pzm-Manas Formation; Pzj-Jaishidanda Formation; pCd-Daling Formation; GHlo-Greater Himalaya structurally lower orthogneiss unit; GHlml-Greater Himalaya structurally lower metasedimentary unit; MFT-Main Frontal Thrust; MBT-Main Boundary Thrust; ST-Shumar Thrust; MCT-Main Central Thrust (After Long et al., 2011). 63

4.2 Geomorphological map of Sarpang area. (a) Shaded map of Sarpang showing the location of MFT and TFT. Black triangle shows the location of study area. (b) Geomorphological map of TFT in Sarpang superimposed on Pleiades DEM. Alluvial terraces are labeled TO (active channel) to T6 (oldest). Blue triangle represent location of paleoseismic trench. Black points show elevation from Pleiades DEM with countour interval of 20 m (After Le Roux-Mallouf et al., 2016). 64

4.3 Detailed log over a 2 m grid at the paleoseismic trench in Sarpang showing major geological and tectonics units. The solid and dashed red lines show the main certain and suspected faults, respectively. Thick black lines labeled EH 1 and EH 2 denote the event horizons. (After Le Roux-Mallouf et al., 2016). . . 65

4.4 1 m spacing Dipole-Dipole model generated using res2dmod involving 2 layers with high resistivity contrast and gently dipping TFT. 68

4.5 Inversion model resistivity section obtained using data generated from the model in Figure 4.4. 68

4.6 Location of electrical resistivity line with respect to the position of the fault and paleoseismic trench. 69

4.7 2D Dipole-dipole array ERT section with 1 m (top), 2.5 m (middle) and 5 m (top) electrode spacing 74

4.8 2D Wenner-Schlumberger array ERT section with 1m (top), 2.5 m (middle) and 5 m (top) electrode spacing 75

4.9 Schematic diagram of the finite difference or finite element used in the res2dmod program (After Loke, 2015). 76

4.10 Simplified geometry of the subsurface used in the forward modeling process . 77

4.11 Results of the forward model using res2dmod to test the effect of different layers (a) ERT pseudo-section with 5 m interval obtained from observed data (b) 3 layers model with 5 m interval and TFT dip angle of 40° (c)4 layers model with 5 m interval and same TFT dip angle (d) 5 layers model with 5 m interval and same TFT dip angle. 78

4.12 Effect of mesh on the model resistivity output 80

4.13 The best fit resistivity value obtained for SL and NL layers defined in Figure 4.10 81

4.14 The best fit dip angle of the fault defined in model in Figure 4.10 82

4.15 The best fit thickness and resistivity value for the fault zone defined in Figure 4.10 . . . 82
4.16 Layout plan for acquisition of seismic data along the profile. The TFT location at the mid-point of profile 2 is shown with red arrow. . . . 83
4.17 First arrival travel-time picks for all in-line shots along the seismic refraction profile . . . 85
4.18 Comparison of first arrival travel-time picks between three pickers . . . 86
4.19 Shot location along the study seismic profile. Color scale indicates first arrival travel-time from each shot location to the geophone positions along the profile. 87
4.20 Tomographic image showing velocity variation on both sides of the TFT. . . . 89
4.21 Ray coverage illustrating the area resolved in tomographic inversion in Figure 4.20. The TFT is located around the 0 m distance. . . . 89
4.22 Measured gravity (top), elevation (middle) and gravity variations corrected for both topographic effect and regional trend (bottom) along the study profile. Data uncertainty is associated with both accuracy of the CG5 gravimeter and error in elevation measurement.. . . . 92

5.1 Location map showing the geophysical study area in Phuentsholing, Lhamoizingkha and Sarpang . . . 150
5.2 Three sites located using google Earth image for reconnaissance study and detailed geophysical investigation. . . . 151
5.3 Thick alluvial fan deposit at the foothills of Site 3. . . . 152
5.4 Panoramic view at site 1 showing formation of three levels of terraces as result of repeated tectonic uplift. . . . 152
5.5 Location of drill bore-holes (BH-01 and BH-02) and geophysics line (yellow line) in Phuentsholing at Site 1. Inset picture shows drilling work in process at BH-02. . . . 153
5.6 Drill core from BH-01 and BH-02. Red rectangle shows the dark, non-cohesive and unconsolidated materials observed between ∼13-18 m at BH-01. . . . 153
5.7 Description of core-log lithology from drill bore-holes, BH-01 and BH-02. . . . 154
5.8 (A) Epicenter location with pattern of linear seismicity corresponding to the Goalpara lineament (Velasco et al., 2007); (B) Major active fault zones imaged by GANSSER project seismic catalog showing the prominent dextral Dhubri-Chungthang Fault zone (After Diehl et al., 2017). . . . 156

5.9 Distribution of geomorphologic surfaces and active faults. Red square shows location of our Site 1 in Phuentsholing (After Yagi et al, 2002). 157

5.10 Structural attitudes of geological outcrops in Phuentsholing and vicinity area. Inset picture shows steeping dipping highly sheared phyllite in-situ exposure at Site 1. 158

5.11 Observed Wenner-Schulumberger ERT pseudo-section with varying current intensity 160

5.12 Dipole-Dipole (top) and Wenner-Schulumberger (bottom) ERT pseudo-sections obtained using 8 mA current injection. 163

5.13 Dipole-Dipole (top) and Wenner-Schulumberger (bottom) ERT pseudo-sections obtained using 15 mA current injection. 164

5.14 Dipole-Dipole (top) and Wenner-Schulumberger (bottom) ERT pseudo-sections obtained using 20 mA current injection. 165

5.15 Dipole-Dipole (top) and Wenner-Schulumberger (bottom) ERT pseudo-sections obtained using 5 mA current injection. 166

5.16 Measured gravity data (a), elevation (b) and topographic corrected gravity variations along the profile (c). The drill bore-hole (BH-01) is located between 66-72 m along the profile. 168

5.17 Geometry of the model used in the stochastic inversion. STL - South Top layer, NTL - North Top Layer, SL - South Layer and NL - North Layer. xfault is the possible location of the fault on the surface with respect to fault gouge observed in bore-hole at ca. 13-18 m depth and resistivity distribution in the subsurface. Model thickness is associated with the thickness investigated by each geophysical method. 170

5.18 Distribution of MFT angle from ERT sections using Wenner-Schulumberger array with different amount of current injection 171

5.19 Distribution of MFT angle from Wenner-Schlumberger ERT sections by combining PHUN2, PHUN3, PHUN4 and PHUN5 shown in Figure 5.19 171

5.20 Bivariate frequency histograms between dip angle and other parameters of the ERT model obtained using Wenner-Schulumberger array 172

5.21 Observed and Calculated Wenner-Schlumberger array and the optimal misfit between Observed and calculated ERT sections that correspond to obtained MFT geometry and petro-physical characteristics. The red rectangle in the model section indicates the location of drill borehole, BH-01. 174
5.22 Comparison between observed (blue circles) and calculated (dark green lines) gravity variations along profile line for 100 best fitting models (top); Density contrast models without drill borehole information but with different SL and NL thickness(Bottom). 175
5.23 Distribution of MFT dip angle from gravity measurements without incorporating bore-hole information in the inversion process. 176
5.24 Relationship between the obtained dip angle and the other parameters of the density model. Note that density means density contrast with respect to density of the North top layer. 177
5.25 Comparision between observed (blue circles) and calculated (dark green lines) gravity variations along profile line for 100 best fitting models (top); Density contrast models with drill bore-hole information and with varying SL and NL thickness(bottom). 179
5.26 Distribution of MFT dip angle from gravity measurements with inclusion of drill bore-hole information in the inversion process. 180
5.27 Relationship between the obtained dip angle and the other parameters of the density model. Note that density means density contrast with respect to density of the North top layer. 181
5.28 (a) Topographical map of Bhutan showing the location of the Lhamoizingkha region . (b) The Lhamoizingkha and vicinity areas show markers indicating intense tectonic activity: a system of perched alluvial terraces, landslides and evidences of surface rupture of the MFT. The black boxes show the location of the different paleoseismic study sites and red box at Chokott Creek is location where geophysical study was performed (Modified from Le Roux-Mallouf, 2016).184
5.29 Location of the Piping paleoseismic trench on the left bank of Wang Chhu. . . 185
5.30 Geological map of the Piping-Lhamoizingkha area (After Le-Roux Mallouf, 2016).186
5.31 Diagram showing how ZZ FlashRes resistivity collects data compared to conventional resistivity equipment. 187
5.32 Geo-electrical resistivity line at Lhamoizingkha to the west of Chokott Creek. . 188

5.33 Electrical resistivity profile line in relation to the inferred MFT and power line 188

5.34 ERT section for 1m electrode spacing using Dipole-Dipole (top) and Wenner (bottom) geometric configuration 190

5.35 ERT section for 2.5 m electrode spacing using Dipole-Dipole (top) and Wenner (bottom) geometric configuration 191

5.36 ERT section for 5 m electrode spacing using Schlumberger (top) and Wenner (bottom) geometric configuration 192

5.37 Location of paleoseismic trench, MFT and proposed geophysical line in Piping area. 194

6.1 Profiles of elevation and slope for 50 km-wide swaths in Nepal (A) and Bhutan (B). Values sampled every 5 km along swath; maximum, minimum, and mean elevations and slopes are for each 5 $\times$ 50 km rectangle along swath. Relief computed as standard deviation of elevations. Gray scale shading between maximum and minimum swath elevations is density plot (histogram) of elevation samples (darker indicates greater concentration of terrain at that elevation). C-F: Comparison of Nepal and Bhutan profiles aligned at high peaks and Main Frontal thrust. Heavy vertical line at position of high peaks; thin solid (Nepal) and dashed (Bhutan) vertical lines are where profiles cross 2 km or 1 km elevations (dotted horizontal lines) (After Duncan et al., 2003). 197

6.2 Topographic and precipitation profiles, in 40-km-wide swaths, across Bhutan Himalayas and Shillong plateau show that an orographic barrier of 1.5-2 km is sufficient to hinder moisture transport. A-eastern Bhutan; B-western Bhutan. Topography (orange) has been derived from Shuttle Radar Topography Mission data; precipitation (blue) is taken from the calibrated Tropical Rainfall Measuring Mission data. There is a strong E-W precipitation gradient: at $\sim$ 1-1.5 km elevation in the east it is $\sim$ 4 m/yr, while in the west it is $\sim$ 6 m/yr. MFT–Main Frontal thrust, MBT–Main Boundary thrust, MCT–Main Central thrust, KT–Kakhtang thrust, STD–South Tibetan detachment, LHS–Lesser Himalayan Sequence, GHS–Greater Himalayan Sequence, TK–Tethyan Klippen, PW–Paro window, TSS–Tethyan Sedimentary Sequence (After Grujic et al., 2006). 200

6.3 Interseismic coupling of the Main Himalayan Thrust in Bhutan. Rectangles show our estimates of interseismic coupling for the different fault segments. The hatched segment represents the flat part of the MHT constrained by the inversion. The colored base map representing seismic coupling estimates and black triangles representing GPS stations are from Stevens and Avouac (2015). Dashed blue lines show the possible limits of the fully coupled zone. Green triangles show the locations of our new GPS stations. (After Marechal et al., 2017). 201
6.4 Tectonics models showing the role of Indian crust in collision dyanamics of western and eastern Bhutan (After Singer et al., 2017). 202
6.5 Seismotectonic model of the Bhutan Himalayas and its link to the foreland deformation. (After Diehl et al., 2016). 203

7.1 Estimated slip rate inferred from both fault geometry and observed uplift rate. (a) Uplift rate along the study profile. Red and green curves are show two end-member models obtained for fault geometry. Thick blue line denotes the far-field shortening rate estimated from GPS measurements (Marechal et al., 2016). It corresponds to the upper limit of uplift rate, which can be associated with a theoretical vertical fault. Gray circle is the observed uplift rate assuming a northward distance of 5 m from the TFT as reported by Berthet et al., 2014. (b) Same as (a) except a northward distance of 10 m is assumed. (c) Estimated slip along the TFT at depth assuming a constant uplift rate along the study profile for the two-end member models denoted by red and green curves. Hatched area around the curves is associated with uplift rate uncertainties. The thick grey dashed lines point out the area of uplift rate assuming a northward distance from the TFT of 5 m and 10 m, respectively. Note that within this area, the uncertainties in the uplift rate spikes up close to the TFT and decreases away from the front towards the north. Thick blue line denotes the far-field shortening rate estimated from GPS measurements (Marechal et al., 2016), which is the upper limit of slip rate. The slip obtained from rigid blocks model with a constant dip angles ranging from 10° to 60° is given by black dashed lines. (d) Fault geometry used. 212

LIST OF TABLES

4.1 List of geophysical equipments used in 2015 field survey 67
4.2 GPS coordinates along the electrical resistivity profile with 5m electrode spacing in Sarpang 70
4.3 Range of *a priori* geophysical parameters used in res2dmod 79

5.1 List of geophysical equipments for geophysical field survey in Phuentsholing . 150
5.2 Inversion results. The parameter values are associated with the most highest relative frequency model. The associated uncertainties are indicated in bracket. Uncertainties on each parameter are given by the full width at half maximum. The symbol '-' means no constraint has been obtained. 173

TABLE OF CONTENTS

1 Introduction: Thesis overview **1**

1.1 Rationale and goal of the thesis 1

1.2 Main question and approach 2

1.3 Thesis structure 3

2 Geodynamic Setting **5**

2.1 Introduction 5

2.2 Geodynamic setting of the Himalayas 7

2.2.1 Indo-Eurasia collision and formation of the Himalayas 7

2.2.2 Geological and tectonic framework of the Himalayas and Tibet 9

2.3 Geophysical constraints on the geodynamics and structures of the Himalayas . 11

2.3.1 Seismic studies 12

2.3.2 Gravity studies 14

2.3.3 Geodesy 16

2.3.4 Earthquake hazard in the Himalayas and contribution role of modern seismology 19

I Methods **27**

3 Near-surface geophysics **29**

3.1 Introduction 29

3.2 Advantages and shortfalls of near-surface geophysical methods 30

3.3 Types of geophysical methods 31

3.3.1 Electrical resistivity 32

3.3.2 Seismic refraction 42

3.3.3 Gravity . . . 48
3.4 Geophysical Inverse theory . . . 52
3.4.1 Conceptual Introduction . . . 52
3.4.2 Mathematical background . . . 54
3.4.3 Stochastic Inversion used in the thesis . . . 56

II Application to south-central and south-west Bhutan 59

4 Characterization of Topographic Frontal Thrust geometry in Sarpang 61
4.1 Geology of study area . . . 61
4.1.1 Introduction . . . 61
4.1.2 Geology and tectonics . . . 61
4.1.3 The Topographic Frontal Thrust (TFT) . . . 62
4.2 Geophysical field campaign 2015 . . . 65
4.2.1 Introduction . . . 65
4.2.2 Schedule of field program . . . 66
4.2.3 List of field equipments . . . 67
4.2.4 Electrical Resistivity Profile . . . 67
4.2.5 Seismic refraction . . . 83
4.2.6 Micro-gravity . . . 90
4.2.7 Results, discussion and conclusion: GJI paper . . . 93

5 Main Frontal Thrust geometry in Phuentsholing and Lhamoizingkha: Preliminary results 149
5.1 Introduction . . . 149
5.2 Field work in Phuentsholing in 2016 . . . 149
5.2.1 List of field equipments . . . 150
5.2.2 Site selection . . . 150
5.3 Geology of study area . . . 155
5.4 Data acquisition . . . 159
5.4.1 Electrical Resistivity and gravity data . . . 159
5.5 Data analysis . . . 161
5.5.1 Electrical resistivity tomography . . . 161
5.5.2 Gravity . . . 167
5.6 Inversion approach . . . 169

5.6.1 Results . . . 169
5.6.2 Discussion and conclusions . . . 179
5.7 Field work in Lhamoizingkha . . . 183
5.7.1 Introduction . . . 183
5.7.2 Geology of Piping-Lhamoizingkha area . . . 185
5.7.3 Field equipment . . . 187
5.7.4 Electrical resistivity data . . . 187
5.7.5 Conclusion . . . 193

6 Lateral variations along the Himalayan arc 195
6.1 Introduction . . . 195
6.2 Lateral variations: Bhutan Himalayas vs Nepal Himalayas . . . 196
6.3 Lateral variations across the Bhutan Himalayas . . . 198
6.3.1 Geology, topography & seismotectonics . . . 198
6.3.2 Geometry of the MFT . . . 204
6.4 Conclusion . . . 205

7 Conclusions 207
7.1 Main results . . . 207
7.2 Discussions . . . 210
7.2.1 Overthrusting slip rate estimation . . . 210
7.2.2 Tectonic deformation at the front . . . 213
7.3 Future works . . . 214
References . . . 217

A Annexes 233
A.1 First paleoseismic evidence for great surface-rupturing earthquakes in the Bhutan Himalayas . . . 233
A.2 Evidence of interseismic coupling variations along the Bhutan Himalayan arc from new GPS data . . . 247
A.3 Segmentation of the Himalayas as revealed by arc-parallel gravity anomalies . . . 265
A.4 Abstract: HKT 2016 . . . 276

CHAPTER 1

INTRODUCTION: THESIS OVERVIEW

1.1 Rationale and goal of the thesis

Since advent of modern seismology (J. Dewey & Byerly, 1969; Agnew et al., 2002; Zoback, 2006), remarkable advances have been made in scientific understanding of earthquake source processes and its associated risk implications to society. Despite this achievement, earthquake still persists to be the greatest harbinger of chaos and destruction to society. The recent devastating events of 25 April 2015 Gorkha earthquake, 11 March 2011 Tohoku Japan earthquake and 26 December 2004 Indian ocean earthquake are a grim reminder of how a single event could cause unthinkable misery and destruction within a matter of 10s of seconds.

Located in one of the seismically active regions of the eastern Himalayas, the Kingdom of Bhutan is highly vulnerable to earthquakes and other geohazards. Continual convergence of India towards Eurasia continent at ca. 20 mm per annum (Bilham et al., 1997; Lavé & Avouac, 2000; Vernant et al., 2014; Marechal et al., 2016) results in a cumulative stress accumulation of $\sim$ 2 m per century, which is accommodated by either co-seismic, pre-seismic, or post-seismic . Most of the interseismic deformation deficit is released during large Himalayan earthquakes of M >8 compared to long term deformation (Bilham et al., 1997; Cattin & Avouac, 2000). Thus study of interseismic deformation pattern is of great significance for seismic hazard assessment. As a result of remaining isolated and cut off from the rest of the world until few decades ago, only limited studies concerning earthquake hazard assessment have been conducted in the Bhutan Himalayas; earthquake disaster resilient measures and public advocacy and awareness are still at its infancy stage. More importantly, in absence of a national seismic hazard map, the seismic code in the Bhutan Building Rules 2002 is based

on extrapolation of the Indian seismic zonation and implemented as per Indian Seismic code IS 1893-1984 and IS 1893-2002.

Development of proper seismic zonation map and seismic resilience building requires good understanding of the geology, active tectonics mapping and accounts on historically significant earthquakes. The biggest challenge is that records of damaging historical earthquakes are scarce and no proper information on active fault systems for the country is yet available. To understand and assess earthquake hazard in the region, detailed mapping of seismogenic fault is a top priority. In the Himalayan region, it is now well known (Lavé & Avouac, 2000; Berthet et al., 2014; Le Roux-Mallouf et al., 2016) that historic major earthquakes mostly occur on the Main Himalayan Thrust (MHT), which expresses on the surface the Main Frontal Thrust (MFT). Thus detailed mapping of the MFT fault system is extremely important to determine the geometry of fault and assess risk posed by this seismogenic fault system.

In the Bhutan Himalayan region, Berthet et al. (2014) reported 8.8±2.1 mm/year of vertical displacement as revealed from geomorphological analysis of the fluvial terraces in Sarpang and Gelephu area. Assuming a fault dip of 25°±5 estimated from bedding structural information of Long et al. (2011) and projection of fault trace observed at the surface, they approximated a horizontal shortening rate of 20.8±8.8 mm/year. The paleoseismic study further revealed that at least two historical events of M>8 have taken place on the MFT in Sarpang region (Le Roux-Mallouf et al., 2016). However, the overthrusting slip rate, which is an important parameter for seismic hazard assessment, is not well constrained due to uncertainty in the fault geometry at shallow subsurface. To address this short fall, near-surface geophysical methods involving seismic refraction, electrical resistivity and gravity are adopted in this thesis to assess the geometry of the fault and study complex near surface geological structures along the southern frontal system of the Bhutan Himalayas.

1.2 Main question and approach

The uncertainty in the MFT geometry, especially at shallow depth, is an important constraint which need to be addressed for proper seismic hazard assessment. Good constraints on the fault geometry at shallow subsurface is crucial for understanding seismic hazard and risk (Suzuki et al., 2000; Kaiser et al., 2009). This is particularly relevant in case of the Bhutan Himalaya region where documentation on historical events are scarce and only limited stud-

ies have been performed so far.

The geometry of MFT is also important for studying lateral variations as well as to test the seismic gap hypothesis proposed by earlier researchers (Bilham & England, 2001; Bilham, 2004). Recent efforts (Berthet et al., 2014; Le Roux-Mallouf et al., 2016) to document historical major events in Bhutan through geomorphological and paleo-seismological studies estimated Holocene vertical uplift rate of 8.8±2.1 mm/year in the Sarpang area and revealed that at least two major seismic events having occurred in Bhutan region during the past millenia. The last major event with epicenter in Bhutan is constrained to have occurred in 1714 AD (Hetényi et al., 2016).

With surface observation only, the horizontal convergence rate and the overthrusting slip rate cannot be properly constrained. Thus to study the fault geometry at shallow subsurface, near-surface high resolution geophysical techniques involving electrical resistivity, seismic refraction and micro-gravity were deployed. Studies conducted in other areas (Suzuki et al., 2000; Demanet et al., 2001; Morandi & Ceragioli, 2002; Louis et al., 2002; Wise et al., 2003; Nguyen et al., 2005; Nguyen, 2005; Kaiser et al., 2009; Berge, 2014; Gabo et al., 2015; Villani et al., 2015) have shown that near-surface geophysical techniques combined with robust *a priori* information can be a powerful tool to accurately image and constrain complex shallow surface fault geometry and other petro-physical parameters.

1.3 Thesis structure

The introduction part covers objectives, goals and approach of this thesis. This is followed by an overview of geodynamic and geological setting of the Himalayan region. The general geological and geodynamic setting of the Himalayas are discussed at length to provide a vivid account of formation of the Himalayas, stages of orogenic processes and its environmental and societal implications in form of natural disaster such as earthquake hazards. Non-exhaustive review of past geophysical works in the Himalayas is presented here to capture the geodynamic and geophysical framework characteristics of the region. Under the methods chapter, the main advantages and limitations of geophysical techniques are discussed. Detailed theoretical aspects and practical applicability of the geophysical techniques adopted in the present study are elaborated. In chapters that ensue, geophysical methods adopted in this thesis are applied to the study areas in southern Bhutan to constrain the geometry of the MFT at shallow surface depth with aim to assess the overthrusting slip rate and study lateral

variations along the front. Detailed accounts of the near-surface geophysical field campaigns conducted in 2015 and 2016 are presented to provide greater insight into preparation stages of the field deployment and challenges associated to it. Data acquisition is given utmost focus as it is the most important input for data analysis, interpretation and deduction of results to the key questions of the thesis. Detailed account of analysis of geophysical data are provided with special emphasis on development of inversion process and incorporation of available *a priori* information in the analysis process. Next an overview of lateral variations along the Himalayan arc as well as within the Bhutan Himalayas are presented and discussed at length to highlight its significance in terms of geodynamics and seismic hazard assessment in the region. In the concluding chapter, results from the near-surface geophysical methods adopted here are synthesized and discussed to constrain the tectonic characteristics and its seismic hazard implication of the study area. The final concluding part of the thesis captures key findings and shortcomings of the study, and recommendations for future potential areas of research in order to substantiate and supplement findings of the current study as well as to improve the general understanding of the Himalayan geodynamics with overarching objective to assess earthquake hazard in the Himalayan region.

The annex sections comprises of three published manuscripts where I am also one of the co-authors. These works were simultaneously implemented as part of the same project on **"Seismic coupling and megaquake along the Himalayan arc"** during the course of my PhD study (2015-2017). Results from my research presented at the 2016 HKT Workshop is also included in the annex.

CHAPTER 2

GEODYNAMIC SETTING

2.1 Introduction

From the Alps to the Andes and the Himalayas, mountain ranges are nature's unequivocal epitome of awe-inspiring majesty and prominent features that dominants the face of the Earth. In ancient times, many believed that mountains were abode of god, and therefore considered holy and sacred. Thanks to advances in modern geology, mountains as we understand today are the ultimate manifestation of continental dynamics ensued over millions of years in geological time scale.

In the mid-19^{th} century, the American geologists James Hall and James Dwight Dana proposed the concept of geosyncline to elucidate formation of mountains based on gradual deepening and filling up of basin as a result of crustal contraction due to cooling and contracting Earth (Knopf, 1948). The geosynclinal hypothesis was widely accepted explanation for origin of most mountain formation until it was replaced by the theory of plate tectonics. Alfred Wegener was the first person who came up with the idea of continental drift theory, which ultimately paved the groundwork for the development of the theory of plate tectonics. In 1915 Wegener proposed that the continents as we know of today were once part of one single super-continent, which he termed as Pangaea (meaning "all lands"). His idea was supported by observations that the coastlines of South America and Africa fit so well and similar rock formations were found on both the continent. However, Wegener's idea was largely dismissed as it failed to explain the mechanism how continents could drift across the Earth's surface. In spite of steep oppositions from the scientific community, subsequent works by different researchers, notably Harry Hess's theory of sea floor spreading provided compelling

driving mechanisms to explain the force required to drive the continents apart. Additional evidences acquired from the sea floor bathometry and paleomagnetism in 1960s lead to the ultimate acceptance of the theory of plates tectonics as first proposed by Alfred Wegener.

The concept of plate tectonics played a major role in understanding how the Earth's mountain ranges and its continental crust evolved. It was Wilson (1965) who first proposed that orogeny resulted from convergent plate motion involving important sideways motion along the convergent belts. His theory helped explain many uncertainties of the nature of orogeny by emphasizing on the definite process of orogeny, such as plate convergence, which is in good agreement with the theory of uniformitarianism (Sengor, 1990). The preceding theory of isostasy (Airy, 1855; Pratt, 1855) and the theory of geosynclines were derived from one-dimensional view of orogenesis wherein only the vertical dimension of orogenic mobility was considered either as vertical uplift or subsidence.

The emergence of plate tectonics theory, however, drastically changed the understanding of orogenic processes by allowing three-dimensional mobility aspects of rock packages within the orogenic belts. Seismological observations, especially following the establishment of World Wide Seismic Station Network (WWSSN), played an important role in further underscoring the relevance of new global tectonics. Distribution pattern of seismicity largely coincides with the rift system, island arcs and active mountain belts and active continental margins (Isacks, B. & Sykes, 1968). This indicates that much of the deformation is being concentrated along the edges of the plates and relatively little deformation is taking place within the plates themselves.

Mountain building generally takes place in two basic ways (J. F. Dewey & Bird, 1970). The thermally driven first type is called the island arc or cordilleran where mountains are formed on leading plate edges above a descending plate. The other type, mostly mechanically driven, is formed due to continent/island arc or continent/continent collision zone. The orogenic process that lead to formation of the Himalayas started with the collision of India and Eurasia at the beginning of Tertiary resulting in the first phase of folding and metamorphism in the Himalayas (Le Fort, 1975). The second cycle in the Miocence time mainly resulted in intra-continental deformation with subduction taking place along south vergent thrusting. The India-Asia continental collision apparently not only created the Himalayas but also was responsible for rejuvenating old orogenic belt, Tien Shan, approximately 1000 km north of the Indus-Tsangpo (also called Yarlung-Tsangpo) suture zone and as a consequence lead to formation of important strike-slip faulting oblique to the suture zone (Molnar & Tapponnier,

1975).

Mountains play important role in the interaction between solid Earth and climate processes (Avouac, 2015). The large-scale interaction between lithospheric deformation and atmospheric circulation potentially makes study of the Himalaya-Tibet orogeny of much greater significance than a simple matter of intracontinental deformation induced due to continental collision (Searle et al., 1987). Mountain ranges are also highly susceptible to various kinds of natural hazards such as landslide, floods and earthquakes. Thus concerted effort to study orogenic process is the key point in better understanding of how mountain ranges evolve and the important role it plays for the greater benefits to the society we live in.

2.2 Geodynamic setting of the Himalayas

2.2.1 Indo-Eurasia collision and formation of the Himalayas

The current configuration of the ∼2500 km long Himalayan arc and the Tibetan plateau was formed as result of collision between India and Asia (Molnar & Tapponnier, 1975; DeCelles et al., 2002; Bouilhol et al., 2013). Prior to the collision in the pre-Valanginian time, the two continents were separated by the Tethys ocean, which subsequently got consumed underneath the southern margin of Asia (Powell & Conaghan, 1973; Avouac, 2008) (Figure 2.1). The exact timing of the collision between the two continents reportedly range from as early as ∼70 Ma in the Late Cretaceous time (Yin & Harrison, 2000) to ∼40 Ma in the Late Eocene time (Bouilhol et al., 2013). Sea-floor spreading history of the Indian ocean (Patriat & Achache, 1984; Besse et al., 1984) constrain the age of collision around 50 Ma corresponding to drastic change in the convergence rate between India and Eurasia from 100-180 mm/year to about 40 mm/year. The uplifting of the Himalayas, however, happened much later in the Early Miocene period coinciding with underthrusting of India beneath the Eurasian continental plate (Powell & Conaghan, 1973). The doubling of the crust beneath the Tibetan plateau as result of underthrusting and crustal shortening required approximately 5 km of surficial uplift to maintain isostatic equilibrium. By Middle Miocene the rising Himalayas started shedding large volume of coarse clastics back in the Indo-Gangetic molasse foredeep (Powell & Conaghan, 1973). Similarly, the autochthonous materials from the pre-Miocene sediments were scraped off the northern margin of the underthrusting Indian plate and regurgitated as thrusts and nappes towards the south.

Since collision of the two continents in the Cenozoic time, India has been indenting into

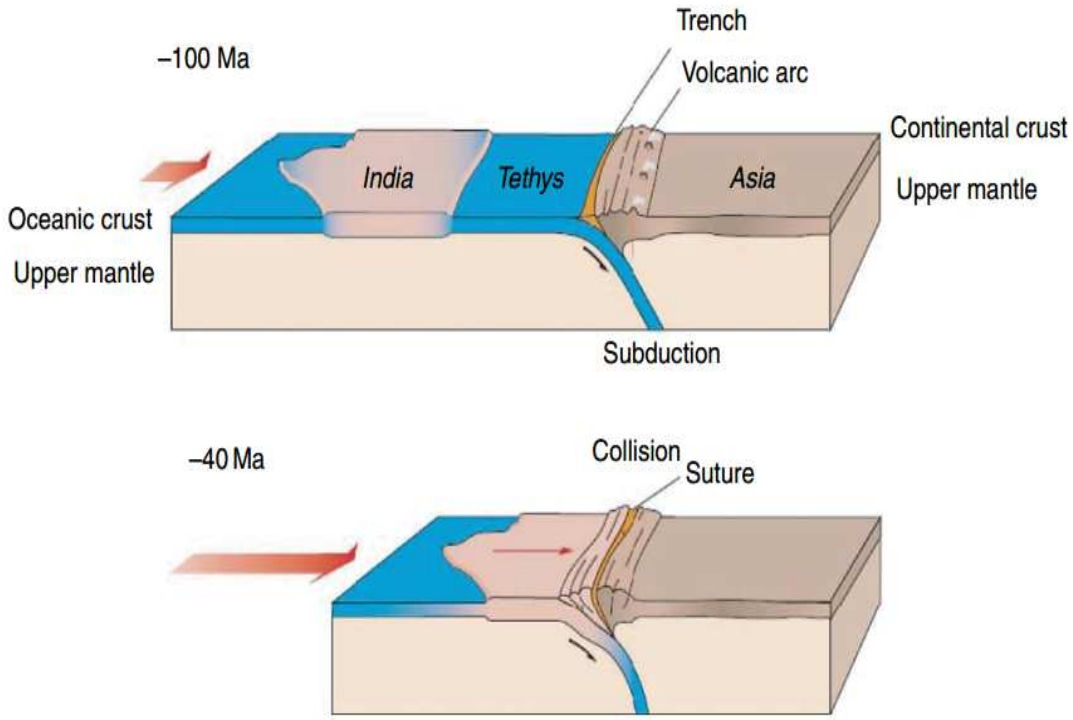

Figure 2.1: Cartoon depicting the Tethys sea that separates India from Eurasia during pre-Valanginian time, gradual subduction of the Tethys along the southern margin of Asia and collision of the two continents leading to formation of the great Himalayas (After Avouac, 2008).

Asia at ∼40 mm per annum (Molnar & Stock, 2009) culminating in a post-collision convergence of ∼2000 km between India and Eurasia. The Tibetan-Himalayan collision zone mainly consists of three belts that absorbed significant proportion of the convergence (Murphy & Yin, 2003). These three belts are 1) the Himalayan fold-thrust belt, 2) the Tethyan fold-thrust belt, and 3) the Indus-Tsangpo suture zone. About 50 % of the convergence between India and Eurasia is accommodated in the fold and thrust belt of the Himalayas (DeMets et al., 1994; Bilham et al., 1997; Lavé & Avouac, 2000) and remainder is transferred to extensional and strike-slip deformation in Tibetan plateau and central Asia (Tapponnier & Molnar, 1979; DeMets et al., 1994; Zhang & Ding, 2003). Estimates of Holocene horizontal shortening rates in the Himalayas ranges from 23.4±6.2 mm/yr in eastern Himalaya (Burgess et al., 2012) and 21.5±1.5 mm/year from central Himalaya (Lavé & Avouac, 2000). These geologically constrained shortening rate generally agree with GPS convergence velocity of ∼20 mm per year (Bilham et al., 1997; Ader et al., 2012; Vernant et al., 2014).

2.2.2 Geological and tectonic framework of the Himalayas and Tibet

Subsequent to closure of the Tethys ocean in Eocene time, deformation propagated towards the south across the Tibetan-Tethys zone to the High Himalaya (Searle et al., 1987). This resulted in deep crustal thrusting, Barrovian metamorphism, migmatization, and development of Oligocene-Miocene leucogranites accompanied by development of south-vergent recumbent nappes inverting metamorphic isograds. Continued convergence in the Late Tertiary led to development of large-scale north-vergent backthrusting along the Indus-Tsangpo suture zone (Searle et al., 1987).

The general geology and tectonic framework of the Himalayas are shown in Figure 2.2. It is now well recognized that the Indus-Tsangpo suture zone (ITSZ) is the zone of collision between the Indian continental plate and Eurasian continental plate along which Tethys Ocean was consumed by subduction processes (J. F. Dewey & Bird, 1970; Powell & Conaghan, 1973; Le Fort, 1975; Searle et al., 1987). The suture zone is characterized with ophiolite mélanges composed of Neotethys oceanic crustal flyschs and ophiolites. Towards the north of the ITSZ, geology is dominated by the linear plutonic complex that runs for almost the entire length of the Himalaya and is known as the Trans-Himalayan Batholith. These plutons are emplaced along the Kohistan-Ladakh region in the west, Kailas-Gangdese in southern Tibet and Lohit region in Arunachal Pradesh (Sharma, 2009). South of the ITSZ lies the Tethyan sediment which is separated from the Higher (or Greater) Himalaya Crystalline by the down-to-the-north low angle normal fault called the South Tibetan Detachment System (STDS). The Tethyan Sedimentary Sequence consists of largely fossileferous and disharmonic thick marine sediments that were deposited on the continental shelf and slope of the Indian continent. The fossiliferous Tethys sediment begins where metamorphism has ended and an independent structure begins along with complex folds and thrusts which are dishormonic in relation to the underlying crystalline unit (Gansser, 1981).

The Higher Himalayan Crystalline, which forms the base of the Tibetan or Tethyan sediments, consists of coarse or banded gneisses with kyanite/silliminite and garnet (Gansser, 1981); locally the gneisses can occur as migmatite. Early to middle Miocene leucogranites intruded the Higher Himalayan sequence and the overlying Tethyan Sedimentary sequence (Le Fort, 1986). The lower extent of the crystalline slab is marked by the Main Central Thrust (MCT). The high-grade metamorphic rocks of the Higher Himalayan Crystalline thrust over the low-grade Lesser Himalaya metasediments along the MCT. Paleogeographically, the Lesser Himalaya belongs to the northern extension of the Indian shield, which borders the

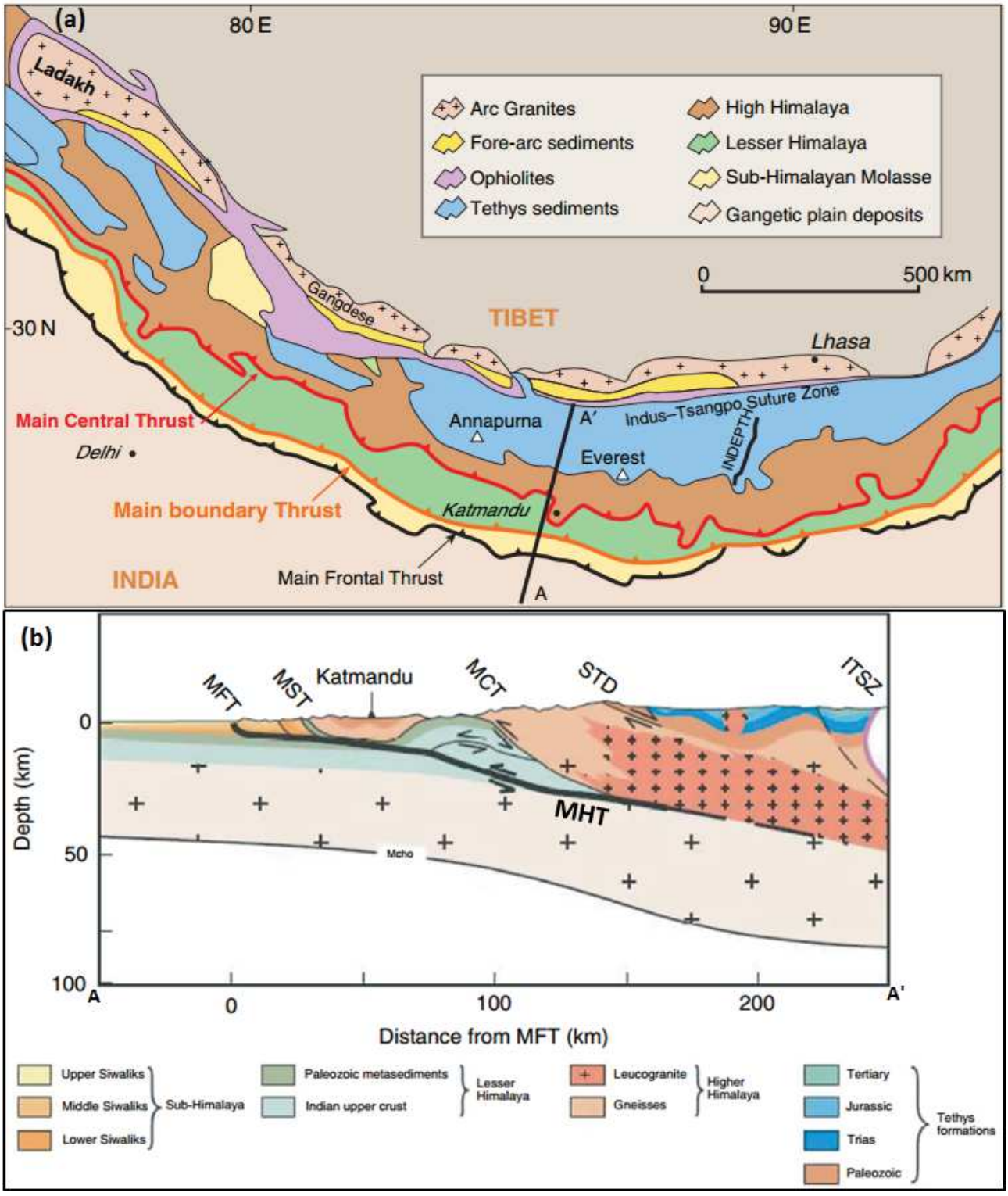

Figure 2.2: (a) Simplified geological map of the Himalayan arc, (b) Cross-section along AA' in (a) along the longitude of Katmandu.Thick black line represents the MHT which expresses at the the surface as MFT at the front of the Siwalik Formation (Modified after Avouac, 2008).

shallow Tethyan sea (Gansser, 1981). It mainly consists of unfossiliferous sedimentary and metasedimentary rocks and is limited to the south by the Main Boundary Thrust (MBT). The low-grade metasediments of the Lesser Himalaya thrust over the unmetamorphosed sub-Himalayan Neogene molasse along the MBT. The Siwaliks molasse of the sub-Himalaya is made of sediments that originated from the Himalaya in the north during the upper Miocene and deposited in the low foothills bordering the north Indian plains (Gansser, 1981). The sub-Himalayan Siwalik is bounded to the south by the Main Frontal Thrust (MFT), which coincides with the present Himalayan topographic front. The MFT is surface expression of active plane of convergence between India and Eurasia; at depth, like the MCT and MBT, it roots into the MHT, a gently dipping plane of décollement (Figure 2.2). South of the MFT, the Quaternary Himalayan foreland sediments overlap on the cratonic rocks of northern India.

2.3 Geophysical constraints on the geodynamics and structures of the Himalayas

"Geology is the study of past; the future is geophysics." E. Argand, 1919

Non-invasive geophysical techniques constitute the primary tool employed in constraining near-surface to deep earth structures for applications ranging from engineering, environmental, mineral resources mapping to geodynamic evolution studies. Combined with information gathered from surface geological studies, availability of high precision geophysical equipment capable of detecting minute changes in measurement signal enables accurate and high resolution imaging of the earth subsurface. Advances in high computing capacity and availability of affordable processing software further promoted wide usage of geophysical methods.

It is no surprise that our current understanding of the earth subsurface is mainly based on measurement and interpretation of observable geophysical signals detected on the surface of the Earth. Over the last several decades many geophysical studies have been conducted in the Himalayan region with goal to improve our understanding of the evolutionary process and geodynamic of the Himalayas and assess its associated geo-hazards, particularly from that of earthquake hazard. Some of the many geophysical studies carried out in the past are discussed below with particular emphasis on their roles in broadening our knowledge on the many scientific questions including (but not limited to): How thick is the crust underneath the Himalaya and the Tibetan plateau? What are the major structures that play critical role in deformation of the collision zone? Are there any significant lateral variations along the arc that might play important role in terms of seismic hazard and geodyamics of the Himalayan

deformation mechanism? What is present convergence velocity between India and Eurasia continent? How does this translate into occurrence of major seismic events? Which are the potential areas/regions that are likely to rupture? What is the likely magnitude of future impending earthquake? Does seismicity correlate with the mapped major tectonic units? What is recurrence interval of great Himalaya events? Are there any perceptible historical pattern that could repeat in future? What are the main parameters such as fault geometry, coseismic slip velocity and horizontal shortening rate at the front for seismic hazard and risk assessment?

2.3.1 Seismic studies

Several seismic studies including reflection and broadband seismic experiments have been conducted in the Himalaya and Tibetan plateau with objective to image deep tectonic structures underneath and in the process help to answer some of the pressing scientific questions pertaining geodynamics of such young and active mountain formation system. Hirn et al. (1984), based on wide-angle reflection data, reported that the Moho beneath south of Yarlung Tsangpo suture is 70 km depth, while further to the south in the Himalayas the Moho appears at 55 km (Figure 2.3). They interpreted that the thickening of crust from north-south across the Himalaya-Tibetan plateau is not due to superimposition of two crusts on each other but rather a result of separate doubling by decoupling and thrusting of the upper and lower crustal layers (and possibly the Moho). This interpretation seems to agree with observation that the 70 km thick Tibetan crust depicts two layers of different mean velocities with each being twice as thick as normal crustal thickness elsewhere.

Similarly, Zhao et al. (1993), as part of INDEPTH (International Deep Profiling of Tibet and the Himalayas) effort observed prominent mid-crustal reflections interpreted as the northern extent of Indian plate thrusting underneath the Tibetan Himalaya along the active plane of décollement termed the Main Himalayan Thrust (Figure 2.4). They also suggested that the mid-crustal reflections along with geometries indicative of large scale structural imbrication supports the view that crustal thickening beneath southern Tibet was attained by wholesome thrusting of the Indian plate underneath the structurally imbricated upper crust of the Tethyan Himalaya. The reflection from the Moho is estimated at 75 km depth and gently dipping ($\sim$15°) towards the north. Existence of locally anomalous amplitudes (bright spots) at 15-18 km underneath southern Tibet near where the décollement reflectors terminates were reported (Brown et al., 1996; Nelson et al., 1996). This bright spot underneath

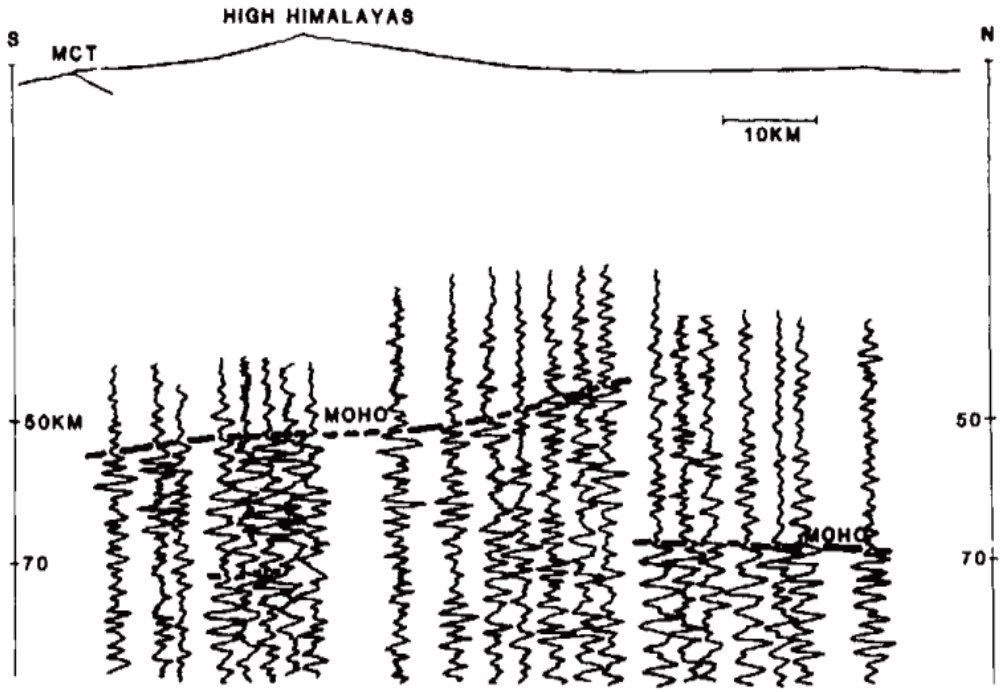

Figure 2.3: Wide-angle seismic data showing variation in the depth of reflections coming from Moho underneath the Higher Himalayas and south of Yarlung Tsangpo (After Hirn et al, 1984)

the Tibetan plateau north of Yadong-Gulu rift is interpreted as magma like fluid, which is consistent with extensional tectonics, abundant geothermal activity and high heat flow of the region.

The Hi-CLIMB (Himalayan-Tibet Continental Lithosphere During Mountain Building) seismological experiment acquired high-resolution images of the crust-mantle boundary (or Moho) underneath the Himalayas and Tibet (Nábělek et al., 2009). The Moho, as presented in Figure 2.5, gently dips at a depth of 40 km underneath the Ganges Basin on the Indian plate to 50 km under the Himalayas. North of the Greater Himalaya, the Moho deepens rapidly reaching to a depth of 70 km beneath the Yarlung-Tsangpo Suture zone at a horizontal distance of 250 km from the Main Frontal Thrust (MFT).

The Moho beyond this point maintains constant depth underneath the extent of the Lhasa block. It again sharply reappears beneath the Qaingthang Block but at a shallower depth of 65 km. The MHT, corresponding to velocity decrease with depth depicted by the continuous blue feature in Figure 2.5, extends from a shallow depth under the Himalayas to mid-crustal depth beneath the Lhasa Block. However, the Indian upper crust is limited till the Lhasa Block and does not underplate it, implying that ductile part of MHT takes up simple shear as well

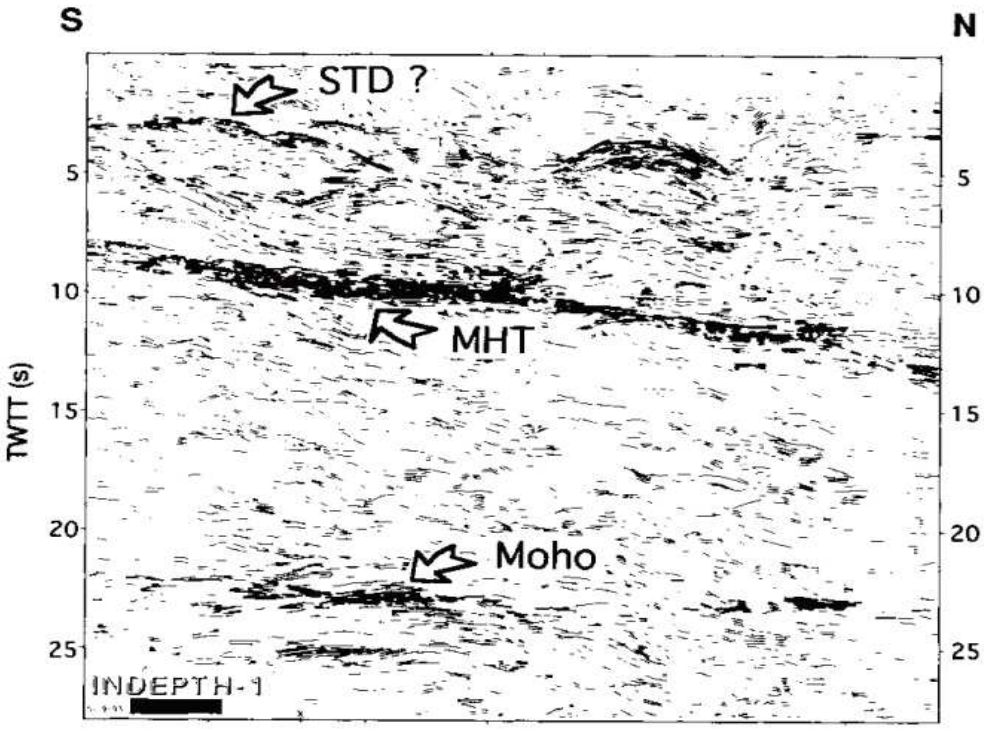

Figure 2.4: Reflections from the INDEPTH deep seismic profile and corresponding interpreted major tectonic features MHT, STD and Moho (After Zhao et al, 1993).

as act as conduit for crustal transfer (Nábělek et al., 2009). The lower Indian crust, north of the Himalayas beneath the Lhasa Block, is characterized with high velocity and high density eclogite materials (Schulte-Pelkum et al., 2005; Hetényi et al., 2007; Nábělek et al., 2009).

2.3.2 Gravity studies

The principle of isostasy is defined as the state of gravitational equilibrium between the Earth's crust and the mantle such that lighter crust floats on the denser mantle. Two main models are employed to explain the theory of isostasy namely: Airy (1855) and Pratt (1855) hypothesis. Airy's idea, (apparently stole from Pratt), is based on Pascal's law that assumes equal density throughout the crust. However, since the thickness of the crust is not uniform everywhere, the Airy hypothesis suggests that the thicker part sinks into the mantle and the thinner part floats on the mantle. In other word mountains have crustal roots (or mass deficiency underneath) that compensate the relief. Pratt's model, on the other hand, explains that density varies laterally and thus low density mountain ranges extends higher above the sea level than other masses with higher density. In general, Airy's model is relevant to continental mountain ranges where mountain ranges have thick crustal roots and Pratt's model for mid-oceanic ridges where topography is supported by density changes.

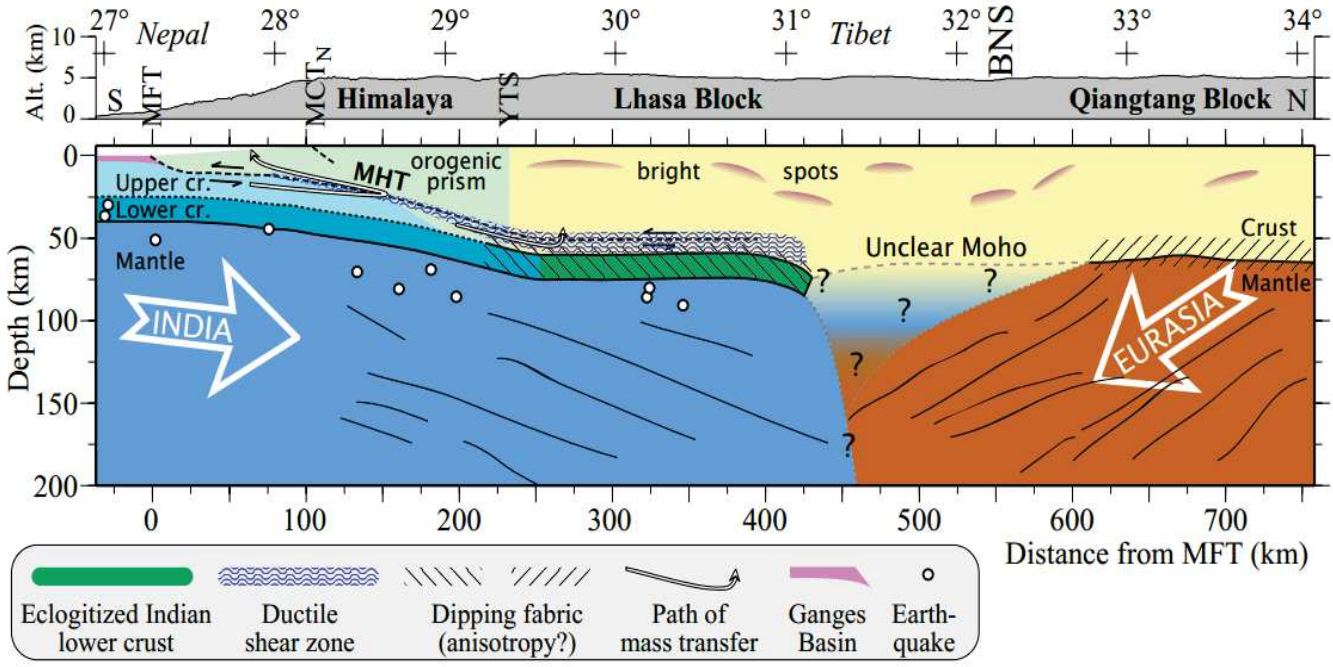

Figure 2.5: Interpretative cross-section of India-Eurasia collision zone. The Indian lithosphere underplates the Himalaya and Tibetan plateau upto ~450 km from the MFT (After Hetényi, 2007).

Based on theory of gravity, existence of anomalous density distribution within the Earth can be measured to discern internal structures of the Earth. The existence of density contrast across the Himalayan range due to excess mass in the range and low density crustal mountain root provides excellent opportunity to perform gravity measurements to study geodynamic characteristics of the Himalayas. Several gravity studies (Lyon-Caen & Molnar, 1983, 1985; Cattin et al., 2001; Hetényi et al., 2007; Tiwari et al., 2006; Berthet et al., 2013; Hammer et al., 2013; Ansari et al., 2014; Hetényi et al., 2016) have been conducted in the Himalayas to constrain subsurface tectonic features which invariably plays an important role in understanding the geodynamics of the Himalayas. Lyon-Caen & Molnar (1983) and Lyon-Caen & Molnar (1985) employed a simple elastic mechanical model to explain the observed gravity anomaly across the Himalayan arc. They noted that to fit the observed gravity anomaly with the calculated one, flexural rigidity underneath the Greater Himalaya (about 130 km north of the Himalayan front) must be less than the plate underneath the Lesser Himalaya, the Ganga Basin and the Indian shield. By only taking into account the weight of the Himalayan mountains, they estimated more negative gravity anomaly than observed. Therefore, a bending moment must be applied at the end of the Indian plate to compensate for the enormous

weight of the Himalayan range. Further the gravity anomaly requires the Moho with dip of 3° beneath the Lesser Himalaya to about 15° underneath the Greater Himalaya. Similar results were reported by other studies (Cattin et al., 2001; Hetényi et al., 2007; Tiwari et al., 2006) supporting the model with flexural rigidity of the underthrusting Indian plate decreasing northwards and steepening of the Moho underneath the Greater Himalaya as the primary factor attributable to the observed gravity anomaly across the range. The Moho is constrained to be deepening from about 35-40 km beneath the Ganges to 70-75 km under Tibet. These findings are in congruent with results reduced from seismological studies. However, unlike earlier studies (Lyon-Caen & Molnar, 1983, 1985) which proposed to explain the flexural rigidity and bending moment as a result of all or part of the Indian crust being detached from the lower part of the Indian lithosphere due to warming and weakening during the collision process, others (Cattin et al., 2001; Hetényi et al., 2007) postulated possibility of eclogitization process underneath southern Tibet to explain the hinge observed in gravity data and better fit with observed gravity anomaly. Based on analysis of the wealth of geophysical information, Hetényi et al. (2007) concluded that Airy-type isostatic compensation is very unlikely process in the Himalayas since it yields unrealistic densities; rather higher density eclogites at the lower Indian crust is required to support the Tibetan plateau as well as interpret the observed gravity anomaly.

The significance of gravity variation parallel to the Himalayan arc was studied by Hetényi et al. (2016). They noted that, unlike along the oceanic subduction area (Song & Simons, 2003) where both negative Arc Parallel Gravity Anomaly (APaGa) and negative Arc Parallel Topography Anomaly (APaTa) corresponds to location of large historical earthquakes, this correlation doesn't seem to be valid in the Himalayas. APaTa in the Himalayas mainly correspond to relief and erosional features, while APaGa strongly indicate presence of lateral segmentation that could act as limiting barrier for rupture during mega-scale Himalayan earthquakes; four such segments are interpreted to exist along the arc (Figure 2.6).

2.3.3 Geodesy

Based on geodetic measurements using Global Positioning System (GPS) (Bilham et al., 1997; Zhang et al., 2004; Bettinelli et al., 2006; Ader et al., 2012; Vernant et al., 2014; Stevens & Avouac, 2015; Marechal et al., 2016) and geological slip rate constraints (Lavé & Avouac, 2000; Burgess et al., 2012; Berthet et al., 2014) approximately 35-50 $\%$ of the convergence between Eurasia and Indian continental is accommodated in the Himalayan collision zone.

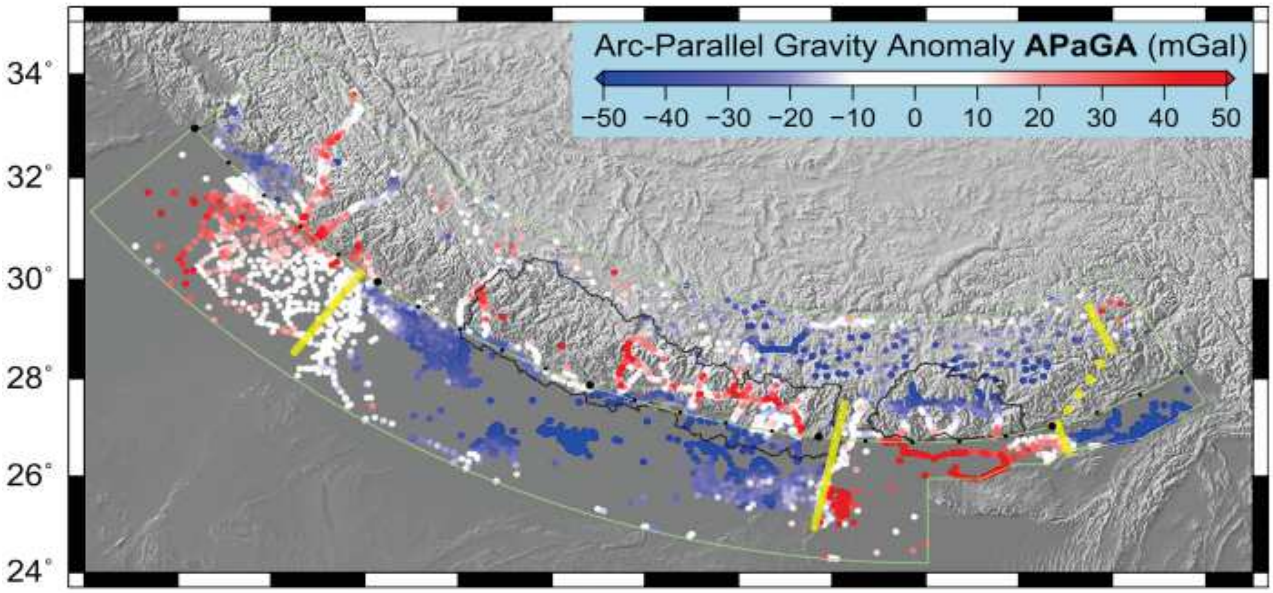

Figure 2.6: Arc-Parallel Gravity Anomaly. Red and blue values represent higher and lower values of gravity, resepectively, compared to the average profile perpendicular to the Himalayan arc. Yellow lines show change in arc-parallel gravity anomaly and highlight segments (After Hétenyi et al., 2016).

This convergence rate of 14-20 mm/year (Figure 2.7) is mainly responsible for the uplift, horizontal shortening and seismicity of the Himalayas (Bilham et al., 1997). Primarily due to wealth of information derived from decades of GPS observations in the Himalayan region, it is now generally understood that most of the convergence across the Himalaya takes place through slip along the plane of décollement—the Main Himalayan Thrust (MHT), which emerges at the surface along the Himalayan foothills as the Main Frontal Thrust (MFT). The rupture along the MHT is generally associated with large Himalayan earthquakes. Thus, constraining the geometry of the MHT and understanding its deformation mechanism over interseismic period is of critical importance in terms of seismic hazard assessment for the Himalayan region.

Past GPS as well as leveling studies (Jackson & Bilham, 1994; Jouanne et al., 2004; Bettinelli et al., 2006; Vernant et al., 2014; Marechal et al., 2016) obtained a preferable MHT dip angle of $\sim 10^{\circ}$ and depth of ca. 20 km from the surface to the décollement plane at the front of the Higher Himalaya range, approximately along the 3.5 km elevation line (Figure 2.8). The northern edge of the locked zone falls in the zone of micro-seismic clusters beneath the front of the High Himalayas (Pandey et al., 1995, 1999; Ader et al., 2012) (Figure 2.8) and it is also approximately coincident with downdip end of locked MHT where strain and stress builds up around the ramp on the MHT during interseismic period (Cattin & Avouac,

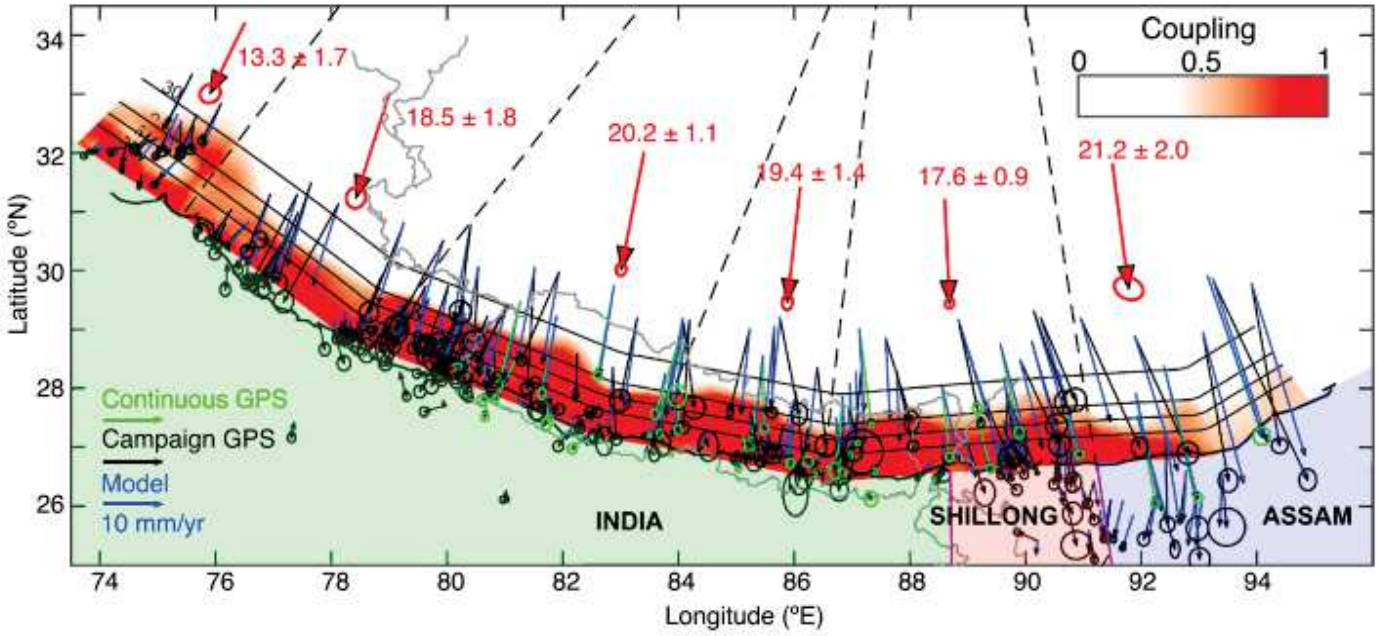

Figure 2.7: Coupling model and fit to the horizontal GPS data. Interseismic area is shown as shades of red. A coupling value of 1 means fully locked and 0 means fully creeping. The green and black arrows show the continuous and campaign gps velocities with their error bars, respectively. The blue arrows shows the modeled velocities which fit with the coupling. The dashed-line shows separation of region within which the long term velocity for that region is calculated show by large red arrow (After Stevens and Avouac, 2015).

2000; Bollinger et al., 2004). The width of the locked zone or interseismic coupling area is estimated to range between 100-120 km from the MFT to the edge of the MHT ramp, beyond which the MHT creeps aseismically. Since the width of the locked zone can be correlated to the width of the rupture (Jouanne et al., 2004) and given that there exists several seismic gaps along the arc that has not experienced major events for many centuries, these gaps are highly susceptible to future great Himalayan earthquakes. Based on interseismic coupling pattern in the central Himalayas, Cattin & Avouac (2000) concluded that the MHT slips freely over long term and it is locked during interseismic period.

Similar to other parts of the Himalayas, recent GPS studies in the Bhutan Himalayas (Vernant et al., 2014; Marechal et al., 2016) reported convergence rate of ca. 16.5-17.5 mm/year and the depth of the flat MHT segments along the Bhutan Himalayas to be around 10 km consistent with earlier studies. However, unlike in other parts of the Himalayas, Marechal et al. (2016) observed significant changes in seismic coupling between western/central and eastern Bhutan. In western/central Bhutan the width of fully coupled section along MHT is 135-155 km north of the MFT with abrupt downdip transition of the coupled zone; whereas

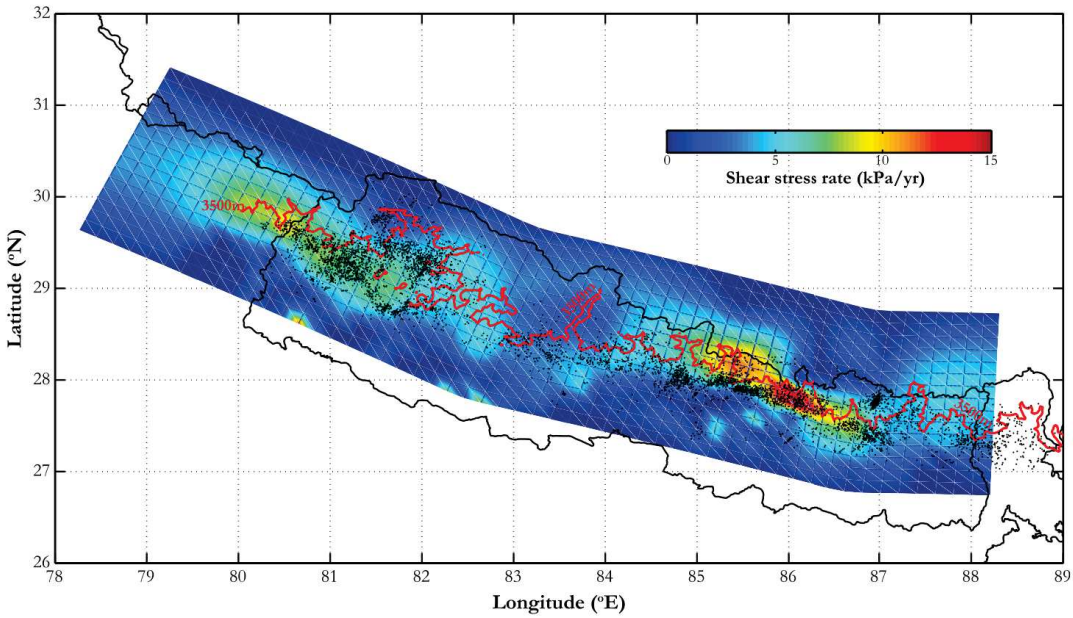

Figure 2.8: Mid-crustal microseismicity from 1996-2008 superimposed on shear stress accumulation rate on MHT, deduced from coupling pattern. The red line shows the 3500 m elevation beyond which the seismicity seems to drop (After Ader et al., 2012).

in eastern Bhutan the fully locked MHT is around 120-130 km limited by partial creeping segments in the updip as well as the downdip sections along the MHT (Figure 2.9). They opined that existence of partially coupled upper section of the MHT may suggest that long term convergence in the region may not be fully expressed in form of large earthquakes.

2.3.4 Earthquake hazard in the Himalayas and contribution role of modern seismology

Observational seismology constitutes an important part of scientific understanding of earthquake source processes and assessment of its associated hazard for disaster risk mitigation. The advent of modern seismology, especially following the introduction of long period seismographs and computers (1934-1962), enabled the exploitation of rich information inherent in seismic signals, both at global and local scales (Ben-Menahem, 1995). A wealth of knowledge now exists in our understanding of the seismotectonic characteristics of the region mainly derived from deployment of numerous temporary network as well as permanent national seismic networks. In spite of setbacks in the initial drive of seismological community to predict earthquake in short term, data from seismic events combined with advanced modeling techniques proved to be important steps in predicting ground motion of future expected earthquakes which can be cooperated in designing improved earthquake resistant infrastructures (Zoback, 2006).

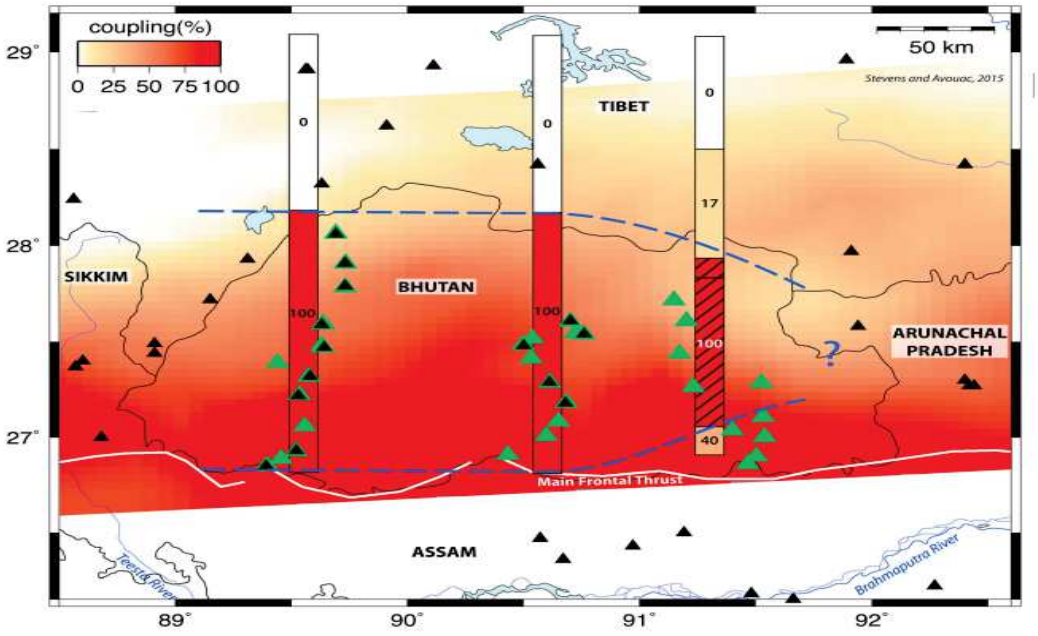

Figure 2.9: Interseismic coupling of the MHT in the Bhutan Himalayas. Rectangles show interseismic coupling for different fault segments. The hatched segment represents flat part of the MHT. Colored base map represents coupling as shown in Figure 2.7. Dashed blue line shows the possible limits of the fully coupled zone.Green triangles show GPS station and black triangles represents GPS stations used in Stevens and Avouac, 2015 (After Marechal et al., 2016).

Seismotectonic characteristics of the Himalayas

Even though written records of historical earthquakes exists for period spanning more than three millenia, the location and magnitude of earthquakes in sub-continent and vicinity areas prior to 1900 remain largely unquantified (Szeliga et al., 2010). Thus, uncertainty in location and magnitude of most historical earthquakes that occurred prior to 1900 is a pertinent issue for earthquake hazard assessment in the region. However, felt intensity information have been used by some authors (for example Szeliga et al., 2010) to quantify historical earthquakes.

Using seismicity data between 1961-1981 along the Himalayan arc, Ni & Barazangi (1984) reported that most epicenters are concentrated between the northerly dipping MBT and MCT (Figure 2.10a). They also noted hypocenter depth of most events to be around 10-20 km with focal mechanism showing predominantly thrust type faulting style along a shallow planer surface dipping $\sim 15^{\circ}$ towards north (Figure 2.10b). However, J. Kayal (2008) noted that fault plane solution in east Nepal Himalaya show mostly dominant strike-slip mechanism, whereas in west Nepal the fault solutions are predominantly low angle thrust faulting. Similarly, studies from the Eastern Himalayas (De & Kayal, 2003; Drukpa et al., 2006; Velasco et

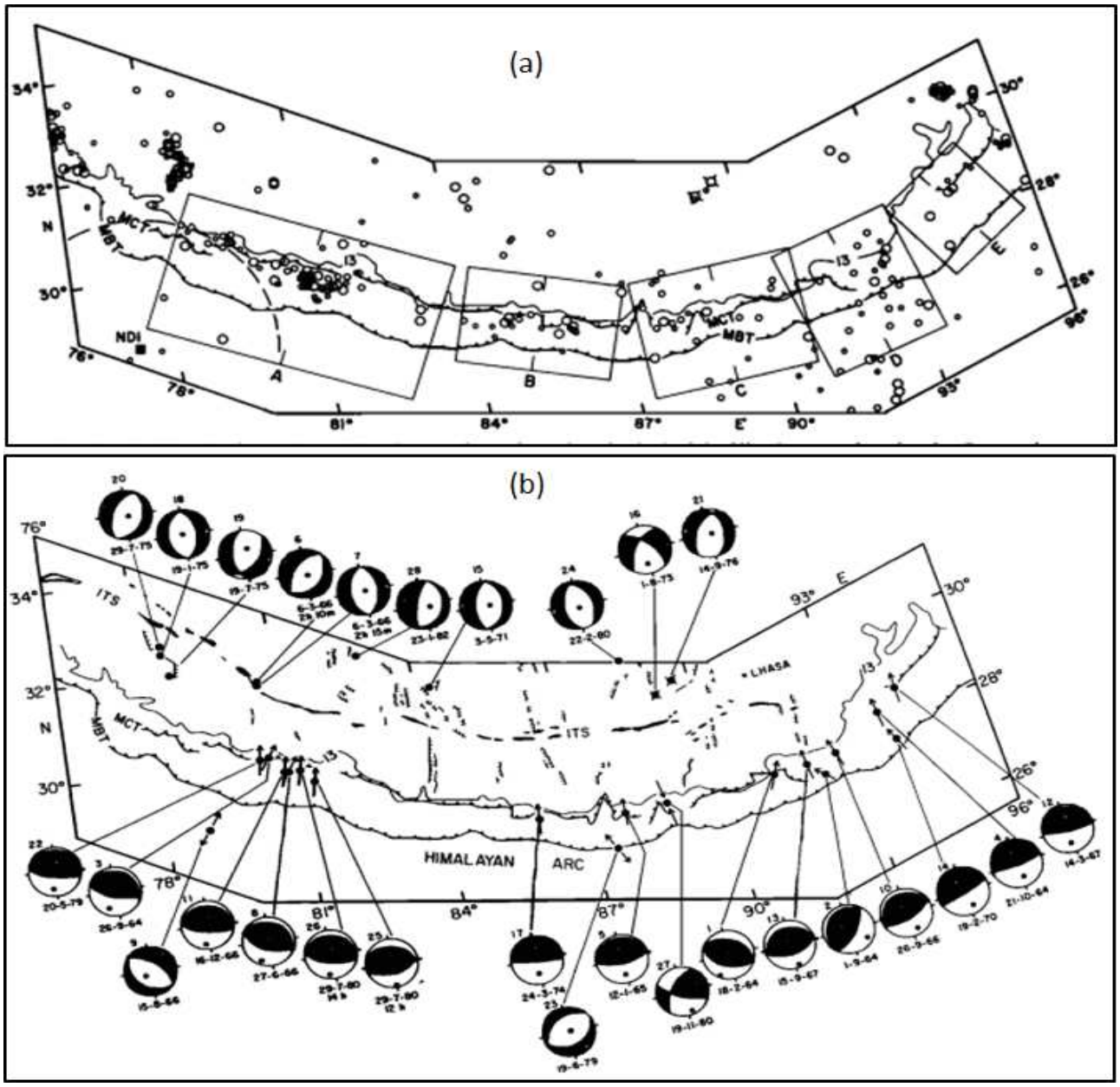

Figure 2.10: (a) Seismicity of the Himalayan region showing location of events that occurred between 1961-1981. Large, medium and small circles show very good, good and fair quality of epicenter location on basis of station locations and travel time residuals. Most of the epicenters lie along a relatively narrow belt of about 50 km between MCT and MBT. Seismicity within the triangles (A, B, C, D, E) are projected linearly on the center line of each triangle. (b) Fault plane solutions of historical events showing mostly compressional regime (After Ni and Barazangi, 1984).

al., 2007; J. Kayal, 2008; J. Kayal et al., 2010) have shown that fault plane solutions of historical earthquakes are dominated by strike-slip motion which can be correlated to the known transverse lineaments such as the Goalpara lineament in south-west Bhutan and Kopili lineament that crosses the Assam valley and transgresses into the Himalayas underneath the Kuri Chhu-Shumar spur in eastern Bhutan.

The name Goalpara lineament was first proposed by De & Kayal (2003) as it appears to be an extension of the Goalpara wedge. However, contrary to what was later observed in the temporary seismic network deployment in Bhutan (Velasco et al., 2007), they noted sparse seismic activity except for M 6.0 in 1980 and few more events with $M < 4$. However, one thing is certain: all studies so far show traverse deformation mechanism in the region unlike the predominantly thrust faulting observed in western and central Himalayas. The Goalpara lineament as observed in the past is capable of generating moderate sized earthquakes and could likely be source of future such events.

The Kopili lineament is a known active fault in Assam that is observed to transgress into the Himalayas underneath the geologically mapped curvi-linear structure of the Main Central Thrust or also known the Kuri Chhu-Shumar spur in eastern Bhutan. The September 21, 2009 eastern Bhutan earthquake (M 6.1) is reported to have occurred on this fault (J. R. Kayal et al., 2010). This fault which generated past large earthquakes could be a potential source of future larger earthquake of $M < 7$.

Specific features of the Bhutan Himalayas

The presence of Shillong plateau to the south of Bhutan is reported to play an important role in terms of seismicity and tectonic framework of the Bhutan Himalaya region. Past studies (Bilham & England, 2001; Clark & Bilham, 2008; Gahalaut et al., 2011) have proposed that low seismicity in the Bhutan region could to be due to partitioning of convergence between Bhutan and Shillong due to 1897 Shillong Plateau “pop-up” . However, it is important to note that apparent low seismicity observed could be due to shorter observation time than the full seismic cycle.

GPS studies and geological slip constraint the northern edge of Indian sub-continent sliding beneath the Himalayas at about 2 cm/yr for millions of years, leading to accumulation of 2 m of potential slip every century (Bilham et al., 2001). The colliding force builds up stress continually for several years and this stress built up, mostly or if not all, must be released in the form of great earthquakes from time to time. Seismologists called such an area as “seis-

mic gap". In the context of seismic threat to Bhutan, two seismic gaps, namely Assam Seismic Gap (the section between the 1934 and 1950 Assam earthquakes) encompassing Bhutan and Central Seismic Gap (the section between the 1905 Kangra earthquake and the 1934 Bihar earthquakes) which lie to the western side of Bhutan are of particular concern. The possibility of great earthquakes from such seismic gaps to release the enormous stress (that has been accumulated over few centuries) is real and frightening. It is through the observation of these "seismic gaps" that led to the conclusion that great earthquakes ($\geqslant$M8) are long overdue in the Himalayas.

At least in the last century, Bhutan has been relatively fortunate with regard to major seismic hazards; not a single earthquake with magnitude 7 or greater hit Bhutan directly except for 1714 event reported by Le Roux-Mallouf et al. (2016) and Hetényi et al. (2016) (Figure 2.11). Most of the events that partly impacted Bhutan were located outside the territory of the Kingdom of Bhutan.

Several hypothesis are proposed by numerous Earth science practitioners vis-à-vis the seismicity of Bhutan region and earthquake hazards in Bhutan. Clark & Bilham (2008) proposes that 1897 earthquake of Shilliong Plateau pop-up apparently cut through the lower Indian crust and thereby interrupted the continual stress build up on the northern part of the Indian continent sliding underneath the Bhutan Himalayas. This event of 1897 Shillong Plateau pop-up apparently provided a hiatus in the stress buildup and delayed the process of a major earthquake hitting the region. However, it is not certain whether partitioning of the stress distribution as result of 1897 earthquake will completely eliminate occurrence of future great Himalayan earthquakes in the region. Clark & Bilham (2008) reported that low seismicity productivity in Bhutan is definitely attributable to partitioned convergence between Bhutan and Shillong. Drukpa et al. (2006) and Velasco et al. (2007) suggest that Bhutan region is undergoing significant brittle deformation with predominantly strike-slip faulting mechanism. A look at past historical events in Bhutan suggests that even though Bhutan lies in the stress shadow of Shillong Plateau, the region is still capable of generating occasional moderate (5<M<5.9) and strong (6<M<6.9) magnitude earthquakes that can be devastating as witnessed in September 2009 M6.1 earthquake that devastated eastern Bhutan. Drukpa et al. (2006) argues that absence of major earthquake and low seismicity in Bhutan part of the Himalayas compared to central and western Himalayas could be an artifact of lack of historical documentations and absence of local earthquake monitoring stations in the former.

On the other hand, seismic gap hypothesis (Bilham & England, 2001; Khattri, 1987) pro-

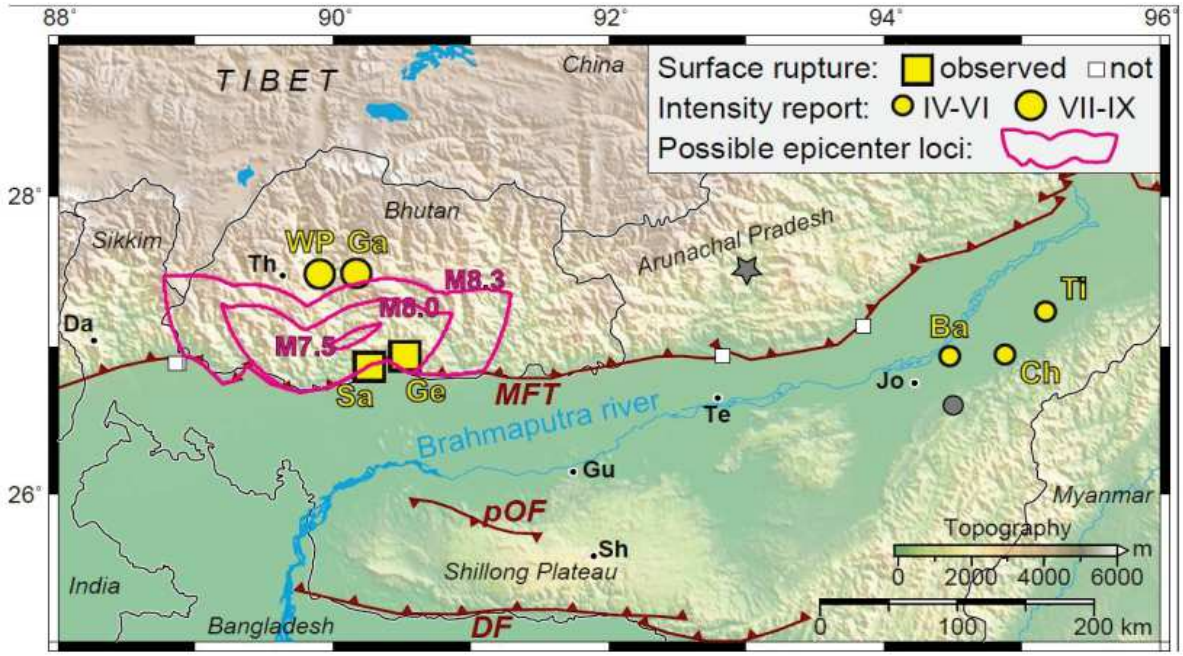

Figure 2.11: Observations and model results related to the 1714 earthquake in the Bhutan Himalayas. Grey star and circle indicate, respectively, the location and intensity of earthquake as reported by Ambraseys and Jackson[2003] Abbreviations: WP-Wangdue Phodrang, Ga-Gangteng Monastery, Sa-Sarpang, Ge-Gelephu, Ba-Bahgara, Ch-Charaideo Hill, Ti-Tinkhong, pOF-proposed Oldham Fault, DF-Dauki Fault. Cities: Th-Thimphu, Da-Darjeeling, Gu-Guwahati, Te-Tezpur, Sh-Shillong, Jo-Jorhat (After Hetényi et al., 2016).

poses that the Bhutan Himalaya region is due for great Himalayan earthquake since no major events occurred in this region for a long period. Khattri (1987) reported that regions which experienced past great earthquakes are preceded and followed by long period (greater than or equal to 19 years) of deceased seismic activity in the epicentral regions. However, this does not seem to be applicable to the Bhutan region since the region did not experience great earthquakes in the past, at least in last 100 years. The only major earthquake that struck the Bhutan region is reported to be the 1713 earthquake (Ambraseys & Jackson, 2003); however, its location is far from certain. Recently Hetényi et al. (2016) re-examined the 1713 event using new historical information from Bhutan combined with paleoseismological constraints obtained by Berthet et al. (2014) and Le Roux-Mallouf et al. (2016) from south central Bhutan. The study concluded that the 1713 event actually happened in 1714. In contrary to the epicenter and magnitude of the event reported by Ambraseys & Jackson (2003), the study based on number of scenarios and sensitivity of model to intensity prediction equation presented a plausible magnitude of 8 ± 0.5 and the location of the event quite different from the earlier report as shown in Figure 2.11.

Based on historical documentations reviewed (Seeber & Armbruster, 1981; Bilham, 2004),

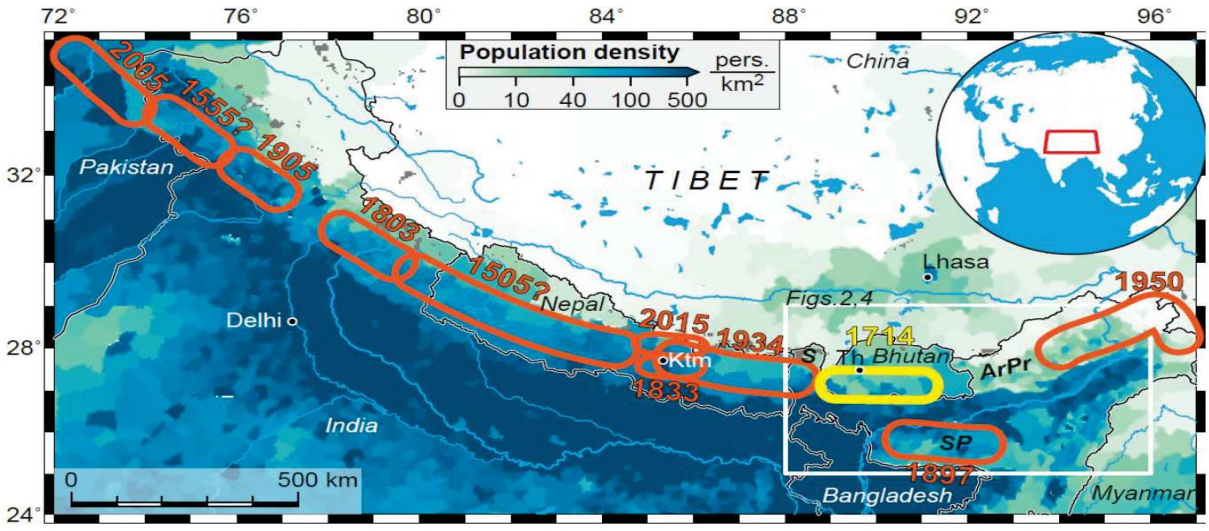

Figure 2.12: Great earthquakes along the Himalayan arc since 1500 AD (After Hetényi et al. 2016).

the accounts of great earthquakes along the 2500 km Himalayan arc is generally understood to be complete since 1800. However, accounts of large great earthquakes may be missing before 1800. Accordingly, great Himalayan earthquakes over the last two centuries have estimated to have occurred at an average rate of one about every 30 years (Seeber & Armbruster, 1981). The largest earthquake in the Himalayan region occurred in the eastern Himalaya syntaxial bend on 15 August 1950 with magnitude estimated around Mw=8.5 to 8.6; other great earthquakes along the arc that occurred since 1500 is shown in Figure 2.12. In the Bhutan Himalayas, based on paleoseismic studies at the frontal areas, at least two major historical events have been documented in Sarpang area (Berthet et al., 2014; Le Roux-Mallouf et al., 2016) and about 6 major surface rupturing events have been uncovered in Piping area (Le Roux-Mallouf et al., submitted) (Figure 2.13).

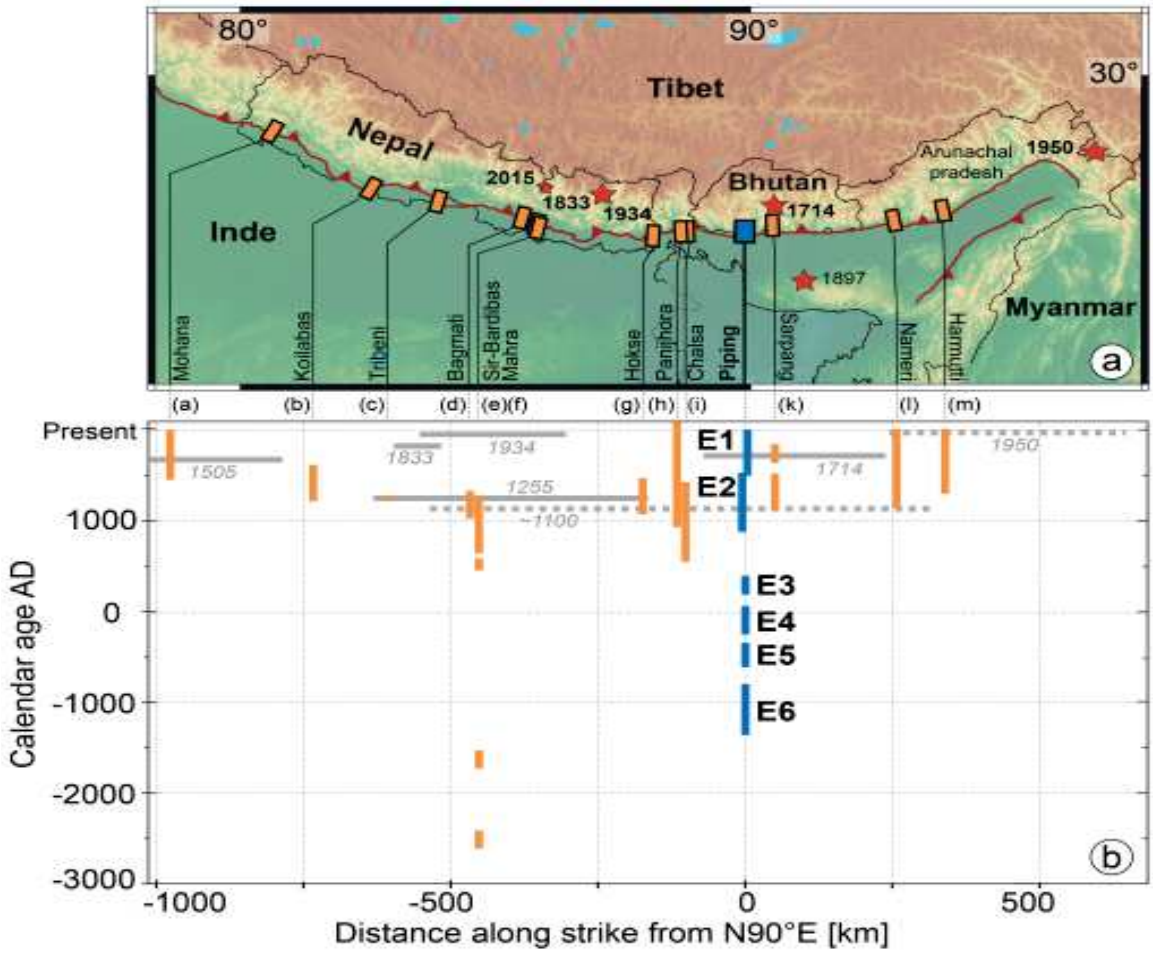

Figure 2.13: Synthesis of paleoseismic records along the Himalayas (a). Synoptic calender and locations of great/large earthquakes along the Himalayan front. Grey bars indicate minimum source lengths with or without observed surface rupture. Vertical orange bars show radio-carbon model constrains on the timing of different events. Vertical orange bars show the ~ 3500 year long record deduced from Piping area (Le Roux-Mallouf et al., submitted).

Part I

Methods

CHAPTER 3
NEAR-SURFACE GEOPHYSICS

3.1 Introduction

Geophysical methods have been widely used for characterization of subsurface tectonic features (Suzuki et al., 2000; Demanet et al., 2001; Morandi & Ceragioli, 2002; Louis et al., 2002; Wise et al., 2003; Nguyen et al., 2005; Nguyen, 2005; Kaiser et al., 2009). Depending on the scale of investigation, geophysical method can be divided into two categories: 1)deep surveys that cover depths > 100 m to several km and 2) shallow surveys or near-surface methods to investigate depths < 100 m. The former is mainly used to study geometry of fault at depth to define regional seismotectonic model. In shallow surveys, which is the targeted depth range of this study, the main objectives are to study the fault geometry for constraining the overthrusting slip rate (a key parameter input for seismic hazard assessment) and delineate shallow surface geology to study lateral variations and mechanism of deformation. In other cases, the objective could also be to resolve depth to bedrock, landslide slip plane, groundwater level, seepage zone, contaminants, etc.

The success of any geophysical method is dependent on several factors including (but not limited to): 1) availability of robust a priori information, 2) presence of strong interface contrast in terms of velocity, density, electrical resistivity, dielectric permittivity, or magnetic susceptibility, 3) practical aspects such as topography, site accessibility, cost of the survey and experience of the geophysicist. In case of our study site, particularly in Sarpang site, we have good a prior information obtained from geological, geomorphological and paleoseismic observations. Through these earlier studies we know the exact location and estimated dip angle of the fault on the surface. Moreover based on the fault zone observed in the paleoseismic trench, we anticipated good physical parameter contrast between different layers associated

with the fault. Fault zones in general are characterized with low resistivity, low seismic velocity, low density and high magnetic susceptibility mainly due to deformation associated with propagation of the fault and rheology of the geologic materials (Boness & Zoback, 2004; Hung et al., 2009; Jeppson et al., 2010). Further our sites in southern Bhutan are located in the foothills, which is characterized with low elevation variations. This specific geographic feature ensures easy accessibility and feasibility. Taking into account the geological setting and depth of the target, we adopted electrical resistivity, seismic refraction tomography and gravity methods to study the shallow surface geometry of the Main Frontal Thrust in southern Bhutan. The use of different geophysical methods allow to image different physical properties at different scales of investigation.

3.2 Advantages and shortfalls of near-surface geophysical methods

Discerning what lies beneath the subsurface has huge societal significance including prospecting for natural resources, site investigations for engineering or archaeological purpose, assessing hazardous waste and ground water pollution sites, and geomorphological, landslide and active fault mapping for disaster risk mitigation. The technique to infer unknowns in the subsurface through measurement of observable signals at or near surface of the Earth that are influenced by the physical properties of concealed geological or other objects of interest is termed as the science of near-surface geophysics. In general geophysical techniques are popular method of investigation mainly due to following advantages:

- Geophysical methods are non-invasive in nature that entail no destruction or excavation of the ground. Most of the methods are silent and environmentally friendly and therefore can be conducted at all hours of the day, including in densely populated urban settlements.
- Geophysical methods can cover large areas rather quickly, compared to invasive techniques such as drilling operation, thus saving valuable time and cost. Geophysical investigations are mostly performed to reduce number of boreholes and compliment other studies.
- Geophysical methods are capable of providing detailed and continuous information of the subsurface whereas other intrusive methods are not.

- Equipments used in geophysical investigations are normally light, compact and portable and can be easily deployed in various kinds of terrain.
- Qualitative interpretation of the data is rapid and straightforward.
- Geophysical methods have proven effectiveness as demonstrated by its wide usage through out the world for the last several decades.
- Different kinds of physical parameters for physical description.

However, like in any other methods, there are limitations to geophysical methods too. These limitations should be well understood prior to conduct of any geophysical investigation. The following are some of shortfalls in geophysical methods:

- Most geophysical methods require existence of significant physical property contrast between the adjacent units to be imaged; non-existence of such contrast will lead to difficulty or even wrong interpretation of the results.
- Results are generally interpreted qualitatively, which requires extensive knowledge and experience in the selected method of investigation.
- Most of the commercially available software and equipments are rather expensive and therefore involves substantive capital investment in the beginning.

3.3 Types of geophysical methods

The selection of geophysical methods for imaging geological investigation is determined by several factors that are specific to a particular method being adopted. The most important factors that must be considered are sensitivity function, penetration depth, spatial resolution and resolving power (Nguyen, 2005).

The sensitivity of geophysical method is an important factor while selecting the appropriate method for subsurface investigation. This is mainly because a particular geophysical method will be sensitive to different physical properties and may provide better or complementary information on the same geological structure (Tang, 2013). For example, in case of electrical resistivity method, to obtain plausible image of the underground structures, there should exist sufficient contrast in the resistivity (inverse of conductivity) of different layers to be characterized. Similarly, for the seismic approach, sufficient acoustic impedance contrast

should exist to reflect/refract from the layers. In case of gravity method, sufficient density contrast between different litho-units is prerequisite.

The depth of penetration is another important factor to be carefully accounted for while planning any geophysical investigation. In general, penetration depth of geophysical methods are inversely related to spatial resolution i.e the deeper the depth of investigation, coarser the spatial resolution and vice-versa. Besides method of investigation and field configuration, the depth of penetration is also dependent on type of the subsurface geology and contrast between different units.

The resolving power of geophysical methods play an important part in its ability to accurately and finely image the subsurface structures, including tectonic fault imaging in the present study. Resolving power is affected by factors such as type of geophysical method, signal-to-noise ratio, field geometrical configuration, inversion algorithm and material type in the subsurface. Since geophysical method involves representation of finite measurements to resolve internal structure of Earth with infinite degrees of freedom, the resolving power of geophysical method is inherently finite (Backus & Gilbert, 1967). Therefore, large independent data is required to address non-uniqueness problem in under-determined geophysical problem (Butler, 2005). Advances in inversion algorithm (Tarantola, 1987; Menke, 1989) have, however, largely being able to address the non-uniqueness problem through imposing regularization techniques and utilization of a priori information about the model. The level of noise present in data determines the ability to perform reconstruction of the model; unfavorable signal-to-noise ratio would inadvertently led to poorly resolving the subsurface structures of interest. Application of 1D or 2D to resolve three-dimensional subsurface geological structure may be another limitation of resolving power.

One way to overcome limitations in geophysical method is to combine different methods and use their respective strengths to enhance the resolution and extract additional information of the subsurface geology. In the following, different near-surface geophysical methods adopted in this thesis are described in detail.

3.3.1 Electrical resistivity

3.3.1.1 Theory: Conceptual Introduction

The fundamental essence of electrical resistivity can be explained by the laws that govern the physics of electronic charge. The three sub-atomic particles that constitute bulk of any

matter include positive charge proton, negative charge electron and neutron, which has no charge. Electrostatic force exists between two elements of like charges (eg. two electrons or two protons), which repel each other and between two opposing charges (eg. a proton and an electron), which attract each other. The neutrons, on the other hand, are unaffected by electrostatic charge. The relationship between the magnitude of electronic charges and the magnitude of resulting forces of repel or attraction is defined by Coulomb's Law as shown below:

$$F = \frac{k \times Q_1 \times Q_2}{d^2} \tag{3.1}$$

where Q_1 represents quantity of charge on object 1 (in Coulombs), Q_2 represents quantity of charge on object 2 (in Coulombs) and d represents distance of separation between the two objects. k is a proportionality constant known as Coulomb's law constant.

An electric field is created when two opposing charges, fixed in the space, exert an electrostatic force to any of the charges in their surrounding. Thus, in a conductive medium, when a current of electrons are introduced at a negative pole (anode) and taken away at a positive pole (cathode), an electric field is produced. Accordingly, if one Joule of work is lost or gained while moving one Coulomb of an electric charge through an electric field, the charge is said to have gone through a potential difference of one Volt. The surface along which no potential difference exists and is always perpendicular to the flow of current is called an equipotential surface.

Similarly, the current flow through a conductor is said to be one Ampere when one Coulomb per second of electric charge flows through a conductor. The current density is then understood to be one Ampere per square meter if one Ampere of current flows through a homogeneous conductor of one square meter cross-sectional area perpendicular to the direction of current flow.

The other important parameters are the resistance and resistivity of the conducting Earth materials which can be determined using Ohm's law of electrical impedance expressed as

$$V = I \times r \tag{3.2}$$

where V is voltage, I is current and r is resistance. This condition implies that if one Volt of potential draws one Ampere of current through a conductor, the resistance of the conductor is one Ohm. The resistivity (inverse of conductivity) of a conductor is one Ohm-meter if one Volt of potential draws a current density of one Ampere square meter across a conductor of

one Ohm resistance and length of one meter which can be represented as

$$R = \frac{rS}{L} \tag{3.3}$$

where R is the resistivity, r is the resistance, S is the cross-sectional area and L is the length.

The measurement of ground resistivity by simultaneously passing current and measuring potential difference between a single pair of electrodes doesn't work due to contact resistance that amounts to thousands of Ohms because of ground moisture and contact area (Milsom, 2007). The problem, however, can be avoided if voltage differences are measured between second pair of electrodes using a high-impedance voltmeter. The voltmeter draws no current and voltage drop at the electrodes is negligible. The resistances at the current electrode limit current flow but do not affect resistivity calculations. Using four electrode arrays a geometric factor correction is applied to convert readings to resistivity.

A single measurement with any array can be associated due to homogeneous medium with constant resistivity. The geometric factor that must be incorporated to determine the apparent resistivity, ρ_a, can be calculated from the following equation

$$V = \frac{\rho_a I}{2\Pi a} \tag{3.4}$$

where a is the distance from the electrode and I is the total current flowing from one current electrode to other through the ground.

In case of linear array with four electrodes (a quadripole), A and B represents the current injection points and the potential measurement points are represented by M and N. The potentials at M and N electrodes are given as

$$V_M = \frac{\rho I}{2\Pi}\left(\frac{1}{AM} - \frac{1}{MB}\right) \tag{3.5}$$

$$V_N = \frac{\rho I}{2\Pi}\left(\frac{1}{AN} - \frac{1}{NB}\right) \tag{3.6}$$

Therefore, the total potential difference between the electrodes M and N can be determined by

$$V_{MN} = V_M - V_N = \frac{\rho I}{2\Pi}\left[\left(\frac{1}{AM} - \frac{1}{MB}\right) - \left(\frac{1}{AN} - \frac{1}{NB}\right)\right] \tag{3.7}$$

Equation (3.7) can be further rearranged to deduce

$$\rho = \frac{V_{MN}}{I}K \tag{3.8}$$

where

$$K = 2\Pi \left[\left(\frac{1}{AM} - \frac{1}{MB} \right) - \left(\frac{1}{AN} - \frac{1}{NB} \right) \right]^{-1} \tag{3.9}$$

In equation (3.8) K is the geometric factor, which depends on the spacing between electrodes and type of array used. If the medium is not homogeneous, we measure the apparent resistivity (ρ_a) since influence from the different layers needs to be incorporated. For instance, in Wenner array, the spacing between all the electrodes are maintained at a constant spacing of a and thus the geometric factor, K reduces to $K = 2\Pi a$. Accordingly, the apparent resistivity in case of Wenner array (Figure 3.1) can be calculated as

$$\rho_{Wenner} = \left(\frac{V_{MN}}{I} \right) K = \left(\frac{V_{MN}}{I} \right) 2\Pi a \tag{3.10}$$

Equation (3.10) represents apparent resistivity of the ground as measured by the surface electrodes and the value of it depends on the apparent resistance (V/I) and the geometric factor, K.

3.3.1.2 Survey methods and electrode configuration

Depending on the scope and objective of a study, resistivity measurement basically involves two main procedures namely: *vertical electrical sounding (VES) or electric drilling* and *lateral profiling or mapping* (Telford et al., 1990). In vertical electrical sounding (VES), the voltage electrodes at centre point of the array remain fixed while the outer current electrodes separation is progressively increased to drive the current deeper in the ground to increase the depth of exploration. The observed resistivity data is usually plotted against half-electrode spacing on double logarithm graph. For interpretation of the results, the subsurface in case of VES, is assumed to consist of horizontal layers with resistivity variation in vertical direction only. Thus the greatest limitation in VES is that it does not take into account horizontal variation in the resistivity layers. The Schlumberger is the most popular array for conducting VES survey; however, other arrays such as Wenner configuration with equal electrode spacing are also employed (Okpoli, 2013). Since VES method is generally insensitive to lateral variation in resistivity of the subsurface, only 1D modeling is performed. In case of significant lateral resistivity variations, the measured resistivity values could be wrongly interpreted to be represented of vertical changes in resistivity of the subsurface layers.

Profiling method or constant separation traversing (CST) is another classical method of resistivity survey. In this method, the spacing between electrodes remain fixed but the entire

setup is moved along a straight line, usually perpendicular to the strike of geologic structures, for a constant depth of exploration (Loke, 2015). Thus, profiling technique is capable of discerning subsurface resistivity in horizontal direction at a given depth but less able to estimate vertical resistivity changes. Interpretation of results using profiling method is usually qualitative in nature. Wenner array is ideal configuration for this method due to equidistant spacing between the electrodes. In general, for delineating steeply dipping structures or accurate mapping of faults, the dipole-dipole array is usually adopted due to its high sensitivity in resolving horizontal resistivity variations. Gradient array is also used due to its advantage of having to move the potential electrodes only. Similar to sounding technique, in profiling method too, the subsurface is assumed to consist of homogeneous and isotropic subsurface with uniform resistivity.

Electrical resistivity tomography (ERT), involving 2D or 3D method, is the most preferred and widely used method nowadays. This method is especially relevant to study geological settings where vertical and horizontal subsurface material variations are, more often than not, the prevalent conditions in subsurface investigations. In ERT survey, tens to hundreds of electrodes are connected to central automatic switching system that activates four electrodes at a time, thus significantly speeding up data collection time in the field. Most modern ERT equipment comes with option to select any or multiple array types that can be used to compare the apparent resistivity results from each method.

As seen in equations (3.7-3.9), calculation of apparent resistivity has direct correlation to the geometric factor (K). In a four electrode configuration, using different combination of current and voltage electrodes, several different types of arrays are available. The commonly used array types (Loke, 2015) that can be configured to measure ground apparent resistivity include: Wenner, Schlumberger, Wenner-Schlumberger, Dipole-Dipole, Pole-Pole, etc., as shown in Figure 3.1. The important considerations while selecting appropriate array type include (Loke, 2015): i) the depth of investigation, ii) the sensitivity of the array to vertical and horizontal changes in subsurface resistivity, iii) horizontal data coverage, and iv) the signal strength.

Wenner array is a robust method that is sensitive to vertical changes (i.e horizontal structures) in the subsurface resistivity and has generally high signal-to-noise (S/N) data. However, the main drawback of Wenner configuration is its relative insensitivity to lateral variation in subsurface resistivity and electro-magnetic coupling problems between the cables connecting the current and potential electrodes. As a rule of thumb, it has moderate depth of

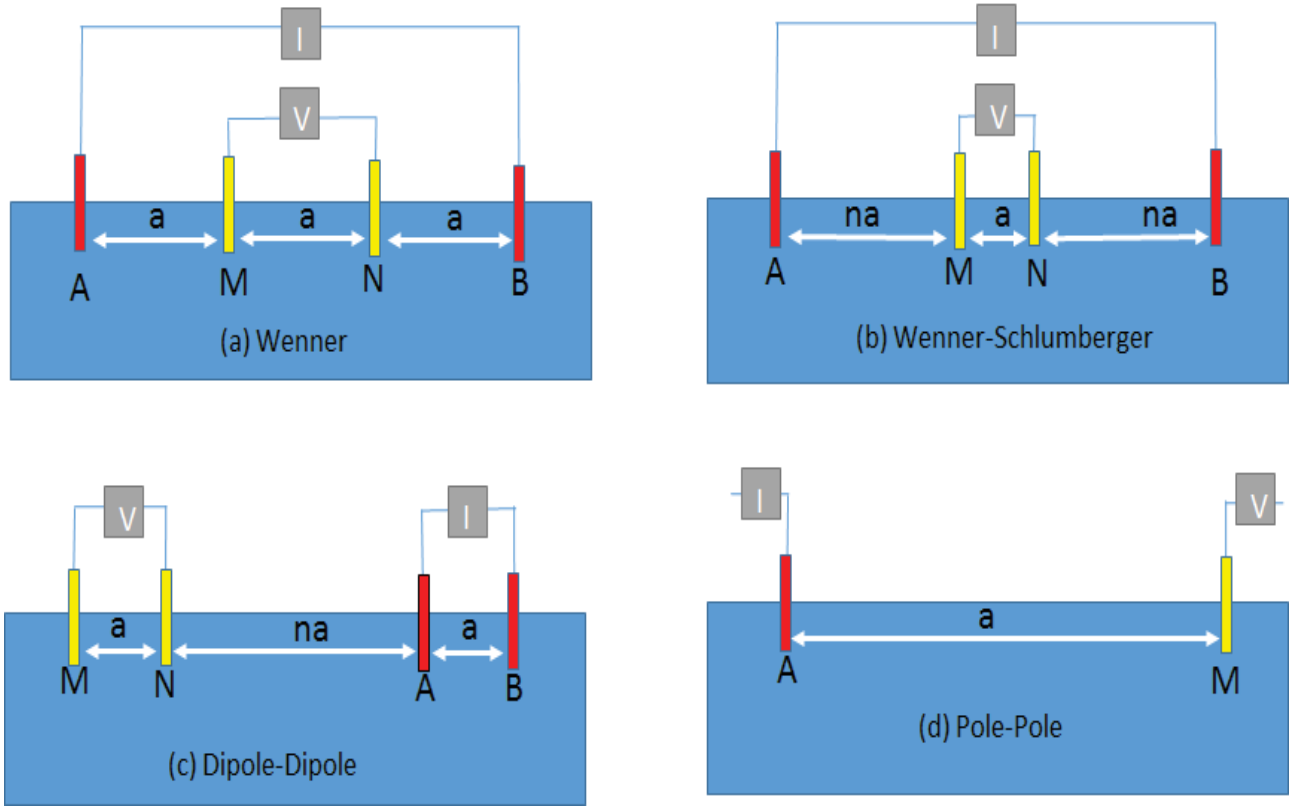

Figure 3.1: Common geometric configurations used in electrical resistivity survey

penetration equivalent to 0.5 times the electrode spacing; however, it has the lowest horizontal data coverage among the common electrode arrays. Due to simple geometric configuration $(2\pi a)$ (see Figure 3.1) consisting of four equally spaced electrodes, Wenner array is easy to deploy in the field and it takes the least amount of time for data collection. As seen in Figure 3.1, current is injected through the outer electrodes (AB) and potential is measured between the inner electrodes (MN).

Schlumberger array is another classical method that is popularly used for electrical resistivity sounding mainly due to its logistic advantage where only two electrodes have to be moved. Similar to Wenner array, it has high signal-to-noise (S/N), sensitive to vertical changes in the subsurface resistivity but relatively insensitive to horizontal resistivity variations. Figure 3.1 shows arrangement of electrode arrangements of Schlumberger array. The potential electrodes (MN) are located at the center of the array, while the current electrodes (AB) occupy the exterior part of the electrode position at half the distance of AB from the midpoint of the electrode alignment.

Wenner-Schlumberger array is a hybrid of Wenner and Schlumberger. It has greater depth of investigation than Wenner method, good signal response and ability to resolve horizontal

and vertical relatively well (Ward, 1990; Loke, 2015). The horizontal data coverage in case of Wenner-Schlumberger is slightly better than Wenner method. In Wenner-Schlumberger method each subsequent deeper data level has two data point less than preceding level, whereas in case of Wenner method the data points decrease by three points with each deeper level. As shown in Figure 3.1, the geometric configuration of Wenner-Schlumberger is more complicated than Wenner wherein the "n" factor is determined by the ratio of distance between AM (or NB) electrodes to the interval between the potential electrodes MN (Loke, 2015). Wenner array is a special case of Wenner-Schlumbeger when "n" factor equals to 1.

Dipole-Dipole array is another widely used method for resistivity and induced polarization (IP) mainly due to its low eletromagnetic coupling between the current and potential electrodes (Ward, 1990; Loke, 2015). It has, however, lower resolution to image horizontal and steeply dipping structures compared to Wenner and Wenner-Schlumberger (Ward, 1990; Seaton & Burbey, 2002). Thus it is a good method to image vertical structures like dykes and cavities but is relatively poor in resolving horizontal structures such as sills and sedimentary layers (Loke, 2015). It also has the lowest signal of all the arrays which makes Dipole-Dipole array highly susceptible to telluric noise. The electrode configuration for Dipole-Dipole is shown in Figure 3.1. The distance between current electrodes, AB, and potential electrodes, MN, is marked as "a". The "n" factor which determines the distance between BM positioned at the center of the array is proportional to the ratio of distance between B and M electrodes and BA or MN dipole length of "a". The depth of investigation using Dipole-Dipole array is dependent both on spacing "a" and the "n" factor. However, as the "n" factor increases, the signal becomes very weak which affects the quality of data. In general, Dipole-Dipole has lower depth of penetration than Wenner and Wenner-Schlumberger arrays but it has higher horizontal data coverage which makes it a viable option in case of multi-electrodes with less number of electrodes (Loke, 2015).

Pole-Pole array has the deepest depth of investigation and widest horizontal data coverage, but the poorest resolution of all the electrode arrays (Robain et al., 1999; Seaton & Burbey, 2002; Loke, 2015); signal strength is lower compared to Wenner and Wenner-Schlumberger but higher than Dipole-Dipole. Similar to Dipole-Dipole method, Pole-Pole array is also susceptible to telluric noise due to long distance between the potential electrodes which in theory is located at infinite distance as shown in Figure 3.1.

3.3.1.3 Electrical properties of Earth materials

The subsurface Earth material is made of mixtures of two or more phases (solid, liquid or gas). To compute the apparent resistivity of the materials, the current flow through each phases should be considered. Electric current flow in the near-surface material is defined by either electronic or electrolytic conduction. In electronic conduction, the flow of the current is through movement of free electrons, whereas in case of electrolytic conduction, the current flow is via movement of ions in groundwater. In most near-surface engineering and environmental investigations, conduction is largely electrolytic, taking place in connected pore spaces, along grain boundaries, in fractures/faults, and in shear zones (Ward, 1990; Loke, 2015). Electronic conduction takes place when conductive minerals such as sulphide and graphite in case of mineral exploration study.

In general, rocks with higher porosity or fissure with larger water content will have higher conductivity (or lower resistivity). The influence of porosity on resistivity of Earth materials, especially in case of sedimentary rocks, can be explained by Archie's law

$$\rho = a\rho_w\phi^{-m} \tag{3.11}$$

where ρ is the resistivity of rock, ρ_w fluid resistivity, ϕ is the fraction of rock filled with the fluid, and a and m are empirical parameters peculiar to the rock types (Keller & Frischknecht, 1966). For most rocks, a is about 1 and m is about 2. Equation 3.11 is valid only in case of sediments with little or no clay; presence of even small amounts of clay leads to strong deviations due to ion exchange between clays and saline water. Thus, for formations with significant amount of clay content, equation 3.10 is not applicable (Klein & Sill, 1982) and alternative complex equations have been proposed (de Lima & Sharma, 1990). Resistivity of the subsurface materials are also influenced by geological processes (Ward, 1990). Dissolution, faulting, shearing and weathering increase porosity and fluid permeability, and thereby reduces resistivity. On the other hand, precipitation of calcium carbonate and silica reduces porosity and inhibits fluid permeability which leads to increase in resistivity of materials.

Among all the geophysical parameters, resistivity shows the largest variations. Sedimentary rocks which are generally more porous and contain higher amount of water, have lower resistivity values compared to igneous and metamorphic rocks. Figure 3.2 shows resistivity of rocks, soil and minerals.

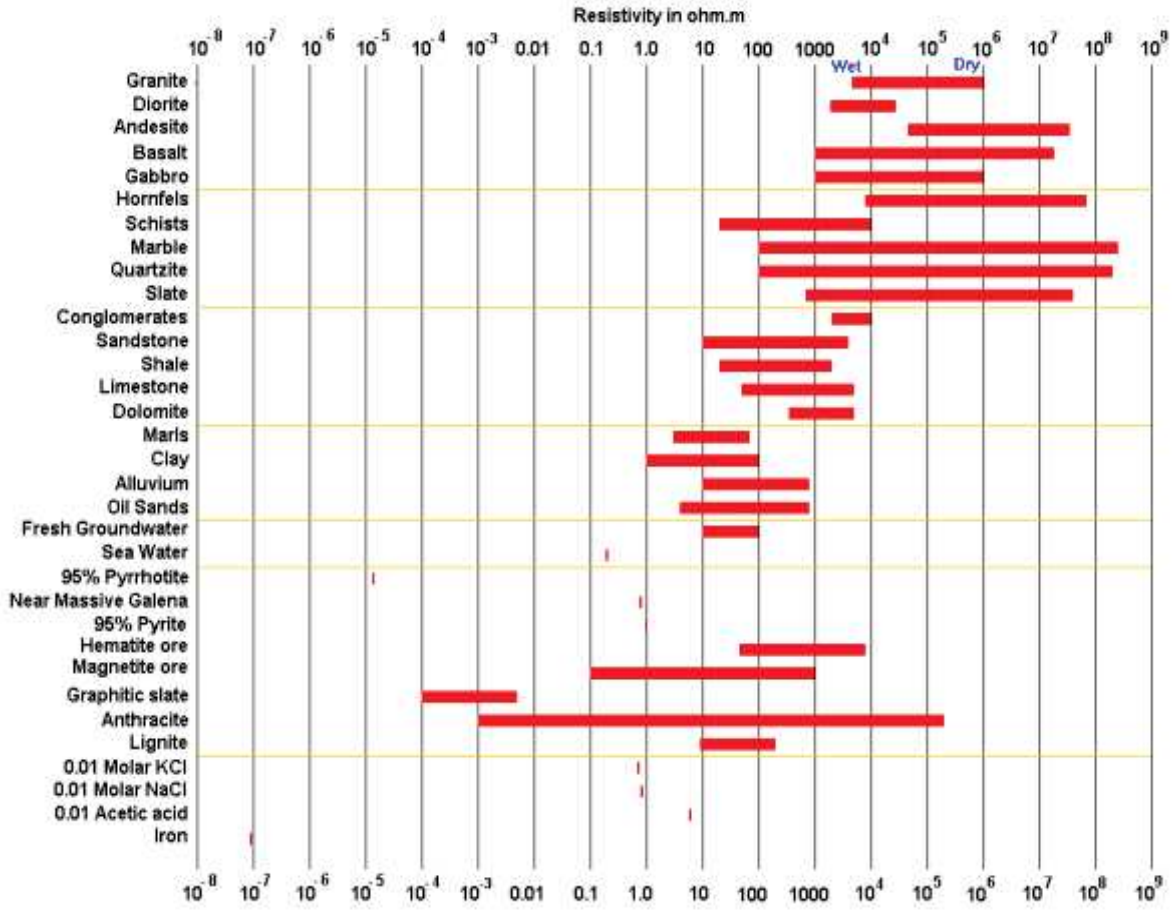

Figure 3.2: The resistivity of rocks, soils and minerals (After Loke, 2015)

3.3.1.4 Electrical resistivity tomography for active fault mapping

The application of electrical resistivity techniques in geomorphological and active fault mapping is well known (Suzuki et al., 2000; Demanet et al., 2001; Louis et al., 2002; Nguyen, 2005; Nguyen et al., 2007; Schrott & Sass, 2008; Gabo et al., 2015). This increased application of ERT techniques in near-surface geomorphological and active fault survey is mainly due to availability of light weight, user-friendly, and efficient state-of-art geophysical equipments to gather non-destructive data and the availability of affordable high computing capacity to perform rigorous inversion processes (Schrott & Sass, 2008). Moreover, alluvial environment is dominated with common materials such as gravels, sands, clays, and conglomerates that show high resistivity contrasts (Nguyen, 2005). Therefore, electrical resistivity method allows effective characterization of layers within the Quaternary deposits as well as accurate delineation of active tectonic deformation and the contact between the bedrock and Quaternary layers. Louis et al. (2002) noted that even though combined use of different geophysical methods permitted tracing of faults with high level of confidence, ERT appears to be the most

robust and reliable method. However, in complex geological regimes with slow tectonic deformation mechanism, conventional ERT inversion techniques fail to generate correct images of the subsurface and exhibit significant artifacts (Nguyen et al., 2007). In such cases all possible anisotropy effects must be taken into account for interpretation of subsurface structures; the result can be greatly improved by performing forward modeling taking into account the measured and inverted data, and *a priori* geological/geomorphological information (Nguyen et al., 2007).

In many instances, geological faults are covered with thick sediment deposits and thereby the exact position of the fault cannot be approximated from subsurface observation. Non-invasive geophysical methods like electrical resistivity techniques are extremely useful for determining the position of fault and deciding the location of confirmatory drilling and trenching. Suzuki et al. (2000) in case studies of active fault mapping underneath thick Quaternary deposits in Japan opined that ERT is an effective technique to image the flexure of structure due to faulting, and combined with other geophysical methods provided accurate information to evaluate faulting activity. Figure 3.3 shows basic flow chart that may be considered for active fault mapping to assess seismic hazard for civil engineering applications (Suzuki et al., 2000).

3.3.1.5 Advantages and limitations of electrical resistivity tomography

The main advantage of ERT method lies in its non-invasive nature whereby resistivity surveys can be performed in any environmental settings. Most of the modern resistivity equipments were light weight, portable and robust with capability to perform investigations in almost any type of terrain conditions. Availability of state-of-the-art ERT equipment and software allows fairly straight forward data acquisition and field surveys. Thanks to availability of wide range of commercial as well as free ERT data analysis software, performing robust and complex inversion are possible, which makes data interpretation more reliable, easy and faster; possibility to have quick analysis at the site becomes handy to have a quantitative assessment of acquired data.

The main limitation of ERT method include the wide range of resistivity values for a single material, depending on degree of porosity and water content. This wide variation in resistivity values makes interpretation of resistivity data rather difficult without sufficient a priori information. To image any subsurface bodies there should exist sufficient resistivity contrast without which resistivity method cannot be applied successfully. Moreover, analysis and in-

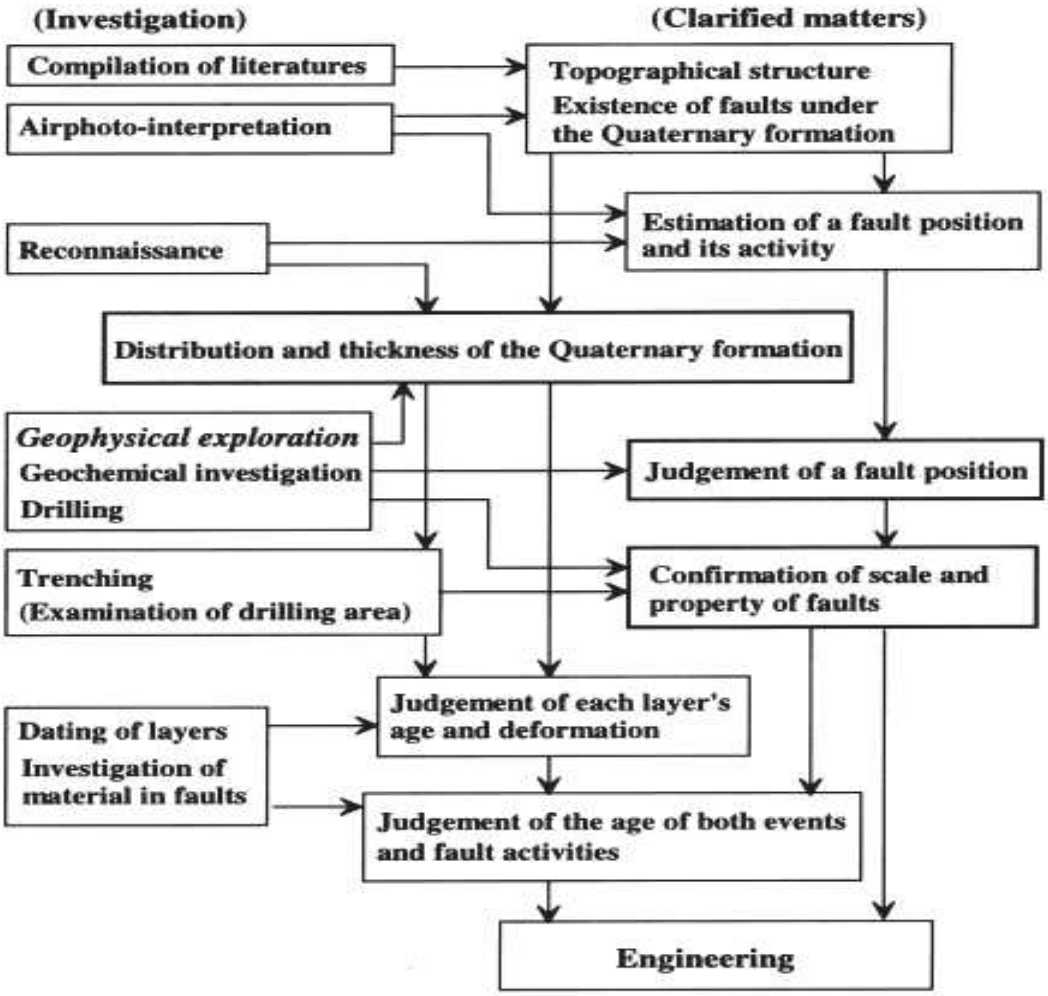

Figure 3.3: Flow chart to characterize fault activity in Quaternary settings for engineering applications (After Suzuki et al. 2000).

terpretation of ERT requires expertise with good experience and knowledge in performing geophysical data analysis.

3.3.2 Seismic refraction

Introduction

Seismic wave velocity depends on the density and elastic moduli as defined below

$$V_p = \sqrt{\frac{K + \frac{4\mu}{3}}{\rho}} \tag{3.12}$$

$$V_s = \sqrt{\frac{\mu}{\rho}} \tag{3.13}$$

where K is the bulk modulus, μ is the shear modulus and ρ is the density; V_p and V_s represents P-wave and S-wave velocity, respectively.

In equation 3.12 and 3.13 it may seem that V_p and V_s decreases with increasing density. However, since μ and K both increases more quickly as a function of density, in general, increasing density results in higher velocity of P- and S-Wave (Telford et al., 1990). Since elastic constants of any materials are always positive, the P-wave of any medium is always faster than S-wave. Also since μ tends to zero in fluids, S-wave cannot propagate through fluids.

Taking advantage of the relationship between seismic wave velocity and material properties as defined in equation 3.12 and 3.13, seismic refraction is a commonly used geophysical technique to image the subsurface by applying the physics of acoustic wave propagation through different materials in the ground. The main physics that governs the propagation of seismic waves in medium with varying density is the Snell-Descartes' law which can be expressed as

$$\frac{sin\, i}{sin\, r} = \frac{V_1}{V_2} \tag{3.14}$$

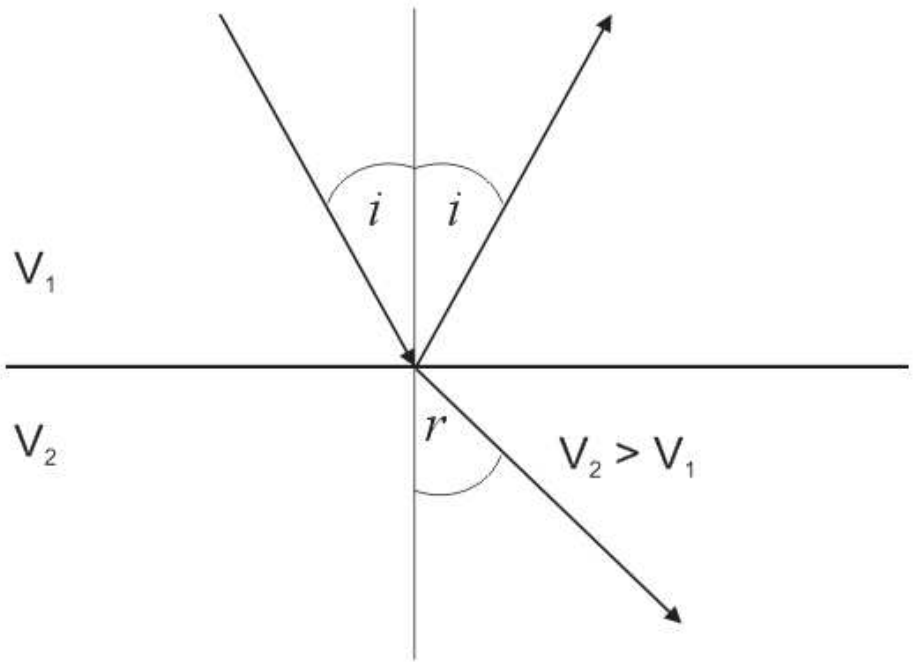

Figure 3.4: Relationship between angle of incidence(i) and angle of refraction (r) in layers with velocity V_1 and V_2 where $V_2 > V_1$.

where V_1 and V_2 represents the velocity of layers 1 and 2, respectively; i represents the

angle of incidence and r represents the angle of refraction. As shown in Figure 3.4, if $V_2 > V_1$, then as i increase r will increase and at a critical angle of incidence (i_c), angle of refraction (r) becomes 90°. Accordingly, the equation (3.11) can be rewritten as

$$\frac{sin\, i_c}{sin\, 90} = \frac{V_1}{V_2} \tag{3.15}$$

$$sin\, i_c = \frac{V_1}{V_2} \tag{3.16}$$

$$i_c = sin^{-1}\frac{V_1}{V_2} \tag{3.17}$$

In seismic refraction, only critically refracted and first arrival energy are considered, while other waveforms such as reflection, direct arrivals, surface waves, etc. are ignored. In Figure 3.5, P-wave is incident on refracting medium at the critical angle, i_c. After refraction, the wave travels along the interface in the lower medium with higher velocity, V_2. The direct wave that travels along the ground surface is the first arrival until the cross-over distance, X_{cross}. Beyond that the refracted wave (or the head wave) overtakes the direct wave as the first arrival wave at the geophones. The cross-over distance (X_{cross}) can be calculated as

$$X_c = 2Z\sqrt{\frac{(V_2 + V_1)}{(V_2 - V_1)}} \tag{3.18}$$

where Z is the depth to the interface layer. From equation 3.18, it may be noted that the crossover distance is always greater than twice the depth to the refractor and it also provides an alternative method of calculating the depth to the refractors, Z_i. The P-wave velocity for the first and second layer can be calculated from the slope of direct wave and head travel-time curves as shown in Figure 3.5. Depending on depth of investigation, shot source and existence of density contrast in the subsurface materials, deeper layers up to 3-4 layers could be constrained by refraction study. The depth to refractive interface layers can be estimated by

$$Z_1 = \frac{T_{i2}V_1}{2cos\left(sin^{-1}\frac{V1}{V2}\right)} \tag{3.19}$$

where Z_1 is the depth to the first refractor, T_{i2} is intercept time for refracted wave from the second layer. Depths to deeper layers, if present, can be calculated. For instance depth to the third layer can be calculated as

$$Z_2 = \frac{\left[T_{i3} - T_{i2}\frac{cos\left(sin^{-1}\frac{V_1}{V_2}\right)}{cos\left(sin^{-1}\frac{V_1}{V_2}\right)}\right]}{2cos\left(sin^{-1}\frac{V_2}{V_3}\right)} + Z_1 \tag{3.20}$$

where Z_2 is the depth to second refractor to be determined, T_{i3} is the intercept time for the refracted wave from the third layer.

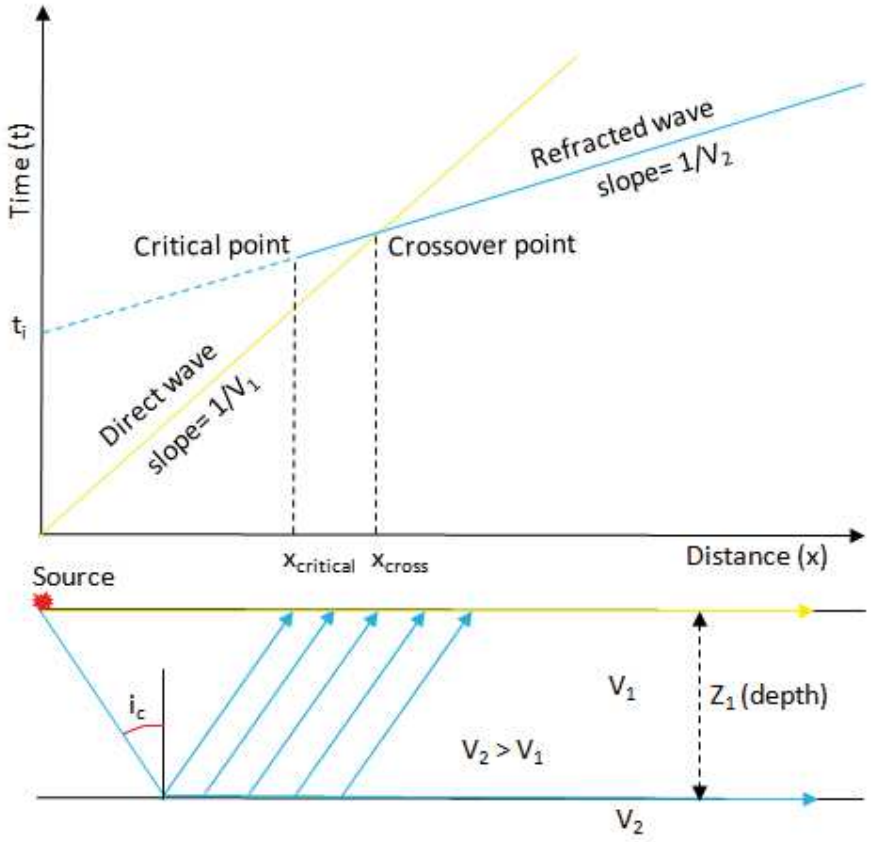

Figure 3.5: Travel-time curves for the direct wave and head wave from a single refractor.

Constraining dipping interfaces

In reality the subsurface geology is far from the idealistic horizontal layered type with smooth variations in physical properties. More often than not the ground below is characterized by dipping interfaces that show strong lithology variations both in horizontal and vertical directions. This is particularly so in case of subsurface geology disturbed by tectonic deformation.

As shown in Figure 3.6, in case of subsurface with dipping interfaces, if shot from downdip is considered, the slope on travel-time digram is too steep which underestimate the velocity and the layer thickness. On the contrary, shot from up-dip direction will overestimate the velocity and layer thickness. The intercept time for the forward (t_i) and reverse shots (t_i'), will also be different. As a result, the reciprocal of the gradients of the travel-time curves no longer represent the velocity of the refractor but it yields the downdip and updip apparent velocities V_{2d} and V_{2u} respectively as shown in Figure 3.6. Once existence of interface dipping

is established by performing forward and reverse shots, the refractor dip angle, α and i_c can be calculated from the apparent velocities of down-dip and updip trajectories. Utilizing the first layer velocity (V_1) coming from the gradient of the direct wave curve, the true velocity of the refractor can be derived using Snell-Descates' law. The perpendicular distances to the interface (z and z$'$) can be calculated from the intercept times (t_i and t_i').

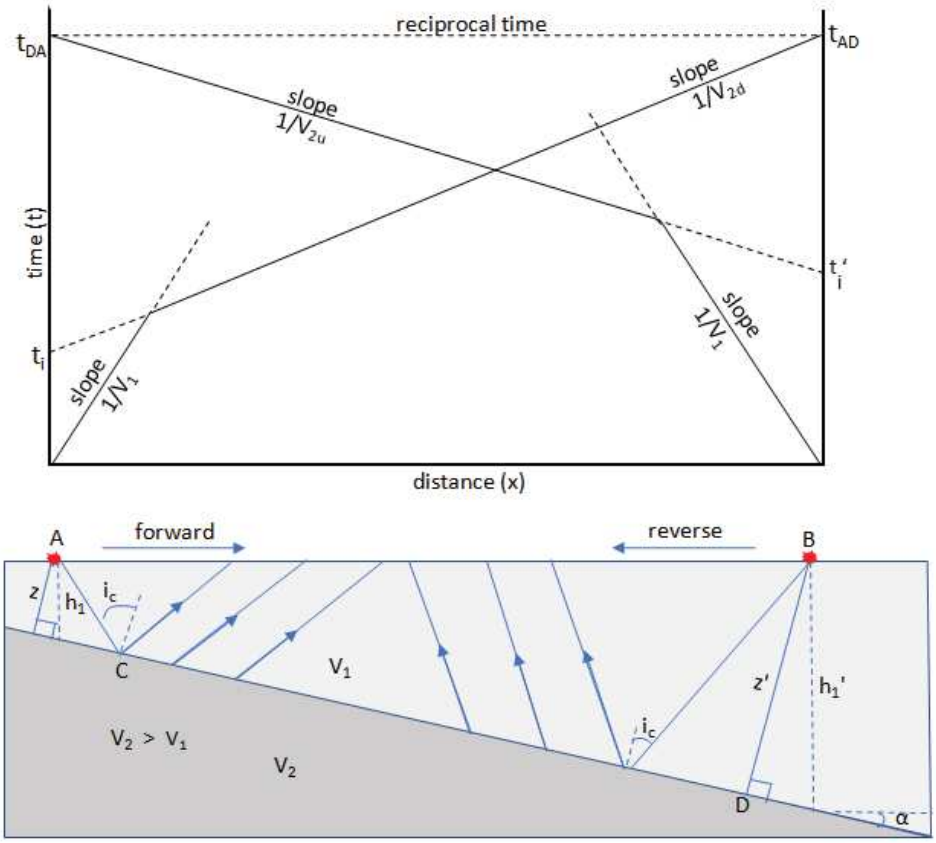

Figure 3.6: Travel-time curves for the head wave arrivals from a dipping interface in forward and reserve directions along a refraction profile (top); Ray-path geometry (Modified after Kearey, 2013)

Seismic refraction data analysis

Essentially there are two fundamental approaches to seismic refraction data analysis: the "layer-cake" and tomographic inversion. The former is the more traditional approach and also requires fewer shot-points in the field which makes data collection much faster but less accurate. The tomographic approach on the other hand requires more more shot points along the survey line and also demand higher computing speed (White, 1989; Morey & Schuster, 1999). However, with availability of modern high processing capacity, tomographic inversion

has gained more popularity than in the past. The traditional “layer-cake” inversion technique include methods such as delay-time method, generalized reciprocal method (GRM), slope intercept method and plus-minus method. These methods are generally associated with the following characteristics:

– layers are defined by interfaces

– all layers have constant velocities

– limited number of layers

– layers increase velocity with depth only

– typically requires subjective input by the user

On the other hand the tomographic inversion comprises of methods such as raytracing algorithms and numerical eikonal solvers (wavepath eikonal traveltime-(WET) or generalized simulated annealing). The models for refraction tomography are generally associated with the following characteristics:

– velocity models are not interface based

– depicts smoothly varying lateral and vertical velocities

– several layers

– imaging of discontinuous velocity inversion possible

Advantages and limitations of seismic refraction method

The main advantages of seismic refraction and limitations are listed below:

Advantages

- Seismic velocity of subsurface materials and depth to the different horizons can be determined by employing seismic refraction method.
- Seismic refraction can be performed simultaneously with seismic reflection or surface wave and the data can be used for other analysis.
- Seismic refraction can be performed at different scales (from shallow to deeper depths) depending on the energy of source and the site geological conditions.

- Traditional seismic refraction can be performed relatively easily with few shot point at offset and geophone locations; however, in case of seismic tomography dense shots are required which prolongs the data acquisition process but increases the quality of the results.

  Limitations

- Picking of first arrival times can be time consuming and tedious task, especially if the signal-to-noise ratio is poor. Therefore, seismic studies are difficult to conduct in noisy areas such as urban environments.

- Seismic refraction method will not work in case of high velocity layer on top of a low velocity layer due to propagation properties of seismic wave accordingly to Snell-Descartes' law. In other words refraction will only work if velocity of subsurface increases with depth.

- Interpretation of seismic refraction results are made in terms of layers which not may always be reflective of the real world geological conditions.

- Sufficient seismic velocity contrasts between layers to be imaged should exist, otherwise seismic method may not successfully resolve the interfaces.

3.3.3 Gravity

Principles of gravity method

The basic principle of gravity method is based on the Newton's Law of universal gravitation which states that force of attraction (F) between two masses m_1 and m_2 separated by distance, r, is given by

$$F = \frac{Gm_1m_2}{r^2} \tag{3.21}$$

where G correspond to the gravitational constant ($6.67 \times 10^{-11} m^3 kg^{-1} s^{-2}$). Equation 3.22 enables us to calculate the gravitational force the Earth is pulling, for instance, on a body on the Earth's surface.

$$F = \frac{GM_Em_b}{R_E^2} \tag{3.22}$$

where M_E is weight of the Earth, m_b is the weight of the body, and R_E is the radius of the Earth. Dividing both sides of equation 3.22 by weight of the body (m_b)

$$\frac{F}{m_b} = \frac{GM_E}{R_E^2} \tag{3.23}$$

Since force equals to weight $\times$ acceleration, equation 3.23 can be written as

$$g = \frac{GM_E}{R_E^2} \tag{3.24}$$

where is g is the acceleration due to gravity. The mean value of g on the Earth surface is 9.80665 m/s^2; 1 cm/s^2 of acceleration due to gravity is normally expressed as Galileo or Gal which is the unit for gravity measurement. Most modern gravimeters are capable of making measurements with accuracy of 0.001 mgal or 0.01 μm/s^2.

Earth gravity field and data reduction

If the Earth were a perfect homogeneous sphere, gravitational acceleration will be constant all over the Earth surface. However, this is not the case and gravity field varies over the Earth surface. The main factors that influence the observed gravity signals are: latitude, elevation, topography of surrounding terrain, Earth tides and density variations in the subsurface (Telford et al., 1990; Kearey et al., 2013). The last factor, which is generally much smaller than latitude and elevation factors but larger than changes in tidal and topography, is the one that we are particularly concerned in gravity measurement to study subsurface anomaly. Therefore, in order to obtain true signal representative of gravity anomaly due to density variations of the materials in the subsurface, a process called gravity data reduction (or reduction to the geoid) is employed to eliminate the influences of other unwanted components. Below the different reduction processes are explained in detail:

a. Latitude correction: Gravity field increases with latitude due to rotation of the Earth and its bulge at the equatorial region. The centrifugal force due to rotation of the Earth is greatest at the equator and zero at the poles. This decreases the gravitational acceleration at the equator, while polar flattening increases gravity at the poles by making the geoid closer to the center of Earth's mass. The latitude correction Δg_L can be obtained by

$$\frac{\Delta g_L}{\Delta s} = \frac{1}{R_E}\frac{\Delta g_t}{\Delta \phi} \tag{3.25}$$

$$\frac{\Delta g_L}{\Delta s} = 0.811\ sin\ 2\phi\ mGal/km \tag{3.26}$$

where Δs=N-S horizontal distance=$R_E \Delta \phi$ and R_E is the radius of Earth ($\approx$ 6368 km), g_t is the theoretical value of g as per Geodetic Reference System, 1967 (GRS67). The

correction is maximum at latitude 45° where it equals 0.01 mgal/(13 m) and it is zero at the poles and equator. The correction is added to g as one moves towards the equator.

b. Free-air correction: As elaborated in equation 3.20, gravity varies inversely with square of distance. Therefore it is important to make correction in elevation between stations in order to bring the readings to a common datum surface. In other words free-air correction is the difference between gravity measured at sea-level and at an elevation,h, with no mass in between. By differentiating equation 3.23, we can obtain the change in gravity due to height as

$$\frac{\Delta g_{fa}}{\Delta R} = \frac{2GM_E}{R_E^3} = \frac{2g}{R_E} \tag{3.27}$$

$$\frac{\Delta g_{fa}}{\Delta R} = 0.3086\, mGal/m \tag{3.28}$$

c. Bouguer correction: The Bouguer correction accounts for the mass of materials between stations and datum reference plane. Thus, we add a plate with an average density of the surrounding rocks to perform the Bouguer correction as follows

$$\frac{\Delta g_b}{\Delta R} = 2\pi G\rho \tag{3.29}$$

$$\frac{\Delta g_b}{\Delta R} = 0.04192\rho\, mGal/m \tag{3.30}$$

where ρ is the plate density in grams per cubic centimeter. If we assume an average crustal rock density of 2670 kg/m^3, then the numerical value of Bouguer correction become 112 kg/m.

Unlike free-air correction, Bouguer correction is subtracted when the station is above the datum reference plan and vice-versa. Bouguer and free-air corrections are often combined into an elevation correction which can be determined as follows

$$\frac{\Delta g_e}{\Delta R} = \frac{\Delta g_{fa}}{\Delta R} - \frac{\Delta g_b}{\Delta R} \tag{3.31}$$

$$\frac{\Delta g_e}{\Delta R} = (0.3086 - 0.04192\rho)\, mGal/m \tag{3.32}$$

d. Terrain correction: In study areas with flat topography, the elevation correction (i.e combined Bouguer and free-air correction) is normally sufficient to account for slight effect of topographic variations on the gravity readings. However, in areas where there are

substantial variation in the elevation, especially close to the gravity stations, a special terrain correction must be performed. One method is to divide the area into zones and compare the elevation in each zone with the station elevation and compute the gravity effect of each zone (Telford et al., 1990). Another popular method nowadays is employing computer programs to compute the terrain correction from digital elevation model (DEM), which can be done fairly quickly compared to traditional methods such as the zoning method.

e. **Regional trend correction:** In shallow surface investigation using gravity study, the target wavelength of interest is the short wavelength gravity anomalies, whereas in case of deeper structure study, longer spatial wavelength is targeted. Since long wavelength regional trends can make analysis of the short wavelength residuals difficult, it is important to remove the regional trend from data in order to clearly image the shallow structure corresponding to the short wavelength gravity anomaly.

f. **Drift correction:** Drift in gravity instrument takes place due to elastic creep in the springs of gravimeter which produces an apparent change in the gravity measurement values at each station over time. Drift is also attributed to tidal distortions of the solid Earth and changes in the ground water level. To correct this drift problem, a standard procedure of looping is normally followed wherein measurements are repeated at the base station. The differences are then interpolated and a correction for profile readings are obtained.

In this thesis, we applied gravity data reductions procedures including: 1) drift correction by creating measurement loop over time between the base station and other stations along the profile, 2) elevation correction using accurate elevation data and assuming an average density of, $\rho = 2670kg/m^3$, and 3) regional trend correction by using the regional trend value of ca. -1.58 $\mu Gal/m$ for deep structures obtained by Hammer et al. (2013).

Advantages and limitation of gravity method

The advantages and limitation of gravity method are listed below:

Advantages

- Unlike other geophysical methods, gravity measurements are not as much susceptible to cultural noises and thus can be performed virtually in any location, including indoors.

- Gravity method is a relatively fast, inexpensive and can be useful for evaluating large survey areas.
- Gravity method is non-destructive since it measures an existing field through passive measurement.
- Deeper investigation depth.

Limitations

- Each station in gravity method has to be surveyed for precise elevation and latitude. Also one needs to perform loops, which could be time consuming and costly, especially for large survey area.
- Like other geophysical methods, models obtained through gravity study are non-unique and therefore require prior knowledge about the subsurface geology of the area for interpretation.

3.4 Geophysical Inverse theory

3.4.1 Conceptual Introduction

> "*Most people, if you describe a train of events to them, will tell you what the result would be.They can put those events together in their minds, and argue from them that something will come to pass. There are few people, however, who, if you told them a result, would be able to evolve from their own inner consciousness what the steps were which led to that result.*" *(Sherlock Holmes)*

Geophysical approach to solving real world problem aims to explain the unknowns through parameterization of the physical system to develop a model. Forward and inverse are the two fundamental approaches used by geophysicists for solving geophysical problems. While forward modeling is performed to predict data trend based on plausible physical characteristics, the more complicated inverse problem, on the other hand, aims to determine the physical characteristics of the system based on observed data. More directly inverse problem is determining cause from effect and direct problem, determining effect from cause. These two fundamental processes can be represented in the following schematic diagram (Figure 3.7).

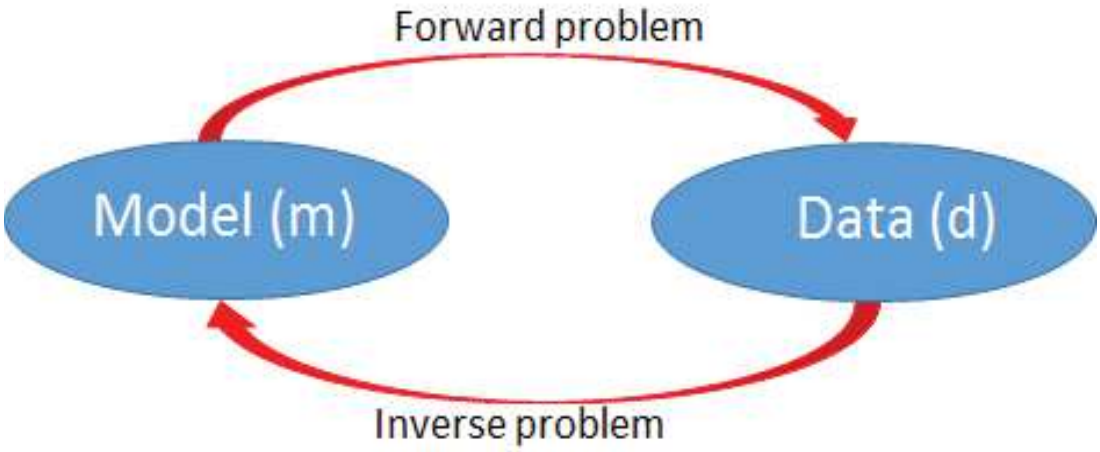

Figure 3.7: Schematic diagram showing the relationship between model and data

Model can be understood as a simplified, idealized representation of the real world space defined by model parameters of physical quantities and its auxiliary functions. It can be associated with either linear or non-linear relationship between parameters. The model parameters are unknowns, or the numerical quantities that one is attempting to estimate. The selection of model parameters are rather arbitrary and purely problem dependent. Data are instrument responses or measurements made to constrain the problem. In solving geophysical inverse problems, Hadamard (1902) states that the mathematical models of physical phenomena should have three important properties that

- A solution exist (existence)
- The solution is unique (uniqueness)
- The solution's behavior changes continuously with the initial conditions (stability)

Based on the above classical theory, all geophysical inverse problems are ill-posed because their solutions are either non-unique or unstable. The non-uniqueness mainly arises from the fact that data are discrete and located at the surface; if data are continuous, the solution will be unique (Backus & Gilbert, 1970). However, generally this problem can be solved to obtain geologically sensible models by using one of the two methods. The first method involves intuitive estimation of possible solutions and selection of sensible geological model by the interpreter. The second method is based on application of several types of regularization methods, which allow automatic selection of the solution by computer using *a priori* knowledge.

3.4.2 Mathematical background

The process of inferring unknown subsurface geophysical properties based on instrument measurements, such as potential field or seismic waves is fundamentally associated with solving the geophysical inverse problem (Scales & Smith, 2000; Tarantola, 2005). Suppose we want to determine the model(m) from known set of data(d), then the discrete linear forward equation can be written as

$$d = Am \tag{3.33}$$

where d is N-dimensional data vector, m is a M-dimensional model parameter vector, where A is a N x M dimensional matrix containing only constant coefficients. The matrix operator A^{-1} then represents the inverse transformation to calculate the estimated model $\hat{m}$

$$A^{-1}Am = A^{-1}d = \hat{m} \tag{3.34}$$

The matrix operator $A^{-1}A$ is called the resolution kernel (or greens functions because of analogy with continuous function case) and it describes how well resolved is the model. In ideal situation when $A^{-1}A$ corresponds to a identity matrix or delta function, $m = \hat{m}$ in the above equation and the model resolution thus obtained is said to be perfect. However, in real world cases $A^{-1}A$ comprises of superposition of a finite number of functions and thus, the resolution kernel cannot be of infinite dimension and the inverse problem is not unique in the sense that there are more models than one to explain the data equally well (non-uniqueness). In essence, the estimated model is a blurred version of the true model. Thus equation 3.34 is an idealistic case of solving the inversion problem.

For realistic case, inversion problem really consists of two steps. Let d denote data and m represent the true model. Then from d one reconstructs a model $\hat{m}$. Besides estimating $\hat{m}$ from d, one also need to define the relationship between $\hat{m}$ and the true model m. This is termed as appraisal problem. In the appraisal problem, essentially, one aims to access what properties of true model are constrained by the estimated model. Thus inversion can be defined as *inverson=estimation+appraisal* (Snieder, 1998).

In inversion problems, there are two main reasons why the estimated model differs from the true model: 1) The first reason is due to non-uniqueness of geophysical inverse problem where there are several models that fit the data, and 2) secondly scientific data are never noise free and therefore the estimated model is affected by measurement noise. Model estimation and appraisal is only well resolved for linear inverse problem; for nonlinear inverse problem other linearization process must be applied to solve the problem.

Linear Problem

In case of finite dimensional linear inverse problem, let the model parameters be ordered in a vector m and accordingly, the data vector can be ordered in a vector d. The matrix A then relates the data to the model through the product Am which describes the physics and mathematics of the selected model. Since data always are contaminated with errors e, the model and the data can be related by

$$d = Am + e \tag{3.35}$$

The estimated model $\hat{m}$ is constructed from the measured data d and the true model is represented by m. The estimated model then can be related to the data by

$$\hat{m} = A^{-1}d \tag{3.36}$$

A^{-1} is known as the generalized inverse of the matrix A. Since in general the number of data is different from the number of the model parameters, matrix A is usually non-square and therefore its formal inverse does not exist. The relationship between the estimated model $\hat{m}$ and the true model m can be expressed by inserting equation 3.35 in equation 3.36

$$\hat{m} = A^{-1}Am + A^{-1}e \tag{3.37}$$

The last term in equation 3.37 shows how errors e are mapped onto the estimated model. Since these errors are not known deterministically, they cannot be subtracted out from the data. However a common way to estimate the model is to determine the model $\hat{m}$ such that L2 or Euclidean norm difference between the real data (d) and the recalculated data $(A\hat{m})$ is as small as possible (Snieder, 1998). This implies that the least-square solution is given by the model that minimizes the following cost function:

$$S = ||d - Am||^2 \tag{3.38}$$

Nonlinear Problem

Even though there is no exact general theory to solve model appraisal problem for truly nonlinear problem with infinite degree of freedom, in practice often the problem is linearized around the estimated model and a linear theory is adopted to make inferences about the resolution and reliability of the estimated model. The nonlinear problem can be expressed as follows:

$$d = A(m) + e \tag{3.39}$$

where A denotes a nonlinear function. The iteration processes begins with a starting model, m_0, and looks for small improvement, δm_0, by linearized inversion of the residuals $\delta d_0 = d - A(m_0)$:

$$\delta d_0 = G_0 \delta m_0 + e \tag{3.40}$$

The matrix G_0 must be derived from the nonlinear function $A(m)$ for each iteration; subscript zero denotes first iteration. The elements of A are partial derviatives of the model with respect to the data and may be expressed as

$$(G_0)_{ij} = \frac{\partial A_i}{\partial m_j}|_{m=m_0} \tag{3.41}$$

In this thesis, we adopted the stochastic inversion approach to constrain the shallow surface geometry of frontal thrust in southern Bhutan. Unlike common inversion approach that seek to look for the simplest model, the stochastic inversion technique has the ability to better constrain the fault geometry since no smoothing is applied. Moreover, the stochastic method provides measurement uncertainties on the dip angle obtained and allow for studying trade-off between the fault geometry and other petro-physical properties. The details of the stochastic inversion approach and other forward modeling approaches used in this thesis is elaborated in the following.

3.4.3 Stochastic Inversion used in the thesis

The stochastic inversion method combines prior information, observed data and forward models to produce models that are consistent with all available data (Ramirez et al., 2005). Following Mosegaard & Tarantola (1995), a Markov Chain Monte Carlo technique is used in this thesis to pseudorandomly generate a large collection of models according to the posterior probability distribution.

The pseudorandom walk through a defined multi-dimensional parameters is controlled by following the rules for the transition between model m_i to model m_j:

- If L(m_j)≥L(m_i), then accept the proposed transition from i to j
- If L(m_j)<L(m_i), then accept the proposed transition from i to j with the probability $\frac{L(m_j)}{L(m_i)}$,

where L(m_i) and L(m_j) are the likelihood of the old and the new model, respectively. Here we assume that the likelihood function can be written as

$$L(m_i) = exp\left(-\frac{1}{n_{obs}}\sum_{n=1}^{n_{obs}}\frac{|calc_n(m_i) - obs_n|}{\sigma_n}\right) \tag{3.42}$$

where n_{obs} is the number of data points, obs is the data vector and σ_n is the total variance, i.e. the uncertainties associated with each data point. $calc(m_i)$ is the forward modeling function associated with the model m_i. The detailed formulation of stochastic inversion procedures are described in Drukpa et al. (2017).

The posterior probability of each model parameter is obtained from the final collection of the large number of sampled models. Compared to commonly used approaches based on the search for the simplest model, the main advantages of the stochastic method include its ability (1) to assess the fault geometry because no smoothing is applied, (2) to provide a measurement of the uncertainties on the obtained dip angle and (3) to allow the study of trade-off between geometric and either electrical resistivity, velocity or density properties. The main limitation of the present approach comes from the total number of tested parameters which cannot exceed in dozen on a standard workstation.

Inversion approach

The stochastic inversion approach involves incorporating a priori information obtained from the ERT solutions and geological studies. Then assuming a simple geometry of the subsurface with possible range of parameters to be determined, a forward model is performed to produce a model that is consistent with the observed data. This process (also termed as likelihood function) measures the fit between the observed data and data predicted from the forward model. Next a Markov Chain Monte Carlo (MCMC) technique is applied to pseudo-randomly generate a large collection of sampled models (5 x 10^5) according to the posterior probability distribution. The posterior probability distribution can be defined as

$$\textit{Posterior probability} = \textit{Prior probability} + \textit{new evidences (likelihood)} \tag{3.43}$$

An example of stochastic inversion approach applied to observed resistivity data from our site in south-central Bhutan is shown in Figure 3.8. The stochastic inversion generates a large collection of models and the 2D model shown in Figure 3.8 is the best fit model which show strong correlation between the observed and computed data.

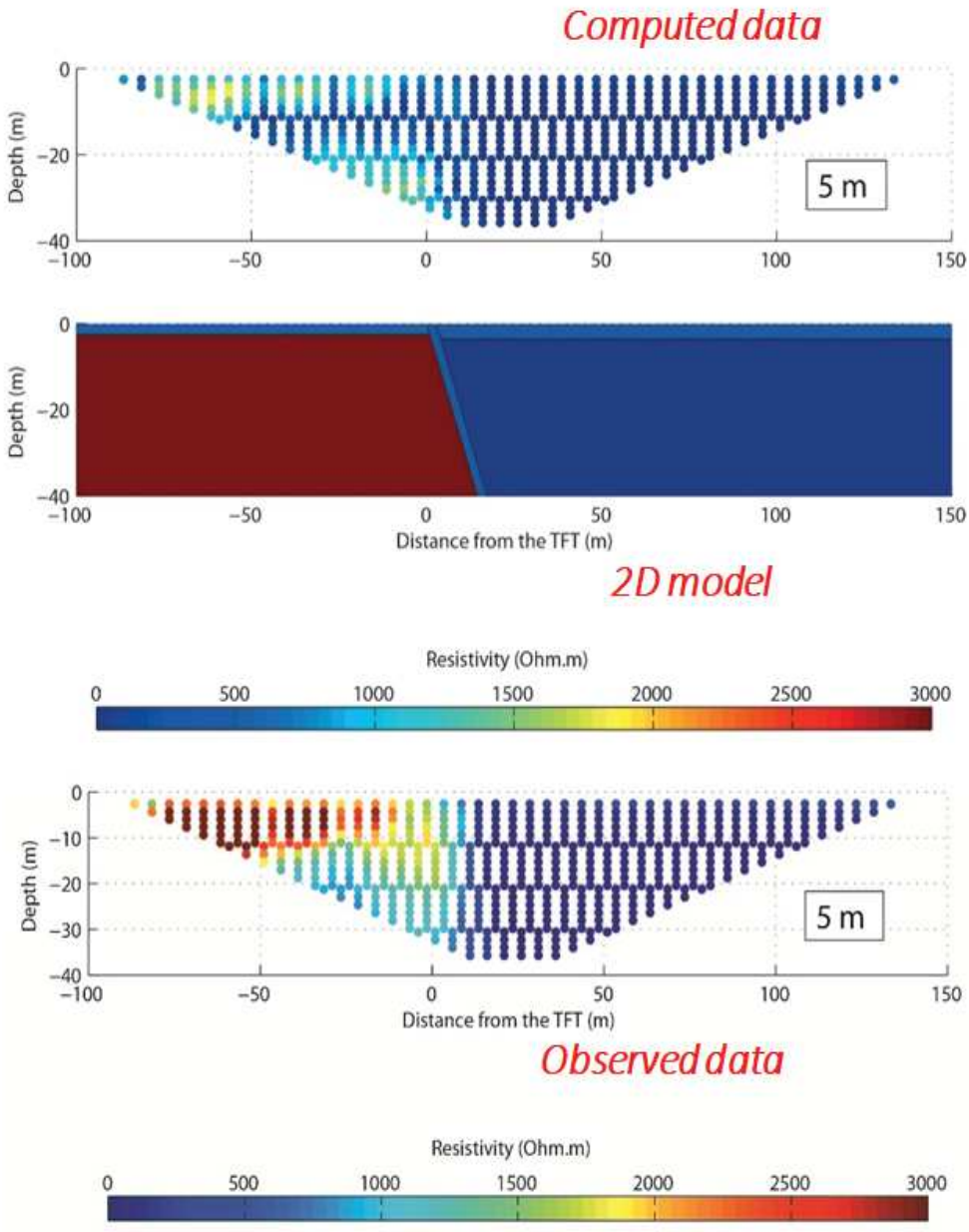

Figure 3.8: A 2D best fit model obtained by comparing the synthetically computed data with the observed data and applying stochastic inversion processes.

Part II

Application to south-central and south-west Bhutan

CHAPTER 4

CHARACTERIZATION OF TOPOGRAPHIC FRONTAL THRUST GEOMETRY IN SARPANG

4.1 Geology of study area

4.1.1 Introduction

In general, the southern part of Bhutan is defined by abrupt transition from the relatively steeper sloping Lesser Himalayas to low lying gentle areas of the sub-Himalayas. As a result, the topography of foothills, especially along the the path of major north-south flowing rivers, originating from the Himalayas, are dominated by huge alluvial deposits. Exposure of alluvial terraces due to river incision, flat topography and easy accessibility provide excellent opportunity for studying active faulting through geomorphological and geophysical approaches.

4.1.2 Geology and tectonics

The southern section of the Himalayas, in general, consists of non-metamorphosed Miocence to Pliocene Siwalik Group molasse sediments (Gansser, 1981; Schelling & Arita, 1991; Loris et al., 2010; Long et al., 2011). The sub-Himalayan molasse is bounded to the north and south by the Main Boundary Fault and Main Frontal Thrust, respectively. However, along major sections of the southern part of the west and central Bhutan the Siwaliks are missing (Long et al., 2011). As shown in Figure 4.1, this is particularly so in the current study area in Sarpang where a 10 km wide re-entrant feature juxtaposes the Lesser Himalaya and

Quaternary alluvium (Long et al., 2011; Le Roux-Mallouf et al., 2016).

Dasgupta et al. (2013) reported presence of the most frontal north facing tectonic scarp which they termed as the Frontal Back Thrust (FBT). They noted that the FBT is active and has the potential to accommodate limited amount of shortening. However, its relationship with other main structures in the area is not yet established. North of the FBT, within the re-entrant where detailed geophological and paleoseismic studies have been conducted (Berthet et al., 2014; Le Roux-Mallouf et al., 2016), the main topographic scarp structurally may correspond to the MBT or one of its splays and is termed as the Topographic Frontal Thrust (TFT) (Le Roux-Mallouf et al., 2016). Towards south of TFT lies the foreland basin comprising of mainly recent sedimentary infills that onlap onto the cratonic rocks of northern India. Based on detailed studies that show complex tectonic setting in Sarpang area as depicted in Figure 4.2, it is safe to state that the location of MFT and MBT shown in Figure 4.1 are probably not correct.

4.1.3 The Topographic Frontal Thrust (TFT)

The southernmost active fault that presumably extends along the entire Himalayan arc is termed as the Main Frontal Thrust (MFT). In general, the MFT is well defined in Nepal Himalayas where it coincides with the present day Himalayan topographic front. However, as mentioned in the previous paragraph, in the Bhutan Himalayas the location estimate of the MFT is far from straightforward. Le Roux-Mallouf et al. (2016) proposed that the main topographic scarp observed within the re-entrant in Sarpang area could correspond to the MBT or one of its splays, and termed the active fault as the Topographic Frontal Thrust (TFT).

Taking advantage of favorable conditions in Sarpang area, the TFT trace observed in the paleoseismic trench and geomorphological framework in the vicinity has been studied in detail (Berthet et al., 2014; Le Roux-Mallouf et al., 2016). The TFT trace located on the left side of Sarpang Chu cuts through the Holocene deposits leading to a cumulative alluvial terrace uplift of about 50m (T6 in Figure 4.2B). At the paleoseismic trench site, T2 terrace is defined by an approximately 6 m topographic scarp where the north-south flowing Sarpang Chu cuts through the alluvial cover and the exposes the east-west trending TFT fault between an abandoned fluvial terrace and modern alluvium. The tectonic scarp also effects the local drainages and guides a lateral tributary into the Sarpang Chu.

The main lithological units encountered in the paleoseismic trench is depicted in Figure

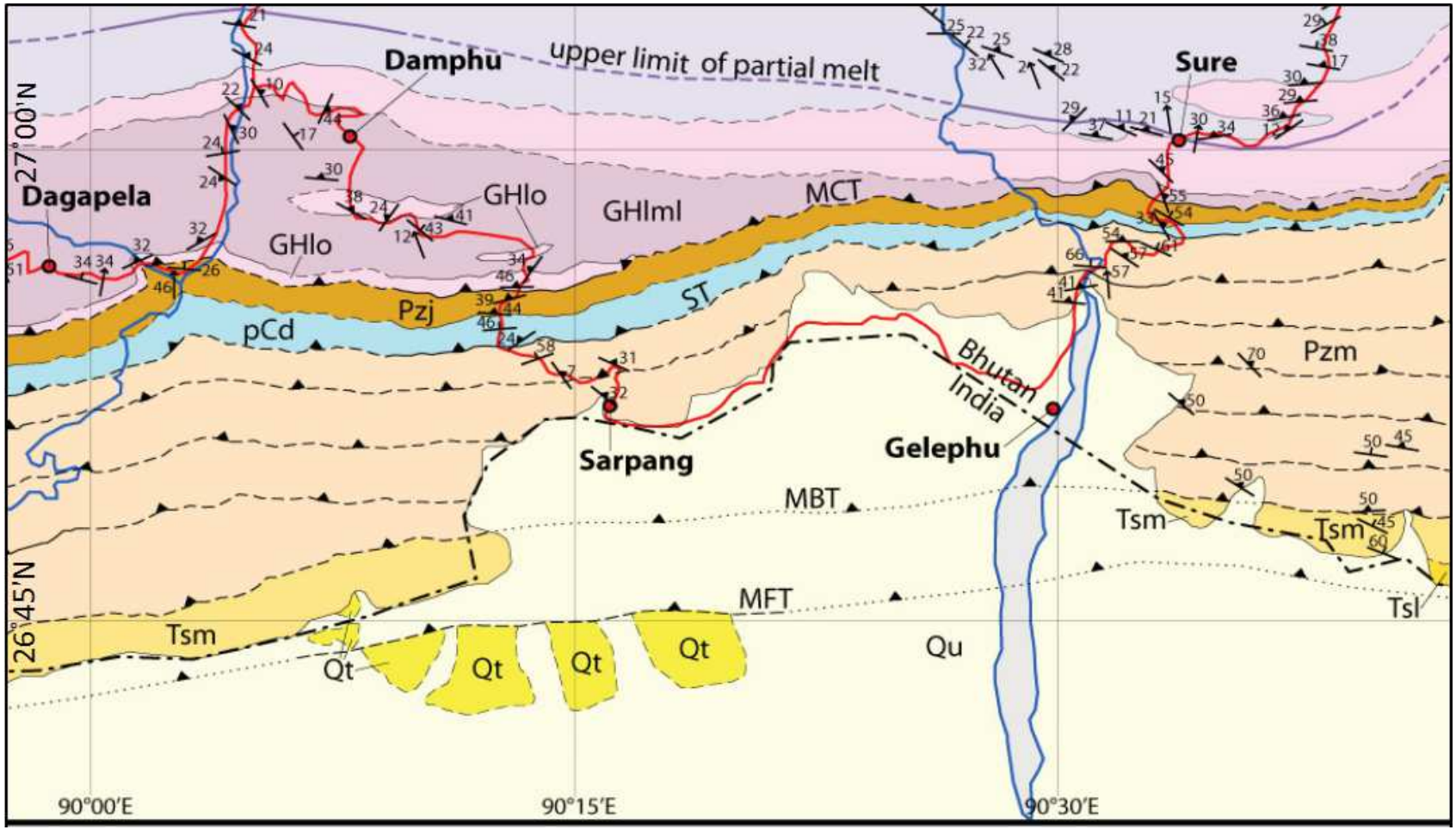

Figure 4.1: Map of Sarpang area showing the major geological and tectonic units (Abbreviation in the map: Qt-River terraces; Qu-Unconsolidated sediments deposited in braided stream;Tsl-Lower member Siwalik Group; Tsm-Middle member Siwalik Group; Pzm-Manas Formation; Pzj-Jaishidanda Formation; pCd-Daling Formation; GHlo-Greater Himalaya structurally lower orthogneiss unit; GHlml-Greater Himalaya structurally lower metasedimentary unit; MFT-Main Frontal Thrust; MBT-Main Boundary Thrust; ST-Shumar Thrust; MCT-Main Central Thrust (After Long et al., 2011).

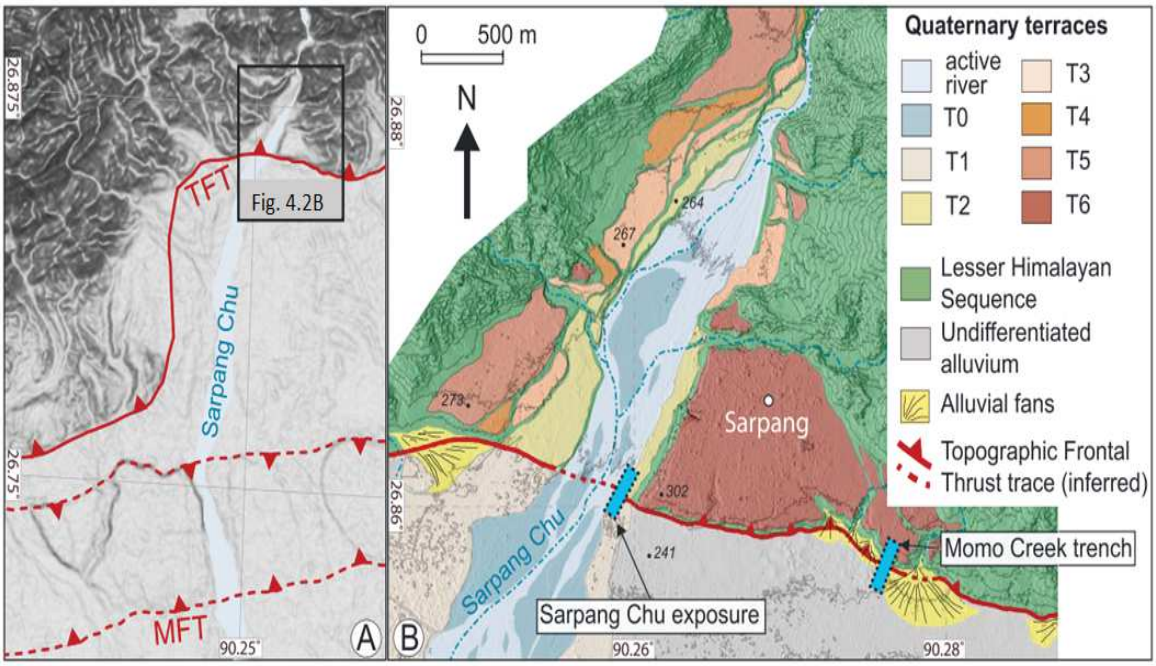

Figure 4.2: Geomorphological map of Sarpang area. (a) Shaded map of Sarpang showing the location of MFT and TFT. Black triangle shows the location of study area. (b) Geomorphological map of TFT in Sarpang superimposed on Pleiades DEM. Alluvial terraces are labeled TO (active channel) to T6 (oldest). Blue triangle represent location of paleoseismic trench. Black points show elevation from Pleiades DEM with countour interval of 20 m (After Le Roux-Mallouf et al., 2016).

4.3. The deepest exposed unit on the hanging wall towards to the northern side is composed of highly deformed, massive, pale purple phyllite that corresponds to the Paleozoic Buxa Formation of the Lesser Himalaya Sequence. Overlying this unit is a 3 m openwork, clast-supported alluvial gravel layer comprising of well-rounded pebbles and cobbles in a sandy matrix. This layer is overlain by a distinct fine sand to silt unit most likely formed as an overbank deposit. In the footwall side towards to the south, the gravel unit observed in the hanging wall is exposed near the base of the trench. On top of this gravel layer sits a 2.5 m thick fine-grained sand layer typical of low energy alluvial deposit interpreted to be coming from the lateral drainage influenced by the fault scarp. Careful observation of the trench section show a shear zone that juxtaposes the layers on the hanging wall and foot wall along a 1m deformed zone comprising of sheared sand and gravel unit. This sheared and highly deformed zone interpreted to the TFT dips at an angle of 17-24° towards north. Nearby the front in Sarpang and vicinity area as shown in Figure 4.1, bedding/foliation of rocks exhibit dips ranging from 10-60° (Long et al., 2011).

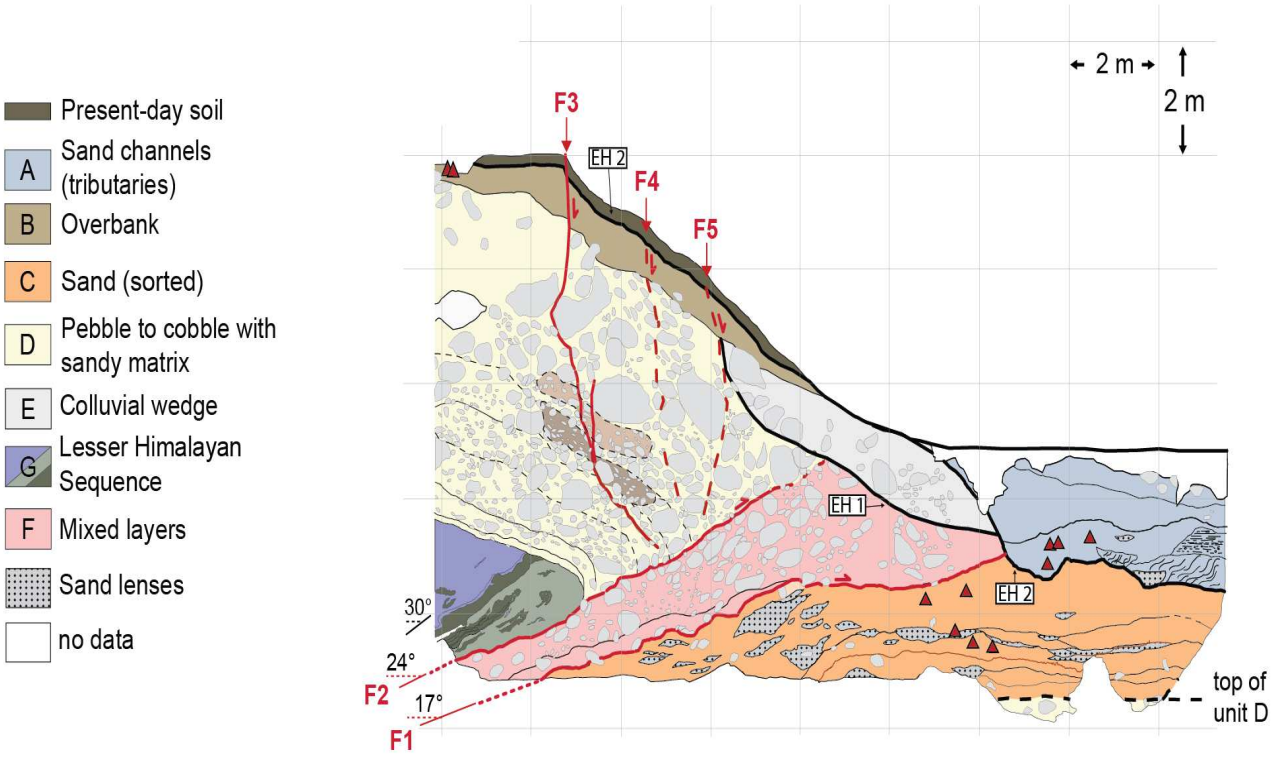

Figure 4.3: Detailed log over a 2 m grid at the paleoseismic trench in Sarpang showing major geological and tectonics units. The solid and dashed red lines show the main certain and suspected faults, respectively. Thick black lines labeled EH 1 and EH 2 denote the event horizons. (After Le Roux-Mallouf et al., 2016).

4.2 Geophysical field campaign 2015

4.2.1 Introduction

Prior to the first geomorphological and paleoseismological study (Berthet et al., 2014; Le Roux-Mallouf et al., 2016) in the south-central Bhutan, very little is known about deformation characteristics at the front and occurrences of large magnitude historical earthquakes. Hetényi et al. (2016), based on new historical information combined with geological evidences, proposed that the 1713 earthquake reported by Ambraseys & Jackson (2003) in fact occurred in 1714 with a updated magnitude estimate of 8±0.5 and epicentral location in western Bhutan. Others have categorized Bhutan as either, in a seismic gap (Bilham & England, 2001) or having apparent reduced seismicity owing to its location in the stress shadow of the great 1897 Shillong plateau earthquake (Gahalaut et al., 2011). The combined effort of geomorphology and paleoseismology through 2013-2015 provided important information

to study deformation mechanism at the front along the Bhutanese Himalayas. Dating of river terrace and dip angle of fault trace on the surface allow a vertical uplift rate of 8.8 ± 2.1 mm/year. Further from paleoseismic study at least two large magnitude events occurred on the active TFT in Sarpang, the last one in 1714 and other event during the medieval time. However, due to uncertainty in the geometry of the fault at shallow surface, the overthrusting slip rate along the fault is poorly constrained. To address this information gap, in 2015, we deployed high resolution near-surface geophysical techniques to assess the fault geometry and other petrophysical properties of the subsurface geology in Sarpang.

4.2.2 Schedule of field program

The following are itineraries in pursuant of the geophysical field survey in Sarpang in 2015:

- 10 March 2015: Arrival of Geosciences Montpellier team in Bhutan
- 10-12 March: Inspection and testing of equipments; test electrical resistivity measurement in Paro, western Bhutan. Absolute gravity measurement in the Department of Geology and Mines office, Thimphu.
- 13 March: Travel from Thimphu to Sarpang/Gelephu.
- 14-18 March: Field work in Sarpang area.
- 19 March: Travel from Sarpang-Thimphu.
- 20-21 March: Packing of instrument and shipment from Paro.
- 22 March: Departure of Geosciences Montpellier (GM) team from Bhutan.

4.2.3 List of field equipments

The following equipments were used for acquisition of geophysical data in the study area.

Table 4.1: List of geophysical equipments used in 2015 field survey

Sl. No.	Equipment Types	Remarks
1	Syscal resistivity meter	48 channels
2	SoilSpy Rosina-Tromino seismic equipment	24 channels
3	Scintrex CG-5 Gravimeter	
4	Leveling equipment	to acquire elevation data for gravity

4.2.4 Electrical Resistivity Profile

Desk study

As a part of desk study and based on the *a priori* knowledge of the area, a test model using Res2dmod® was performed on a simple two layers model with steep to shallow dipping fault employing dipole-dipole geometric configuration. Based on the lithological contrast in the area, we assigned 10 Ω.m for hanging wall and 30 Ω.m for the foot wall as shown in the model section (Figure 4.4). The corresponding inverted section (Figure 4.5) clearly shows the resolving power of the resistivity method to image the dipping structure given sufficient resistivity contrast between the interfaces.

Data acquisition

The electrical resistivity profile was aligned almost in the north-south direction and perpendicular to the strike of the fault as shown in Figure 4.6. This setup has done mainly to ensure proper imaging of the contrast coming from the fault zone. We adopted the commonly used Wenner-Schlumberger and Dipole-Dipole configuration to achieve good compromise between vertical and horizontal resolution and effect of noise (Dahlin & Zhou, 2004; Loke, 2015). Using Syscal® resistivity meter equipment with 48 channels, 3 profiles were performed with different electrode spacing of 1m, 2.5 m and 5 m corresponding to a total profile spread length of 47 m, 117.4 m and 235 m, respectively, as shown in Figure 4.6. All the resistivity profiles have the first electrode position at southern end on the footwall side of the fault.

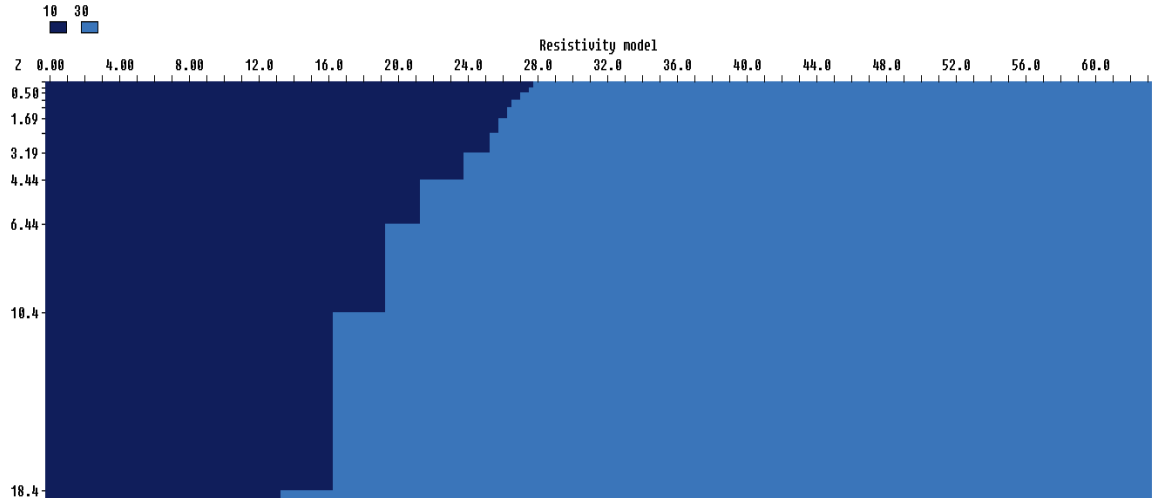

Figure 4.4: 1 m spacing Dipole-Dipole model generated using res2dmod involving 2 layers with high resistivity contrast and gently dipping TFT.

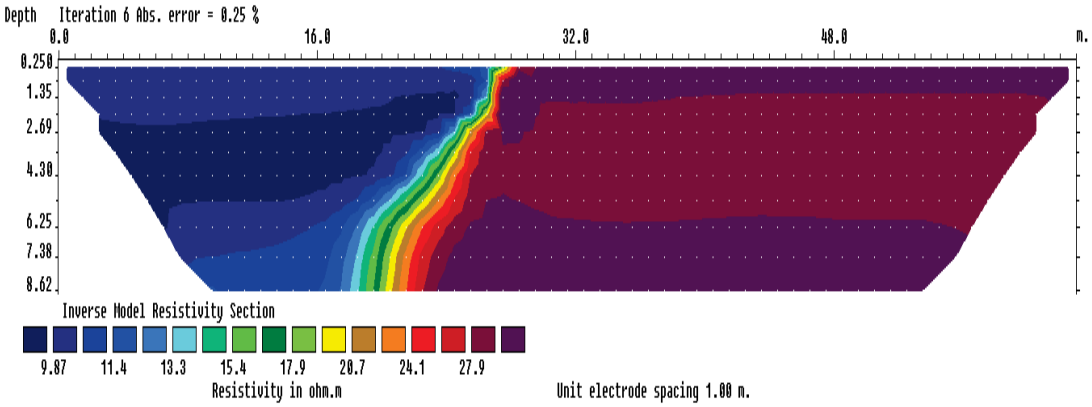

Figure 4.5: Inversion model resistivity section obtained using data generated from the model in Figure 4.4.

To attain maximum depth of investigation for assessing the fault geometry at depth, we positioned the center of the profiles at the paleoseismic trench where the TFT outcrop was intersected (Figure 4.6). The TFT is approximately located at 20 m from south in case of 1m spacing profile, 36 m for 2.5 m electrode spacing, and 98 m for the 5 m spacing profile. The GPS location with respect to the electrode positions and TFT location along the resistivity profile is given in Table 4.2.

Figure 4.6: Location of electrical resistivity line with respect to the position of the fault and paleoseismic trench.

Table 4.2: GPS coordinates along the electrical resistivity profile with 5m electrode spacing in Sarpang

GPS points	**GPS location**		**Elevation (m)**	**Remarks**
	Latitude (deg-min)	**Longitude (deg-min)**		
094	N26 51.618	E90 15.500	280	South end
095	N26 51.621	E90 15.503	280	
096	N26 51.623	E90 15.504	280	
097	N26 51.626	E90 15.505	280	
098	N26 51.628	E90 15.506	280	
099	N26 51.631	E90 15.508	280	
100	N26 51.633	E90 15.509	280	
101	N26 51.635	E90 15.511	280	
102	N26 51.638	E90 15.512	280	
103	N26 51.640	E90 15.514	281	
104	N26 51.643	E90 15.515	281	
105	N26 51.645	E90 15.517	281	
106	N26 51.648	E90 15.518	281	
107	N26 51.650	E90 15.520	281	
108	N26 51.652	E90 15.521	281	
109	N26 51.654	E90 15.523	281	
110	N26 51.657	E90 15.525	281	
111	N26 51.659	E90 15.526	281	
112	N26 51.661	E90 15.528	281	
113	N26 51.663	E90 15.530	281	TFT
114	N26 51.665	E90 15.532	281	TFT
115	N26 51.667	E90 15.534	281	TFT
116	N26 51.669	E90 15.536	280	
117	N26 51.672	E90 15.537	280	
118	N26 51.674	E90 15.539	280	
119	N26 51.677	E90 15.540	281	
120	N26 51.679	E90 15.542	281	

GPS points	**GPS location**		**Elevation (m)**	**Remarks**
	Latitude (deg-min)	**Longitude (deg-min)**		
121	N26 51.681	E90 15.543	282	
122	N26 51.684	E90 15.545	282	
123	N26 51.686	E90 15.547	282	
124	N26 51.688	E90 15.548	282	
125	N26 51.691	E90 15.550	282	
126	N26 51.693	E90 15.551	282	
127	N26 51.695	E90 15.553	283	
128	N26 51.697	E90 15.554	283	
129	N26 51.700	E90 15.556	283	
130	N26 51.702	E90 15.557	283	
131	N26 51.704	E90 15.559	283	
132	N26 51.707	E90 15.560	282	
133	N26 51.709	E90 15.562	282	
134	N26 51.711	E90 15.564	282	
135	N26 51.713	E90 15.565	283	
136	N26 51.716	E90 15.567	283	
137	N26 51.718	E90 15.569	283	
138	N26 51.720	E90 15.570	283	
139	N26 51.722	E90 15.572	284	
140	N26 51.724	E90 15.574	284	
141	N26 51.727	E90 15.575	284	north end

Smoothest model inversion

In a first step, to perform electrical resistivity tomography, the Res2dinv software was adopted. The res2dinv technique uses smoothness-constrained least-squares method (deGroot Hedlin & Constable, 1990; Sasaki, 1992). However, in case of large data set that requires huge memory, other much faster least-squares method based on a quasi-Newton optimization technique (Loke & Barker, 1996) is also available. The smoothness-constrained least-squares inversion technique is based on the following equation

$$\left(J^T J + uF\right) d = J^T g \tag{4.1}$$

where $F = f_X f_X^T + f_Z f_Z^T$

f_X =horizontal flatness filter

f_Z =vertical flatness filter

J =matrix of partial derivative

J^T =transpose of J

u =damping factor

d =model perturbation vector

g =discrepancy vector

The res2dinv program divides the subsurface into number of small rectangular prisms and in the process, calculates the resistivity value of each prism with goal to reduce the difference between observed and calculated apparent resistivity values. The inversion process then output a resistivity model along with a measure of fit between the observed and calculated value given by the root-mean-squared (RMS) error. Loke (1999, 2015) suggests that it is advisable to select the model at the iteration after which the RMS error doesn't change significantly. This is normally attained at 4^{th} or 5^{th} iterations.

In case of data set with topography information, the inversion subroutine automatically incorporates the topography information into the model by using either the finite-element or finite difference method.

The cleaned and sorted resistivity data set from the study area were imported into the res2dinv program. Since elevation along the resistivity profile is almost flat, no topographic information is incorporated in the data. The inverted model resistivity sections for dipole-dipole array and Wenner-Schlumberger array with different electrode spacing are shown in Figures 4.7 $\&$ 4.8, respectively. Because of high quality data with good signal-to-noise ratio (SNR), the inversion attains good fit between the observed and calculated data with RMS

error of $\sim$5$\%$ in case of dipole-dipole configuration and $\sim$3$\%$ for the Wenner-Schlumberger array. The inversion achieves convergence at 4^{th} or 5^{th} iterations.

The model inversion sections for all electrode spacing (Figures 4.7 $\&$ 4.8) show high resistivity contrast, especially at depths greater than 5m. As expected the strong resistivity contrast with northerly dipping features is observed at the location of the fault encountered in the paleoseismic trench. This clearly show that the ERT method is able to image the fault geometry. In general, the inversion model section indicates that fault has shallow dip angle at the top and steepens at depths. The top alluvial layer is also clearly delineated especially in the model sections with 1 m and 2.5 m electrode spacing in accordance with the observations in the paleoseismic trench.

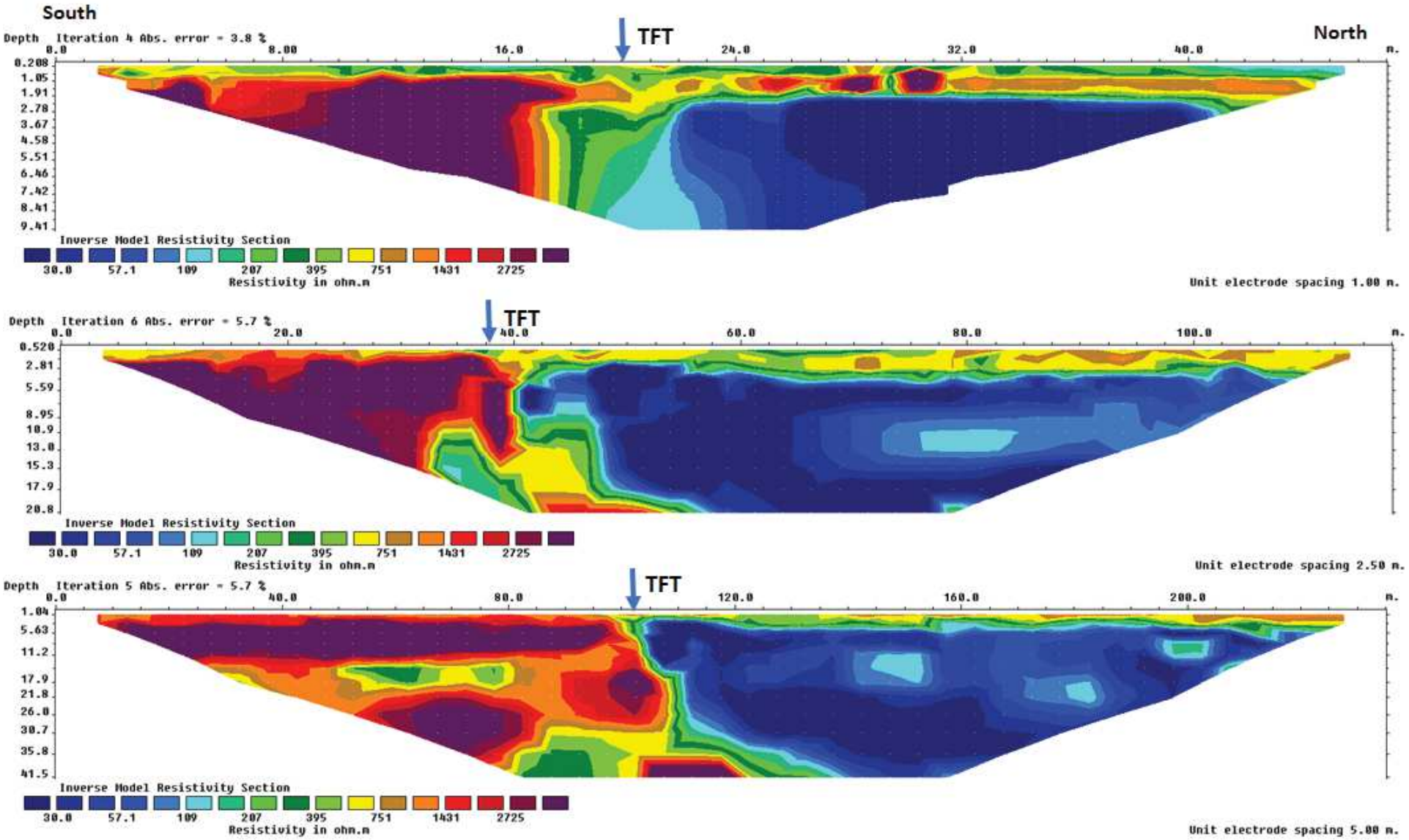

Figure 4.7: 2D Dipole-dipole array ERT section with 1 m (top), 2.5 m (middle) and 5 m (top) electrode spacing

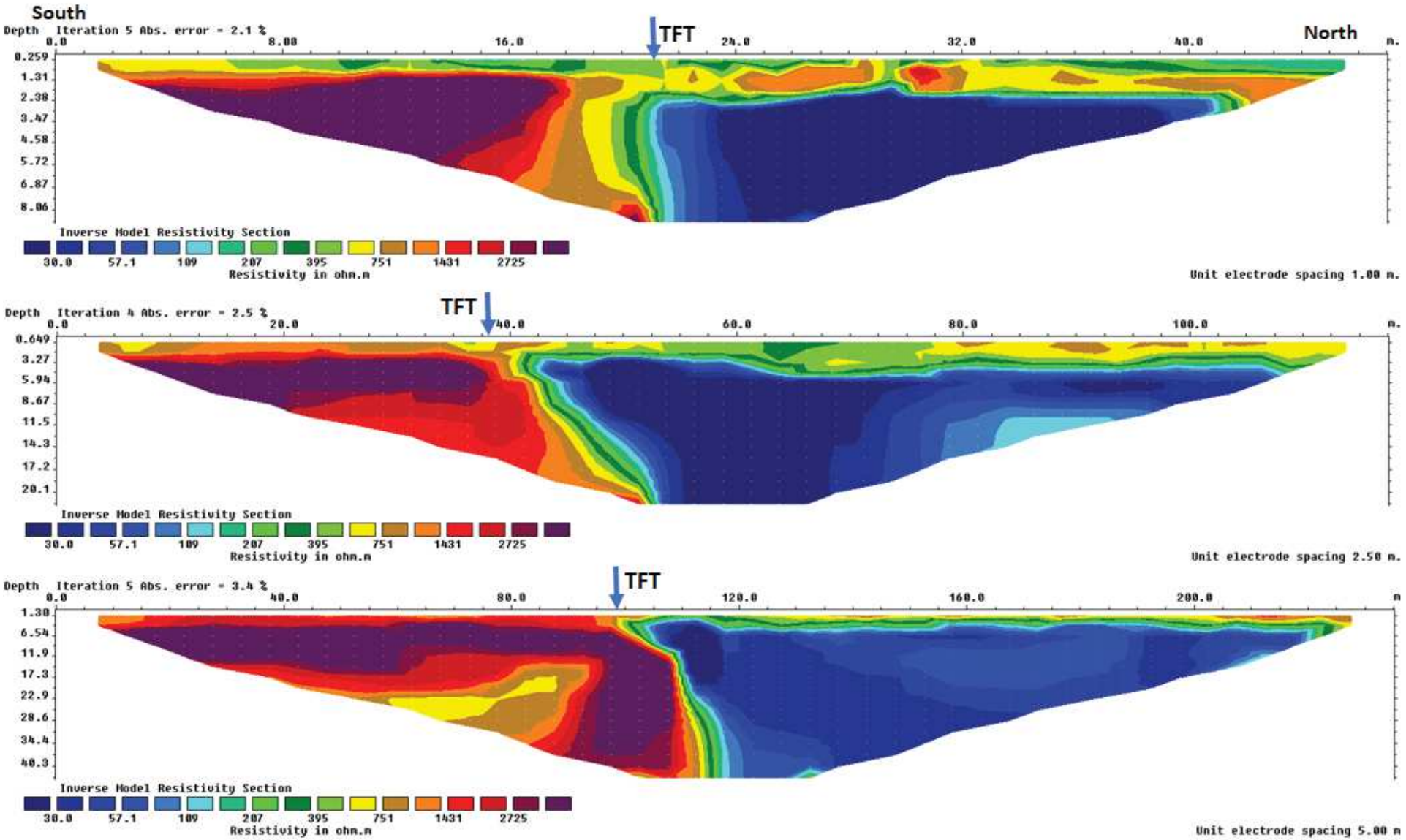

Figure 4.8: 2D Wenner-Schlumberger array ERT section with 1m (top), 2.5 m (middle) and 5 m (top) electrode spacing

Stochastic approach

In a second step, to quantitatively constrain the fault geometry and shallow geological features, an alternative approach based on forward modeling approach of Loke (2015) and stochastic method for imaging shallow structures as explained in part 3 are adopted. This method is expected to compliment the smoothest model inversion and validate the outputs thus obtained.

A priori information & model setting

The res2dmod uses either finite difference or finite element model wherein the surface is divided into number of blocks using rectangular mesh (Figure 4.9).

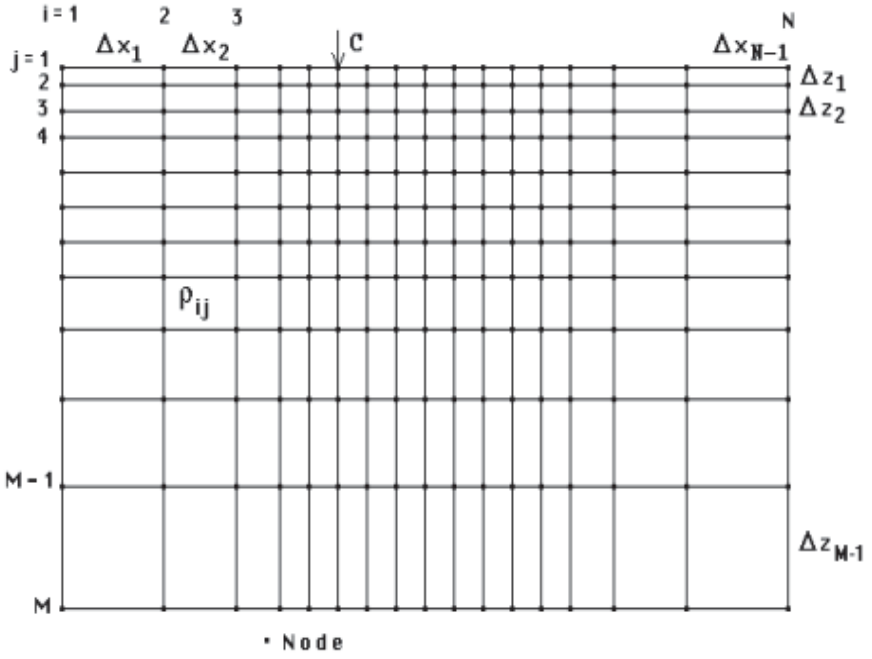

Figure 4.9: Schematic diagram of the finite difference or finite element used in the res2dmod program (After Loke, 2015).

Notice that the grid model has N-1 columns and M-1 rows and the blocks can have different resistivity values. By employing sufficiently finer mesh, with possibility of using either 2 or 4 horizontal nodes per unit electrode spacing, complex geological structures can be modeled (Loke, 2015). Utilizing resistivity variation inputs derived from ERT sections (Figures 4.7 & 4.8), a priori geometry information from structural and geomorphic observations (Long et al., 2011; Le Roux-Mallouf et al., 2016) and assuming a simple geometry, each 2D model as depicted in Figure 4.10, is associated with five bodies including a south (STL) and north

(NTL) top layers, a south (SL) and north (NL) shallow layers and a fault layer. This model configuration was then incorporated in res2dmod to develop 2D subsurface model by assigning 4 nodes per electrode spacing (the model has option to either use 2 or 4 nodes). The model mesh for 1 m, 2.5 m and 5 m electrode offset with 48 electrodes consist of 47 nodes, 94 nodes and 188 nodes, respectively. The vertical spacing between adjacent horizontal mesh lines near the surface were kept smaller; larger spacing were assigned at deeper mesh lines to obtain sufficiently accurate results.

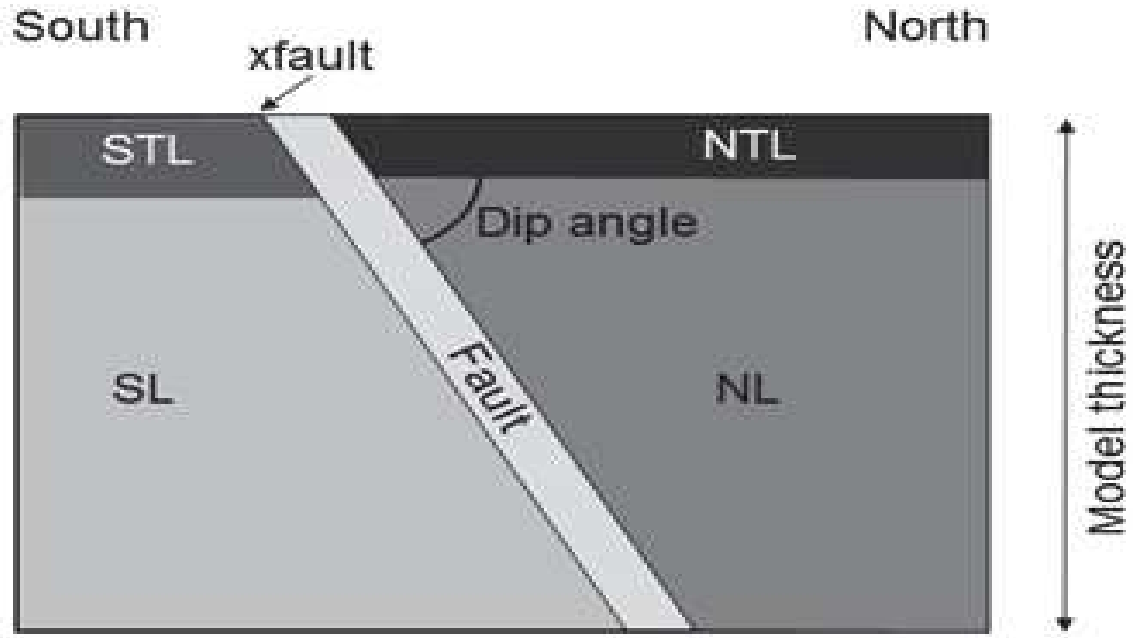

Figure 4.10: Simplified geometry of the subsurface used in the forward modeling process

Constraining the parameters

Res2dmod

The range of model inputs for testing different parameters including fault dip angle and resistivity and thickness of the five bodies defined in Figure 4.9 are set as shown in Table 4.3.

In the initial process, different combination of the parameters defined in Table 4.3 were performed in res2dmod to determine a qualitative visual match with the ERT sections. The forward model test favours a better fit with the ERT sections using 5 bodies compared to 3 or 4 bodies (Figure 4.11).

In terms of fault geometry, even though it is difficult to determine the optimum fault dip angle that matches with the observed data, the fault geometry with dip angle of $>40^{\circ}$ seems

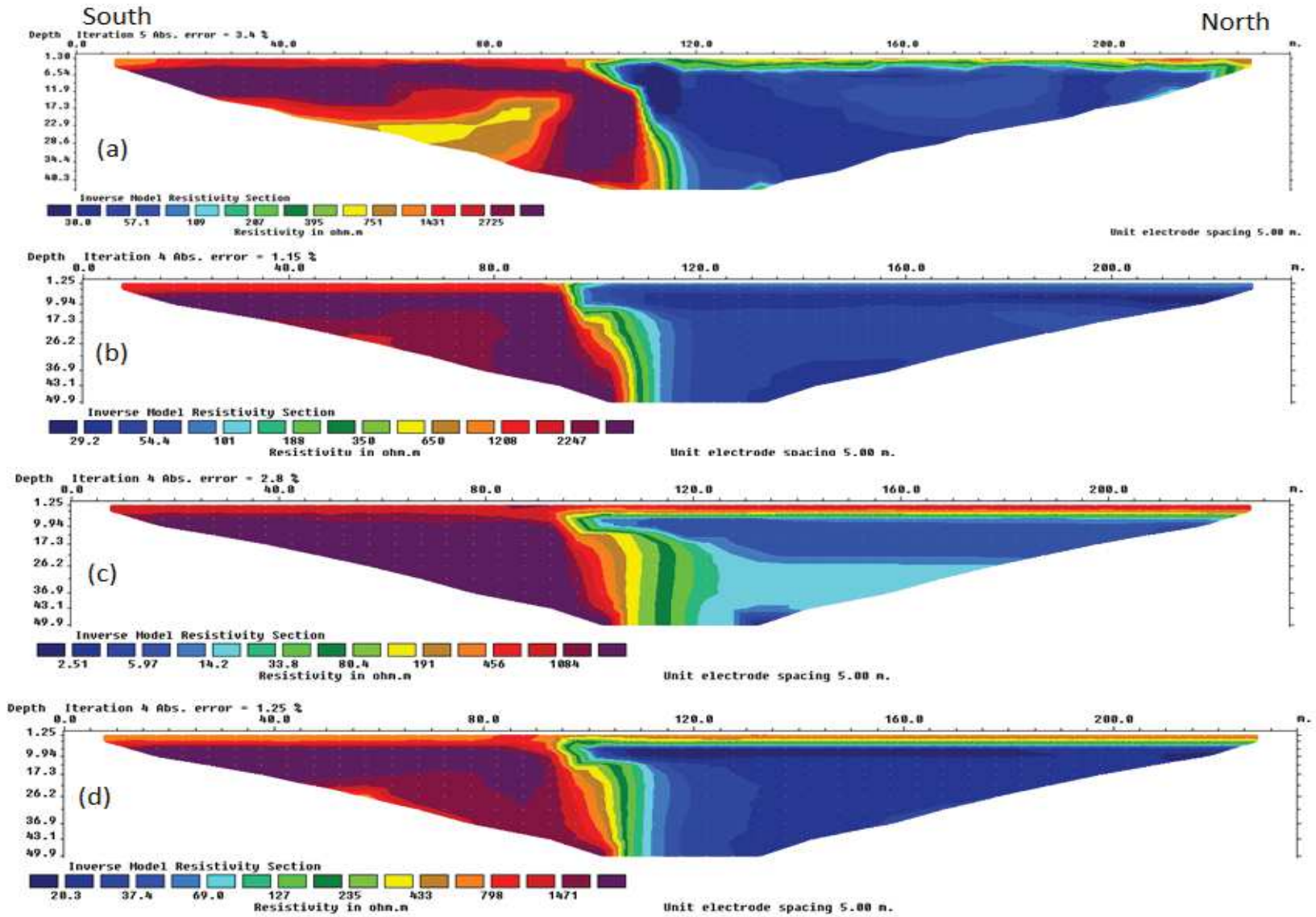

Figure 4.11: Results of the forward model using res2dmod to test the effect of different layers (a) ERT pseudo-section with 5 m interval obtained from observed data (b) 3 layers model with 5 m interval and TFT dip angle of 40° (c)4 layers model with 5 m interval and same TFT dip angle (d) 5 layers model with 5 m interval and same TFT dip angle.

Table 4.3: Range of *a priori* geophysical parameters used in res2dmod

Sl. No.	**Body name**	**Dip range (degree)**	**Resistivity range (ohm.m)**	**Thickness range (m)**
1	South Top Layer (STL)	-	100-600	1-5
2	North Top Layer (NTL)	-	100-600	1-5
3	South (SL)	-	2500-4000	-
4	North (NL)	-	1-100	-
5	Fault Layer	20-80	200-750	0-5

have better fit with the observed ERT section, especially in case of 5 m Wenner-Schlumberger array as shown in Figure 5.11(d). Similarly, the thickness of top alluvial materials is constrained to be around 3.5 m for the north and 1.5 m for the south section using mainly Wenner-Schlumberger and Dipole-Dipole configurations with 1m and 2.5 m electrode spacing. The width of the fault is difficult to ascertain as there is no perceptible changes in the model output by varying the width of fault. The resistivity values for the 5 bodies are constrained to be 800 Ω.m for the south top layer, 400 Ω.m for the north top layer, 200 Ω.m for the fault zone, 2500 Ω.m for south and 10 Ω.m for the north layer.

Quantitative approach

Next a quantitative approach to further constrain the geometry and other structural parameters was pursued. This approach was done by preparing a matlab script that automatically calculates the fit between the observed and calculated data and returns the best fit model parameters; input information for the calculated model is derived from a priori information defined in Table 4.2 and constrains deduced from the res2dmod model. The misfit between the observed and calculated data is defined as

$$Misfit = \sum_{i=1}^{n} \sqrt{\frac{(obs - calc)^2}{n}} \tag{4.2}$$

where *obs* is the observed resistivity value and *calc* is calculated resistivity value from the forward model and *n* is the number of resistivity values considered. Below describes the process in determining optimal model parameters calculated by employing above equation 5.1

1) **Effect of meshing**: Loke (2015) suggests employing smaller vertical spacing between the adjacent horizontal mesh lines near the surface and larger spacing for deeper mesh lines to obtain sufficiently accurate results. To test the effect of depth of mesh lines, models with different numbers of rows of rectangular blocks of 20, 40, 60, 80 and 100 were used as shown in Figure 4.12. Accordingly, the depths to each horizontal mesh lines are defined by considering number of rows as well as ensuring incremental mesh size with increase in depth. Notice in Figure 4.12 that as the mesh grid line is made finer, there is noticeable change in model resistivity output. Thus in all the forward model analysis a finer mesh grid line is used.

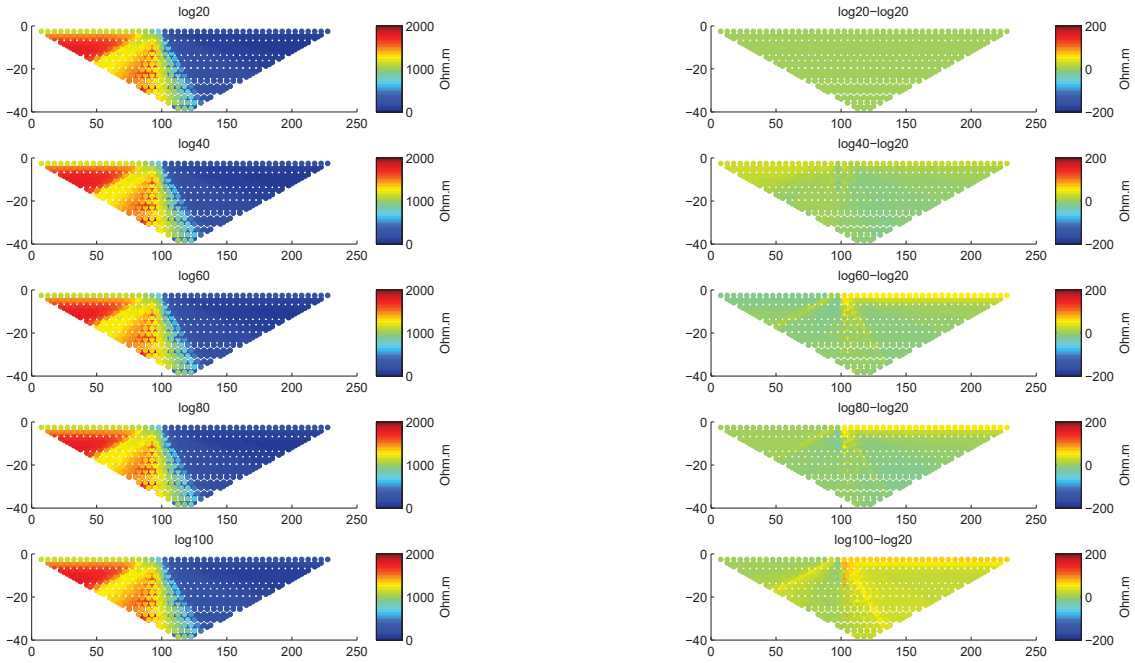

Figure 4.12: Effect of mesh on the model resistivity output

2) **Resistivity of North and South deep layers**: The observed resistivity data show significant resistivity contrast between the north and south deep layers. Utilizing a priori resistivity value range of 2500-4000 Ω.m and 1-100 Ω.m for the south and north deep layers, respectively, various combination of resistivity values were tested to calculate the misfit between the observed and calculated pseudo-resistivity. The best misfit model with resistivity value for the north and south deep layer is constrained to be around 30 Ω.m and 3250Ω.m, respectively as shown in the misfit graph in Figure 4.13.

3) **Fault dip angle**: To quantitatively assess the dip of the fault, using a matlab script

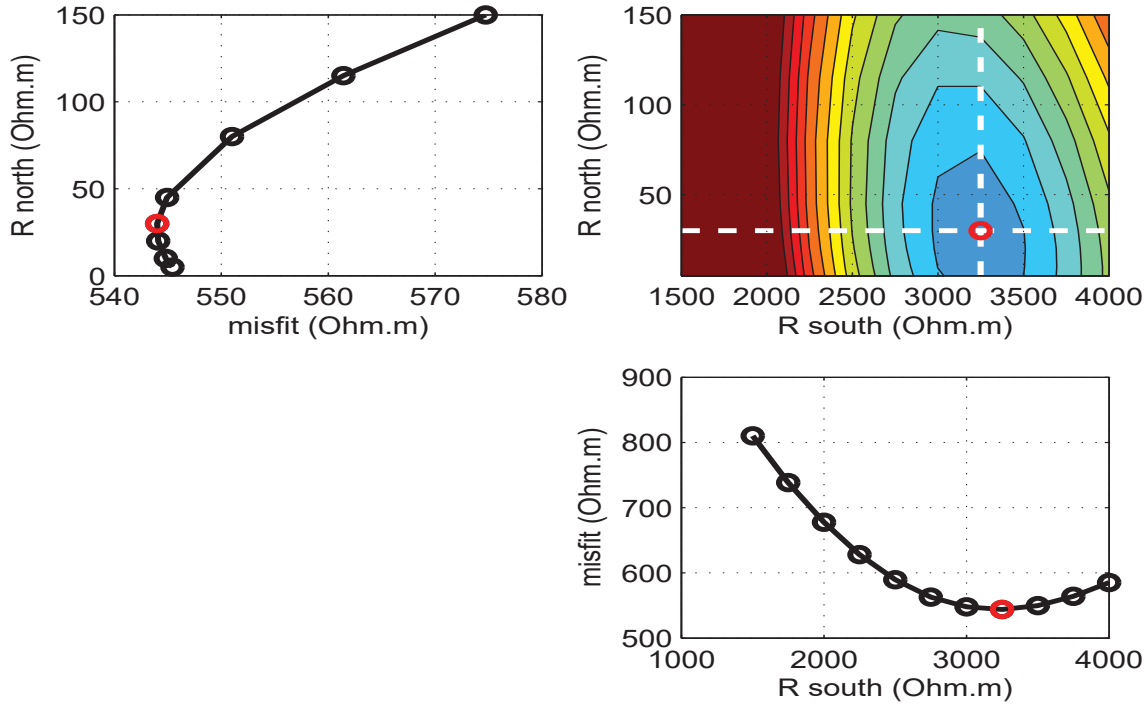

Figure 4.13: The best fit resistivity value obtained for SL and NL layers defined in Figure 4.10

the dip angle was varied from 20° to 80°. The misfit curve in Figure 4.14 shows better fit between the observed and calculated pseudo-section with increase in dip amount, obtaining best misfit at dip angle of 80° .

4) **Thickness and resistivity of the fault zone**: By varying the resistivity value of the fault zone from 200 Ω.m to 600 Ω.m and changing the fault thickness from 2 m to 6 m, the thickness of the fault zone and resistivity value of the zone is calculated to be 6 m and 520 Ω.m, respectively as shown in Figure 4.15.

As described above, the approach using res2dmod is very time consuming. Hence an alternative approach using R2 (Binley & Kemna, 2005; Binley, 2015) has been developed, especially to better explore space parameters. This last approach is described in detail in GJI paper (see Section 4.2.7).

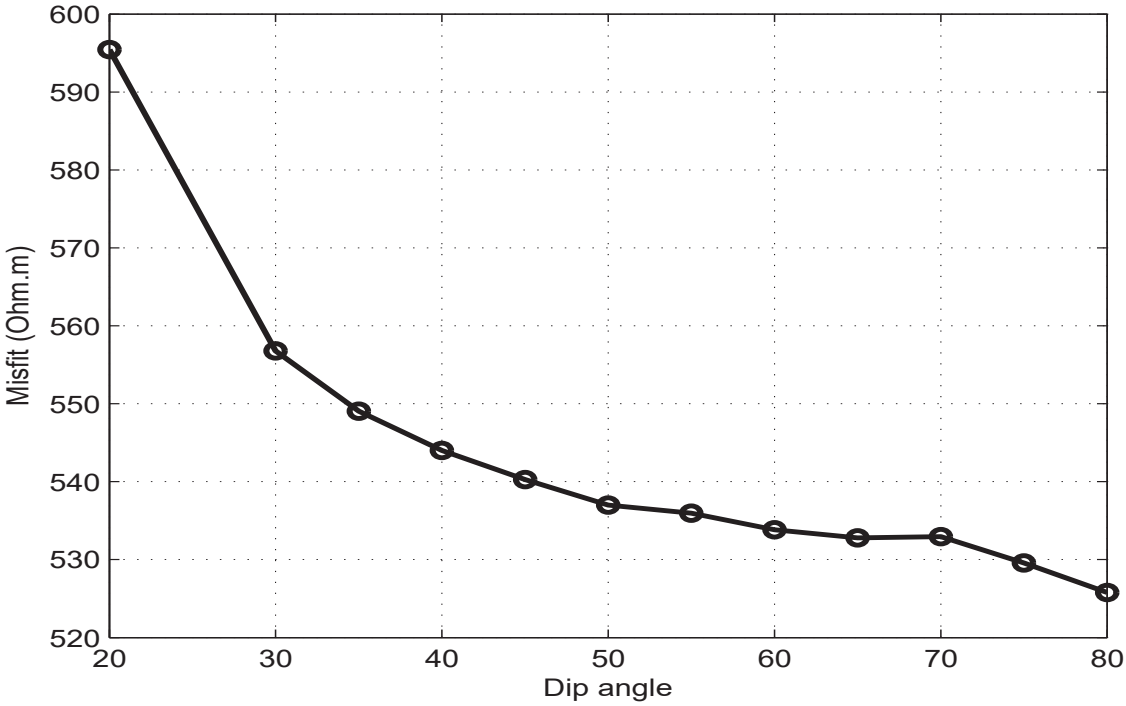

Figure 4.14: The best fit dip angle of the fault defined in model in Figure 4.10

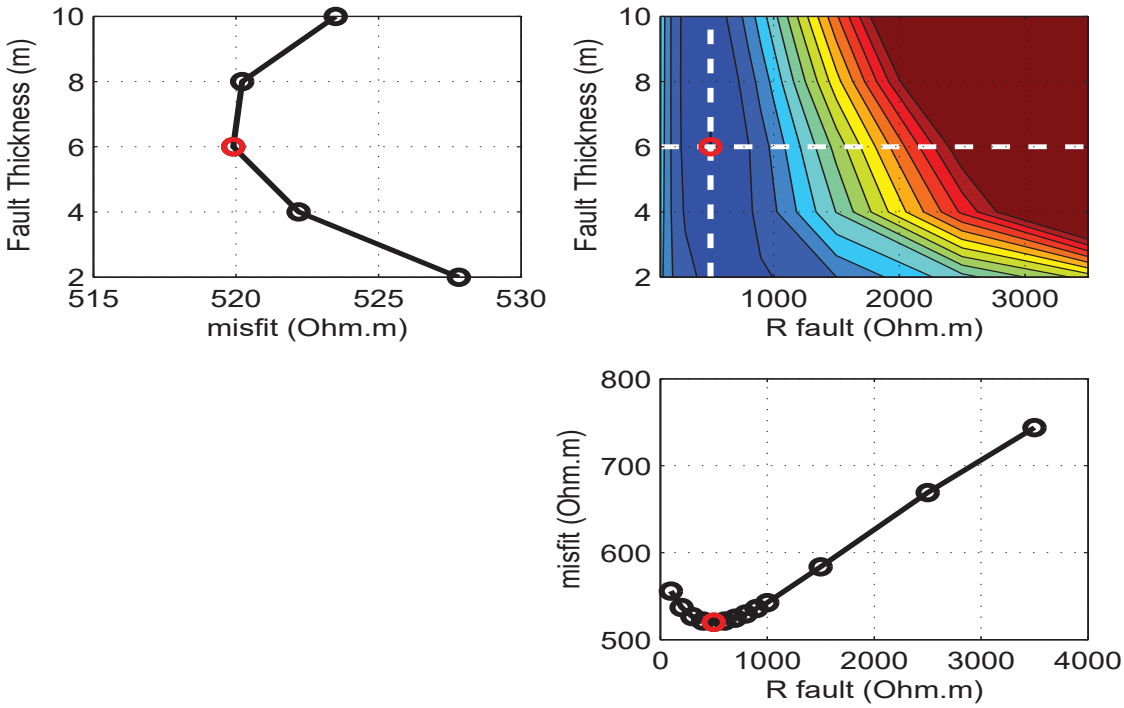

Figure 4.15: The best fit thickness and resistivity value for the fault zone defined in Figure 4.10

4.2.5 Seismic refraction

Data acquisition

The seismic refraction line is coincident with the eletrical resistivity profile. Similarly to the ERT line, the mid-point of seismic line was also positioned at the paleoseismic trench location. Using Moho®–SoilSpy Rosina seismic equipment with 24 channels, data were acquired as per the data acquisition layout plan shown in Figure 4.16. Using hammer and iron plate as seismic source and maintaining a geophone interval of 1m, shots were made at every 1m interval with maximum offset shots at -24 m and +20 m to the south and north end of the profile, respectively. To obtain a continuous data along the profile, a rollover method was used whereby an overlap of 4 geophones were maintained in all the seismic sections subsequent to the first line, sarp1, as shown in the data acquisition layout plan (Figure 4.16). Overall a total spread length of 103 m seismic refraction line was conducted at the study area.

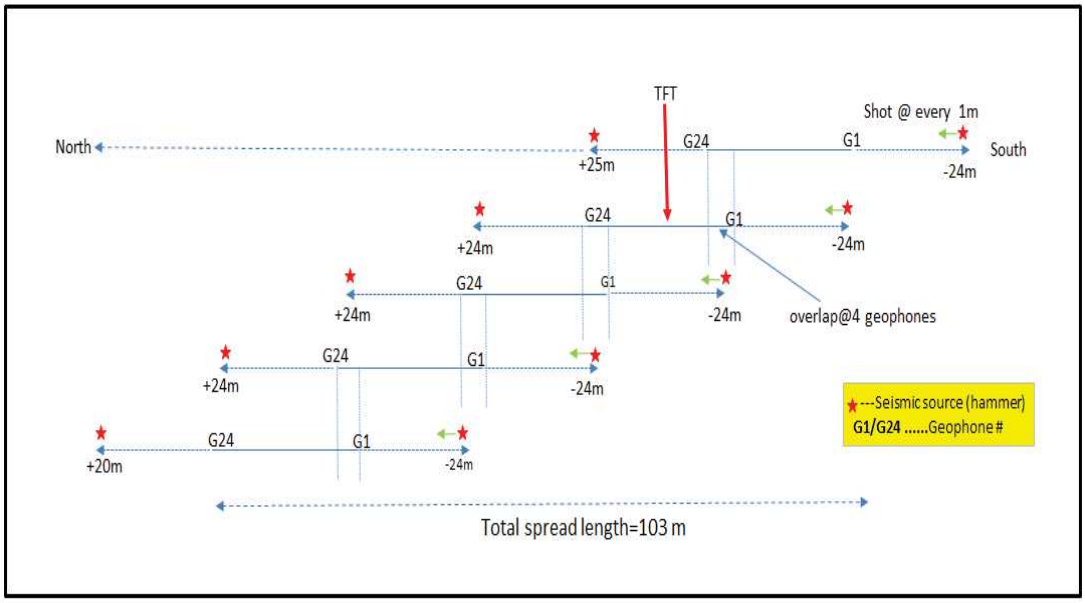

Figure 4.16: Layout plan for acquisition of seismic data along the profile. The TFT location at the mid-point of profile 2 is shown with red arrow.

Travel-time picking

The seismic data were first cleaned from any data inconsistency and sorted for further processing. Next using SeismImager® software, nearly 5760 first-arrival travel-times were manually picked. An example of first arrival travel-time pick which includes only the inline shots

is shown in Figure 4.17. In order to check the robustness of our pickings, a comparison of travel picks (1656) performed by myself, Stephanie Gautier and Rodolphe Cattin are depicted in Figure 4.18. The maximum frequency distribution in Figure 4.17 is centered around picking difference of 0 ms indicating the robustness of the first-arrival pickings. The highest picking difference is observed to be ± 2 ms.

From the travel-time graph in Figure 4.17 at least two layers, and possibly a third layer can be inferred. The higher delay time and steeper slope of time-distance curve suggest predominantly lower velocity in southern part of the profile compared to the northern section. Moreover, a transition in velocity along the profile can be observed around 28-32 m towards the north (Figures 4.17), coincident with the TFT trace location intersected in the paleoseismic trench. From the time-distance curve, it can be deduced that the seismic wave is affected by presence of the fault zone. Figure 4.19 illustrates the shot locations along the seismic line and color scale shows the first arrival travel-time from each shot position to the geophone positions along the profile. Notice that in Figure 4.19 the northern part of profile show small values of first arrival times ($\sim$ 10 ms) whereas an abrupt transition between small ($\sim$ 10 ms) and higher ($\sim$ 25 ms) picking times are observed in the south, suggesting a northward increase in velocity and presence of a shallow interface at depth towards the north.

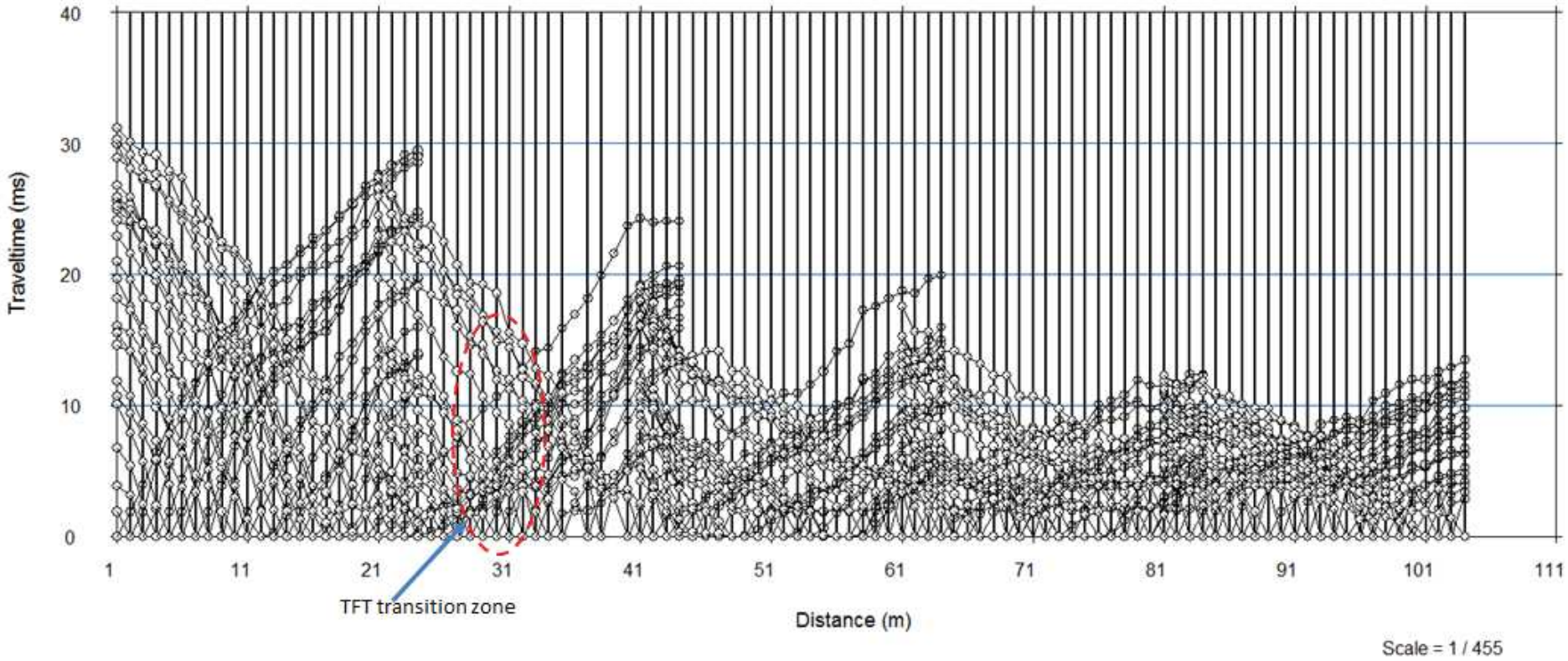

Figure 4.17: First arrival travel-time picks for all in-line shots along the seismic refraction profile

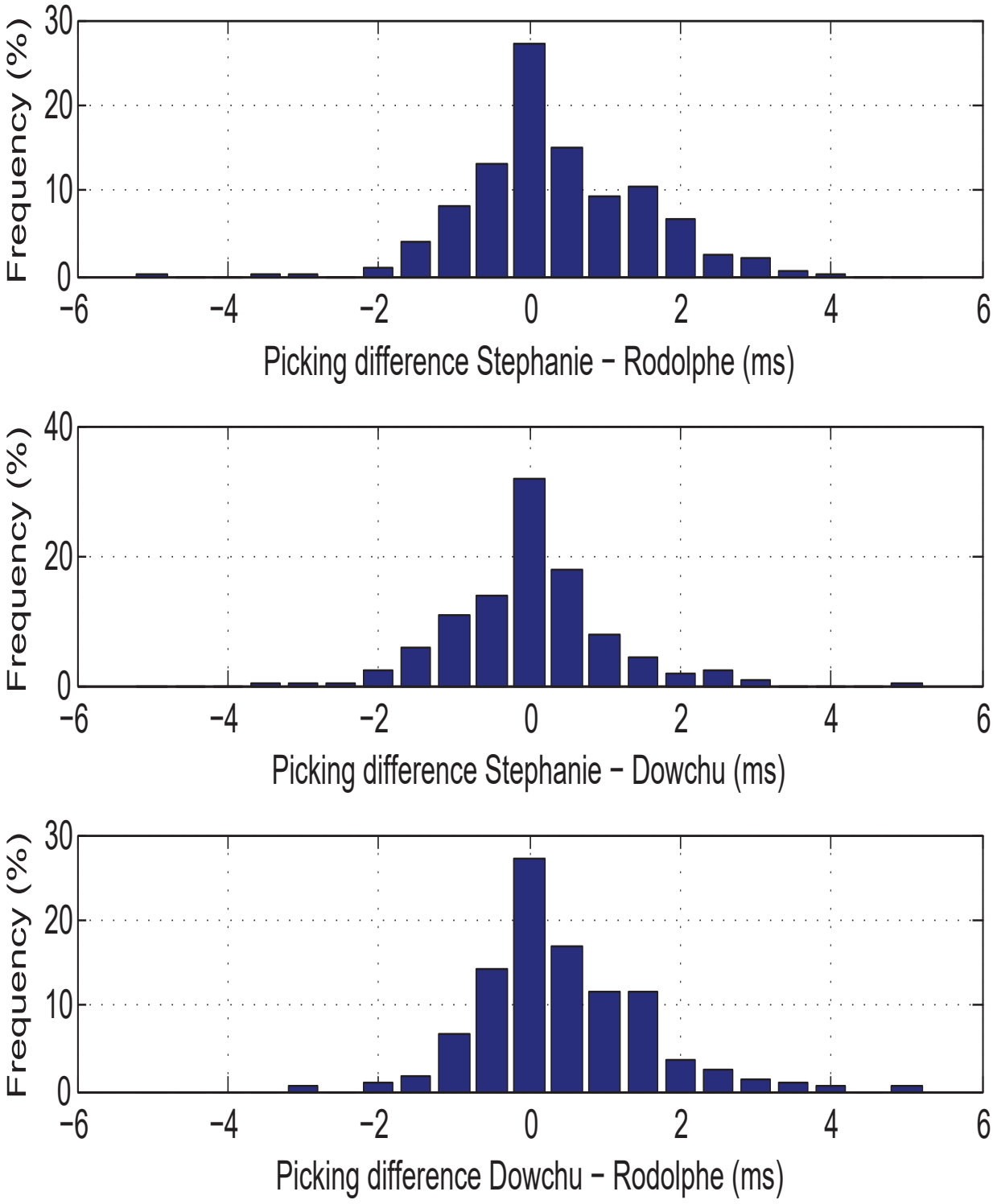

Figure 4.18: Comparison of first arrival travel-time picks between three pickers

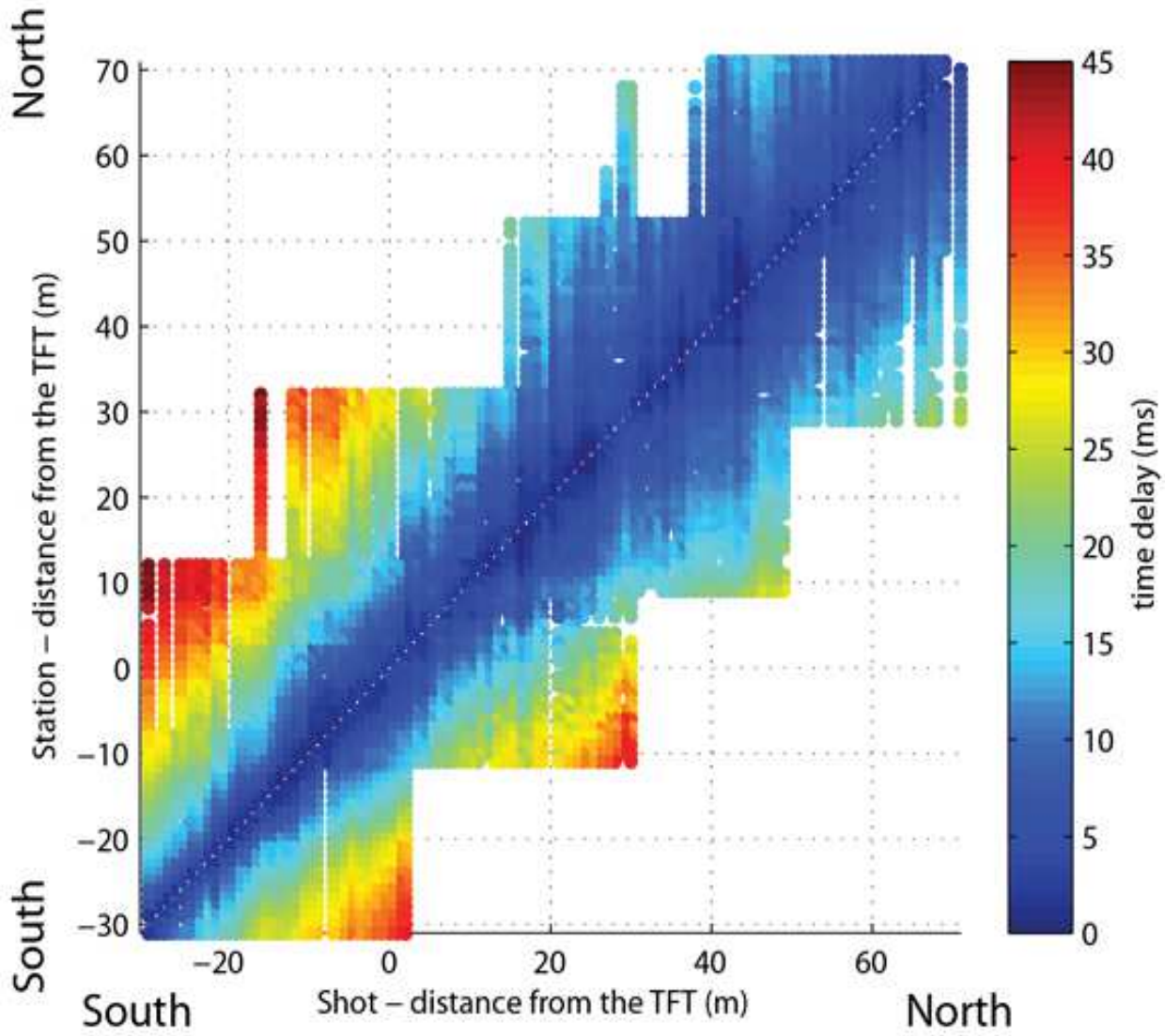

Figure 4.19: Shot location along the study seismic profile. Color scale indicates first arrival travel-time from each shot location to the geophone positions along the profile.

Seismic tomography inversion

The first-break picks in ASCII format were then imported into the Rayfract® software and the geometry information were updated to perform seismic refraction tomography. As in all seismic inversion process, a initial starting model input is required to execute the tomographic inversion. Options for the starting model include 1) an automatic inversion that assumes a smooth vertical velocity gradients (Zelt & Smith, 1992), 2) an alternative low resolution starting model generated using tau-p method (Diebold & Stoffa, 1981), and 3) a detailed starting model generated using generalized reciprocal method (GRM) (Palmer, 1981). For this study, we adopted a simple 1D smooth vertical velocity gradient as initial model (Dix, 1955). Using the smoothed or apparent 1D starting models from the travel-time data with Delta-tV method (Rohdewald, 1999), we obtained good initial fit between modeled and picked times. The starting model is then refined by applying Wavepath Eikonal Traveltime (WET) inversion techniques. In conventional ray tracing tomography, the technique is limited to modeling of one ray per first break, whereas WET inversion technique models multiple signal propagation paths contributing to one first break. The final tomographic inversion result is shown in Fig.4.20 along with the corresponding ray coverage illustrating the resolved area shown in Fig.4.21. Notice that both the velocity pattern and ray path are influenced by the presence of the fault. However, it must be emphasized that the tomographic inversion is not able to generate a quantitative assessment of the fault geometry, which is important for constraining the overthrusting slip rate. Thus we performed a more robust stochastic inversion technique similar to the ERT which enabled us to quantitatively determine the geometry of the TFT in the area. The details of the stochastic approach is discussed in the GJI paper (see Section 4.2.7).

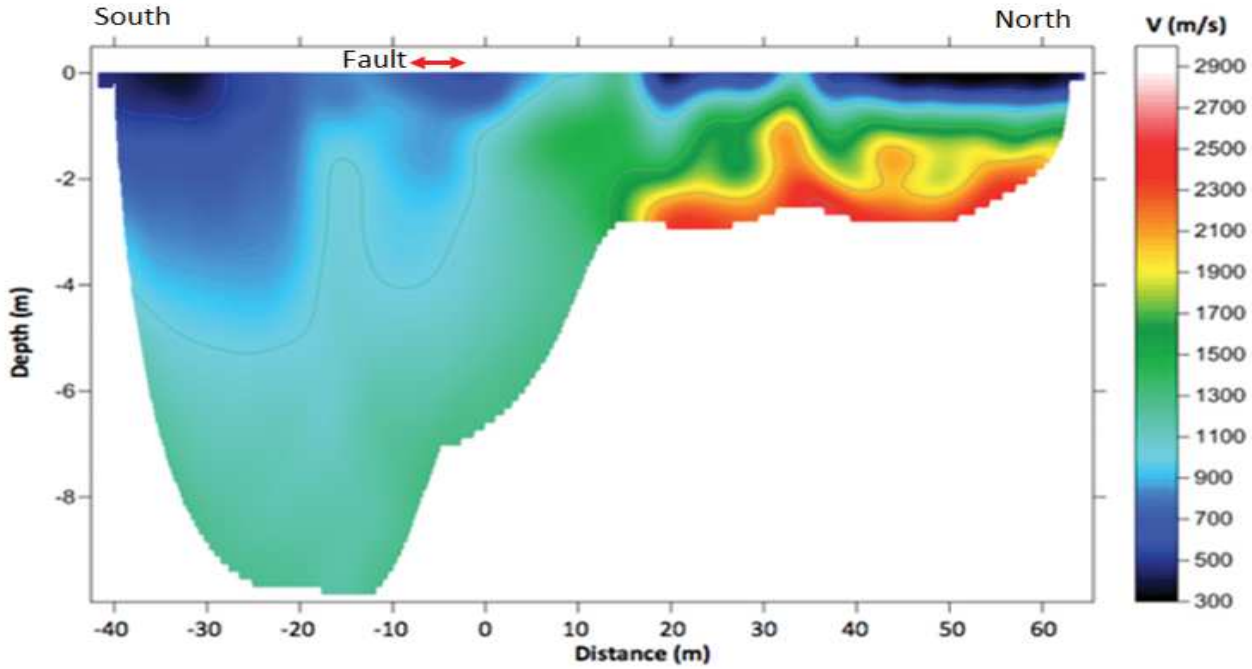

Figure 4.20: Tomographic image showing velocity variation on both sides of the TFT.

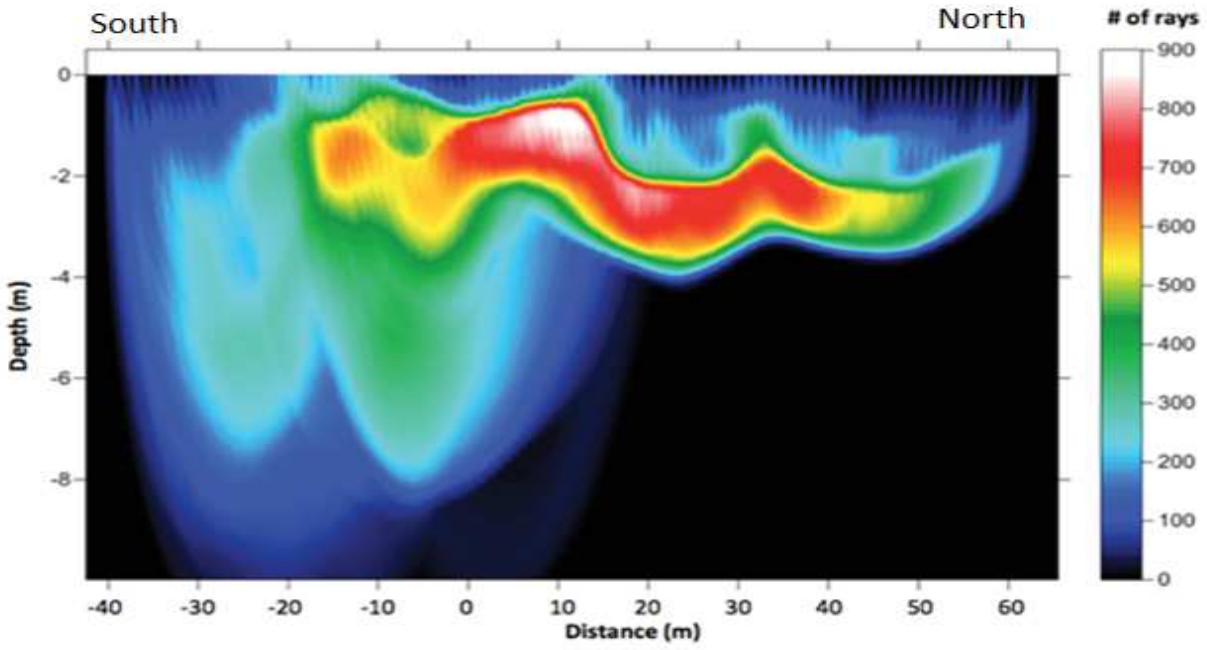

Figure 4.21: Ray coverage illustrating the area resolved in tomographic inversion in Figure 4.20. The TFT is located around the 0 m distance.

4.2.6 Micro-gravity

To compliment the seismic and resistivity study, micro-gravity measurements were also carried along the same profile. Gravity data from the field are effected by different factors such as the elevation, instrument drift, regional trend, etc. Therefore to extract the true signal or gravity anomaly corresponding to density contrast of the subsurface geological structures, the raw gravity data collected has to undergo data reduction processes. We used the GravProcess (Cattin et al., 2015), a set of MATLAB routines to process data from complex campaign data and calculate the associated gravity anomaly.

Drift correction

Drift in gravity instrument takes place due to elastic creep in the springs of gravimeter which produces an apparent change in the gravity measurement values at each station over time. Moreover, gravity instrument can effected by tidal drift problem. To correct this instrument drift problem, a standard procedure of looping was followed wherein repeat measurements were made at the base stations along the profile. The differences between gravity measurements at each looped station and time difference is noted to calculate the instrument drift. For example, if the gravity measurement at the first station is G_1 at time T_1 and after time T_1' the remeasured gravity reading at first station is G_1', the instrument drift can be corrected using the following relationship

$$Drift, D = \left(\frac{G_1' - G_1}{T_1' - T_1}\right) \tag{4.3}$$

Similarly, drifts at other stations over time can be accordingly calculated. The drift correction to the gravity data is performed using the following relationship

$$G_{drift-corrected} = G - D \times (T - T_1) \tag{4.4}$$

where D is the drift from equation 5.2 and T represents time of the gravity measurement along the profile.

Elevation correction

Using accurate elevation data gathered along the profile by leveling method and assuming an average density, $\rho = 2670\ kg/m^3$, the elevation correction (δg_E) was performed using the

relationship between elevation (δg_E), free-air (δg_F) and Bouguer (δg_B) corrections as shown in the following equation.

$$\delta g_E = \delta g_F - \delta g_B \tag{4.5}$$

Substituting the normally accepted free air correction, $\delta g_F = 0.3086h$, and bouguer air correction, $\delta g_B = 0.04192\rho h$ in equation 4.5, the elevation correction can be performed as follows

$$\delta g_E = (0.3086 - 0.04192\rho)h \tag{4.6}$$

where h is the height in metres at locations along the gravity profile line.

Trend removal

In shallow surface investigation using gravity study, the target wavelength of interest is the short wavelength gravity anomalies, whereas in case of deeper structure study longer spatial wavelength is targeted. Since long wavelength regional trends can make analysis of the short wavelength residuals difficult, it is important to remove the regional trend from data in order to clearly image the shallow structure corresponding to the short wavelength gravity anomaly.

Using the regional trend from Hammer et al. (2013), a trend of -1.58 $\mu Gal/m$ was corrected. The final corrected gravity result shown in Figure 4.22 shows consists of 139 corrected gravity measurements, which highlight variations along the profile. No change at the fault trace is observed but a transition occurs at around 27 m north of the TFT. The southern part of the profile is characterized by a moderate northward increase of ca. 4 μGal/m. The northern part shows an increase twice as large with a northward increase of ca. 450 μGal in 65 m. A stochastic approach similar to the ERT and seismic refraction was performed for gravity data set as described in the GJI paper (see Section 4.2.7).

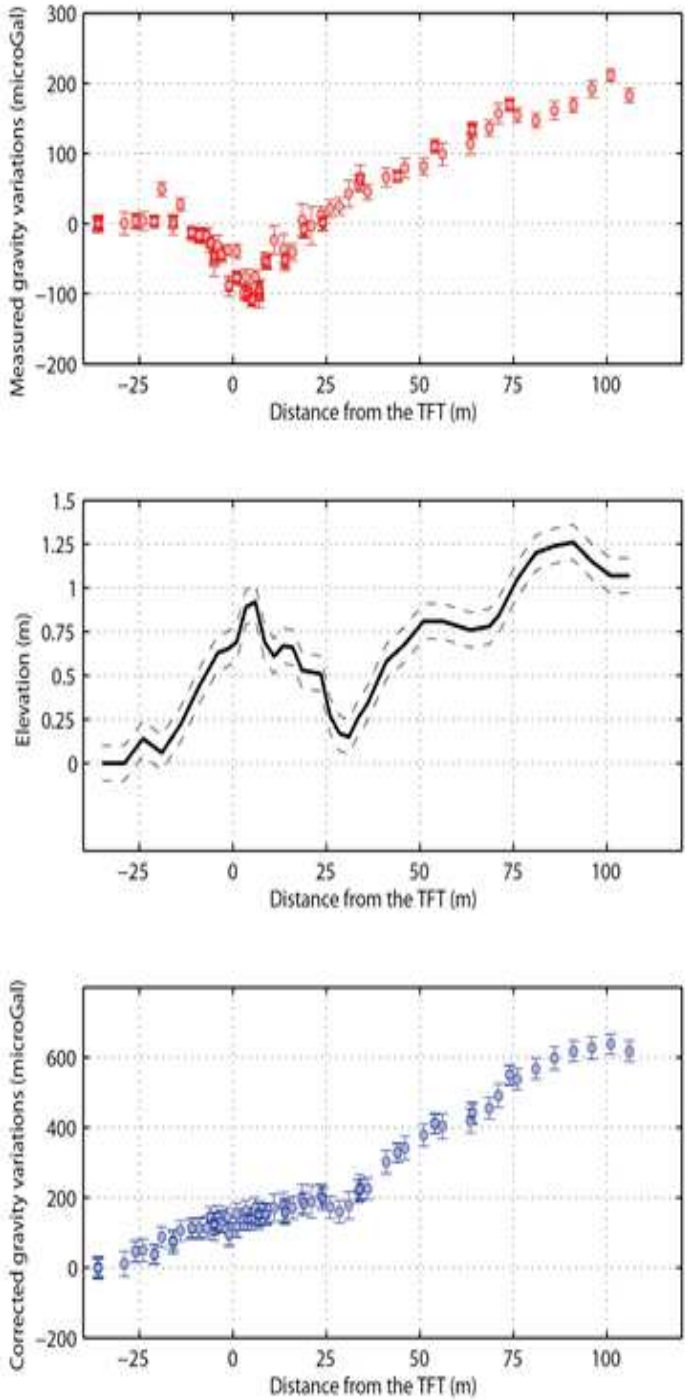

Figure 4.22: Measured gravity (top), elevation (middle) and gravity variations corrected for both topographic effect and regional trend (bottom) along the study profile. Data uncertainty is associated with both accuracy of the CG5 gravimeter and error in elevation measurement..

4.2.7 Results, discussion and conclusion: GJI paper

This paper presents results of stochastic inversion approach performed to constrain the shallow surface geometry of the topographic frontal thrust (TFT) in south-central Bhutan. Our approach using ERT, seismic and gravity data suggest a flat and listric-ramp geometry of the TFT and emphasizes the importance of studying shallow surface fault geometry to constrain overthrusting slip rate. Our new results from Sarpang area allow us to estimate a minimum overthrusting slip rate of 10$\pm$2 mm/year along the TFT, which is about 60 $\%$ of the far-field GPS convergence rate of ca. 17 mm/year. Based on the obtained geometry of the TFT, our findings questions the validity of commonly used approach to estimate a mean uplift rate by combining several uplifted terraces located at various distances from the front.

Impact of near-surface fault geometry on secular slip rate assessment derived from uplifted river terraces: Implications for convergence accommodation across the frontal thrust in southern Central Bhutan.

Journal:	*Geophysical Journal International*
Manuscript ID	GJI-S-17-0378.R1
Manuscript Type:	Research Paper
Date Submitted by the Author:	18-Sep-2017
Complete List of Authors:	Drukpa, Dowchu; Seismology and Geophysics Division, Department of Geology and Mines Gautier, Stephanie; Universite de Montpellier Cattin, Rodolphe; Universite de Montpellier Namgay, Kinley; Seismology and Geophysics Division, Department of Geology and Mines Le Moigne, Nicolas; Universite de Montpellier
Keywords:	Geomorphology < GENERAL SUBJECTS, Asia < GEOGRAPHIC LOCATION, Electrical resistivity tomography (ERT) < GEOMAGNETISM and ELECTROMAGNETISM, Gravity anomalies and Earth structure < GEODESY and GRAVITY, Image processing < GEOPHYSICAL METHODS

Impact of near-surface fault geometry on secular slip rate assessment derived from uplifted river terraces: Implications for convergence accommodation across the frontal thrust in southern Central Bhutan.

Drukpa Dowchu[1,2], Gautier Stephanie[1], Cattin Rodolphe[1], Namgay Kinley[2], Le Moigne Nicolas[1]

[1] Geosciences Montpellier, UMR5243, Université de Montpellier, Place E. Bataillon, 34095 Montpellier, France

[2] Seismology and Geophysics Division, Department of Geology and Mines, Ministry of Economic Affairs, Post Box 173, Thimphu, Bhutan

Corresponding author: Dowchu Drukpa (dawchu@gmail.com)

Summary

Vertical velocities obtained from uplifted river terrace dating near mountain fronts are commonly converted into overthrusting slip rates assuming simple geometry of the fault at depth. However, the lack of information on the dip angle of these shallow structures can lead to misinterpretation in the accommodation of convergence, and thus to erroneous conclusions on the transfer of shortening to the emergent thrust faults. Here, to assess the impact of fault geometry, we focus on the eastern Himalayan region in the south Central Bhutan, where the topographic frontal thrust (TFT) has been already documented by GPS, paleoseismic, geomorphic and geological studies. The present study is based on high-resolution near-surface geophysical investigations, including electrical resistivity, seismic and gravity measurements. Using a similar stochastic

inversion approach for all data-sets, new quantitative constraints on both fault geometry and petrophysical parameters are obtained to image shallow depths, in the upper ca. 80 meters. The combined results from both surface observations and geophysical measurement provide a TFT geometry that is dipping northward with a shallow angle at the top (0-5 m), steeply dipping in the middle (5-40 m) and flattening at deeper depths (>40 m). Together, our new constraints on the fault geometry allow us to estimate a minimum overthrusting slip rate of 10±2 mm/yr, which is only a part of the ca. 17 mm/yr GPS convergence. This suggests that, in the study area, significant deformation partitioning on several faults including TFT and the Main Boundary Thrust cannot be ruled out. More importantly, assuming constant slip rate, the obtained dip angle variations lead to uplift rate changes with distance to the TFT. This underlines that taking into account uplift rate from terrace dating only at the front location and assuming a constant dip angle fault geometry based on surface observations may significantly bias the slip rate estimates.

Keywords: Himalaya, Bhutan, near-surface geophysics, river terrace, fault geometry, Topographic Frontal Thrust, slip rate

1. Introduction

The Himalaya that stretches ca. 2500 km from the Hazara-Kashmir syntaxis in the west to the Namcha Barwa syntaxis in the east constitutes one of the most seismically active regions of the world. In this area, many previous studies (e.g. Molnar & Tapponnier, 1975; Seeber & Armbruster, 1981; Bilham et al., 1997; Pandey et al., 1995; Lavé & Avouac, 2000; Cattin & Avouac, 2000; Decelles et al., 2002; Kumar et al., 2010 ;

Duputel et al., 2016) have shown that the occurrence of major earthquakes can be related to the India-Eurasia shortening, which has been accommodated along the Main Himalayan Thrust (MHT), a mid-crustal decollement where the India plate is underthrusted beneath the Himalayas and Tibet.

In central Nepal and Arunachal Pradesh, estimates of Holocene horizontal shortening rates have been already obtained from studies of uplifted river terraces (Lavé & Avouac, 2000; Burgess et al., 2012) nearby the Main Frontal Thrust (MFT), which is the most recent surface expression of the MHT (Schelling & Arita, 1991; Pandey et al., 1995). In these areas, it has been reported that the MFT absorbs most of the shortening rate across the Himalaya, whereas the MFT is locked over interseismic periods (Ader et al., 2012). This leads to the current understanding of seismic cycle in central Himalaya where most of the interseismic deformation deficit is released during M>8 earthquakes that rupture the MFT up to the surface (Bilham et al., 1997; Cattin & Avouac, 2000).

Located in the eastern part of the Himalayas, the Kingdom of Bhutan remains one of the least studied segments of the Himalayan range in terms of active tectonics and its associated seismic risk assessment (Drukpa et al., 2006). Over the last decade several geological and geophysical studies have been carried out in Bhuthan to fill this information gap (e.g. Hammer et al., 2013; Berthet et al., 2014; Vernant et al., 2014; Le Roux-Mallouf et al., 2015 and 2016; Hetényi et al., 2016a and 2016b; Marechal et al. 2016; Singer et al., 2107; Diehl et al. 2017). In particular, a multidisciplinary approach including geomorphology, paleoseismology and geodesy has been conducted in Sarpang, a small town in south Central Bhutan (Fig. 1). In this area, these studies suggest a seismic behavior similar to the one observed in other parts of Himalayas, with

(1) present-day deformations indicating a fully locked thrust-fault at the surface over the interseismic period (Marechal et al., 2016) and (2) evidences of occurrence of major earthquakes over the last millennium (Berthet et al., 2014; Le Roux-Mallouf et al., 2016).

Tectonic scarps and well-preserved abandoned terraces on both banks of the Sarpang river also attest to the accumulation of vertical deformation through time (Fig.1). Based on both radiocarbon and cosmogenic ^{10}Be dating, Berthet et al. (2014) estimate a Holocene vertical uplift rate of 8.8 ± 2.1 mm/yr for these terraces. By assuming a constant dip angle of 25°±5° towards the north, Berthet et al. (2014) calculated a Holocene slip rate of ~20 mm/yr along the main thrust fault in Central Bhutan, suggesting that the entire convergence rate across Bhutan Himalaya is accommodated at the front without any deformation partitioning. However the most recent geological map of Bhutan proposed by Long et al. (2011) presents dip angle values in ranges of 10°- 60° for the Sarpang area, making slip rate difficult to assess from fault geometry deduced from surface observations only.

Additional constraints on the geometry are thus required to estimate the amount of shortening rate accommodated along the frontal fault in Bhutan, which is a key input parameter for seismic hazard assessment. Here, we image the shallow structures from high resolution near-surface geophysical methods including electrical resistivity, seismic refraction and gravity measurements. Both electrical and seismic methods are proved to be essential tools in active fault imaging by providing new constraints on fault geometry, fault offset and abrupt variations of sediment thickness (e.g. Morey and Schuster, 1999; Karastathis et al., 2007; Nguyen et al., 2007; Storz et al., 2000; Stephenson and

McBride, 2003; Dorn et al., 2010; Villani et al., 2015). In comparison with the paleoseismic trench studied by Le Roux-Mallouf et al. (2016), these two methods allow for a wider investigation area and larger exploration depth. Because gravimetry takes into account large-scale anomalies (Benson and Mustoe, 1995; Wise et al., 2003), we also conduct a gravity survey in order to investigate deeper structures.

After a brief presentation of the study area, we describe data acquisition. Next we present inversion approaches implemented to assess the frontal fault geometry. Finally we discuss our results and implications in terms of shortening accommodated along the frontal fault.

2. Study area

The Kingdom of Bhutan, located in the eastern part of the Himalaya, accounts for approximately 14% of the total length of the Himalayan arc. Our study area is approximately 90 km southeast of the capital city, Thimphu. It is located in the Himalayan foothills along the Sarpang river in south Central Bhutan, close to the border with India (Fig. 1).

While the MFT is well-defined in Nepal and coincides with the present-day Himalayan topographic front, its location in Bhutan is less straightforward to define (Le Roux-Mallouf et al., 2016). In the Sarpang area where a 10-km-wide re-entrant feature directly juxtaposes lesser Himalaya and Quaternary alluvium (Long et al., 2011), the most frontal structure expressed in the geomorphology is an anticline that likely accommodates a limited, though, undetermined fraction of the shortening (Dasgupta et al., 2013). For consistency with previous studies, the main topographic scarp studied here will be referred to as the Topographic Frontal Thrust (TFT) of Bhutan (Fig. 1).

This site has been selected for several reasons. First, in many parts of Bhutan the TFT is located at the Indian border. The study site is in the Sarpang re-entrant, where the topography front is 10 km farther north compared to other foothill areas (Long et al., 2011). Furthermore, since the site is located along a river in the foothill, it is characterized by low elevation variations. This specific geographic feature ensures easy field accessibility and feasibility. Second, a host of information is now available regarding geology, geomorphology and paleoseismology for this area. The main lithological units in the fault zone documented on the trench log (Le Roux-Mallouf et al., 2016) comprises highly deformed phyllite in the deepest exposed unit on the hanging wall that corresponds to the Paleozoic Buxa Formation of the Lesser Himalaya Sequence. An alluvial layer is overlying this unit. Southward, in the footwall side, the gravel unit observed in the hanging wall is underlain by a fine-grained sand layer deposited by the lateral drainage system. A shear-zone juxtaposes the hanging wall and footwall along a 1 m deformed zone comprising of sheared sand and gravel unit. In the trench, this sheared and highly deformed zone with a dip angle of 17°-24° is interpreted to be the TFT (Fig.2). Abandoned fluvial terraces and radiocarbon dating suggest a Holocene uplift rate of 8.8 ± 2.1 mm/yr (Berthet et al., 2014) in this area. As previously mentioned, the secular slip rate assessment is however not straightforward because near the front in Sarpang and vicinity area, bedding and foliation of rocks exhibit high variations in their dip angles, with values ranging from 10° to 60° (Long et al., 2011).

Together, these features make the Sarpang area a relevant site for geophysical investigations to assess the geometry of the TFT at shallow depth.

3. Data

We acquired geophysical data along the east side of Sarpang river where the east-west trending TFT trace was intersected by the previously mentioned paleoseismic trench down to 1 m depth (Figs. 1 and 2). Taking into account the geological setting and the depth of the target, geophysical investigations included 2-D electrical tomographies, seismic refraction tomographies, and gravimetry measurements. The use of different geophysical methods allow to image different physical properties at different scales of investigation. All geophysical data were collected along the same N-S profile, with different spread lengths depending on the methods. The midpoints of the geophysical surveys were positioned at the fault location at the surface deduced from the paleoseismic study. We observed little and smooth topographic variation (< 1.3 m) along the geophysical line and therefore envisaged no topographic correction for the seismic and resistivity data analyses.

3.1. Electrical resistivity tomography (ERT)

We acquired 3 ERT profiles using 48 electrodes with 1 m, 2.5 m and 5 m electrode spacing in order to combine high resolution at shallow depth (1 m spacing) and large investigation depth (5 m spacing) using an Iris Syscal multi-electrodes system. We adopted the commonly used Wenner-Schlumberger and Dipole-Dipole configuration to achieve a good compromise between vertical and horizontal resolution and effect of noise (Dahlin & Zhou, 2004; Loke, 2015). The resistivity values obtained from the measurement were checked for any inconsistency and cleaned. Both the Wenner-Schlumberger and Dipole-Dipole arrays provided consistent results. Hereinafter, we present only Wenner-Schlumberger electrical images because of a greater sensitivity to

both lateral and vertical variations (Nguyen et al., 2007). The obtained ERT pseudo-sections show high electrical resistivity contrasts (~1:100) across the fault zone with a nearly vertical contact down to ~40 m depth (Fig. 3). Vertical resistivity changes are also highlighted at shallow depth south of the fault, underlying a high sensitivity of the Quaternary layers to electrical properties. The fault zone is characterized by an apparent resistivity of 100-1000 Ω.m. The north side shows a uniform apparent resistivity layering with a thin upper layer resistivity of 200-1000 Ω.m overlying a layer with a very low resistivity <100 Ω.m. The south side shows relatively constant apparent resistivity values (1000-4000 Ω.m) with a very high resistivity zone located at 5-15 m depth at the southern end of our profile. A thin upper layer of low resistivity is also observed southward.

3.2. Seismic tomography

A seismic survey coincident with the ERT profiles was carried out in order to obtain a near-surface velocity model around the fault zone. We used a MoHo® Soilspy Rosina digital multi-channel seismic acquisition system with 24 4.5-Hz vertical component geophones to record P-waveform traces to deduce P-wave velocity profile. A 1 m receiver spacing and five roll-alongs (shift of 20 geophones and overlap of 4 geophones each time) was used to finally acquire a 103 m long seismic profile. We shot with a 10 kg sledgehammer every 1 m along each seismic line. We recorded inline shots at every geophone positions and also offset shots starting 25 m before the first trace and ending 20 m after the last geophone. An average of 72 shots was recorded along each line resulting in a total of 360 shots along the 103 m long profile (Fig.1). Our data has good quality with clear first breaks on waveform traces. We hand-picked a total of 5760 first-

arrival traveltimes (Fig. 4). First-arrival times show smooth changes at ~30 m north of the fault trace. The northern part of the profile presents small values of first arrival times (~10 ms) whereas an abrupt transition between small (~10 ms) and higher (~25 ms) arrival times is observed in the south, indicating the presence of a shallow interface at depth on this side.

3.3. Micro-gravity

In addition to electrical resistivity and seismic investigations, we performed micro-gravity measurements using Scintrex CG-5 gravimeter (~10 microGal resolution) along the same North-South profile. From the center point of the survey line positioned at the paleoseismic trench, we collected gravity readings every 5 m on the either side of the profile covering a distance of 30 m and 105 m to the south and to the north, respectively. Spacially denser gravity points every 1 m were also collected in the vicinity of the fault area. Using the GravProcess software (Cattin et al., 2015) network adjustment was performed and topographic effect was corrected from accurate elevation data gathered along the same profile assuming a constant density of 2670 kg/m^3. A regional trend of -1.58 µGal/m obtained by Hammer et al. (2013) is also taken into account. Finally our dataset consists of 139 corrected gravity measurements, which highlight variations along the profile. No change at the fault trace is observed but a transition occurs at around 27 m north of the TFT. The southern part of the profile is characterized by a moderate northward increase of ca. 4 µGal/m. The northern part shows an increase twice as large with a northward increase of ca. 450 µGal in 65 m (Fig. 5).

4. Inversion approach

Following Ramirez et al. (2005), we use a stochastic method for imaging shallow structures from the obtained geophysical datasets. The approach combines prior informations and forward modeling to produce models consistent with the available data. Following Mosegaard & Tarantola (1995), a Markov Chain Monte Carlo technique is used to pseudo-randomly generate a large collection of models according to the posterior probability distribution.

Assuming a simplified geometry, each model is associated with only five bodies including a south (STL) and north (NTL) top layers, a south (SL) and north (NL) shallow layers and a fault layer (Fig. 6). On the basis of this formulation, a model combines 10 parameters, including the velocity, the resistivity and the density of each body as well as the thickness of layers, the fault location and the fault dip angle.

A priori parameter ranges for resistivity and velocity values are obtained from preliminary deterministic inversion using Res2dInv (Loke and Barker, 1996) and Rayfract (Schuster and Quintus-Bosz, 1993; Sheehan et al., 2005; Pasquet et al., 2015), respectively (Fig. S6 and S7). We assume prior density contrasts between NL and the other bodies in -500 to 500 kg/m^3 range Concerning the geometry prior information comes from structural and geomorphic observations (e.g. Long et al., 2011; Le Roux-Mallouf et al., 2016), which yield top layer thickness less than 5 m and a fault dip angle between 10° and 80° (see Table S1).

The pseudo-random walk through this multidimensional parameters space is controlled by the following rules for the transition between model m_i to model m_j :

1. If $L(m_j) \geq L(m_i)$ then accept the proposed transition from i to j.

2. If $L(m_j) < L(m_i)$ then accept the proposed transition from i to j with the probability $\frac{L(m_j)}{L(m_i)}$,

where $L(m_i)$ and $L(m_j)$ are the likelihood of the old and the new model, respectively. Here we assume that the likelihood function can be written as

$$L(m_i) = exp\left(-\frac{1}{n_{obs}}\sum_{n=1}^{n_{obs}}\frac{|calc_n(m_i)-obs_n|}{\sigma_n}\right)$$

where n_{obs} is the number of data points, obs is the data vector and σ^2 is the total variance, i.e. the uncertainties associated with each data point. $calc(m_i)$ is the forward modeling function associated with the model m_i. Depending of the considered dataset this function is obtained using the following forward formulations:

- Two-dimensional geoelectrical modeling is performed with the software package R2 (Binley and Kemna, 2005; Binley et al., 2015). The current flow between electrodes is obtained using a quadrilateral mesh. The number of nodes in the vertical direction is fixed to 50 with an exponentially increasing node spacing from 0.05 m at the surface to 45 m at 300 m depth. In the horizontal direction a constant node spacing of 0.5 m is used along the study profile.
- Synthetic travel-times are computed using the real receiver-shot configuration and solving the Eikonal equation with a finite-difference algorithm (Podvin and Lecomte, 1991). Rays are traced in the obtained time field with the a posteriori time-gradient method. More precise travel-times are then estimated along ray paths (Gautier et al., 2006; Priollo et al., 2012). The velocity model is a 106 m x 5 m area and extends to 10 m depth in order to include all ray paths (Fig. S7). The model is discretized on a regular grid of 425 by 21 by 45 nodes with a spacing of

0.25 m and the velocity field is parametrized by trilinear interpolation between grid nodes.

- Gravity variations along the profile are calculated from the formulations developed by Won and Bevis (1987), which provide the gravitational acceleration due to n-sided polygons. Here the polygons are associated with the geometry of the fives bodies described above. The model is extended to 10 km southward and northward to avoid edge effects at the two terminations.

The posterior probability of each model parameter is then obtained from the final collection of the 5.10^5 sampled models (Fig. S1-S5). Compared to commonly used approaches based on the search for the simplest model, the main advantages of our method include its ability (1) to assess the fault geometry because no smoothing is applied, (2) to provide a measurement of the uncertainties on the obtained dip angle and (3) to allow trade-off analysis between geometric and either electrical resistivity, velocity or density properties. Using parallelism, the computation time associated with electrical, seismic and gravity inversion on a 10 core work station is ca. 10 hours, 1 day and 30 minutes, respectively.

5. Results

5.1. Electrical Resistivity Tomography

The set of most likely models derived from the stochastic approach explains the main features of the observed apparent resistivity pattern (Fig. 7) and points out a high fault dip angle of ca. 70° (Fig. 8). This is obtained for both Dipole-dipole and Wenner-Schlumberger configuration as well as for electrode spacings between 1 m and 5 m. Bivariate frequency histograms indicate no tradeoff between dip angle and the other

geometric and electrical parameters (Fig. S1-S3). Those histograms suggest a 2.5 m thick fault zone. However the resistivity of this unit remains poorly resolved. The inversion approach images thin low-resistive top layers, both on the southern (~2.5 m, ~550 Ω.m) and northern sides (~3.5 m, ~350 Ω.m) (see Table S1 for details). The small resistivity contrasts between those two top layers can prevent the estimation of the fault geometry at very shallow depth (< 5 m). In contrary, due to the very high resistivity contrast between the two deeper bodies (SL ~ 3300 Ω.m vs NL ~ 30 Ω.m), we consider the obtained fault dip angle as a well-constrained parameter down to 40 m depth. This is confirmed by the narrow posterior distribution obtained for dip angle (Fig. 8). Finally, one can mention some discrepancies between the observed and calculated pseudo-sections on the south part (Fig. 7). Based on the simplified geometry of the model assuming horizontal layering, our inversion procedure is not able to explain the north-south resistivity variations in the footwall of the TFT.

All together these information on both geometry and resistivity contrast suggest a very clear resistivity contrast between the two sides of the fault as well as a constant dip angle of ~70° over a depth ranging between ca. 5 m and ca. 40 m.

5.2. Seismics

The set of final velocity models (Fig. 9) resulting from the stochastic inversion approach provides low travel-time residuals of +/-3 ms for most of the source-receiver pairs. This suggests that our simple geometry captures the main features of the velocity field. Furthermore, travel-time residuals show a quite homogeneous pattern, except close to the fault trace between -5 and 15 m where residuals abruptly increase from -5 ms to 4

ms northward. This demonstrates that seismic data are influenced by the presence of the fault.

Ray coverage (Fig. S7) indicates a shallower resolution depth compared to ERT investigations. Resolution depth varies between the two sides of the fault, from ca. 8 m to ca. 5 m in south and north, respectively. At these depths, thevelocity models resulting from both the stochastic inversion (Fig. 9) and tomography (Fig. S7) point out high velocity variations of ca. 50% at the transition of the fault zone. Figure 9 also emphasizes strong vertical velocity changes on both sides of the fault. High velocity contrasts between top and bottom layers induce a concentration of rays (Fig. S7) at a depth between 2 and 4 m, which prevents deeper investigations, in particular in the north.

Taking into account this shallow investigation depth, the velocity field can be characterized by two deeper units of Vp ~ 1100 m/s (SL) and Vp ~ 2100 m/s (NL) below two superficial low-velocity layers (STL: ~5 m, ~900 m/s and NTL: ~3 m, ~1600 m/s) (Fig. 9). Our inversion procedure also reveals that seismic data are sensitive to the dip angle parameter (Fig. 10). Our result suggests a northward dipping fault with a low-angle of ca. 20°-30° at depths down to ca. 5 m, which is consistent with field observations in the trench (Le Roux-Mallouf et al., 2016). This observation is also in agreement with both pseudo-sections and ERT profile (Fig. 3 and S6), which displays a change in dip angle with a more gentle slope of the TFT fault near the surface. Because we assumed a constant fault dip angle and we used the same model for the different ERT configurations, the inversion procedure was not able to image this dip angle change near the surface with resistivity data only.

Hence, field observations with the obtained seismic and electrical resistivity images together suggest a northward dipping fault with a low angle of ca. 20°-30° at very shallow depth, increasing gradually up to ca. 70° at a depth of 5-10 m.

5.3. Gravity

The observed short wavelength decrease at 27 m (Fig. 11) from the fault is related to topography correction. As previously mentioned, gravity measurements are mostly affected by the deeper part of our model. Thus in the following we focus on the long wavelength of the gravity profile associated with the two south-north gravity gradients described in section 3.3.

The result of our inversion suggests that the observed northward increase of gravity measurements is mostly related to both $\Delta\varrho$ the density contrast between SL and NL and α the fault dip angle (Fig. 11-12). As indicated on figure S5, gravity measurements cannot be used to assess the other density and geometric parameters, which remain poorly constrained.

Our result reveals a clear tradeoff between $\Delta\varrho$ and α: the higher the density contrast, the lower the fault dip angle. For $\Delta\varrho$ = -350 kg/m^3 the fault dip angle is ca. 30°, whereas for $\Delta\varrho$ = -200 kg/m^3 the fault dip angle is ca. 60° (Fig. 11). This leads to a wide distribution of fault dip angle (Fig. 12). The maximum of the distribution obtained at α~ 30-40° and for a model thickness ranging between between 70 m and 90 m suggest however a fault that flattens at depths below the investigation depth of 40 m obtained with ERT.

6. Discussion

The geometry of the fault, especially at shallow depth, is a key parameter in estimating the slip rate on the fault from uplifted terrace dating. Here we discuss our account on the new constraints for the TFT geometry deduced from near-surface geophysical techniques and its implication on convergence partitioning at the frontal thrust zone in south Central Bhutan.

6.1 Subsurface imaging

We take advantage of the various scales of investigation coming from ERT, seismic and gravity methods to obtain an accurate description of shallow structures and fault geometry at depth, which can be subdivided in three main zones: (1) a very shallow part up to 5 m depth well-constrained by both field observations and seismic data considering the ray coverage, (2) an intermediate depth part well-imaged by ERT sections between 5 and 40 m depth due to high resistivity contrasts, (3) a deeper part documented by gravity measurements below 40 m depth. The fault geometry discussed here arises from the integration of these three scales.

The obtained fault thickness remains poorly constrained. Assuming an a priori thickness between 0 m and 5 m, the gravity approach gives no information on this parameter and both the electrical and the seismic studies suggest a fault thickness of 2-5 m. In terms of lithological setting and water content, the geophysical datasets suggest a thin layer (~3-5 m) that appears to be present on both sides of the fault trace and which probably corresponds to recent alluvial deposits. Along the profile, resistivity and velocity variations at shallow depth may probably be due to a northward decrease of water

saturation. Below these superficial layers, in the hanging wall of the TFT, the obtained very low-resistivity values of < 30 Ώ.m, the high Vp of ca. 2100 m/s and the relatively low densities can be associated with a phyllite unit, which can be observed in the field.Overall, the geophysical methods image a more complex fault geometry than proposed by earlier studies (Berthet et al., 2014; Le Roux-Mallouf et al., 2016). Our results show a TFT with a flat and listric-ramp geometry with a low dip angle of 20°-30° at shallow depth, steeply dipping at ~70° in the middle and gradually flattening in a shallower dip angle of 30°- 40° in its deeper part (Fig. 13).

6.2 Overthrusting slip rate assessment

Berthet et al. (2014) estimate a Holocene vertical slip rate of 8.8 ± 2.1 mm/yr by dating two uplifted river terraces in the Sarpang area. Assuming a dip angle of 20-30°, they propose a slip rate of 20.8 ± 8.8 mm/yr, which is consistent with the GPS convergence rate of 17 mm/yr obtained across central Bhutan (Marechal et al., 2016). Finally they conclude that the Himalayan convergence is mostly accommodated by the TFT. However, this major conclusion can be revisited from our new constraints on the TFT geometry.

First, assuming a constant overthrusting slip rate along the TFT, a vertical velocity profile is calculated from this observed uplift rate (Okada, 1985). As expected this calculated profile depends on TFT geometry (Fig. 14a): a higher fault dip angle implies a higher uplift rate. More surprisingly, it also depends on the distance between the TFT and the location of dating samples. For instance, a distance of 5 m with respect to the TFT yields two very different vertical velocity profiles associated with the two end-member models for the fault geometry (Fig. 14a). On the contrary, if uplift rate is

measured about 10 m north from the TFT, the uplift rate difference drastically reduces (Fig. 14b). In other words, due to the flat and listric-ramp geometry of the shallow TFT, the uplift rate measured on the top of river terraces are spatially variable and cannot be constant. This result questions the validity of commonly used approaches for which a mean uplift rate is obtained by combining several uplifted terraces located at various distances from the front. Furthermore, assuming that the far-field GPS shortening rate corresponds to an upper limit for the uplift rate, our calculation shows that part of the models are unrealistic (see green curve on figure 14a). This suggests that both the convergence rates derived from GPS and the uplift measurements can be used to reduce the *a priori* geometric parameter ranges tested in our stochastic approach.

Second, assuming no prior information on the relative location of uplift rate measurements, one can deduce the overthrusting slip rate from the TFT geometry (Fig 14c). The slip rate associated with a rigid block model with a constant dip angle α can be easily estimated from:

$$slip\ rate = \frac{uplift\ rate}{sin\ (\alpha)}.$$

As previously proposed by Berthet et al. (2014), this simple approach gives a minimum dip angle of 30° for which most of the convergence across central Bhutan is accommodated along the TFT (Fig. 14c). However, the steeper is the dip angle, the greater is the chance for slip partitioning with other faults. Assuming a constant uplift rate of 8.8 ± 2.1 mm/yr along the profile, corresponding to the hypothesis of no information on the sampling location, the slip rate can also be estimated from a less straightforward modeling based on the obtained geometry. In that case using dislocations embedded in a homogeneous half space (Okada, 1985), the obtained slip

rate exhibits high variations along the profile from 20-40 mm/yr above the very shallow part of the fault to 10-20 mm/yr in the northern part of the profile. Using the convergence rate as a maximum value for the slip, this result suggests a minimum distance of 8 m for the steepening of the TFT and an accommodation of at least 10±2 mm/yr of the 17 mm/yr of convergence on the TFT. The obtained uncertainties associated with this slip rate estimate arise mainly from the location of samples for terrace dating and the fault geometry inferred from geophysical inversion.

6.3 Deformation at the topographic front

Based on our new constraints on the TFT geometry and the resulting slip rate, we propose that at least 60% of the convergence rate due to ongoing underthrusting of India beneath the Himalaya is accommodated by the TFT. It results that additional faults must be active in this area, which is consistent with results obtained by Dey et al. (2016) in the Kangra section of the Indian Himalaya where, besides the MFT, other out-of-sequence faulting such as the Jwalamukhi Thrust (JMT) accommodates part of the Sub-Himalayan shortening. In our study area, one can mention either the north-propagating emerging thrust front (FBT) documented by Dasgupta et al. (2013) in the Brahmaputra plain, or the Main Boundary Thrust (MBT), which accommodates present-day deformation in eastern Bhutan (Marechal et al., 2016).

From recent studies, it is now well-established that at least two major events have occurred on the TFT in the past, the last major event having occurred about 300 years ago (Le Roux-Mallouf et al., 2016; Hetényi et al., 2016a). Thus, a slip deficit of 3-5 m has accumulated on the TFT during this interseismic period, and could potentially be

released in a large magnitude earthquake with high probability of rupture reaching the surface.

7. Conclusion

We have presented high-resolution near-surface geophysical imaging results based on a joint approach including electrical resistivity, seismic and gravity data to constrain the TFT geometry in south Central Bhutan.

For each dataset, an inversion is performed using a stochastic approach, which combines (1) prior information on both geometric (dip angle, fault location, layer thickness) and petrophysical (resistivity, velocity and density) parameters and (2) forward models taking into account heterogeneity associated with a fault zone and superficial layers. Compared to commonly used approaches based on the search for the simplest model, the main advantages of our method include its ability to assess the fault geometry and its uncertainty on the obtained dip angle, as well as to trade-off analysis between geometric and either electrical resistivity, velocity or density properties. A joint inversion of the three datasets with physical properties linked to lithology/petrological information will be very useful, but it requires additional work that is beyond the scope of this present study.

Our results show that the upper part of the TFT is characterized by a flat and listric-ramp geometry with high variations of dip angle. This geometry clearly differs from the constant fault dip angle inferred from surface observation only. Estimating the slip rate without additional constraints from depth can therefore induce significant errors, arising

both from the terrace dating process to determine the uplift rate and the projection of the fault dip angle based on surface observations.

By combining information from surface observations with our new constraints on the fault geometry, we estimate that at least 60% of the Himalayan convergence is accommodated by the TFT, making this fault a zone of high seismic hazard. The hypothesis of slip partitioning cannot be totally ruled out, and other faults as the FBT emerging in the Brahmaputra plain and the MBT can also be active. Therefore, further studies combining geomorphology and near-surface geophysics along the front, especially towards the eastern part of the Bhutan, will be useful to study potential lateral variations in the fault geometry and its implication on the present-day strain partitioning. Moreover, local variability across the TFT may be assessed by studying areas located within few 100s of metres along strike with respect to the Sarpang study area.

Acknowledgements

This study is funded by the French Agence Nationale de la Recherche (ANR-13-BS06-006-01). The 2015–2016 surveys benefited from the support of the French RESIF-GraviMob Research Infrastructure (http://www.resif.fr). The field campaign in southern Bhutan would not have been possible without the unfailing support of the staff and drivers of the Department of Geology and Mines, Bhutan. We sincerely extend our gratefulness to each and every one who assisted us in deployment of geophysical measurements in the field. Our thanks also go to A. Binley for providing the R2

resistivity software. We thank Mark Everett, György Hetényi, and an anonymous reviewer for their helpful and constructive comments.

References

Ader, T., Avouac, J.P., Liu-Zeng, J., Lyon-Caen, H., Bollinger, L., Galetzka, J., Genrich, J., Thomas, M., Chanard, K., Sapkota, S.N. and Rajaure, S. (2012). Convergence rate across the Nepal Himalaya and interseismic coupling on the Main Himalayan Thrust: Implications for seismic hazard. Journal of Geophysical Research: Solid Earth, 117(B4).

Benson, A.K., Mustoe, N.B. (1995). Analysing shallow faulting at a site in the Wasatch Fault zone, Utah, USA, by integrating seismic, gravity, magnetic and trench data. Eng. Geol., 40, 139– 156.

Berthet, T., Ritz, J. F., Ferry, M., Pelgay, P., Cattin, R., Drukpa, D., Braucher, R. and Hetényi, G. (2014). Active tectonics of the eastern Himalaya: New constraints from the first tectonic geomorphology study in southern Bhutan. Geology, 42(5), 427–430.

Bilham, R., Larson, K. and Freymueller, J. (1997). GPS measurements of present-day convergence across the Nepal Himalaya. Nature, 386(6620), 61.

Binley, A. (2015). A Tools and Techniques: Electrical Methods. p. 233-259. In: Gerald Schubert (editor-in chief), Treatise on Geophysics, 2nd edition, Vol 11. Oxford: Elsevier.

Binley, A., & Kemna, A. (2005). Electrical Methods. p. 129–156. In Hubbard, S., Rubin, Y. (eds.), Hydrogeophysics. Springer.

Burgess, W. P., Yin, A., Dubey, C. S., Shen, Z. K. and Kelty, T. K. (2012). Holocene shortening across the Main Frontal Thrust zone in the eastern Himalaya. Earth and Planetary Science Letters, 357, 152-167.

Cattin, R., Mazzotti, S. and Baratin, L. M. (2015). GravProcess: An easy-to-use MATLAB software to process campaign gravity data and evaluate the associated uncertainties. Computers & Geosciences, 81, 20-27.

Cattin, R., Avouac, J. P. (2000). Modeling mountain building and the seismic cycle in the Himalaya of Nepal. Journal of Geophysical Research, 105(B6), 13389.

Dahlin, T., Zhou, B. (2004). A numerical comparison of 2D resistivity imaging with 10 electrode arrays. Geophysical Prospecting, 52(5), 379–398.

Dasgupta, S., Mazumdar, K., Moirangcha, L. H., Gupta, T. D. and Mukhopadhyay, B. (2013). Seismic landscape from Sarpang re-entrant, Bhutan Himalaya foredeep, Assam, India: Constraints from geomorphology and geology. Tectonophysics, 592, 130–140.

DeCelles, P. G., Robinson, D. M. and Zandt, G. (2002). Implications of shortening in the Himalayan fold-thrust belt for uplift of the Tibetan Plateau. Tectonics, 21(6).

Dey, S., Thiede, R. C., Schildgen, T. F., Wittmann, H., Bookhagen, B., Scherler, D. and Strecker, M. R. (2016). Holocene internal shortening within the northwest Sub-Himalaya: Out-of-sequence faulting of the Jwalamukhi Thrust, India. Tectonics.

Diehl, T., Singer, J., Hetényi, G., Grujic, D., Clinton, J., Giardini, D. and Kissling, E. (2017). Seismotectonics of Bhutan: Evidence for segmentation of the Eastern Himalayas and link to foreland deformation, Earth and Planetary Science Letters, 471, 54-64, doi.org/10.1016/j.epsl.2017.04.038.

Dorn, C., Green, A.G., Jongens, R., Carpentier, S., Kaiser, A.E., Campbell, F., Horstmeyze, H., Campbell, J., Finnemore, M. and Pettinga, J. (2010). High-resolution seismic images of potentially seismogenic structures beneath the northwest Canterbury Plains, New Zealand, J. geophys. Res., 115(B11)

Drukpa, D., Velasco, A. A. and Doser, D. I. (2006). Seismicity in the Kingdom of Bhutan (1937-2003): Evidence for crustal transcurrent deformation. Journal of Geophysical Research: Solid Earth, 111(6), 1–14.

Duputel, Z., Vergne, J., Rivera, L., Wittlinger, G., Farra, V. and Hetényi, G. (2016). The 2015 Gorkha earthquake: A large event illuminating the Main Himalayan Thrust fault. Geophysical Research letters, 43, 2517-2525.

Gautier, S., Latorre, D., Virieux, J., Deschamps, A., Skarpelos, C., Sotiriou, A., Serpersidaki, A. andTselentis, A. (2006). A new passive tomography of the Aigion area (Gulf of Corinth, Greece) from the 2002 data set. Pure and Applied Geophysics, 163(2-3), 431-453.

Hammer, P., Berthet, T., Hetényi, G., Cattin, R., Drukpa, D., Chophel, J., Lechmann, S., Le Moigne, N., Champollion, C. and Doerflinger, E. (2013). Flexure of the India plate underneath the Bhutan Himalaya. Geophysical Research Letters, 40(16), 4225-4230.

Hetényi, G., Le Roux-Mallouf, R., Berthet, T., Cattin, R., Cauzzi, C., Phuntsho, C., and Grolimund, R. (2016a), Joint approach combining damage and paleoseismology observations constrains the 1714 A.D. Bhutan earthquake at magnitude 8 ± 0.5, Geophys. Res. Lett., 43, doi:10.1002/2016GL071033.

Hetényi, G., Cattin, R., Berthet, T., Le Moigne, N., Chophel, J, Lechmann, S., Hammer, P., Drukpa, D., Sapkota, S., Gautier, S. and Thinley, K. (2016b). Segmentation of the

Himalayas as revealed by arc-parallel gravity anomalies, Nature Scientific Reports. Scientific Reports 6, Article number : 33866, doi:10.1038/srep33866.

Karastathis, V.K., Ganas, A., Makris, J., Papouilla, J., Dafnis, P., Gerolymatou, E. and Drakatos, G. (2007). The application of shallow seismic techniques in the study of active faults: The Atalanti normal fault, central Greece. Journal of Applied Geophysics, 62(3), 215-233.

Kumar, S., Wesnousky, S.G., Jayangondaperumal, R., Nakata, T., Kumahara, Y. and Singh, V. (2010). Paleoseismological evidence of surface faulting along the northeastern Himalayan front, India: Timing, size, and spatial extent of great earthquakes. Journal of Geophysical Research: Solid Earth, 115(B12).

Lavé, J., Avouac, J. P. (2000). Active folding of fluvial terraces across the Siwaliks Hills, Himalayas of central Nepal. Journal of Geophysical Research, 105(B3), 5735.

Le Roux-Mallouf, R., Godard, V. Cattin, R., Ferry, M., Gyeltshen, J., Ritz, J.F., Drupka, D., Guillou, V., Arnold, M., Aumaître, G. Bourlès, D. L. and Keddadouche, K. (2015) Geophys. Res. Lett., Evidence for a wide and gently dipping Main Himalayan Thrust in western Bhutan, doi : 10.1002/2015GL063767

Le Roux-Mallouf, L., Ferry, M., Ritz, J. F., Berthet, T., Cattin, R. and Drukpa, D. (2016). First paleoseismic evidence for great surface-rupturing earthquakes in the Bhutan Himalayas. Journal of Geophysical Research: Solid Earth, 121(10), 7271-7283.

Loke, M. H. (2015). Tutorial: 2D and 3D electrical imaging surveys. Penang, Malaysia, Universiti Sains Malaysia. Unpublished course notes, http://www.geotomosoft.com/.

Loke, M.H., Barker, R.D. (1996). Rapid least-squares inversion of apparent resistivity pseudosections by a quasi-Newton method. Geophysical Prospecting, 44, 131–152.

Long, S., McQuarrie, N., Tobgay, T., Grujic, D. and Hollister, L. (2011). Geologic Map of Bhutan. Journal of Maps, 7(1), 184–192.

Marechal, A., Mazzotti, S., Cattin, R., Cazes, G., Vernant, P., Drukpa, D., Thinley, K., Tarayoun, A., Le Roux-Mallouf, R., Thapa, B. B., Pelgay, P., Gyeltshen, J., Doerflinger, E., Gautier, S. (2016). Evidence of interseismic coupling variations along the Bhutan Himalayan arc from new GPS data. Geophysical Research Letters, 43, doi:10.1002/2016GL071163.

Molnar, P., Tapponnier, P. (1975). Cenozoic tectonics of Asia: effects of a continental collision. Science, 189(4201), 419-426.

Morey, D., Schuster, G.T. (1999). Paleoseismicity of the Oquirrh fault, Utah, from shallow seismic tomography. Geophys. J. Int., 138, 25–35.

Mosegaard, K., Tarantola, A., Monte Carlo sampling of solutions to inverse problems, Journal of Geophysical Research, 100, B7, 12431-12447, 1995.

Nguyen, F., Garambois, S., Chardon D., Hermitte D., Bellier O. and Jongmans D. (2007). Subsurface electrical imaging of anisotropic formations affected by a slow active reverse fault, Provence, France. Journal of Applied Geophysics, 62 (4), 338-353.

Okada, Y. (1985). Surface deformation due to shear and tensile faults in a half-space. Bulletin of the seismological society of America, 75(4), 1135-1154.

Pandey, M. R., Tandukar, R. P., Avouac, J. P., Lave, J., & Massot, J. P. (1995). Interseismic Strain Accumulation on the Himalayan Crustal Ramp (Nepal). Geophysical Research Letters, 22(7), 751–754.

Pasquet, S., Bodet, L., Dhemaied, A., Mouhri, A., Vitale Q., et al.. (2015). Detecting different water table levels in a shallow aquifer with combined P-, surface and SH-wave surveys: Insights from VP/VS or Poisson's ratios. Journal of Applied Geophysics, 113, 38-50.

Podvin, P., & Lecomte, I. (1991). Finite difference computation of traveltimes in very contrasted velocity models: a massively parallel approach and its associated tools. Geophysical Journal International, 105(1), 271-284.

Priolo, E., Lovisa, L., Zollo, A., Böhm, G., D'Auria, L., Gautier, S., Gentile, F., Klin, P., Latorre, D., Michelini, A., Vanorio, T. and Virieux, J. (2012). The Campi Flegrei Blind Test : evaluating the imaging capability of local earthquake tomography in a volcanic area. Int. Journal of Geophysics, 2012, 37-75.

Ramirez, A. L., Nitao, J. J., Hanley, W. G., Aines, R., Glaser, R. E., Sengupta, S. K., Dyer, K.M., Hickling, T.L. and Daily, W. D. (2005). Stochastic inversion of electrical resistivity changes using a Markov Chain Monte Carlo approach. Journal of Geophysical Research: Solid Earth, 110(B2).

Schelling, D., & Arita, K. (1991). Thrust tectonics, crustal shortening, and the structure of the far-eastern Nepal Himalaya. Tectonics, 10(5), 851-862.

Schuster, G.T. and Quintus-Bosz, A. (1993). Wavepath eikonal traveltime inversion: Theory. Geophysics, 58(9), 1314-1323.

Seeber, L., & Armbruster, J. G. (1981). Great detachment earthquakes along the Himalayan Arc and long-term forecasting. Earthquake prediction, 259-277.

Sheehan, J.R., Doll, W.E. and Mandell, W.A. [2005] An evaluation of methods and available software for seismic refraction tomography analysis. Journal of Environmental & Engineering Geophysics,10(1), 21-34.

Singer, J., Obermann, A., Kissling, E., Fang, H., Hetényi, G. and Grujic, D. (2017). Along-strike variations in the Himalayan orogenic wedge structure in Bhutan from ambient seismic noise tomography, Geochem. Geophys. Geosyst., 18, 1483–1498, doi:10.1002/2016GC006742.

Stephenson, W.J. and McBride, W. J. (2003) Contributions to neotectonics and seismic hazard from shallow geophysical imaging. Tectonophysics, 368, 1–5.

Storz, H., Storz, W., Jacobs, F. (2000). Electrical resistivity tomography to investigate geological structures of the Earth's upper crust. Geophys. Prospect., 48(3), 455–471.

Vernant, P., Bilham, R., Szeliga, W., Drukpa, D., Kalita, S., Bhattacharyya, A. K., Gaur, V. K., Pelgay, P., Cattin, R., Berthet, T. (2014). Clockwise rotation of the Brahmaputra Valley relative to India: tectonic convergence in the eastern Himalaya, Naga Hills and Shillong Plateau, J. Geophys. Res., doi:10.1002/2014JB011196

Villani, F., Tulliani, V., Sapia, V., Fierro, E., Civico, R., Pantosti, D. (2015). Shallow subsurface imaging of the Piano di Pezza active normal fault (central Italy) by high-resolution refraction and electrical resistivity tomography coupled with time-domain electromagnetic data. Geophys. J. Int., 203(3), 1482-1494.

Wise, D.J., Cassidy, J., Locke, C.A. (2003). Geophysical imaging of the Quaternary Wairoa North Fault, New Zealand: a case study. Journal of Applied Geophysics, 53(1), 1-16.

Won, I. J., Bevis, M. (1987). Computing the gravitational and magnetic anomalies due to a polygon: Algorithms and Fortran subroutines. Geophysics, 52(2), 232-238.

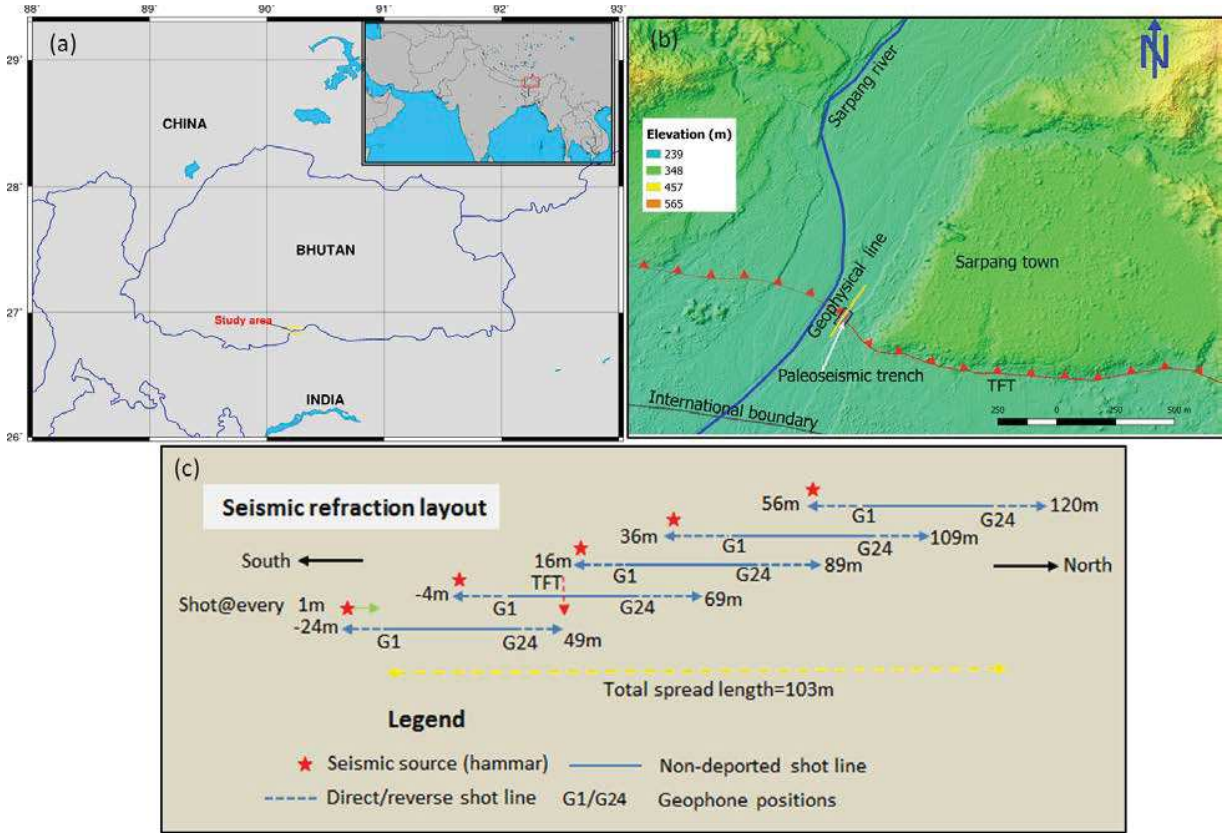

Figure 1. (a) Location of the Kingdom of Bhutan and the study area in south Central part of Bhutan. (b) High resolution Pleiades image of the study area showing the Topographic Frontal Thrust (TFT) fault trace, the location of the paleoseismic trench studied by Le Roux-Mallouf et al. (2016) and our geophysical profile (yellow line). (c) Seismic survey layout plan.

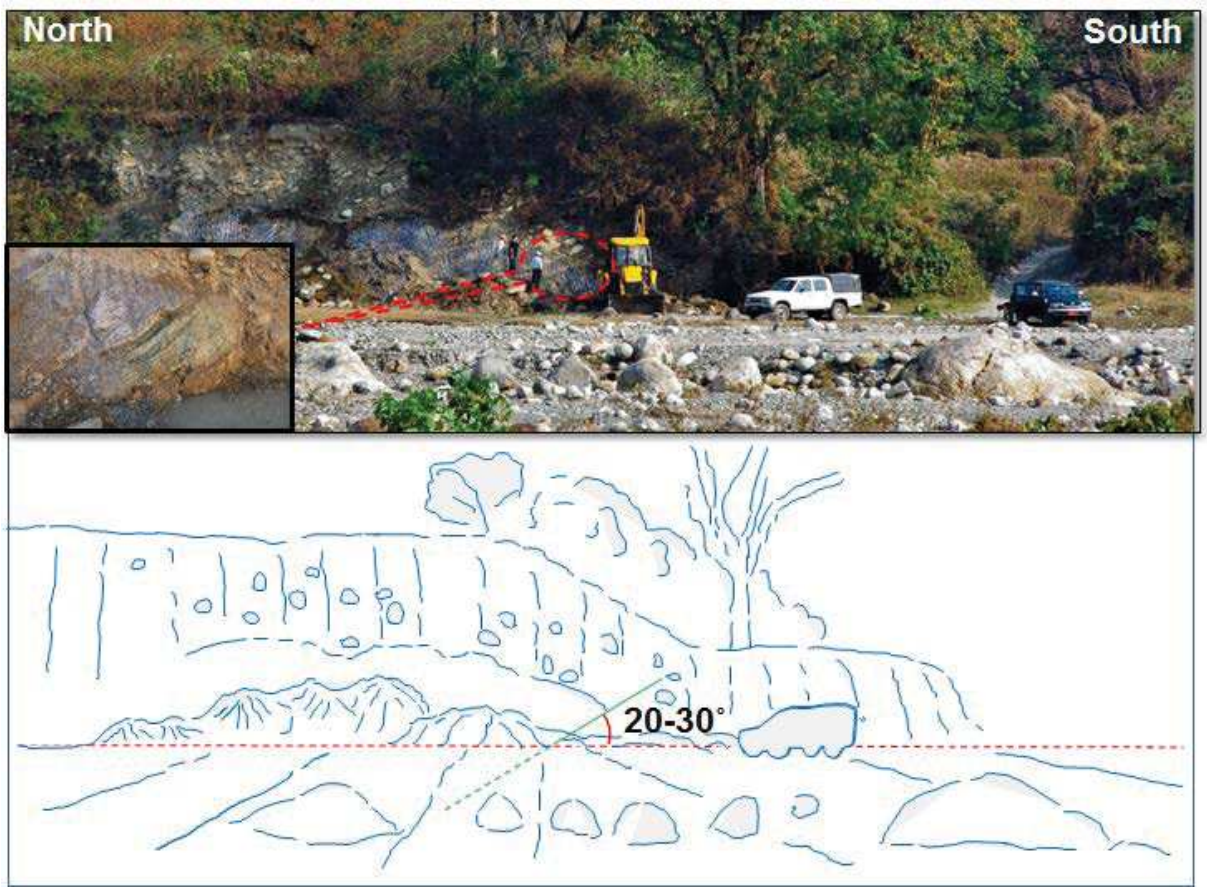

Figure 2. Picture of excavated site in Sarpang area with inset in the bottom left corner showing the TFT trace at the surface. A sketch of the outcrop shows the estimated dip angle of the fault as observed in the trench.

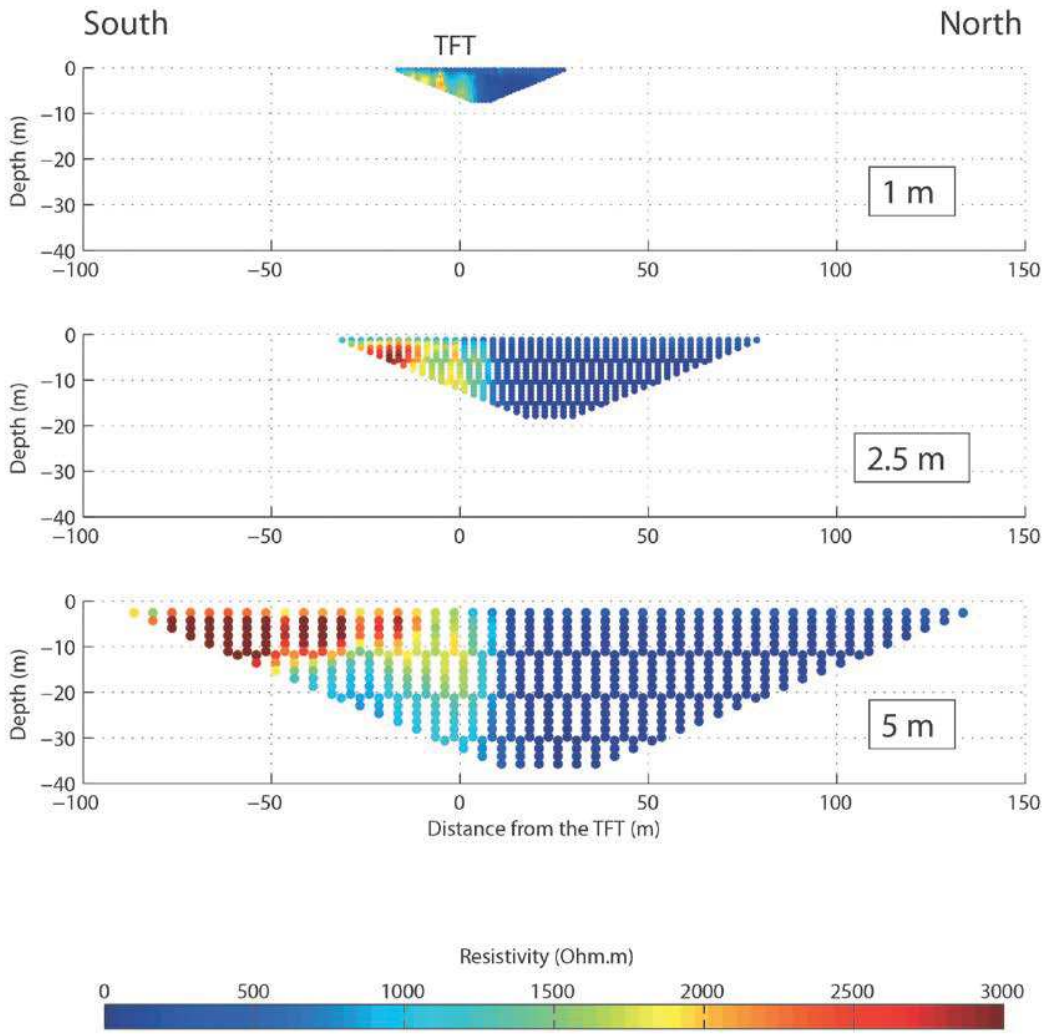

Figure 3. ERT pseudo-sections (Wenner-Schlumberger array) observed along the study profile for electrode spacing of 1 m (top), 2.5 m (middle) and 5 m (bottom).

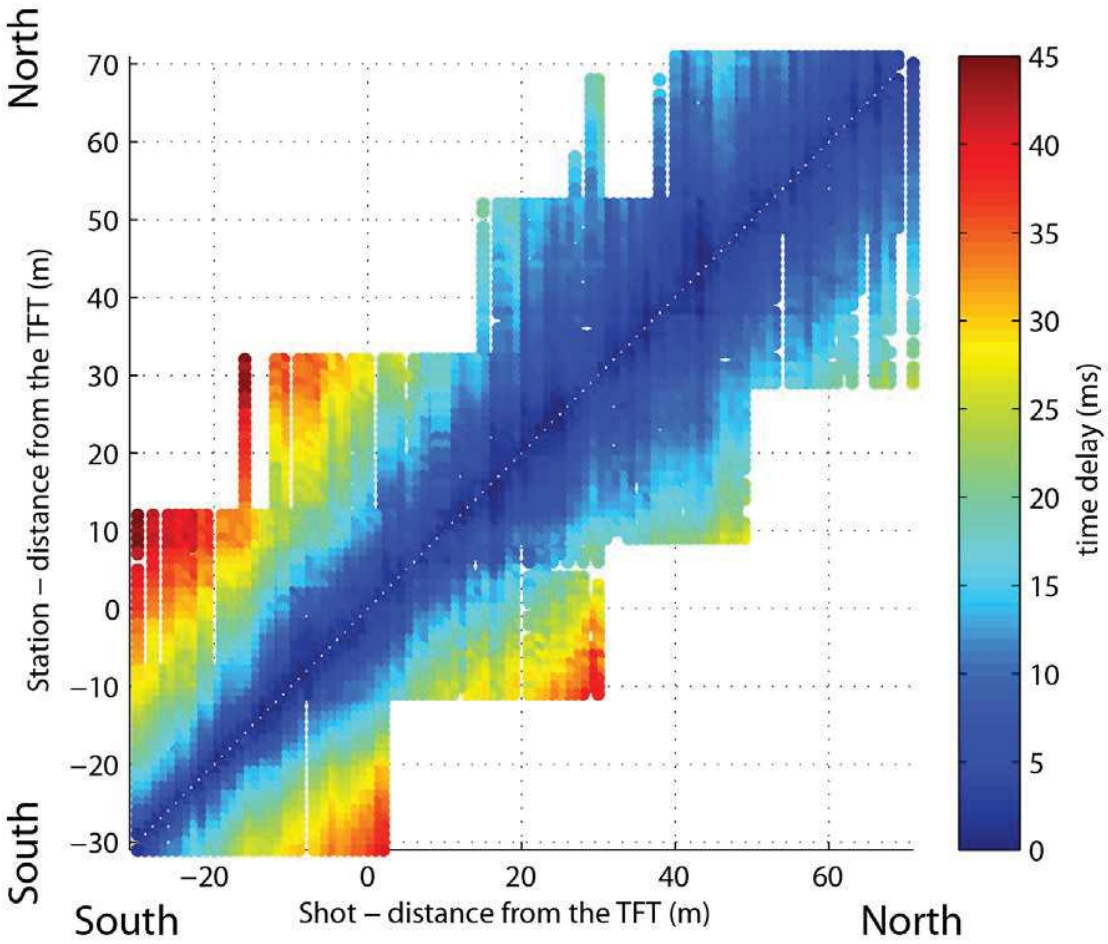

Figure 4. Hodochrone of the hand-picked first-arrival traveltimes associated with the roll-along seismic acquisition. Color dots correspond to a first-arrival time for a given geophone positions along the profile. White dots correspond to the case, for which shot and station are at the same location along the seismic profile. The color scale represents the value of first-arrival times.

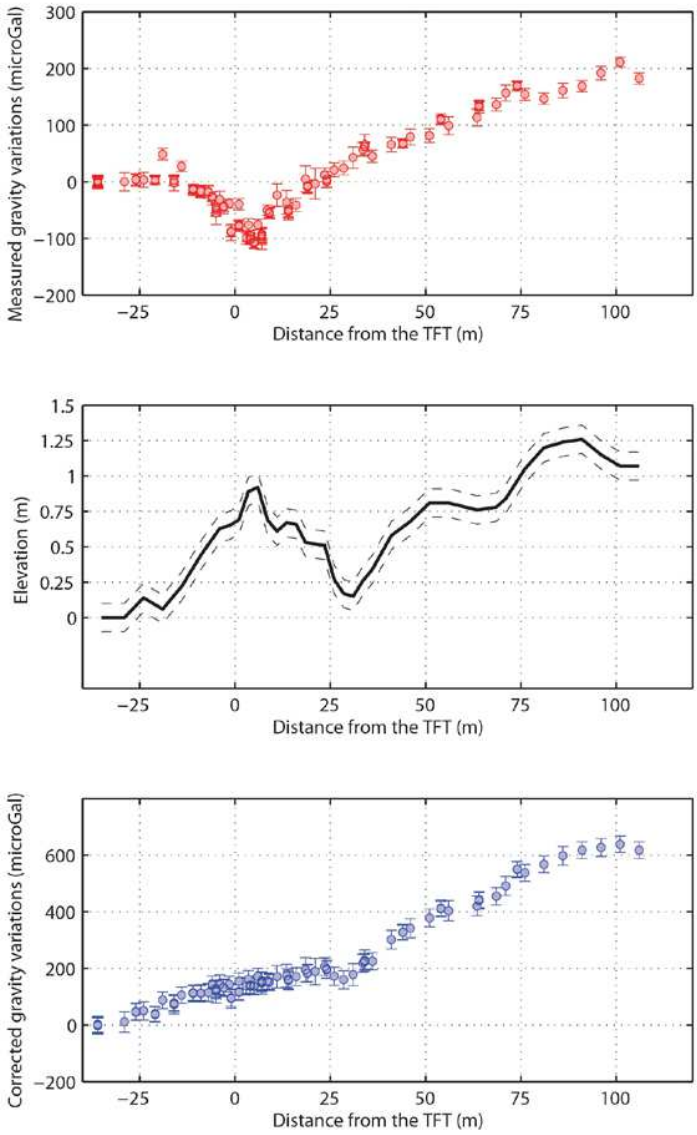

Figure 5. Measured gravity (top), elevation (middle) and gravity variations corrected for both topographic effect and regional trend (bottom) along the study profile. Data uncertainty is associated with both accurary of the CG5 gravimeter and error in elevation measurement.

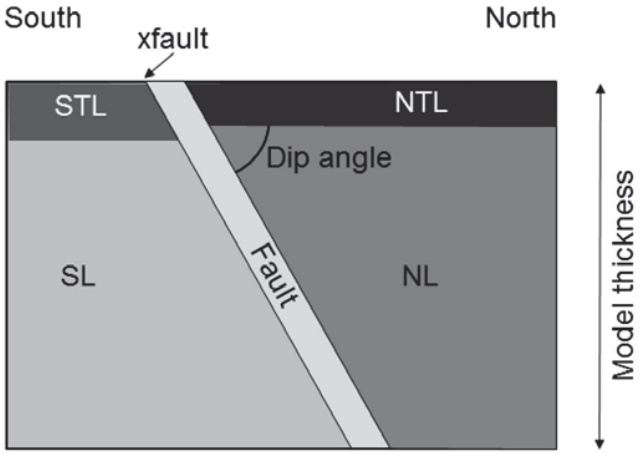

Figure 6. Geometry of the model used in the stochastic inversion. STL - South Top layer, NTL - North Top Layer, SL - South Layer and NL - North Layer. xfault is the prior location of the fault as observed in the field. Model thickness is associated with the thickness investigated by each geophysical method.

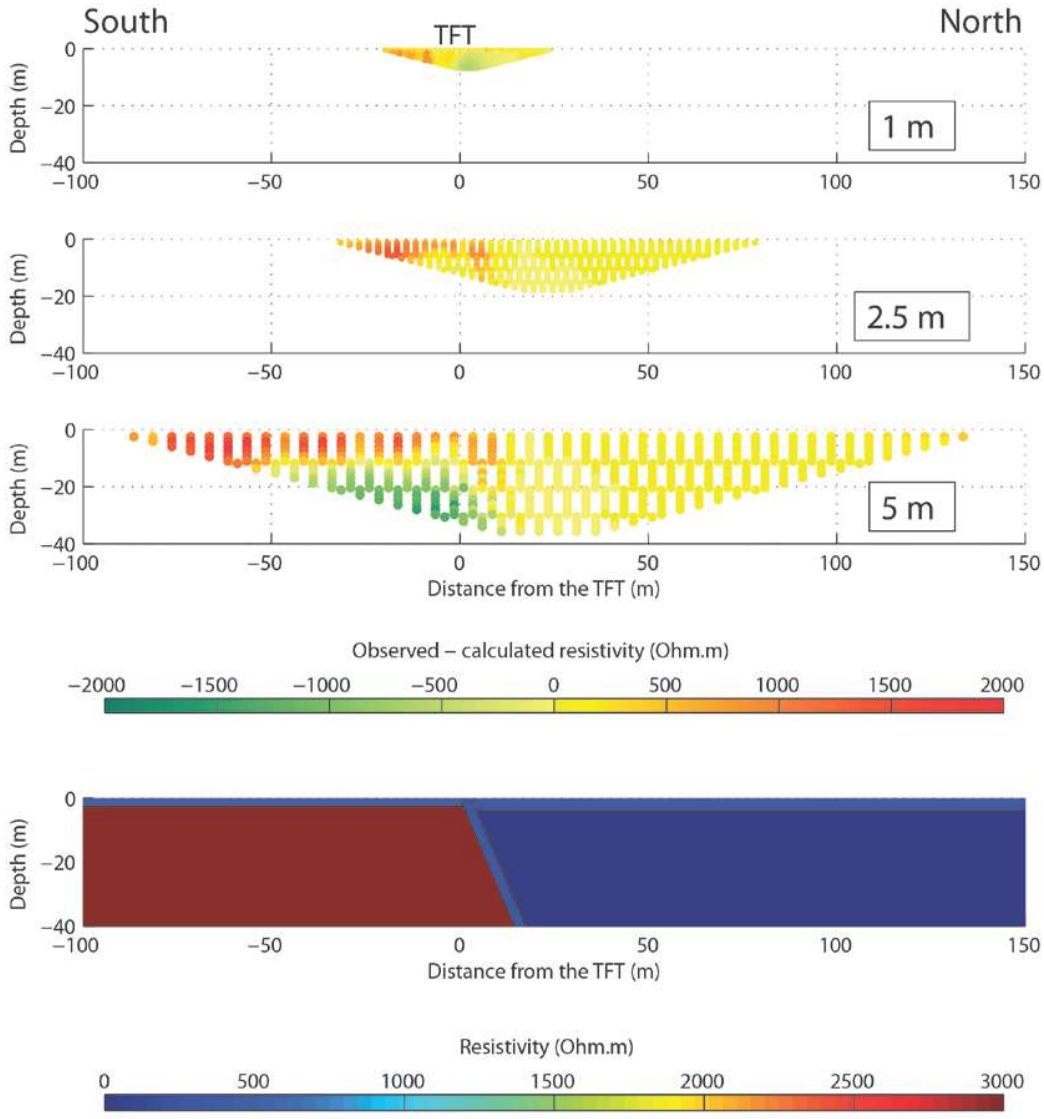

Figure 7. Misfit between observed and calculated ERT pseudo-sections for electrode spacing of 1 m, 2.5 m and 5 m using Wenner-Schlumberger configuration. This misfit is defined as the difference between the observed and calculated resistivities using the electrical model plotted at the bottom. Bottom color scale is the same as figure 3 for comparison.

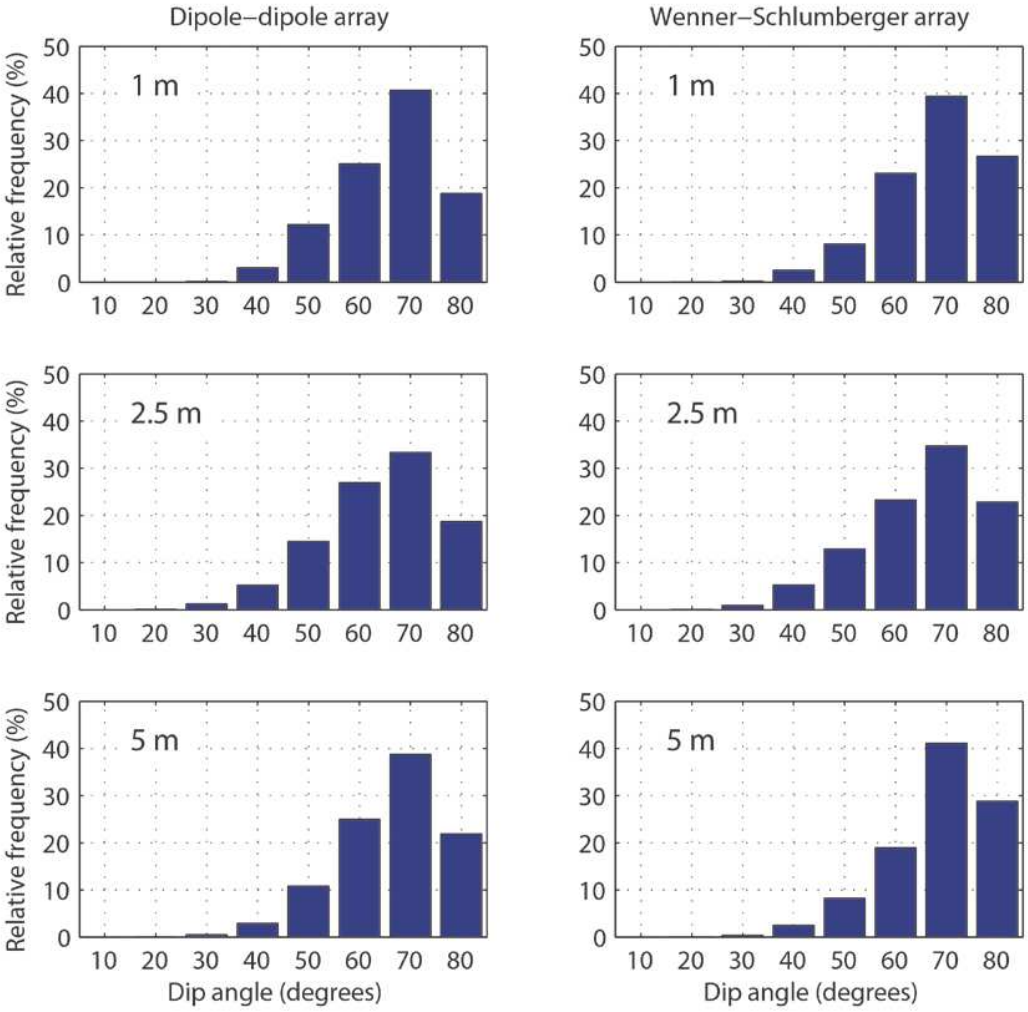

Figure 8. Distribution of TFT dip angle from ERT sections using both dipole-dipole and Wenner-Schlumberger arrays. Electrode spacing ranges from 1 m (top) to 5 m (bottom).

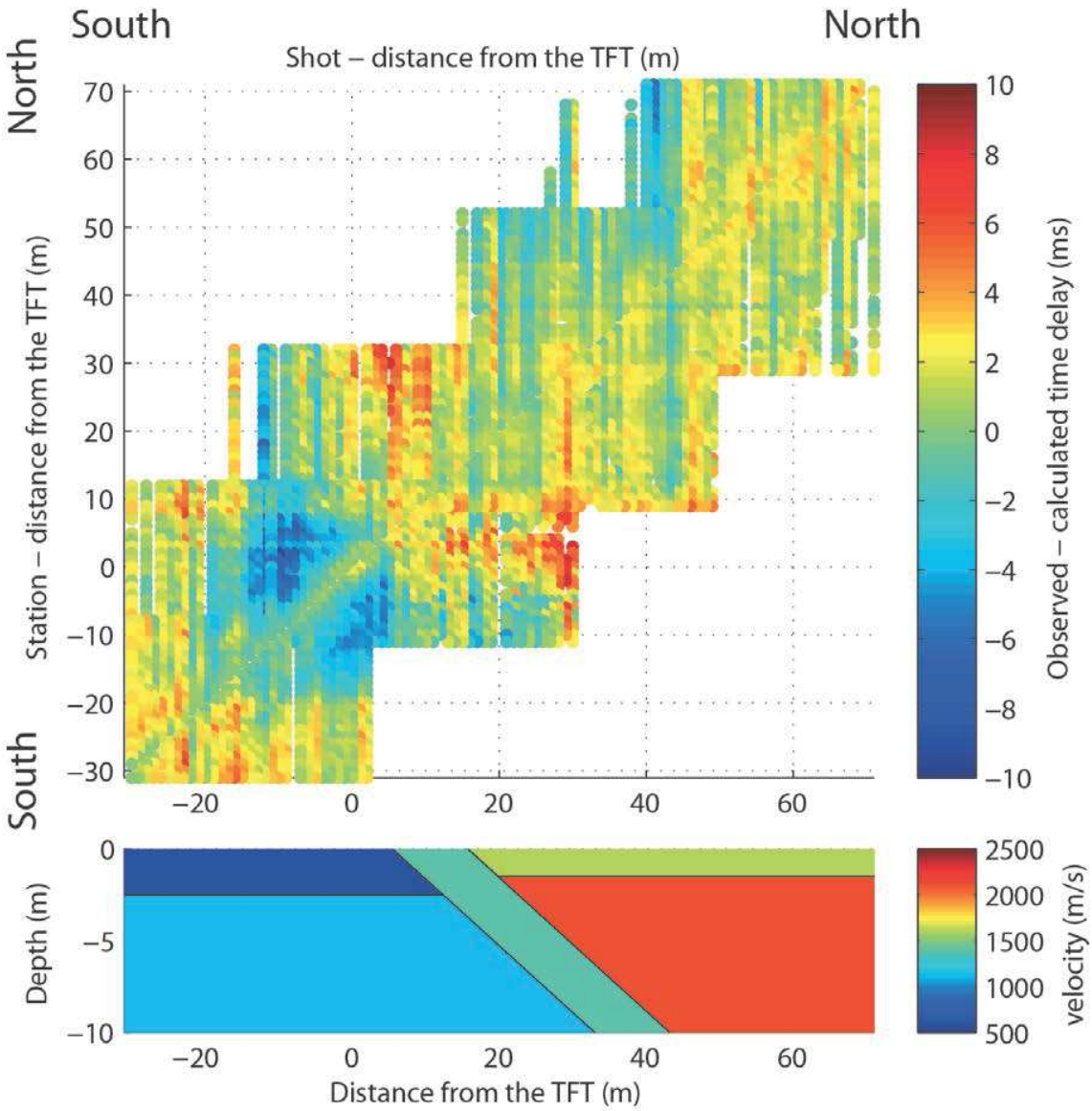

Figure 9. Hodochrone of the residuals between observed data and theoretical first-arrival times computed in the velocity model plotted at the bottom. Compared to the resistivity model figure 7, note the lower limit of the y-axis, which corresponds to a shallower depth of investigation.

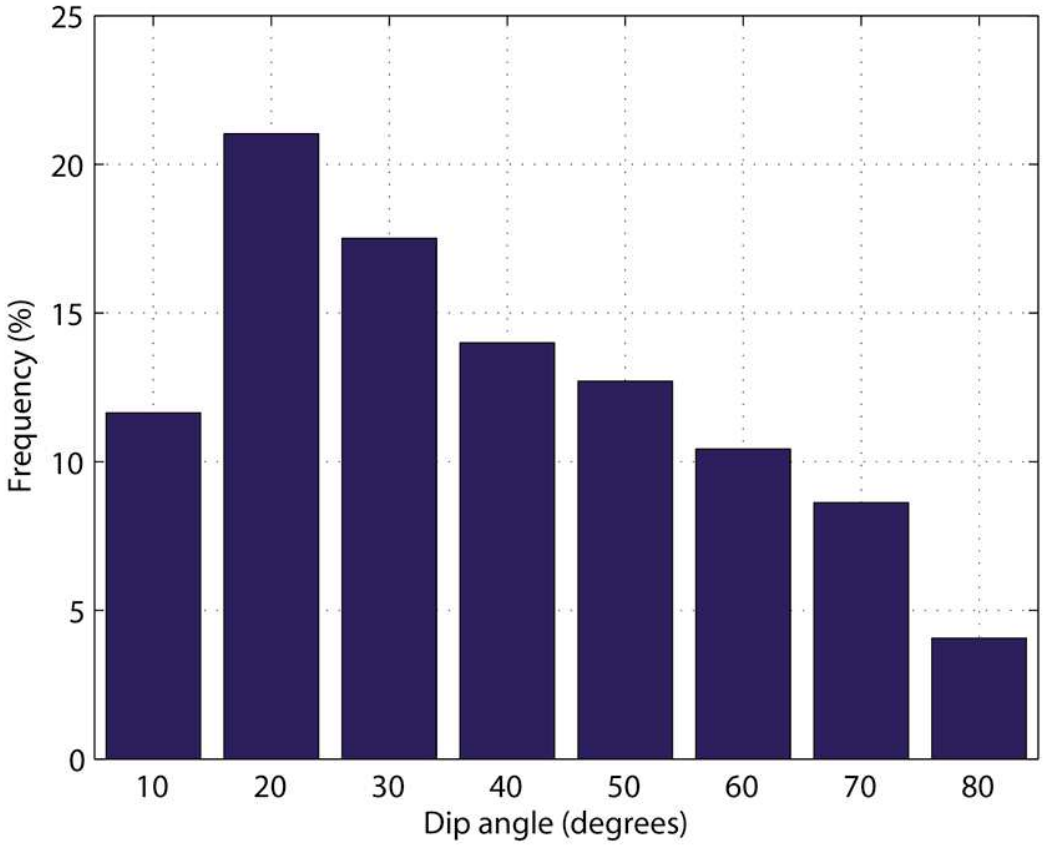

Figure 10. Distribution of TFT dip angle obtained from seismic measurements.

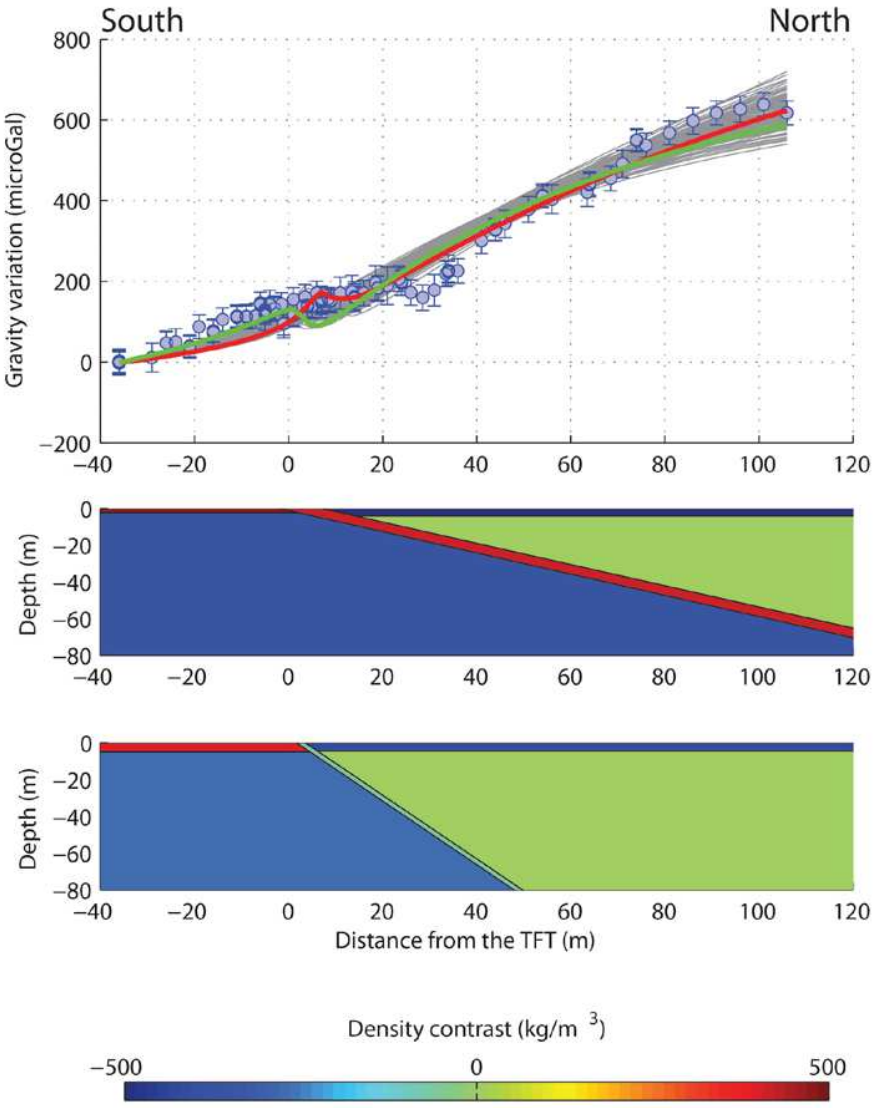

Figure 11. (Top) Comparison between observed (blue circles) and calculated (gray lines) gravity variations along the study profile obtained for the 100 best-fitting models. (Bottom) Density contrast models associated with the red and green lines plotted above and corresponding to a fault dip angle of 30° and 60°, respectively.

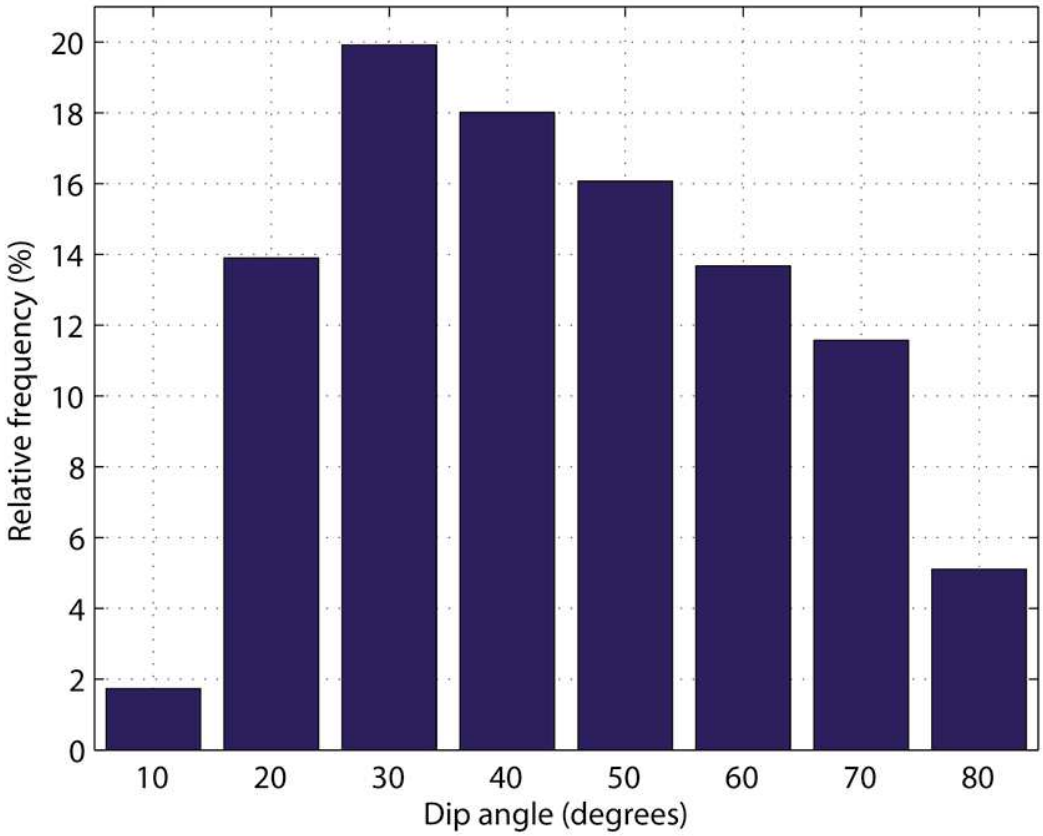

Figure 12. Distribution of TFT dip angle obtained from gravity measurements.

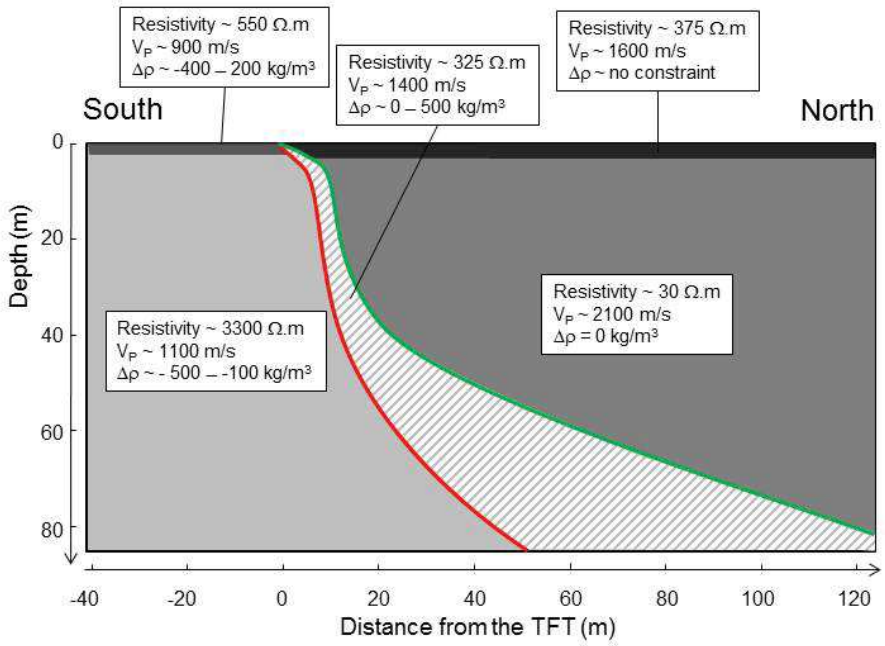

Figure 13. Simplified cross section showing the final model obtained from electrical resistivity tomography, seismic refraction and gravity measurements. Together geophysical results suggest a TFT with a flat and listric-ramp geometry, with a surface dip angle of ~20° reaching ~70° at 20 m depth and flattening in its deeper part. Note that the dashed area is bounded by the two end-member models of fault geometry given by the green and the red lines. Hence, this area does not represent the fault thickness, which is estimated to be 2.5 m.

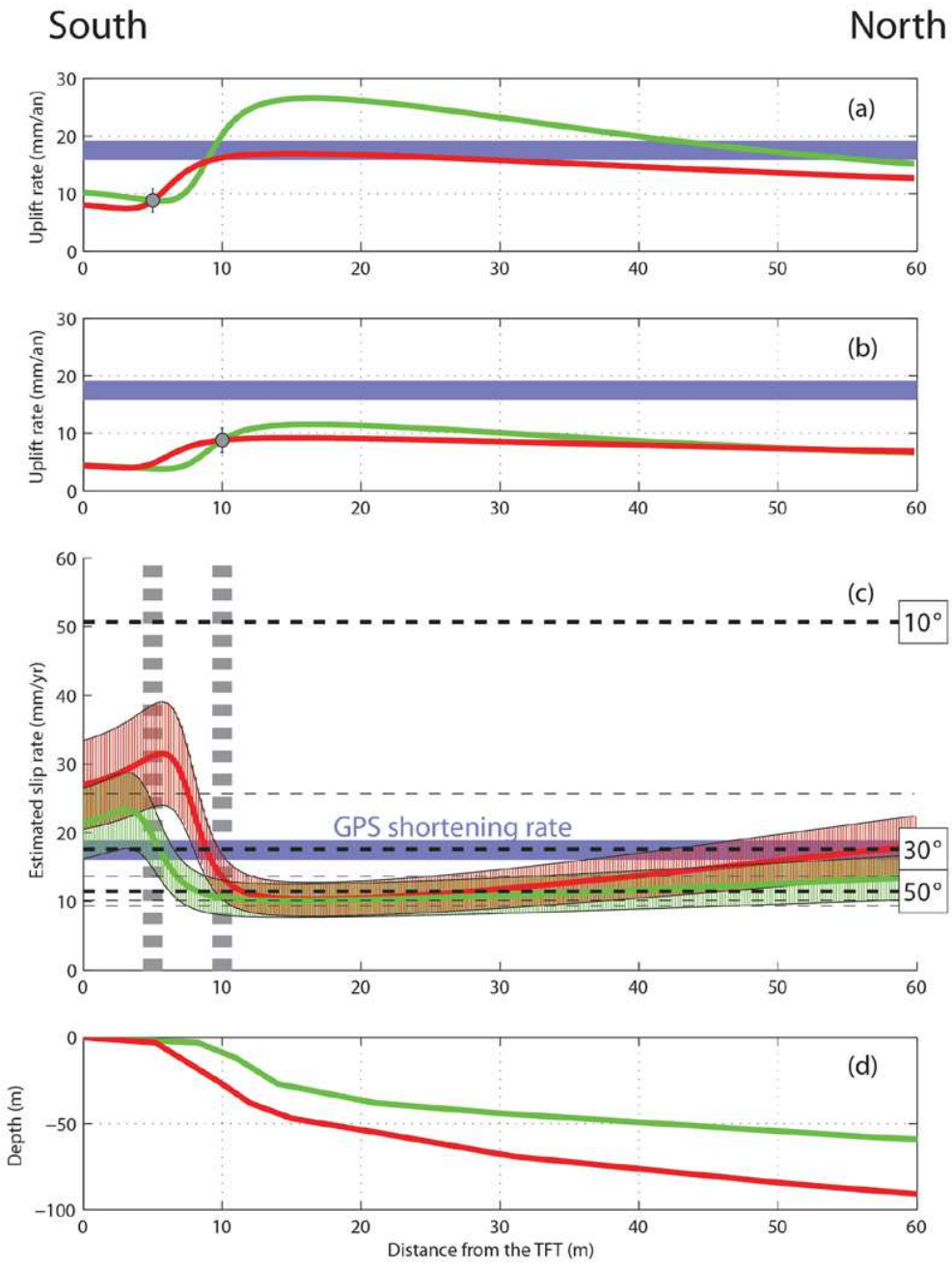

Figure 14. Estimated overthrusting slip rate inferred from both fault geometry and observed uplift rate. (a) Uplift rate along the study profile. Red and green curves are associated with the two end-member models obtained for fault geometry described figure 13. Thick blue line denotes the far-field shortening rate estimated from GPS measurements (Marechal et al., 2016). It corresponds to the upper limit of uplift rate,

which can be associated with a theoretical vertical fault. Gray circle is the observed uplift rate assuming a northward distance of 5 m from the TFT as reported by Berthet et al., 2014. (b) Same as (a) except a northward distance of 10 m is assumed. (c) Estimated slip along the TFT at depth assuming a constant uplift rate along the study profile for the two-end member models denoted by red and green curves. Hatched area around these curves is associated with uplift rate uncertainties. The thick grey dashed lines point out the area of uplift rate assuming a northward distance from the TFT of 5 m and 10 m, respectively. Note that within this area, the uncertainties in the uplift rate spikes up close to the TFT and decreases away from the front towards the north. Thick blue line denotes the far-field shortening rate estimated from GPS measurements (Marechal et al., 2016), which is the upper limit of slip rate. The slip obtained from rigid blocks model with a constant dip angle ranging from 10° to 60° is given by black dashed lines. (d) Fault geometry used.

Supplementary material

Contents

Table S1

Figures S1 to S10

Introduction

This supporting information contains the range of model parameters, Markov Chain Monte Carlo inversion results and the images obtained from the commonly used Res2inv and TomoRefract softwares. The bivariate frequency histograms show the relationship between the obtained dip angle and the other model parameters associated with the inversion of datasets, which include ERT with different electrode spacing for Wenner-Schlumberger array, seismic refraction and gravity variations.

Table S1. Inversion results. The range column gives the prior parameter range used in the inversion. The obtained parameter values are associated with the highest relative frequency model. The associated uncertainties are indicated in bracket. Uncertainties on each parameter are given by the full width at half maximum. The symbol '-' means no constraint has been obtained.

Parameter	Range	Posterior value							
		Dipole-dipole			Wenner -Schlumberger			Seismic	Gravity
		1m	2.5 m	5 m	1 m	2.5 m	5 m		
Geometry									
X fault (m)	[-5 5]	-3.5 [-5 -1]	1.5 [-4 4]	0 [-5 5]	-3.5 [-5 -1]	-1.5 [-5 4]	-2.5 [-5 4]	-	-
Depth of investiga-tion (m)		~ 8	~20	~40	~ 8	~20	~40	3 -8	> 40
STL thickness (m)	[1 5]	2.5 [2 4]	2.5 [1 4]	2.5 [1 4]	2.5 [1 4]	2.5 [1 4]	2.5 [1 4]	4.5 [3 5]	-
NTL thickness (m)	[1 5]	3.5 [2 4]	3.5 [2 4]	3.5 [2 5]	3.5 [2 4]	4.5 [3 5]	4.5 [2 5]	3.5 [2 5]	-
Fault thickness (m)	[1 5]	2.5 [2 4]	2.5 [2 4]	2.5 [2 5]	2.5 [2 4]	2.5 [3 5]	2.5 [2 5]	3.5 [2 5]	-
Fault dip angle (degre)	[10 80]	70 [60 80]	70 [60 80]	70 [60 80]	70 [60 80]	70 [60 80]	70 [60 80]	20 [10 50]	35 [20 60]
Electrical resistivity									
STL resistivity (Ohm.m)	[100 600]	500 [300 600]	575 [300 600]	550 [300 600]	525 [350 600]	575 [400 600]	525 [350 600]	-	-
NTL resistivity (Ohm.m)	[100 600]	325 [300 600]	-	-	350 [200 500]	450 [300 600]	-	-	-
Fault resistivity (Ohm.m)	[100 600]	325 [300 500]	-	-	-	-	-	-	-
SL resistivity (Ohm.m)	[2500 4000]	3600 [3250 4000]	-	3100 [3000 4000]	3600 [2750 4000]	3200 [2750 4000]	2900 [2750 3750]	-	-
NL resistivity (Ohm.m)	[1 100]	15 [10 30]	35 [20 50]	45 [30 60]	15 [1 60]	40 [20 50]	35 [20 50]	-	-

Seismic velocity									
STL velocity (m/s)	[500 2500]	-	-	-	-	-	-	900 [1000 500]	
NTL velocity (m/s)	[500 2500]	-	-	-	-	-	-	1600 [1000 2000]	
fault velocity (m/s)	[500 2500]	-	-	-	-	-	-	1400 [750 1750]	
SL velocity (m/s)	[500 2500]	-	-	-	-	-	-	1100 [750 1250]	-
NL velocity (m/s)	[500 2500]	-	-	-	-	-	-	2100 [1750 2500]]	-
Density contrast with respect to layer NL									
STL density contrast (kg/m^3)	[-500 500]	-	-	-	-	-	-	-	-150 [-400 200]
NTL density contrast (kg/m^3)	[-500 500]	-	-	-	-	-	-	-	-
Fault density contrast (kg/m3)	[-500 500]	-	-	-	-	-	-	-	350 [0 500]
SL density contrast (kg/m3)	[-500 500]	-	-	-	-	-	-	-	-300 [-500 -100]

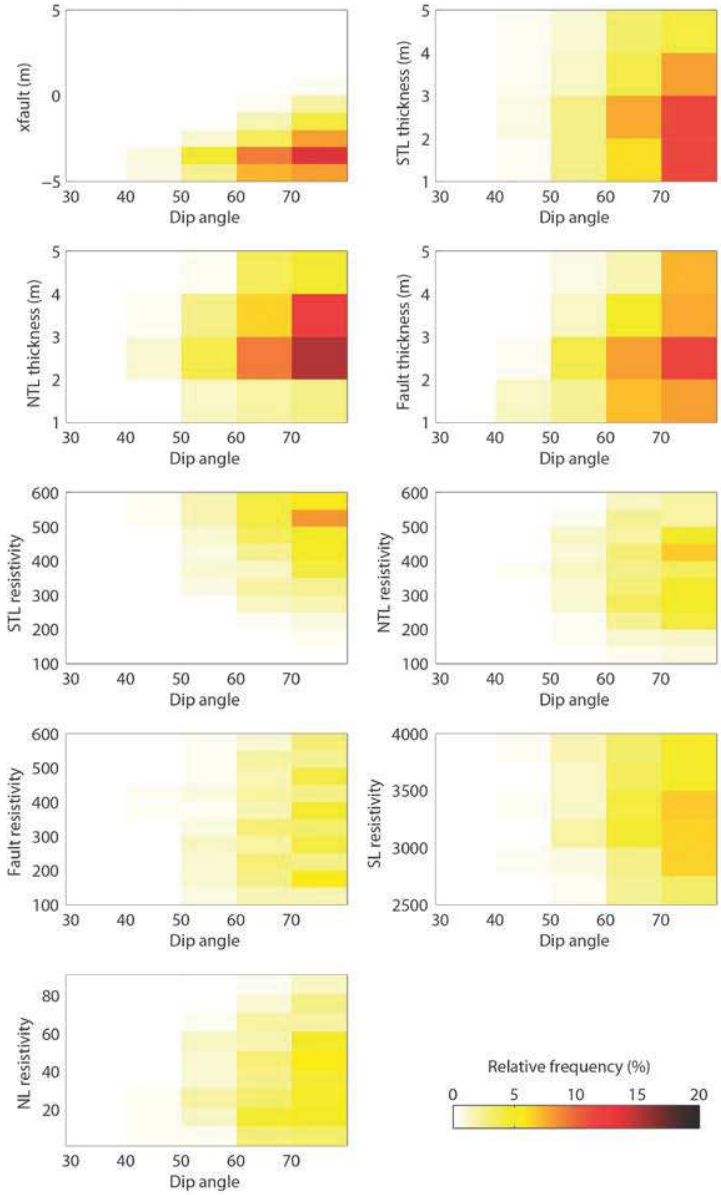

Figure S1. Bivariate frequency histograms between dip angle in degrees and the other parameters of the ERT model obtained from Wenner-Schlumberger array and electrode spacing of 1 m. Color scale gives the probability of occurrence of parameter pairs within our *a priori* range of parameters.

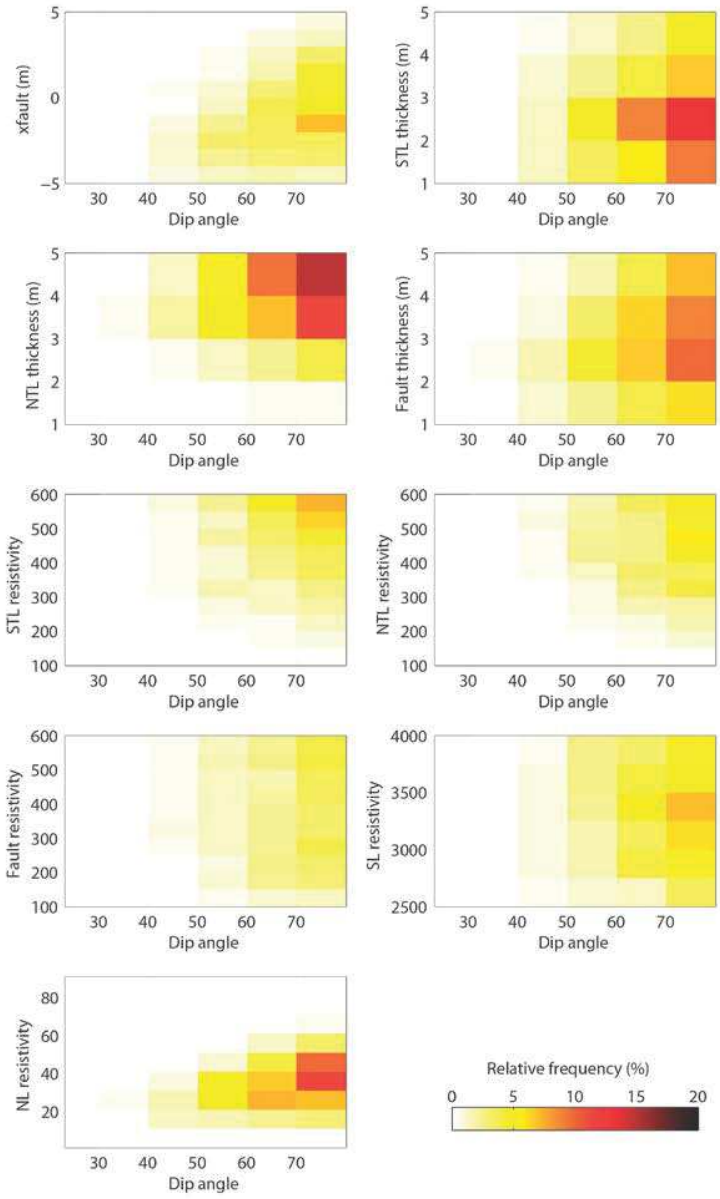

Figure S2. Same as figure S1, except for electrode spacing of 2.5 m.

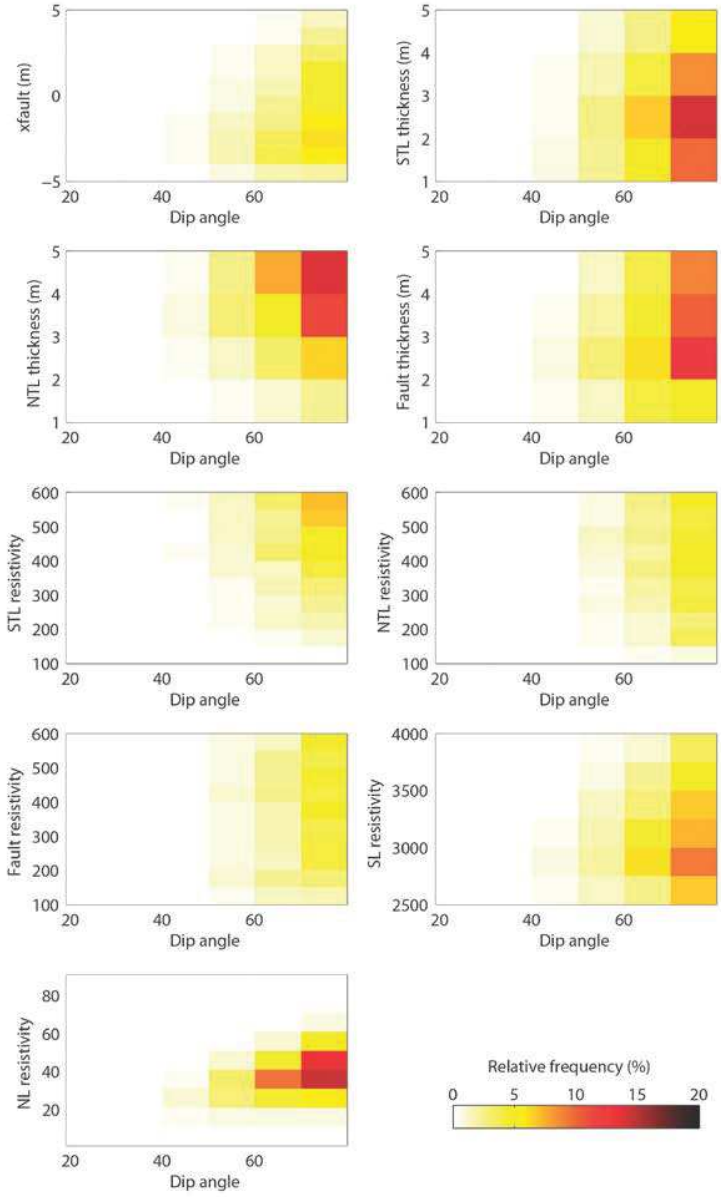

Figure S3. Same as figure S1, except for electrode spacing of 5 m.

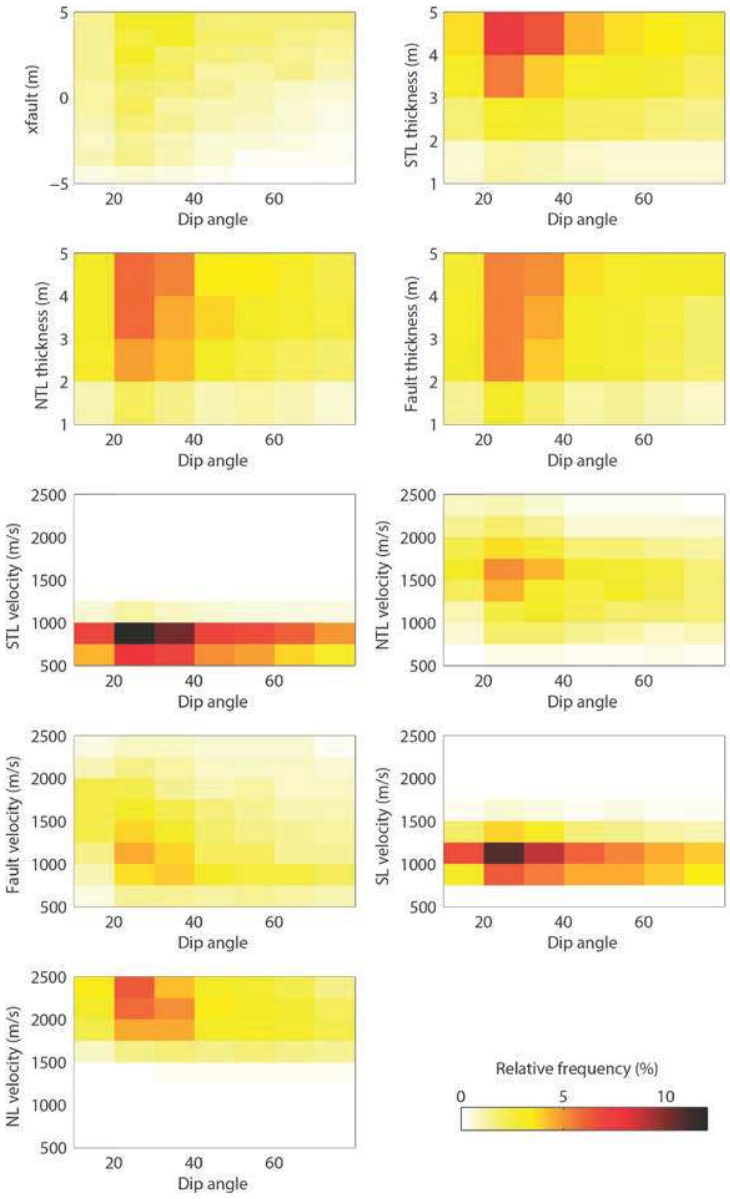

Figure S4. Relationship between the obtained dip angle in degrees and the other parameters of the velocity model.

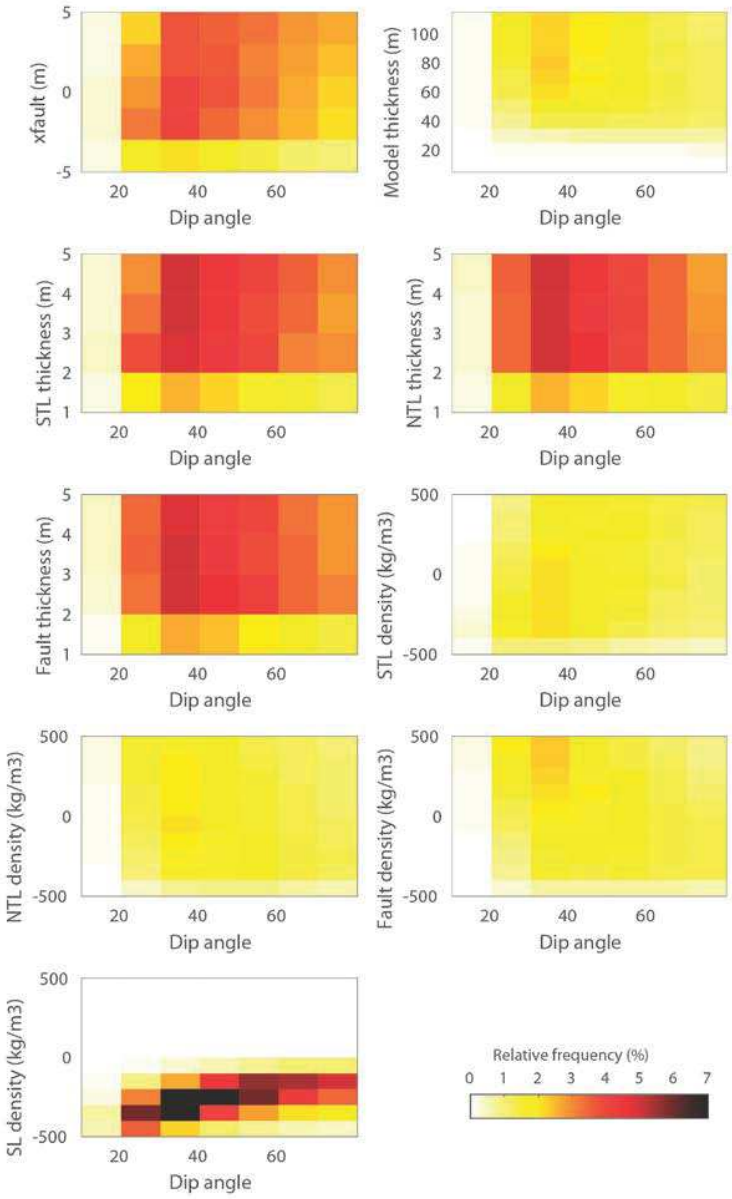

Figure S5. Relationship between the obtained dip angle in degrees and the other parameters of the density model. Note that density means density contrast with respect to density of the North deep layer (NL).

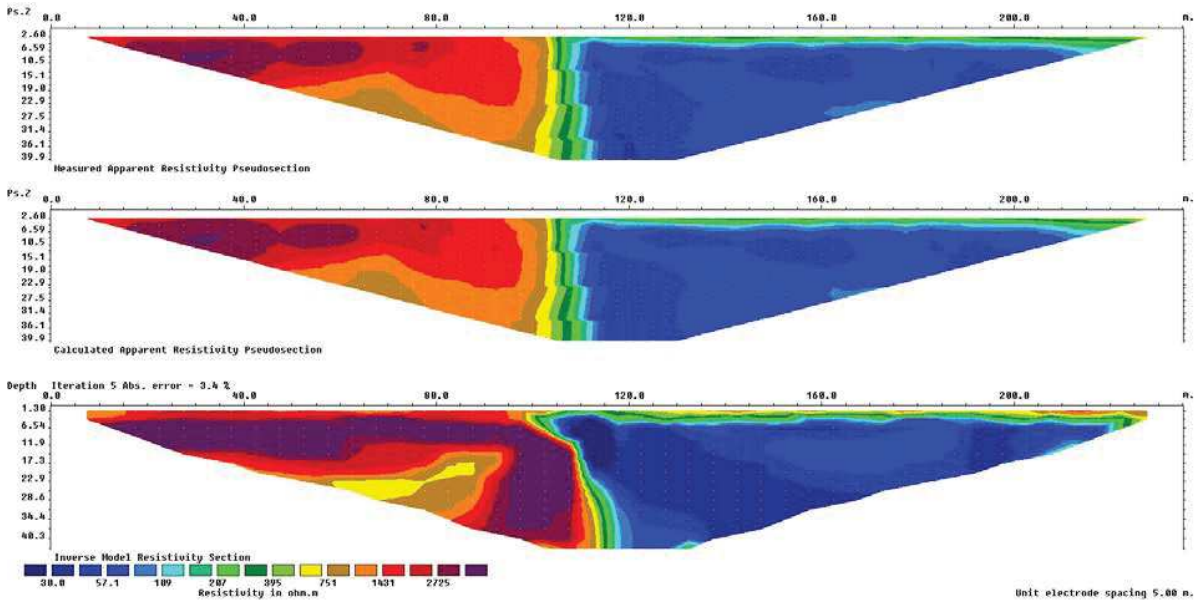

Figure S6. Res2dinv generated inverse model resistivity section for Wenner-Schlumberger array with 5m spacing (bottom). The observed (top) and calculated (middle) apparent resistivity pseudo-section are also shown.

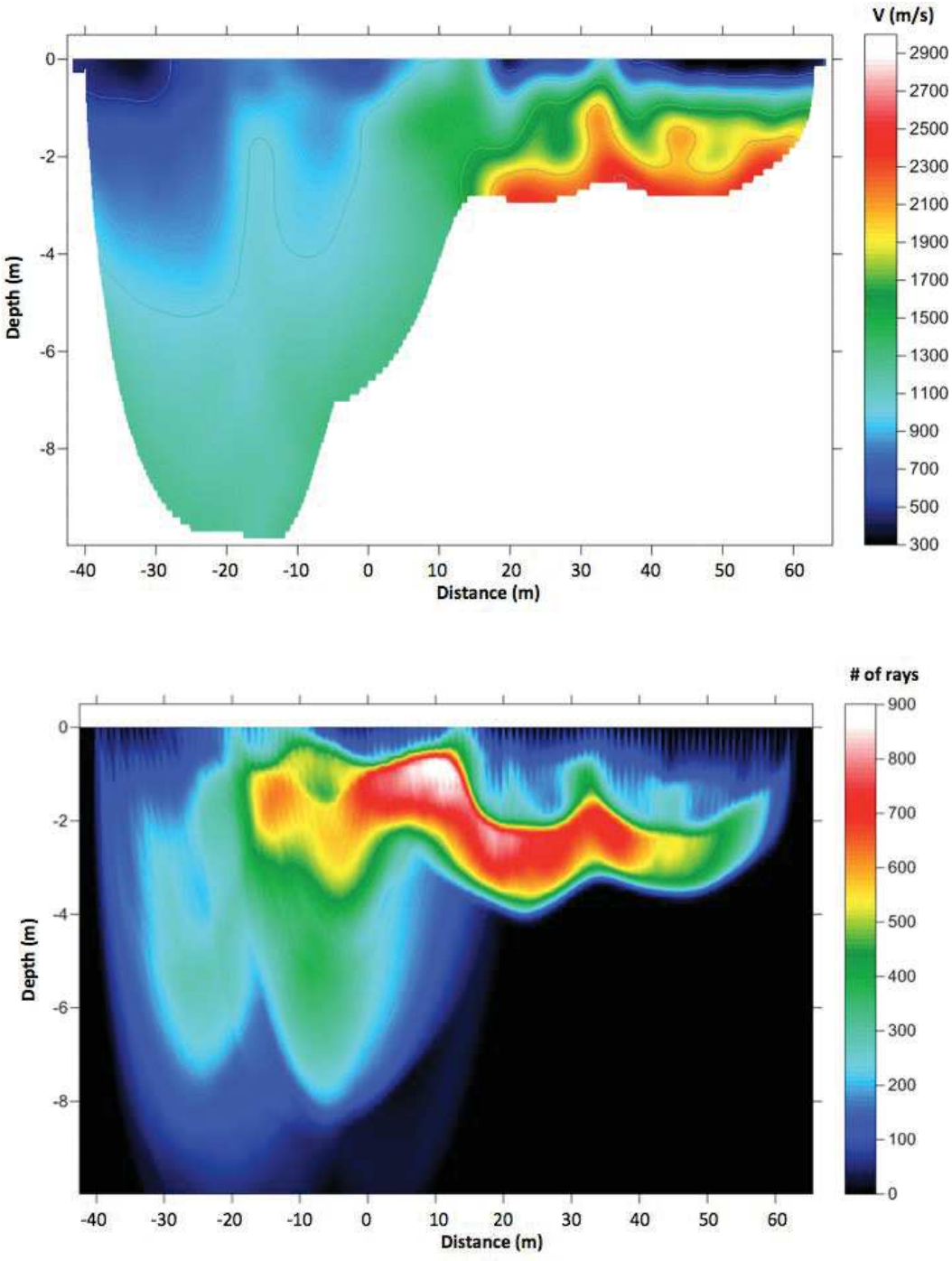

Figure S7. Top: tomographic image showing the velocity variations of both sides of the TFT using a threshold value of 100 for the ray coverage. After 20 iterations, we obtained travel-time residual of 1.41 ms corresponding to a rms value of 3.1%. Bottom: ray coverage illustrating the resolved area.

CHAPTER 5

MAIN FRONTAL THRUST GEOMETRY IN PHUENTSHOLING AND LHAMOIZINGKHA: PRELIMINARY RESULTS

5.1 Introduction

Following detailed geomorphological, paleoseismic and geophysical studies in Sarpang in south Central part of Bhutan (Berthet et al., 2014; Le Roux-Mallouf et al., 2016; Drukpa et al., 2017), we performed high resolution near-surface geophysical studies in Phuentsholing and Lhamoizingkha (Figure 5.1). The main objectives of selecting these sites are to study the geometry of frontal thrust in order to constrain the slip rate and strain partitioning pattern in the area. While little or no prior information is available for Phuentsholing area, paleoseismic trenching and geomorphological studies have been performed in Lhamoizingkha area (Le Roux-Mallouf et al., submitted).

5.2 Field work in Phuentsholing in 2016

The initial plan in March 2016 to conduct geophysical study in Lhamoizingkha area, where the geomorphological team conducted geomorphological and paleoseismic trenching, had to be changed due to reported security concerns in Lhamoizingkha area. Accordingly, we changed our study area from Lhamoizingkha to the site in Phuentsholing (Figure 5.1). The study area in Phuentsholing is located at the base of Lesser Himalayas in the sub-Himalaya Foothills. The area is made of relatively thick alluvium deposits accumulated as result of sediments brought down by the swift flowing rivers from the Himalayan mountains.

Figure 5.1: Location map showing the geophysical study area in Phuentsholing, Lhamoizingkha and Sarpang

5.2.1 List of field equipments

The following (Table 5.1) shows equipments used for geophysical data acquisition in the study area.

Table 5.1: List of geophysical equipments for geophysical field survey in Phuentsholing

Sl. No.	Equipment Types	Remarks
1	Electra resistivity meter	64 channels
2	Moho seismic equipment	48 channels
3	Scintrex CG-5 Gravimeter	

5.2.2 Site selection

Using the criteria of uplifted fluvial terraces, we selected three sites (Figure 5.2) as potential sites for geophysical investigation in Phuentsholing area. Following this, we made field visits to these sites to determine the ideal location for near-surface geophysical investigation. Of the three sites identified, we found Site 1 located to the west of Phuentsholing town and on

Figure 5.2: Three sites located using google Earth image for reconnaissance study and detailed geophysical investigation.

the left side of Amo Chhu to be most feasible. Site 2 is located outside the Bhutanese territory and Site 3 is observed to be not feasible for geophysical study due to thick alluvial cover at the frontal area (Figure 5.3).

At Site 1, notice in Figure 5.4, at least three stages of alluvial terraces are clearly visible indicating sequence of interseismic deformation. The site is located on an alluvial fan deposited by the seasonal stream that flows almost in the north-south direction. To the south it is bounded by the north-south flowing Amo Chu, which at this particular location flows in the east-west direction. As part of bridge foundation study in the area, we encountered two drill holes (Figure 5.5). Drill hole BH-01 was already completed with maximum core depth of 35 m, while drill hole BH-02 was under progress with total depth of 22 m achieved at the time of our field work. Figure 5.6 shows photo of core drills from BH-01 and BH-02. In general, the lithology of the core-log is made of disintegrated greyish quartzite up to a depth of 12.5 m and 7.5 m in BH-01 and BH-02, respectively. The subsequent layers comprises of gravels and silty sand and clay materials. However, between 13-18 m depth in BH-01, we observed a dark, non-cohesive and unconsolidated materials, which resembles fault gouge. The detailed description of drill core-log is shown in Figure 5.7. The information coming from the drill cores are used as a priori constraints for interpretation of geophysical results.

Figure 5.3: Thick alluvial fan deposit at the foothills of Site 3.

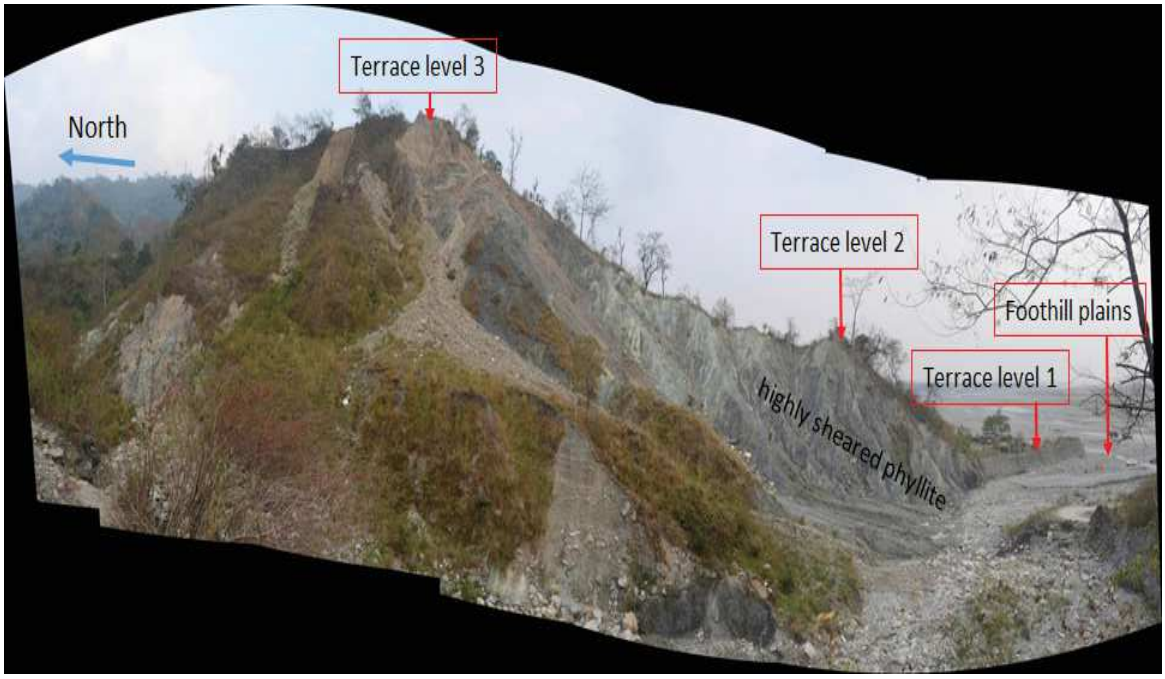

Figure 5.4: Panoramic view at site 1 showing formation of three levels of terraces as result of repeated tectonic uplift.

Figure 5.5: Location of drill bore-holes (BH-01 and BH-02) and geophysics line (yellow line) in Phuentsholing at Site 1. Inset picture shows drilling work in process at BH-02.

Figure 5.6: Drill core from BH-01 and BH-02. Red rectangle shows the dark, non-cohesive and unconsolidated materials observed between ~13-18 m at BH-01.

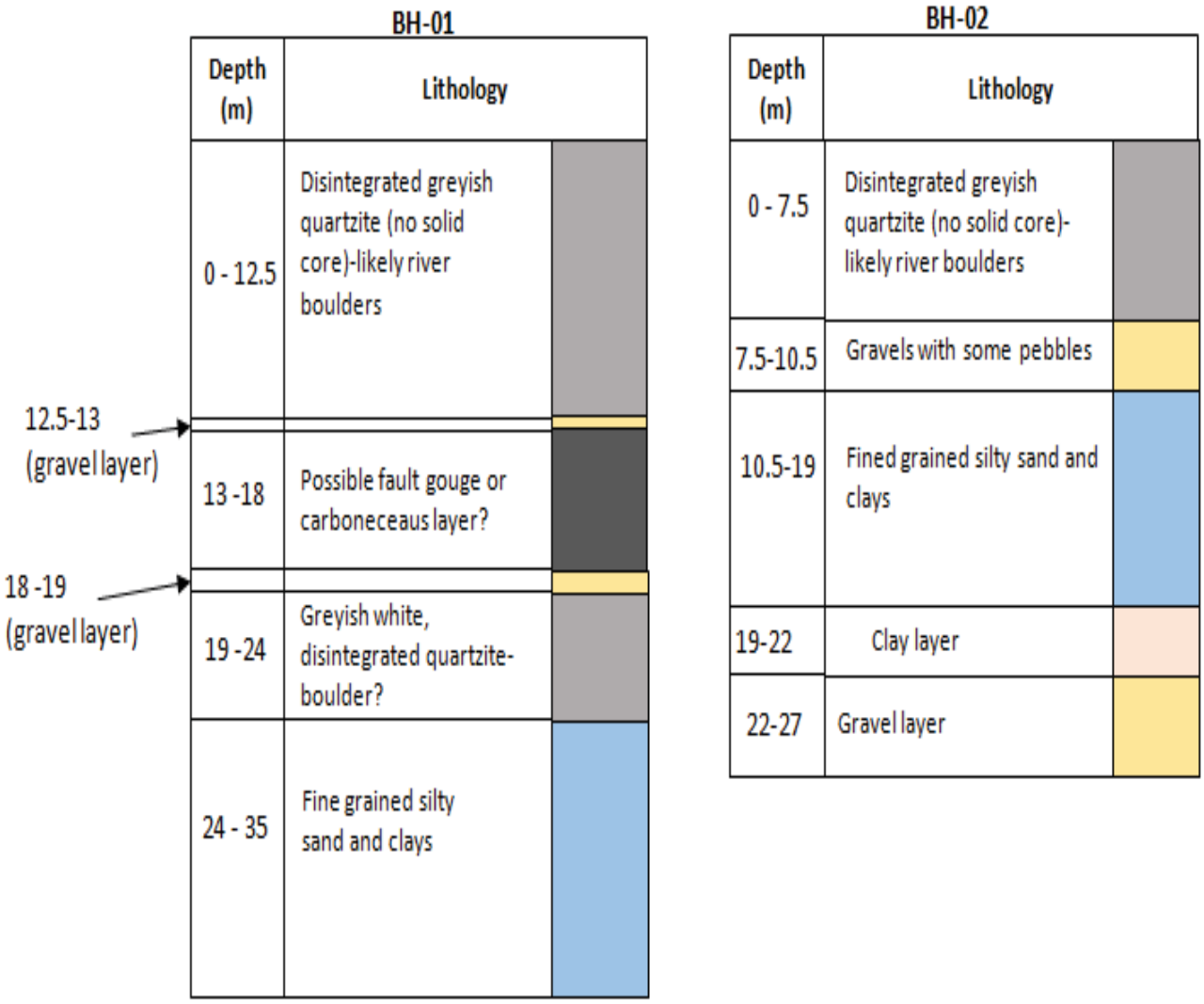

Figure 5.7: Description of core-log lithology from drill bore-holes, BH-01 and BH-02.

5.3 Geology of study area

The geology of the Phuentsholing area is composed of undifferentiated alluvium at the southern flat and low lying areas, which forms a part of the re-entrant in the area. Because of the re-entrants, Siwaliks are not recognized in the area. The MBT is not mapped in this area and it is interpreted to be underneath the Amo Chhu (aka Torsa river) (Yagi et al., 2002). North of the alluvium foothills lies the lower slope of the Bhutan Himalayas comprising mainly of meta-sediments of Buxa Formation and Shumar Formation belonging to Precambrain to Lower Cambrian.

The study area in Phuentsholing falls in a complex tectonic setting where Diehl et al. (2017) observed linear seismicity along what they termed as the mid-crustal dextral Dhubri-Chungthang Fault zone (DCF). Similarly, the Goalpara lineament (De & Kayal, 2003; Velasco et al., 2007) also extends through our site in the northwest to southeast direction (Figure 5.8). However, no evidences of surface offsets were observed in the field. This may be because of deeper depth of these structures and thick alluvial cover at the Phuentsholing site. Active faults have been recognized and mapped in Phuentsholing area by Yagi et al. (2002). Based on geomorphic features they categorized the area into four levels such as Highest, Higher, Middle and Lower surfaces (Figure 5.9). These surfaces were presumably formed according to the river flow from the mountains into the plains without any topographic gap at that time. However, at the present day these surfaces is observed to be stepping on to the south-facing foothill slope of the Bhutan Himalayas which suggests that uplift of the Bhutan Himalayas continued through the late Quaternary. Besides active faults observed by this study, several active scarps have been identified (Figure 5.9).

As observed in Sarpang and other foothill parts of the Bhutan Himalayas, the structural attitude of bedrocks in the study area show high dip angles ranging from 32-64° (Long et al., 2011)(Figure 5.10). At Site 1 in Phuentsholing area, we observed highly sheared phyllite outcrop with thin inter-layers of quartzite showing steep dip angle of 64° as shown in Figure 5.10.

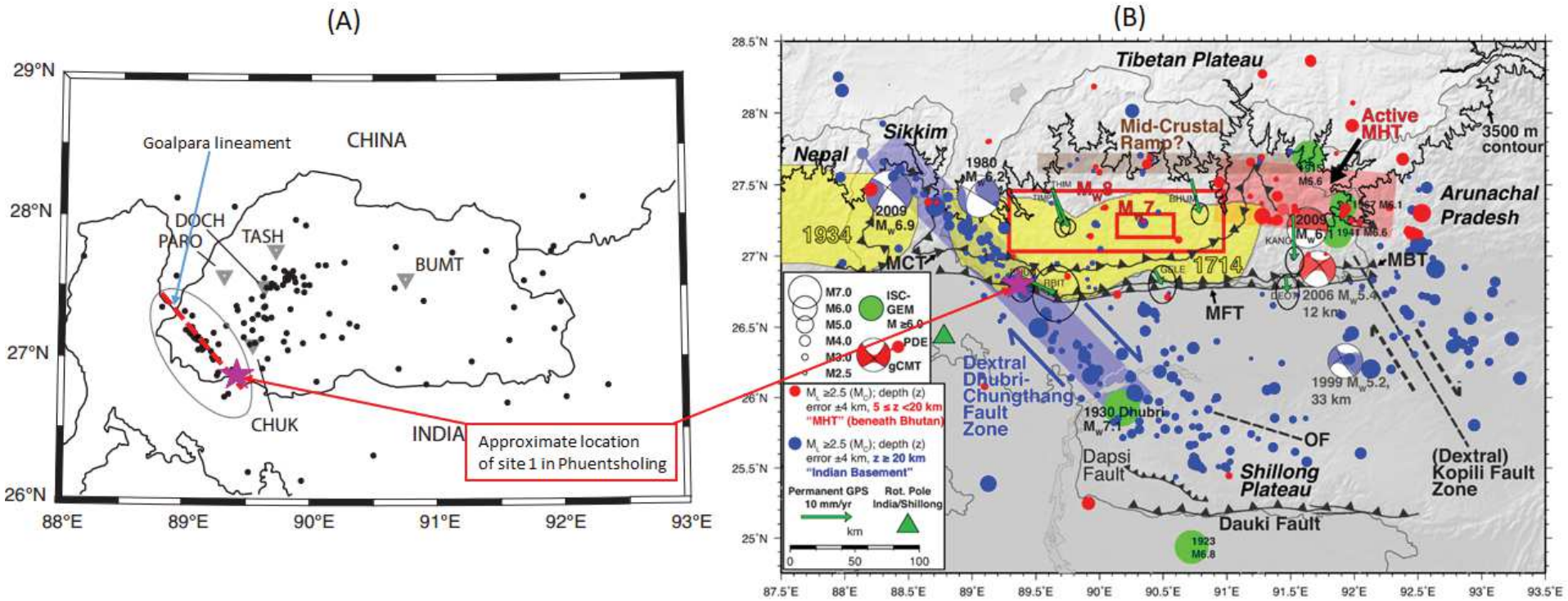

Figure 5.8: (A) Epicenter location with pattern of linear seismicity corresponding to the Goalpara lineament (Velasco et al., 2007); (B) Major active fault zones imaged by GANSSER project seismic catalog showing the prominent dextral Dhubri-Chungthang Fault zone (After Diehl et al., 2017).

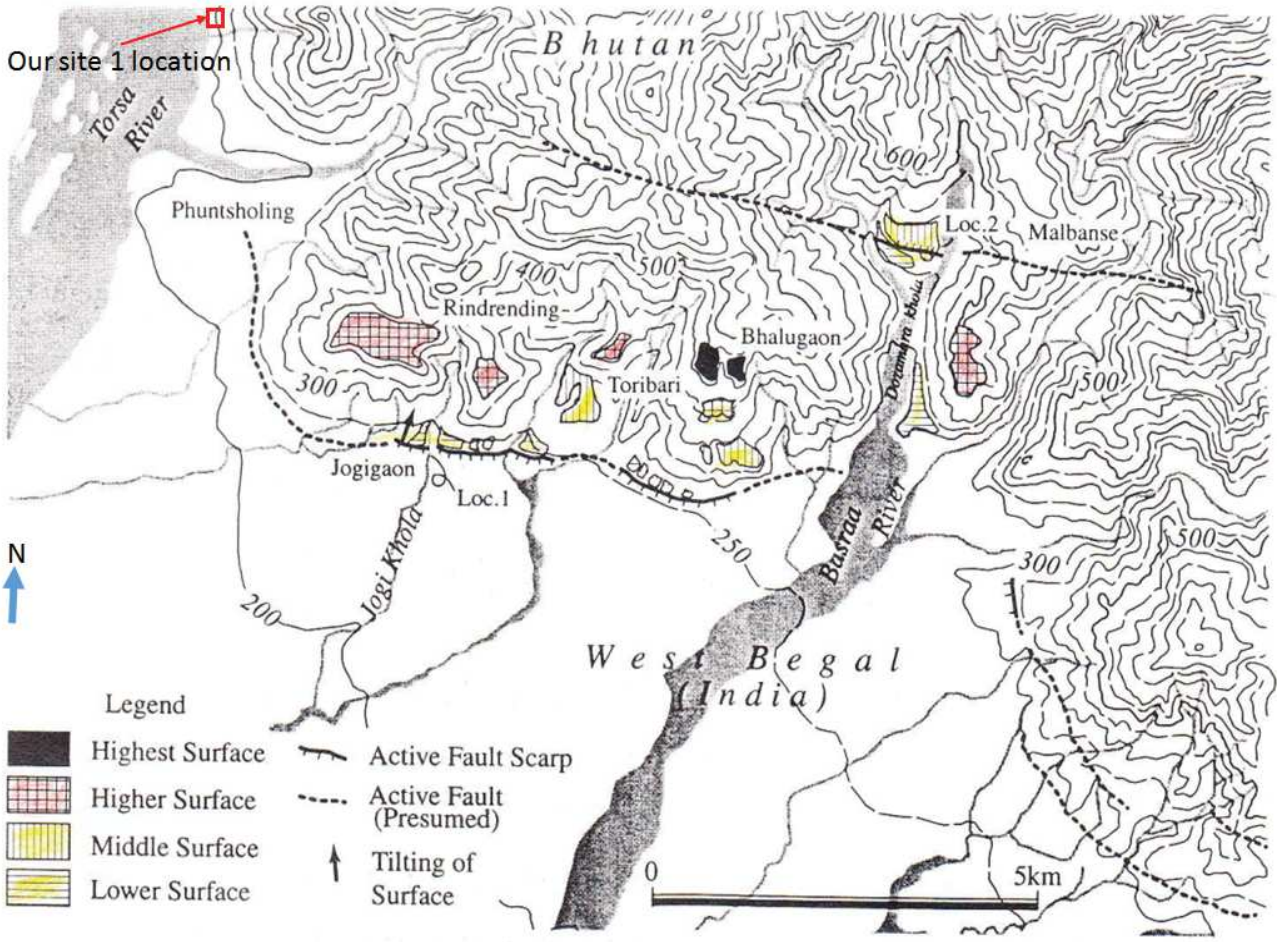

Figure 5.9: Distribution of geomorphologic surfaces and active faults. Red square shows location of our Site 1 in Phuentsholing (After Yagi et al, 2002).

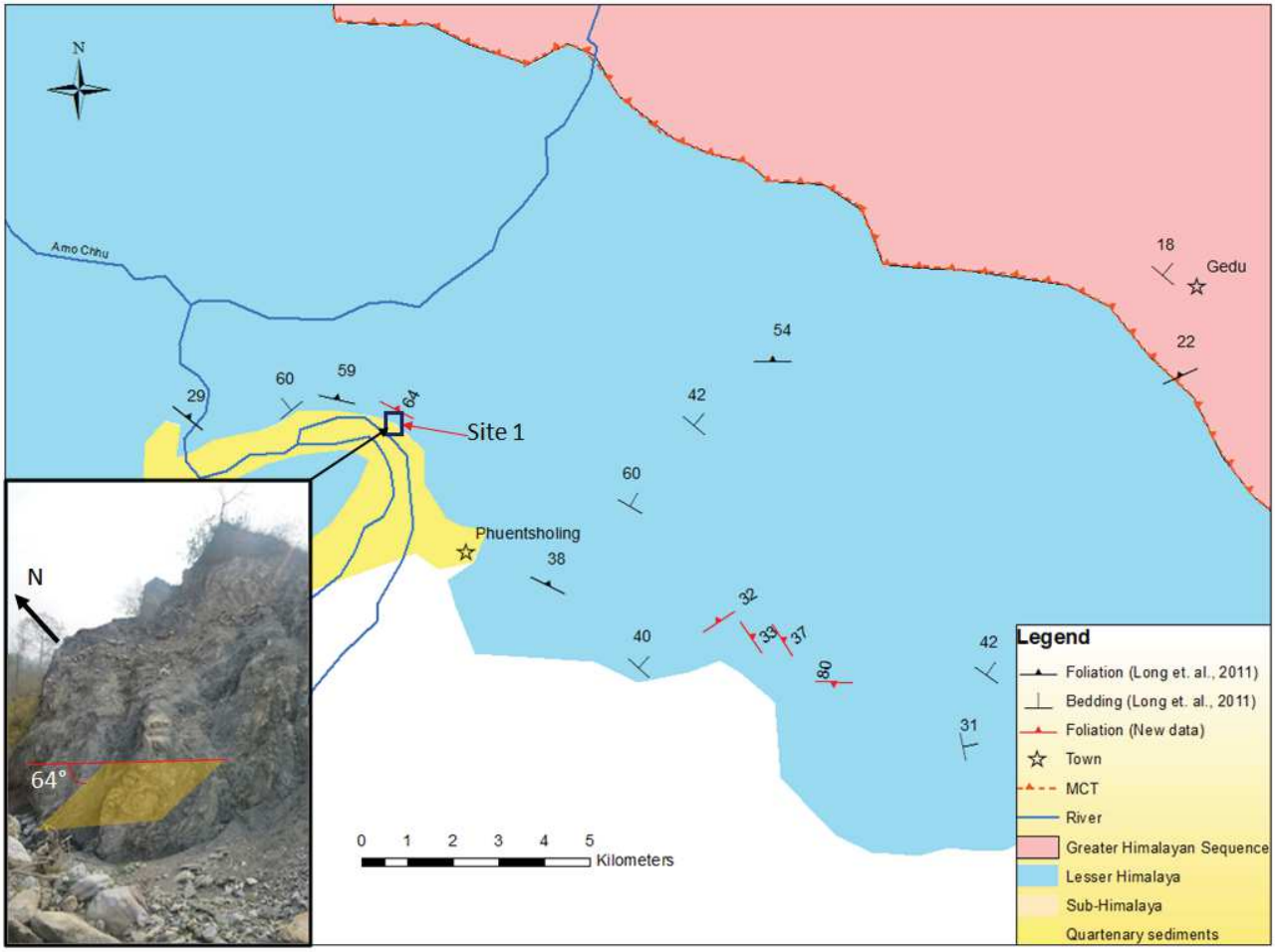

Figure 5.10: Structural attitudes of geological outcrops in Phuentsholing and vicinity area. Inset picture shows steeping dipping highly sheared phyllite in-situ exposure at Site 1.

5.4 Data acquisition

5.4.1 Electrical Resistivity and gravity data

The electrical resistivity line involving 32 electrodes (other 32 electrodes were not used due to site space constraints) with electrode spacing of 3 m corresponding to a total spread length of 93 m were used in the study area (Figure 5.11). The Dipole-Dipole and Wenner-Schlumberger geometric configuration were used to acquire resistivity data. Since the site was dry with loose alluvial materials, we performed resistivity measurements by varying the amount of current injection to select the current injection options. The following tests were performed:

- PHUN2 corresponds to resistivity data obtained using 8 mA current injection
- PHUN3 corresponds to resistivity data obtained using 15 mA current injection
- PHUN4 corresponds to resistivity data obtained using 20 mA current injection
- PHUN5 corresponds to resistivity data obtained using 5 mA current injection

The electrical resistivity survey line was aligned almost in the north-south direction, and perpendicular to the inferred location of the MFT as shown in Figure 5.11. The electrode position 1 is located towards the southern end of the profile. The resistivity line is along a relatively thick alluvial fan deposit formed by the stream that flows in the north-south direction and cross the drill borehole (BH-01) at 66-72 m along the profile.

Based on the relationship, $V = I \times R$, it can be deduced that increase in current intensity results in higher potential difference, or the resistance of a material is inversely proportional to the intensity of current injected. On the left column in Figure 5.11, resistivity sections corresponding to varying current intensity are presented. The resistivity sections generally show fairly consistent results. On the right column in Figure 5.11, the qualitative assessment of resistivity distribution by varying the current intensity is shown. The maximum resistivity value differences is observed in case of PHUN5. This suggest that lower injection of current (5 mA) compared to the reference current (PHUN2, 8 mA) results in negative differences in resistivity values, while higher amount of current injection (PHUN3, 15 mA and PHUN4, 20 mA) compared to the reference current results in positive resistivity distributions. It can be concluded that selection of appropriate current intensity is important depending on site conditions.

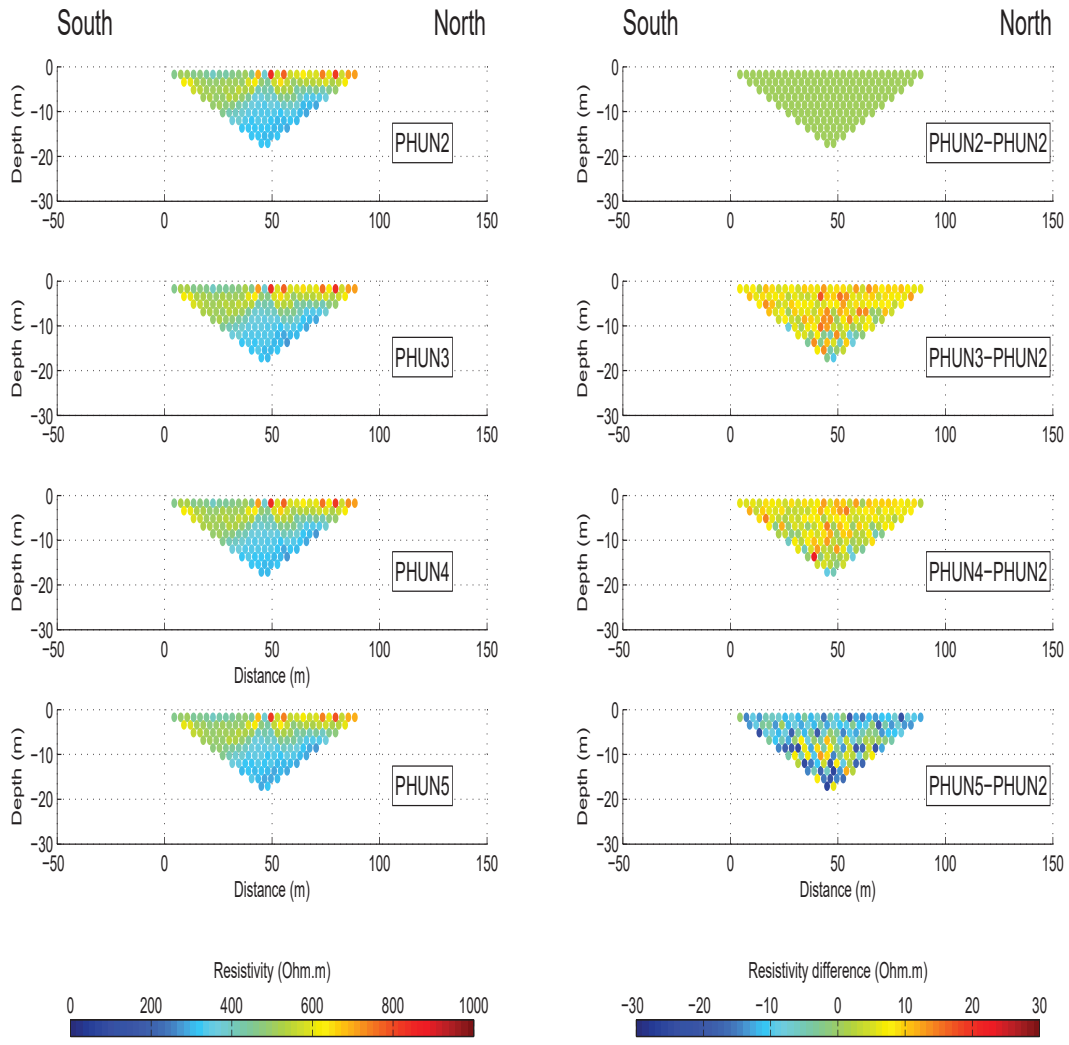

Figure 5.11: Observed Wenner-Schulumberger ERT pseudo-section with varying current intensity

Micro-gravity measurements were conducted coincident with the resistivity line (Figure 5.5). Starting from the south end, gravity measurements were made at every 6 m interval.

5.5 Data analysis

5.5.1 Electrical resistivity tomography

Unlike in Sarpang, analysis and interpretation of data from Phuentsholing site is hindered by lack of good a prior information that includes uncertainties in the location and dip angle of the fault trace on the surface, thickness of the alluvial cover, etc. The only constraints we have is from the drill bore-hole where a fault gouge resembling layer is observed in the core-log (Figure 5.6 and 5.7). Secondly due to site limitations, longer line geophysical survey could not be performed, which affected on our effort to image structures at deeper depths. Nevertheless the ERT data collected provides useful insights to study the subsurface geological structures in the area.

Irrespective of intensity of current injection, the Wenner-Schlumberger provided consistent data but dipole-dipole array was slightly affected by noise due to difficulty in injecting current especially at higher datum levels or higher n-factor (i.e ratio of the distance between C1-P1 electrodes and P1-P2 dipoles). Using res2dinv software, a tomographic inversion of the resistivity data is performed to determine the subsurface resistivity distribution in the area. Prior to execution of the inversion process, the elevation information are incorporated in the observed data. The dipole-dipole and Wenner-Schlumberger ERT pseudo-sections with different current intensity injection are presented in Figure 5.12, 5.13, 5.14 and 5.15. Notice that all the resistivity pseudo-sections show consistent results except in case of dipole-dipole section with current injection intensity of 20 mA (Figure 5.14) where we observed greater extent and more pronounced low resistivity zone at 10-15 m depth. The Dipole-Dipole geometric configuration returns a rooot-mean-square (RMS) error much higher than the Wenner-Schlumberger array due to low signal-to-noise ratio of the Dipole-Dipole method. Thus only the Wenner-Schlumberger is used in the subsequent stochastic inversion process. The resistivity pseudo-sections show marked electrical resistivity contrast between 54-57 m distance along the profile at a depth of 6-8 m. The top layer up to 4-6 m show relatively high resistivity values which correlates well with the drill core-log showing dry alluvial deposits with quartzite boulders at the upper layer. The ERT pseudo-sections also consistently show a

steeply dipping, sharp interface which may be interpreted as the MFT in the area.

Considering the location of fault with respect to the fault gouge observed in the drill core and subsurface resistivity distribution from ERT, the dip angle of the MFT could depend on the xfault as shown in Figures 5.12 to 5.15. If xfault is located further away to the south of the bore-hole, the MFT displays a gentle dip angle of ca. 20° and gradually steeping at depth. On the contrary, if xfault is located close by the drill bore-hole, the MFT favors a steeper dip angle of ca. 60°.

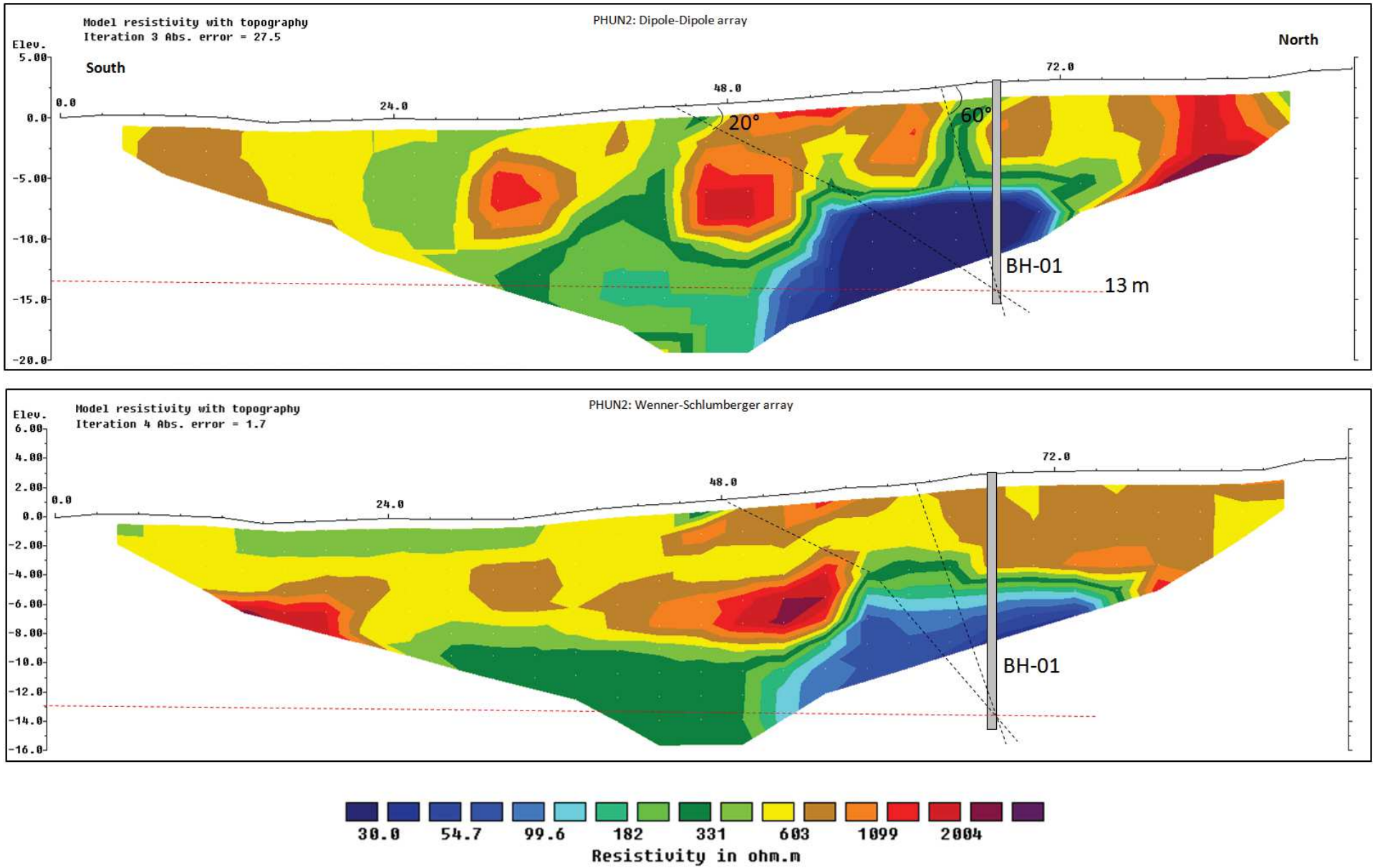

Figure 5.12: Dipole-Dipole (top) and Wenner-Schulumberger (bottom) ERT pseudo-sections obtained using 8 mA current injection.

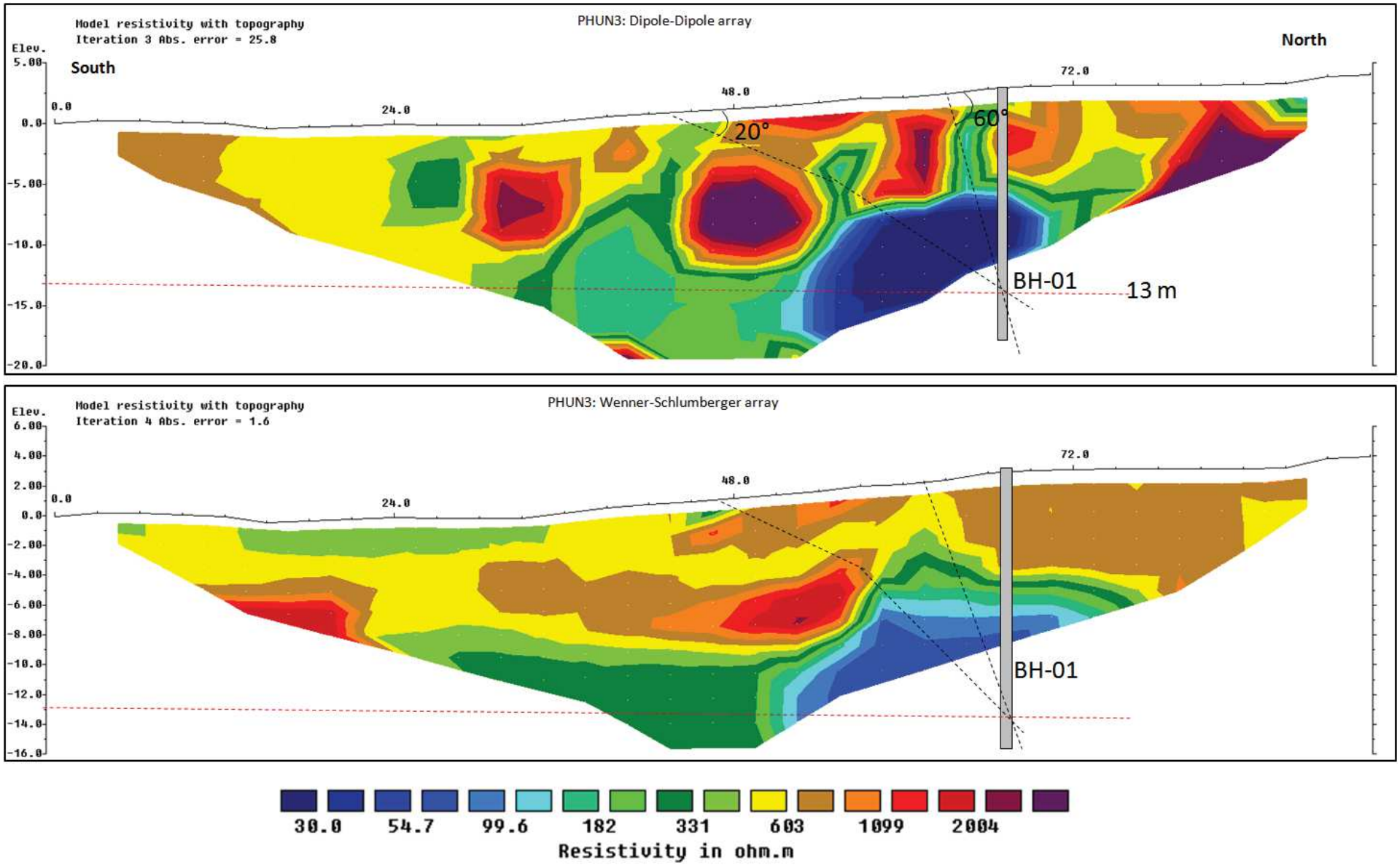

Figure 5.13: Dipole-Dipole (top) and Wenner-Schulumberger (bottom) ERT pseudo-sections obtained using 15 mA current injection.

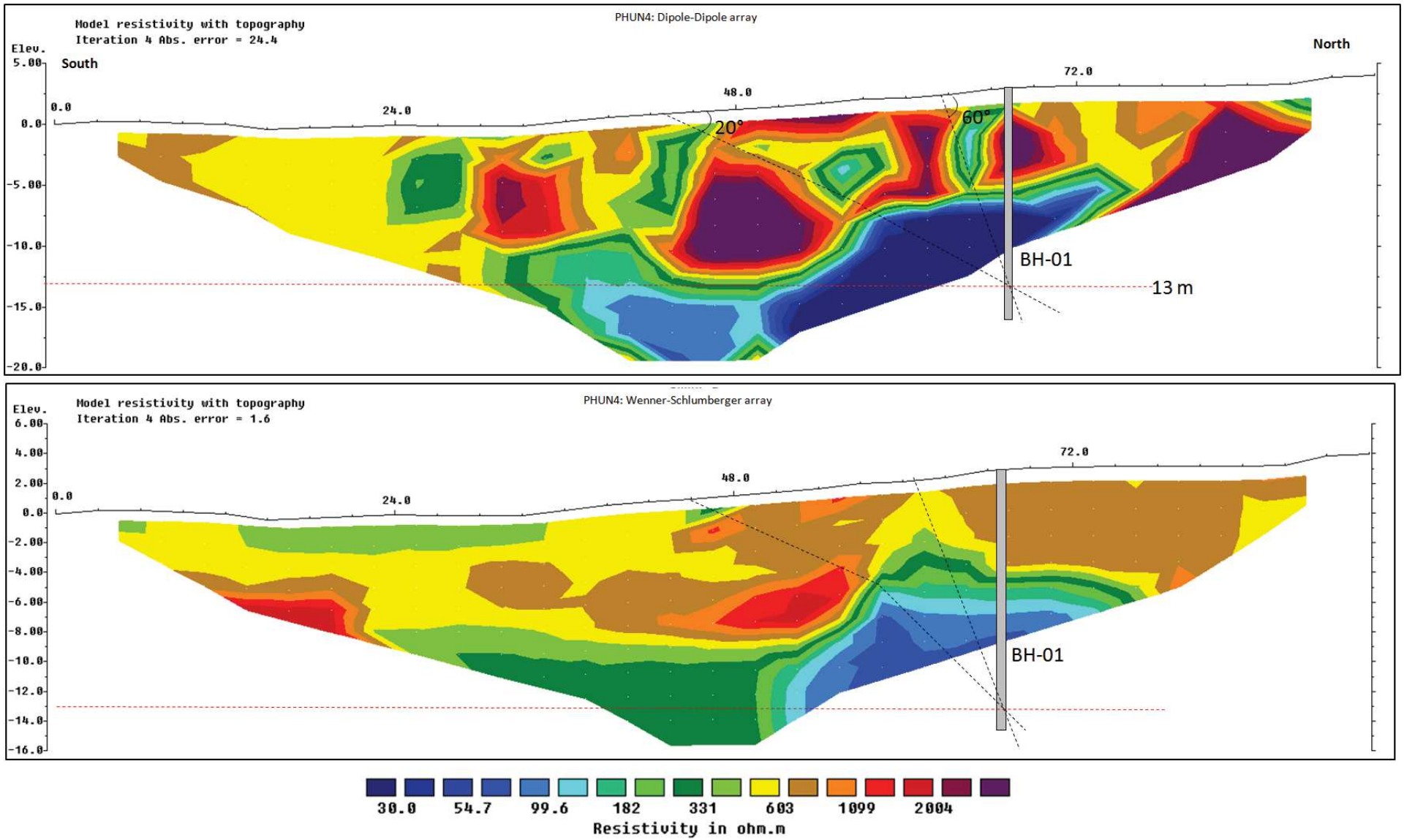

Figure 5.14: Dipole-Dipole (top) and Wenner-Schulumberger (bottom) ERT pseudo-sections obtained using 20 mA current injection.

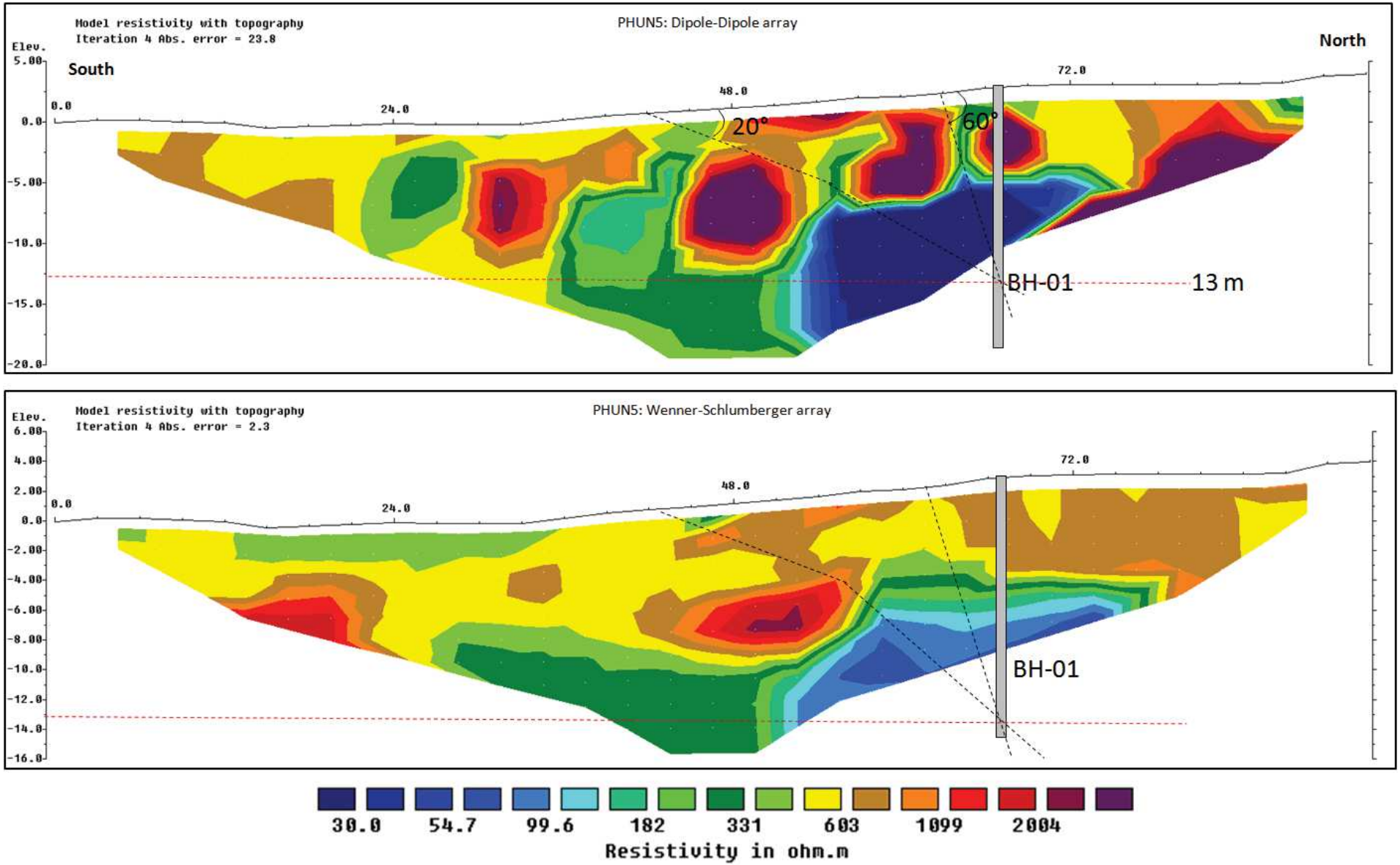

Figure 5.15: Dipole-Dipole (top) and Wenner-Schulumberger (bottom) ERT pseudo-sections obtained using 5 mA current injection.

5.5.2 Gravity

Using GravProcess software (Cattin et al., 2015), network adjustment was performed and topographic effect was corrected using accurate elevation data collected by leveling method along the profile and assuming a constant density of 2670 kg/m^3. The instrument drift correction was performed as shown in Figure 5.16. A regional trend of 0.0658 μGal/m deduced from Hammer et al. (2013) is subtracted from the observed gravity data. The final data set consist of 20 corrected (drift, elevation and trend) gravity measurements showing characteristic variations along the profile (Figure 5.16). Notice that transition of gravity readings occur around 30-35 m that could be representative of subsurface geological structures. Further the northward incremental decrease in gravity readings suggests higher density materials to the south and lower to the north. As shown in Figure 5.16 (c) the drill bore-hole (BH-01) is located at $\sim$ 66-72 m. Taking tangent of fault dip angle ranging from 10°-60° and estimated horizontal distance of $\sim$ 24 m between the bore-hole and inferred location of the fault on the surface deduced from resistivity pseudo-section, the drill hole is projected to intersect the fault at depths of 4 m to 42 m assuming constant dip angle of the fault.

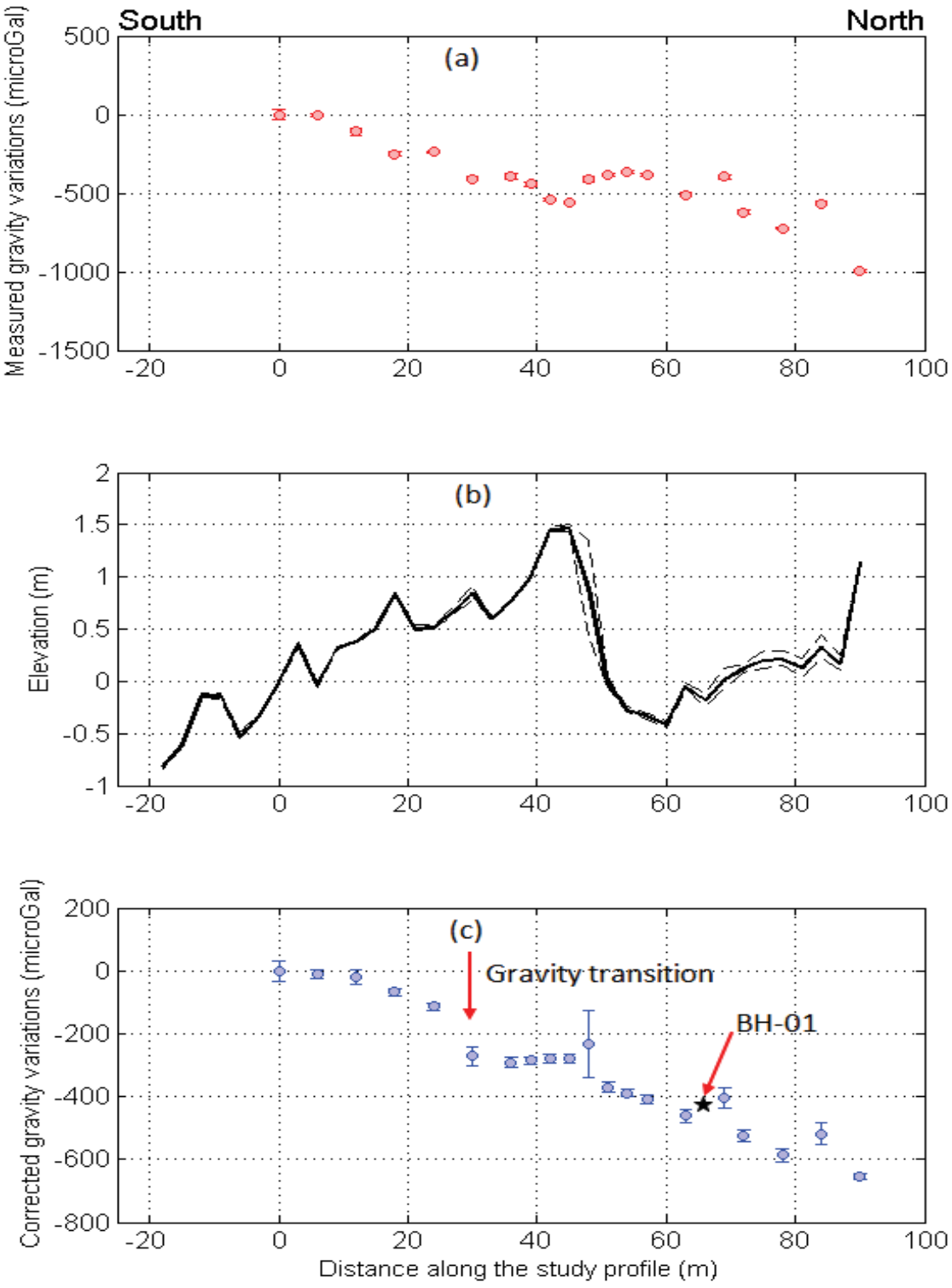

Figure 5.16: Measured gravity data (a), elevation (b) and topographic corrected gravity variations along the profile (c). The drill bore-hole (BH-01) is located between 66-72 m along the profile.

5.6 Inversion approach

The stochastic inversion approach used in Sarpang has been applied to the observed electrical resistivity and gravity data from Phuentsholing to study the geometry of MFT in the area. Similar to Sarpang (Drukpa et al., 2017), a simplified geometry is considered and each model is associated with only five bodies including a south (STL) and north (NTL) top layers, a south (SL) and north (NL) shallow layers and a fault layer (Figure 5.17). However, it should be noted that unlike in Sarpang where we have robust a priori information, in Phuentsholing study area, the only a priori information is from the drill core-log. Accordingly we assumed a range of parameters and tested as the follows:

- the location of the fault on the surface (xfault) is assumed to be anywhere between -100 to 100 m along the profile based on geomorphological observations on the surface,
- thickness of the fault ranging between 2-8 m considering the fault thickness of ∼5 m estimated from the drill core-log,
- the dip angle of the fault ranging between 10°-80° based on dip angle measured on the in-situ bedrock at the front and steep dip angle observed in the ERT pseudo-sections,

On the basis of the above simplified geometry formulation, a set of model results for a given dataset consists of 10 parameters estimation that include either the resistivity or density of each body as well as the thickness of layers, the fault location and the fault dip angle. A priori parameters ranges for resistivity values are obtained from preliminary deterministic inversion using Res2dInv (Loke & Barker, 1996). For gravity data analysis, a priori range of density contrasts between NL and the other bodies range between -1000 and 1000 kg/m^3.

5.6.1 Results

Electrical Resistivity Tomography

The frequency histogram in Figure 5.18 and Figure 5.19 does not show any preferable dip angle of the fault. Similarly, the bivariate frequency histogram (Figure 5.20) shows no trade-off between the dip angle and other electrical parameters. However, the stochastic inversion outputs a fault zone with resistivity value of ∼800 Ω.m and thickness of ca. 4m. The top layers, NTL and STL, show resistivity value of ∼800 Ω.m indicating no resistivity contrast at the top layers and thus the uncertainty in constraining the fault geometry at this shallow

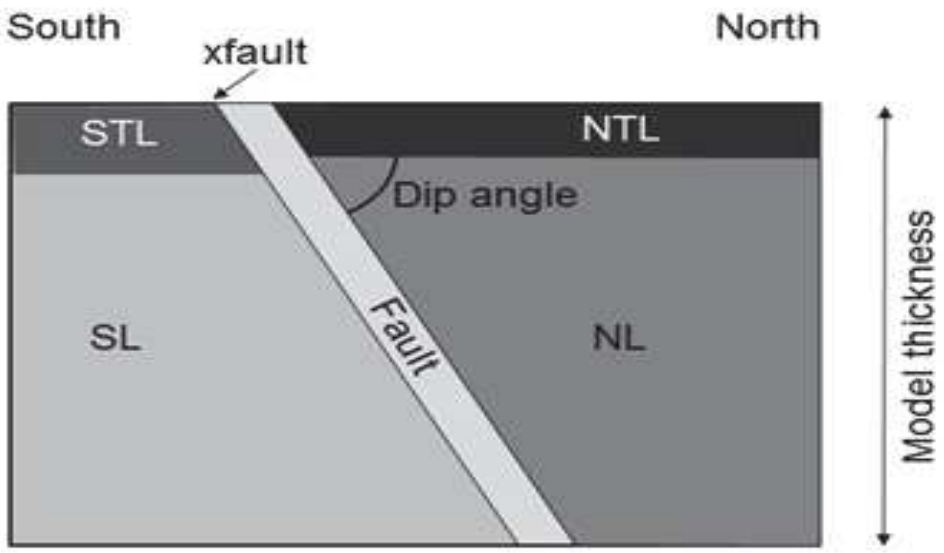

Figure 5.17: Geometry of the model used in the stochastic inversion. STL - South Top layer, NTL - North Top Layer, SL - South Layer and NL - North Layer. xfault is the possible location of the fault on the surface with respect to fault gouge observed in bore-hole at ca. 13-18 m depth and resistivity distribution in the subsurface. Model thickness is associated with the thickness investigated by each geophysical method.

level. The thickness of STL and NTL layers are not well constrained but is estimated to be 10-20 m thick. The details of others parameters are presented in Table 5.2. On the other hand, prevalence of high resistivity contrast between layers, NL, with $\sim$2800 Ω.m and $\sim$200 Ω.m for SL , allow the geometry of the fault at the deeper level, up to a depth of 15m, to be better constrained.

The combined forward modeling, based on fit between the observed and calculated resistivity, and the stochastic inversion method yield a fault geometry shown in Figure 5.21. Notice that, in general, the maximum discrepancy between the observed and calculated data is being observed at the shallow and northern deeper level of the pseudo-section. The red rectangle in Figure 5.21 on the model geometry indicates the location of the borehole, BH-01, where presence of fault gouge in the drill core between depths of 13-18 m show that the drill borehole possibly intersected the fault at this location.

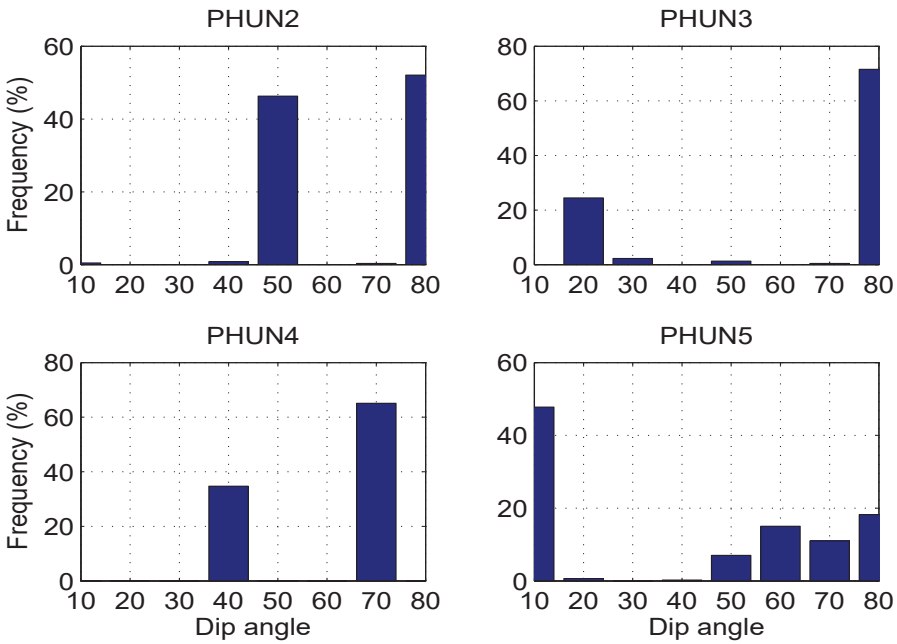

Figure 5.18: Distribution of MFT angle from ERT sections using Wenner-Schulumberger array with different amount of current injection

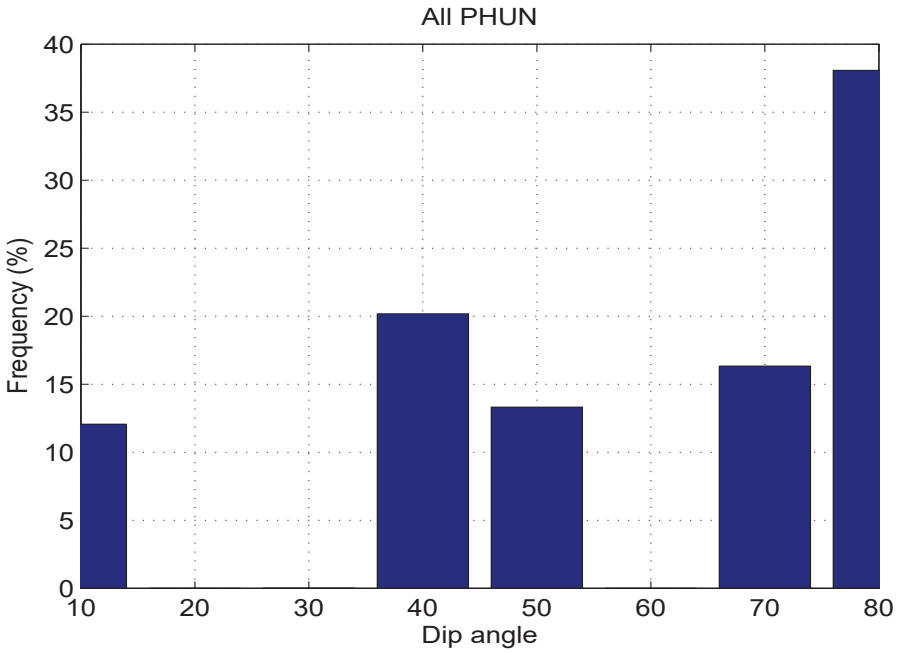

Figure 5.19: Distribution of MFT angle from Wenner-Schlumberger ERT sections by combining PHUN2, PHUN3, PHUN4 and PHUN5 shown in Figure 5.19

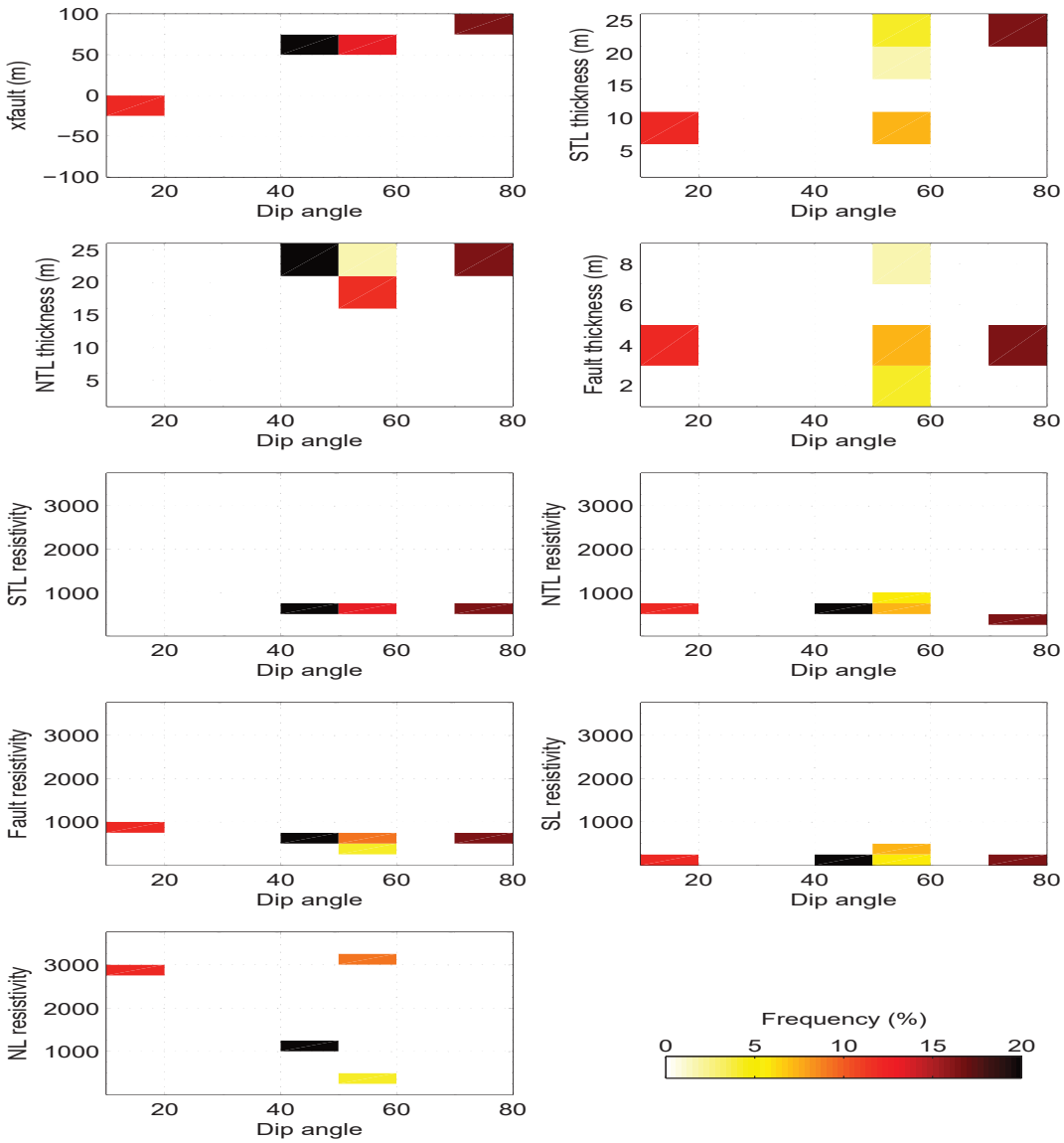

Figure 5.20: Bivariate frequency histograms between dip angle and other parameters of the ERT model obtained using Wenner-Schulumberger array

Table 5.2: Inversion results. The parameter values are associated with the most highest relative frequency model. The associated uncertainties are indicated in bracket. Uncertainties on each parameter are given by the full width at half maximum. The symbol '-' means no constraint has been obtained.

Parameter	**Range**	**Posterior value**	
		Wenner-Schlumberger	Gravity
Geometry			
xfault	[-100 100]	60 [-20 100]	20 [-20 60]
Depth of investigation (m)		15	80
STL thickness (m)		7.5 [5 25]	-
NTL thickness (m)		22 [15 25]	-
Fault thickness (m)		4 [2 8]	-
Fault dip angle (degree)	[10 80]	70 [40 80]	20 [15 40]
Electrical resistivity			
STL resistivity (Ω.m)		800[500 1000]	-
NTL resistivity (Ω.m)		800 [500 1000]	-
Fault resistivity (Ω.m)		600[500 1000]	-
SL resistivity (Ω.m)		200[100 500]	-
NL resistivity (Ω.m)		1000[500 3000]	-
Density contrast with respect to layer NTL			
STL density contrast (kg/m3)	[-1000 1000]	-	-800[-1000 200]
NTL density contrast (kg/m3)	[-1000 1000]	-	0[-800 200]
Fault density contrast (kg/m3)	[-1000 1000]	-	0[-800 500]
SL density contrast (kg/m3)	[-1000 1000]	-	700[400 1000]

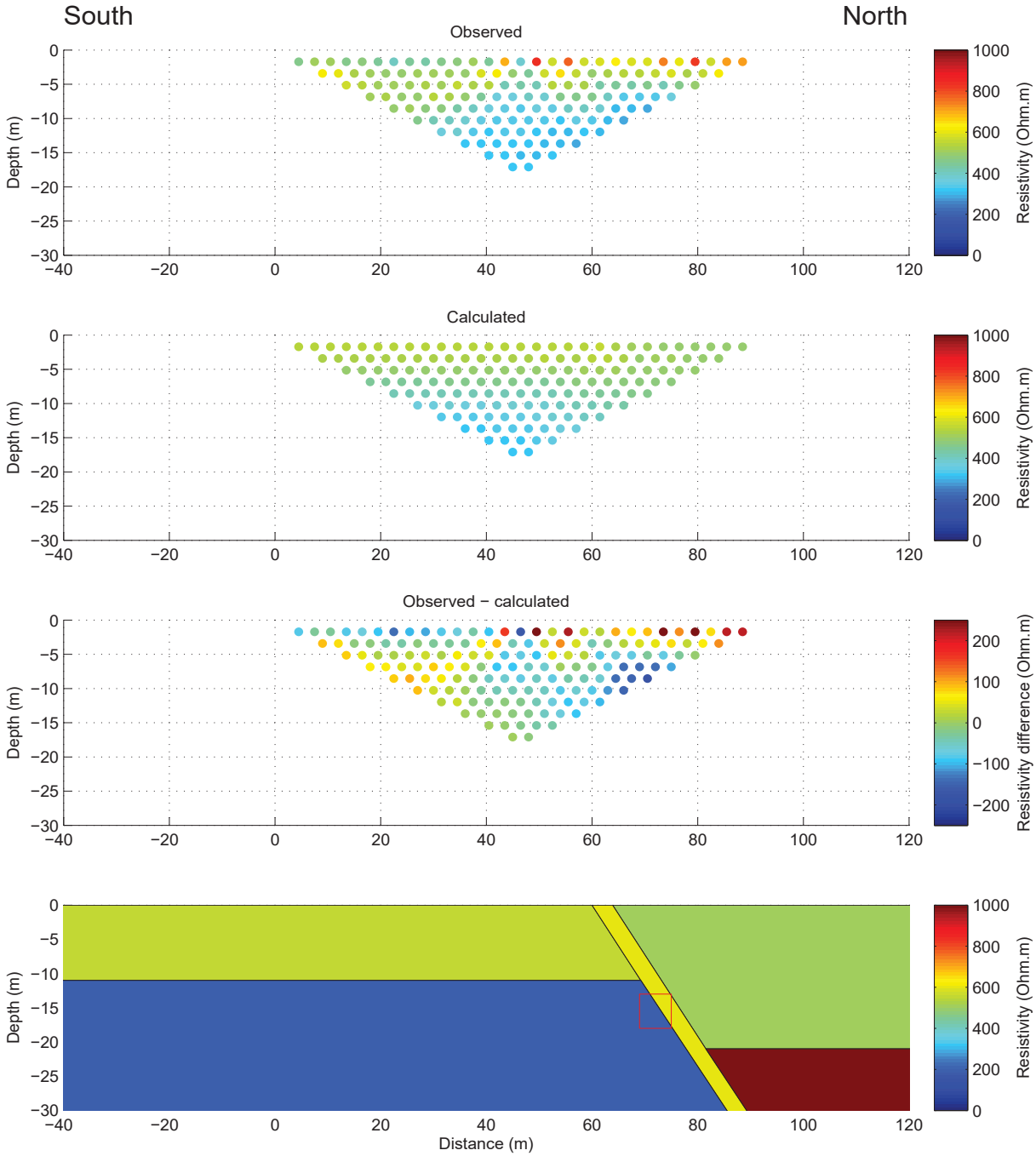

Figure 5.21: Observed and Calculated Wenner-Schlumberger array and the optimal misfit between Observed and calculated ERT sections that correspond to obtained MFT geometry and petro-physical characteristics. The red rectangle in the model section indicates the location of drill borehole, BH-01.

Gravity

To obtain good fit between the observed and calculated gravity measurements (Figure 5.22), the model requires higher density materials at the foot wall of the MFT in the south vis-à-vis the hanging wall on the northern side. A short wavelength decrease in gravity measurement is observed at around 38-40m along the profile which may be attributable to density contrast between the top layers, STL and NTL. However, the longer wavelength south-north decrease in the gravity observations may be associated to density contrast of the deeper layers, for instance, the SL and NL layers. The red rectangle in Figure 5.22 indicates the location of the borehole, BH-01. However, in case of Figure 5.22, the a priori drill bore-hole information is not incorporated in the inversion process.

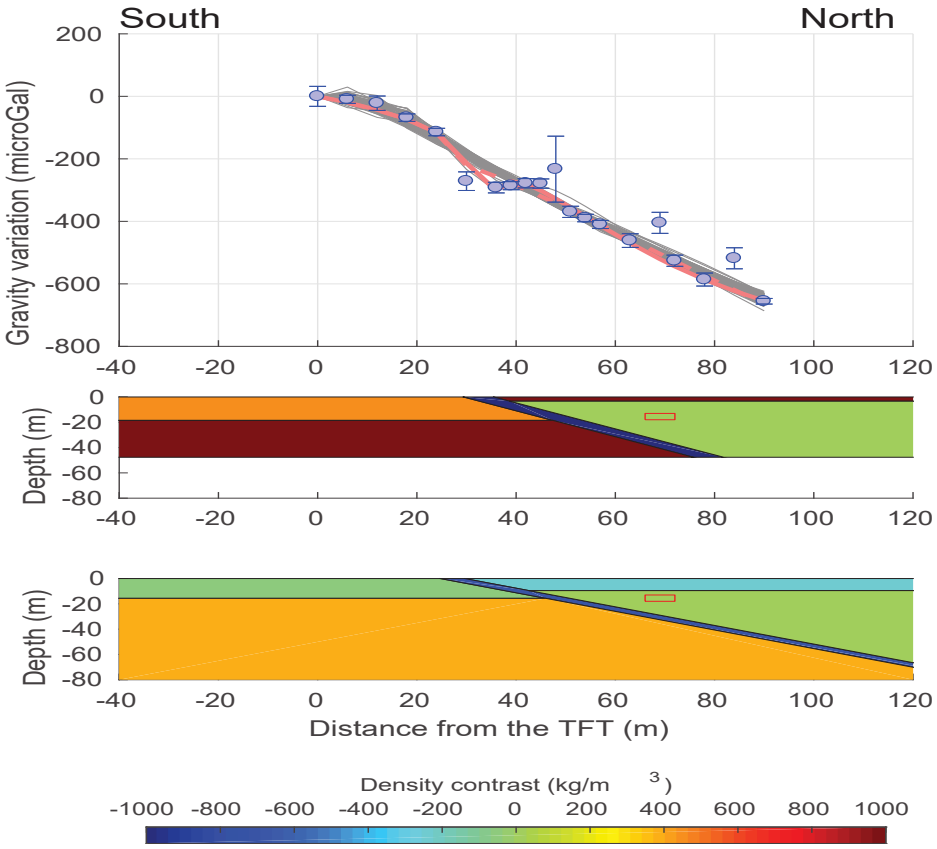

Figure 5.22: Comparison between observed (blue circles) and calculated (dark green lines) gravity variations along profile line for 100 best fitting models (top); Density contrast models without drill borehole information but with different SL and NL thickness(Bottom).

Figure 5.23 represents a frequency histogram obtained from the stochastic inversion process that favors a shallow MFT dip angle of ca. 20°. The bivariate frequency histogram (Figure 5.24), in general, favors a lower MFT dip angle of ca. 20° irrespective of thickness and density of the layers used in the model. However, exception is noted whereby decrease in the density of SL layer corresponds to gradual increase in the dip angle of the MFT. By and large, as indicated in Figure 5.24, the gravity measurement is unable to constrain other parameters such as the thickness and the density of the layers, which remain poorly resolved.

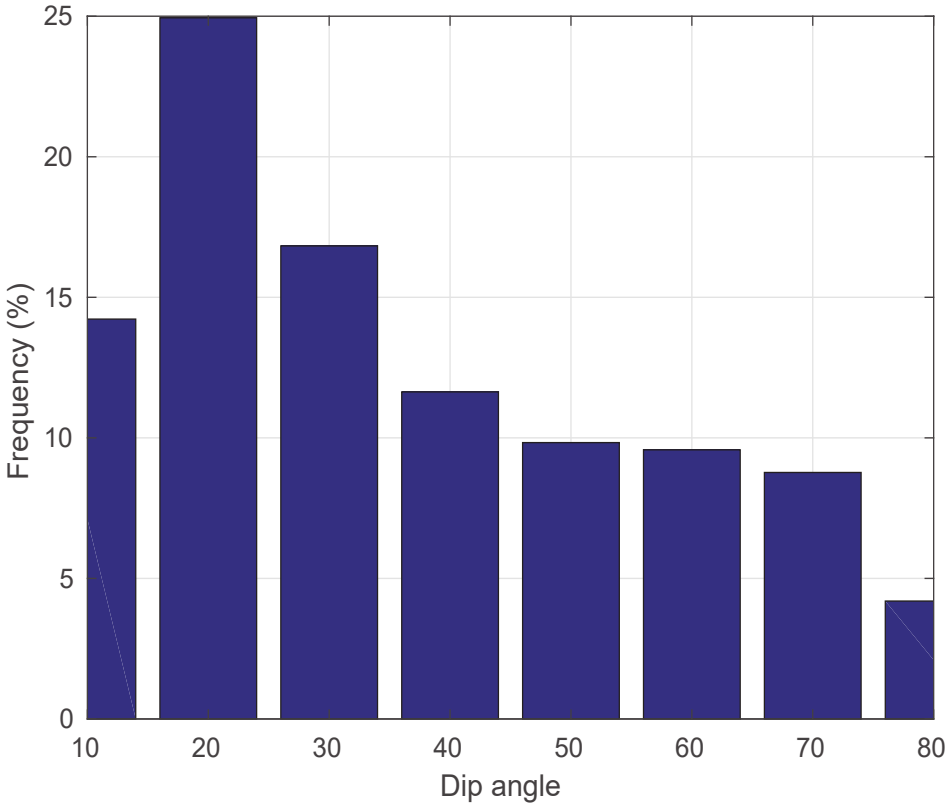

Figure 5.23: Distribution of MFT dip angle from gravity measurements without incorporating bore-hole information in the inversion process.

The model geometry with incorporation of drill bore-hole information is displayed in Figure 5.25. In contrast to the model without drill bore-hole information, the inclusion of drill bore-hole information (location of drill hole indicated by red rectangle) in the inversion process show a best-fit model that has the following characteristics:

- High density contrast between the foot wall and the hanging wall shows two sets of fault dip angle model as shown in Figure 5.26. One set favors a lower MFT dip angle of ca. 20° and the other set favors a high dip angle of ca. 70°. The later is comparable

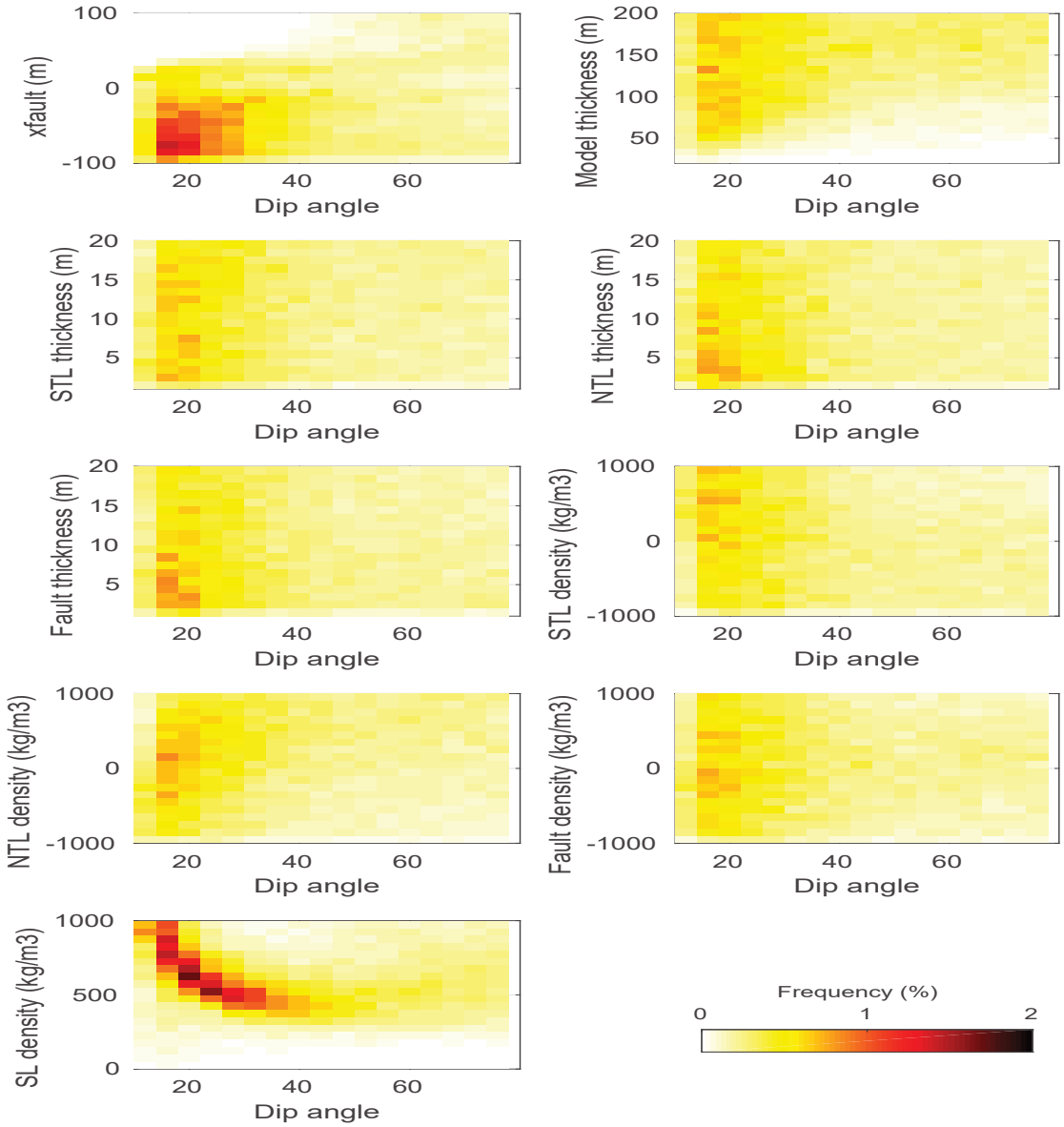

Figure 5.24: Relationship between the obtained dip angle and the other parameters of the density model. Note that density means density contrast with respect to density of the North top layer.

with the results obtained from ERT showing steep dip angle of the MFT.

- Comparatively thicker fault zone characterized by density similar to the STL layer and high density thin NTL layer.
- The model with relatively lower density contrast between the foot wall and hanging wall requires lower density but comparatively thicker NTL layer and exclusion of the STL layer as well relatively higher MFT dip angle.
- the relationship between obtained dip angle and other parameters (Figure 5.27) are similar to ones obtained in Figure 5.25 except here there is clear trade-off between the xfault and dip angle of the MFT as shown in Figure 5.27. Other parameters such as the thickness and the density of the layers remain poorly resolved.

Over all the gravity inversion result show a clear trade-off between density contrast and dip angle of the fault i.e the higher the density contrast, the shallower the dip angle of the fault and vice-versa (Figure 5.25).

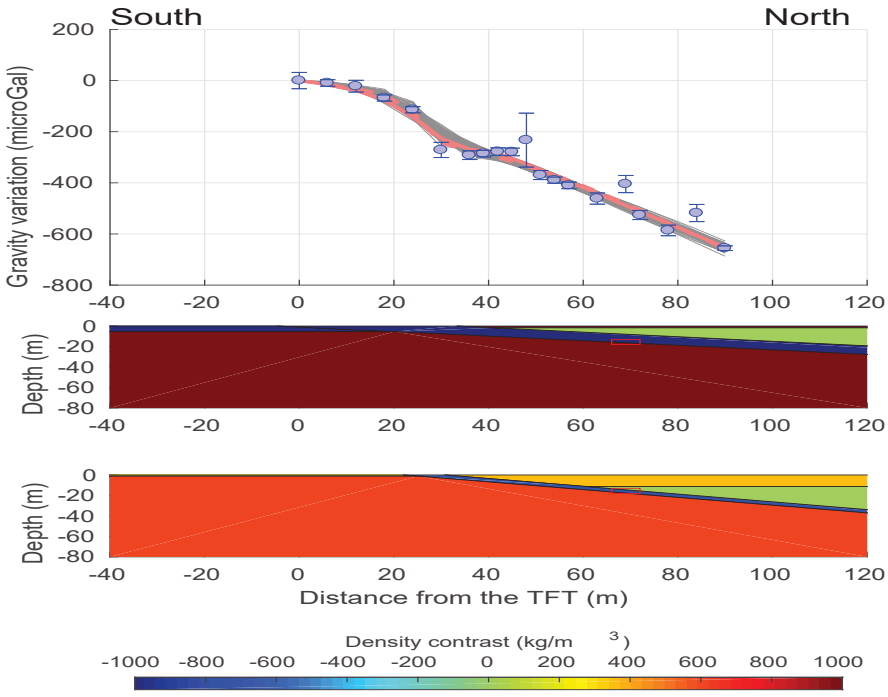

Figure 5.25: Comparision between observed (blue circles) and calculated (dark green lines) gravity variations along profile line for 100 best fitting models (top); Density contrast models with drill bore-hole information and with varying SL and NL thickness(bottom).

5.6.2 Discussion and conclusions

Based on the results of the stochastic inversion method performed on the near-surface geophysical data from Phuentsholing area, we present here *preliminary* constraints on the geometry of the MFT.

From the geomorphological observations described above, at least three levels of terraces were observed at the site in Phuentsholing. Drill core-log shows possible fault gouge layer between 13-18 m depth in BH-01. The electrical resistivity tomography performed in the area shows certain level of resistivity contrast between different interfaces, thereby indicating the suitability of resistivity method to study the fault geometry. However, relatively thick deposit of alluvial materials at the top layer hinders proper constraining of the fault geometry. The stochastic inversion procedure shows a MFT dip angle in the range of 40-70° with the obtained geometry better constrained at deeper depths due to prevalence of high resistivity contrast between the SL and NL layers. The ERT section and stochastic inversion results are

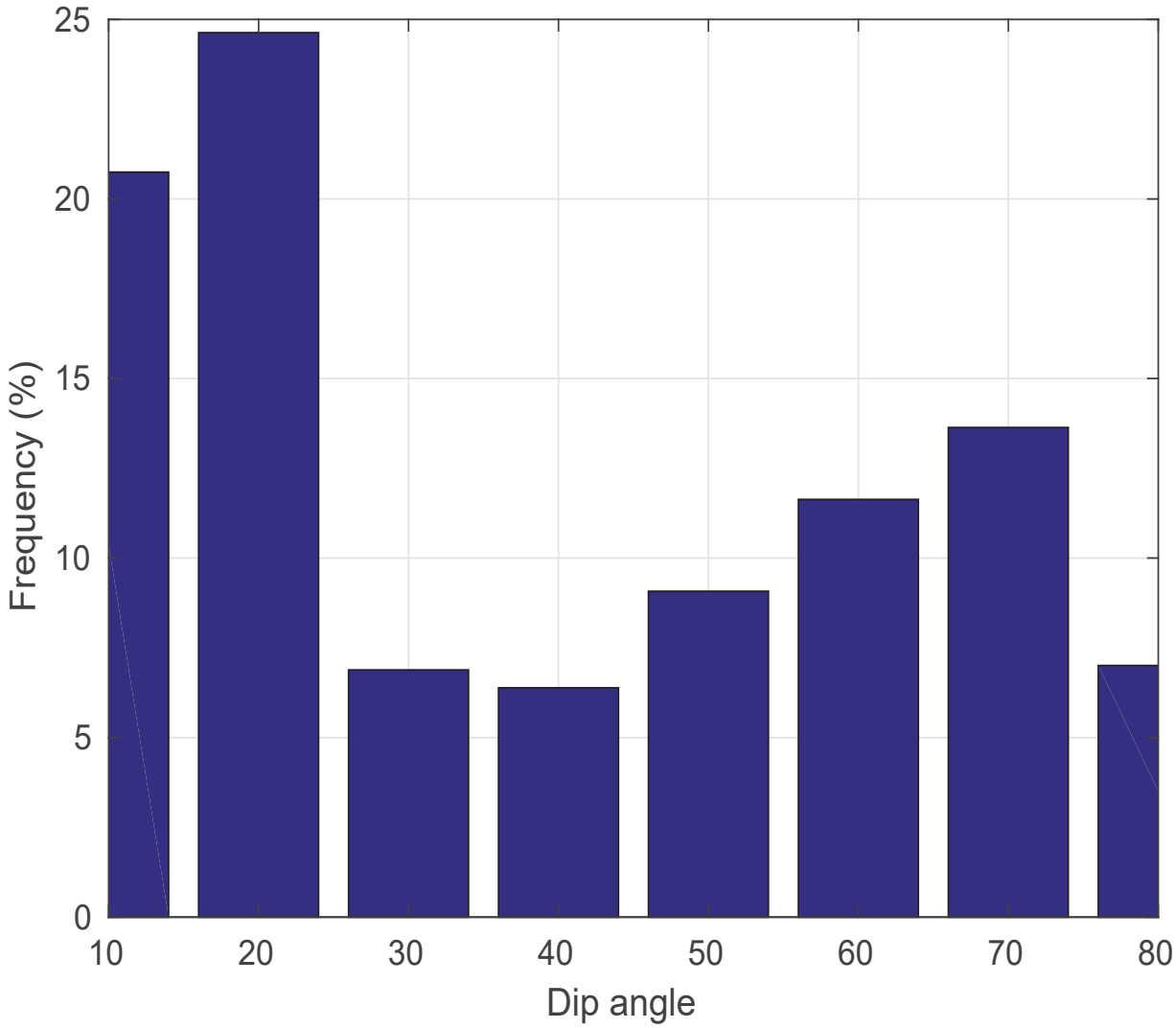

Figure 5.26: Distribution of MFT dip angle from gravity measurements with inclusion of drill bore-hole information in the inversion process.

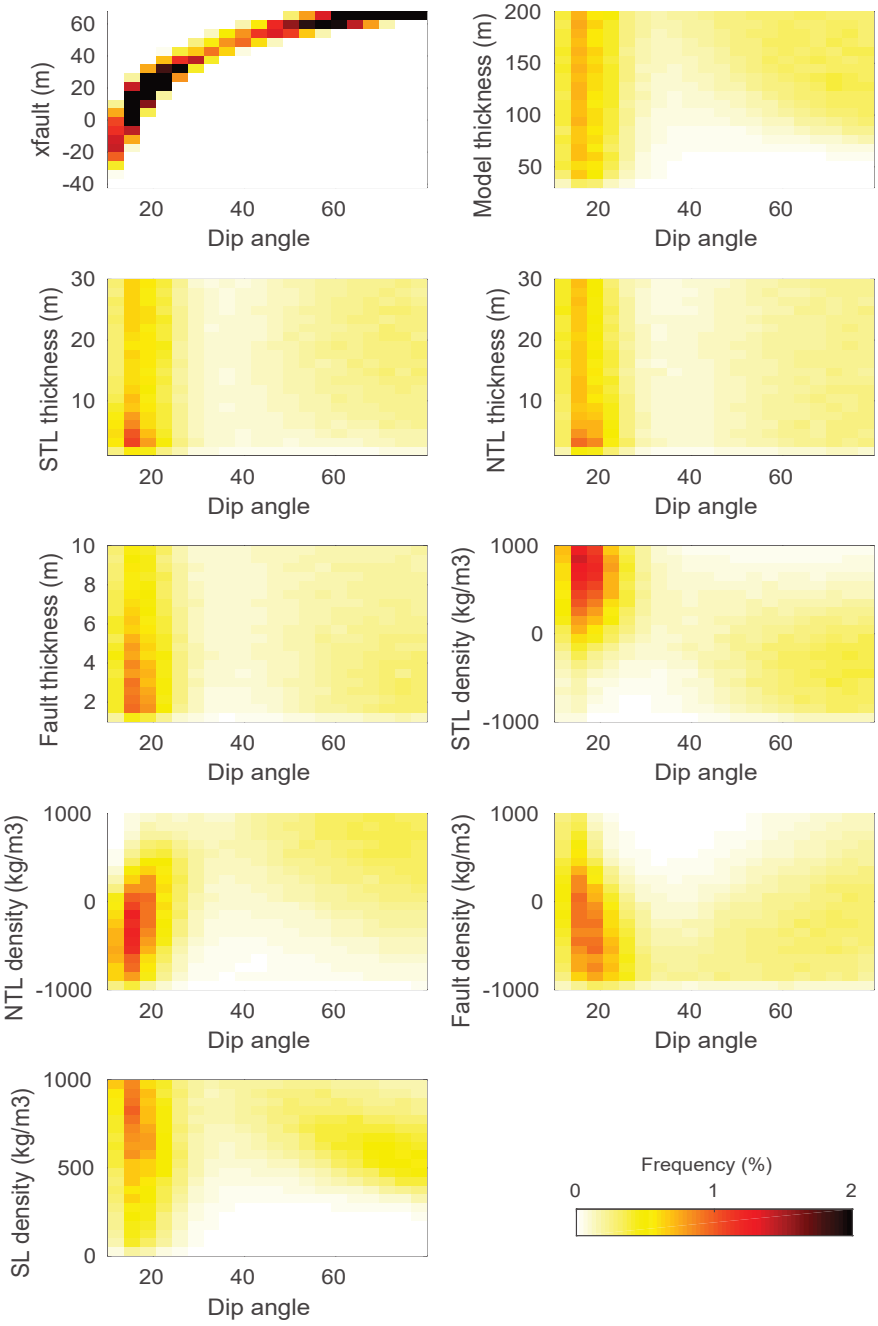

Figure 5.27: Relationship between the obtained dip angle and the other parameters of the density model. Note that density means density contrast with respect to density of the North top layer.

found to be fairly consistent with the drill core-log, which indicates intersection of the fault zone at 13-18 m depths.

The gravity method on the hand constrains a shallow MFT dip angle of ca. 20° indicating that long wavelength gravity signals are influenced by the deeper layers where the dip angle of the MFT is presumably lower, similar to results from Sarpang site. Thus the geometry of fault constrained by the gravity method is interpreted to be due to influence of density contrast coming from the deeper layers, SL and NL. Integrating information of the drill core-log from BH-01 in the inversion process requires same density between the fault zone and STL. This feature may be interpreted due to the materials from the STL being pushed and dragged along the fault underneath the NTL. The other likely model requires either high density contrast between NL and SL, or merging of STL and SL and assigning relatively lower density. Inclusion of bore-hole information in the inversion process constrains the dip angle with two possible model sets: one model set with lower dip angle of ca. 20° and the other model set with high dip angle of ca. 70° as shown in the frequency histogram in Figure 5.27. The later one seems to match with the results obtained from the ERT showing steep dip angle of the MFT. However, it may be cautioned here that the steeper dip angle (ca. 70°) could be a mere artifact (or local maximum) coming from the the borehole constraint. Since xfault and the fault depth in the borehole are connected with a straight line in the model with no dip variation, as xfault approaches close to the borehole location on the surface, the dip of fault gets to a high value.

Overall, unlike in Sarpang area, the geometry of the MFT remains poorly constrained mainly due to unavailability of robust a priori information and relatively thick cover of alluvial deposits. Nevertheless, based on stochastic inversion approach, the geometry of the MFT in Phuentsholing show steep dip angle at moderate depth and shallow dipping at deeper depths (>80 m) constrained by the resistivity and gravity method, respectively. This may indicate that, in terms of geometry of the MFT, there is not much lateral variation in comparison to Sarpang site. At the shallow depth, since there exists little or no resistivity contrast between STL and NTL layers, the geometry of the MFT at this depth remains poorly constrained. Moreover, in Phuentsholing area, since no geomorphological and terrace dating studies have been performed to determine the uplift rate, it is not possible to calculate the overthrusting slip rate and assess possibility of slip partitioning pattern along other faults as observed in south-central Bhutan in Sarpang. However, unlike in Sarpang, there is no reported active structures south of the study area in Phuentsholing. Thus we presume that the shallow

surface structure imaged by this study is the MFT. Another important observation at this site is that the elevation difference between the foothill and terrace level 3 is approximately 103 m; however, due to lack of terrace dating, the vertical uplift rate for this area could not be estimated. Through the present study, we have been able to determine the location of the MFT and performed a preliminary assessment of the fault geometry. Additional information are needed to facilitate better estimation of vertical uplift rate and overthrusting slip rate in the area.

5.7 Field work in Lhamoizingkha

5.7.1 Introduction

Lhamoizingkha is a sub-district under Dagana district. It is located in southern Bhutan between Sarpang in the east and Phuentsholing in the west (Figure 5.28). Subsequent to detailed geomorphological and paleoseismic study conducted in Piping and Lhamoizingkha by the geomorphology team (Le Roux-Mallouf, 2016; Le Roux-Mallouf et al., submitted), we performed preliminary geophysical investigation in Lhamoizingkha area to identify the MFT and study its geometry at shallow surface to constrain the overthrusting slip rate. The field investigation at Lhamoizingkha was lead by myself with field support staff from the Department of Geology and Mines, Bhutan. The field work was conducted in December 2016.

First, we visited the site on the left bank of Wang Chu river at Piping (Figure 5.28 and 5.29) where the geomorphological team conducted detailed paleoseismic study in 2015 and 2016. However, following heavy rainfall in June 2016, the site is not accessible by motor vehicle due to several landslides along the dirt road that leads to the paleoseismic trench site. Because of intense side erosion by the river and sliding, the trench site is also fully covered with debris. Thus conducting geophysical profile along the paleoseismic trench was not possible. As suggested by the geomorphological team, we considered conducting geophysical survey on the right side of Wang Chhu. However, there is no direct road accessibility to the other side of the river and Indian trucks that used to across the river to collect river boulders were no longer operating as the access till the Wang Chhu left bank was completely disrupted.

We next checked the site towards the west side of Lhamoizingkha town where the geomorphological team conducted paleoseismic trenching at the Chokott Creek on the left side

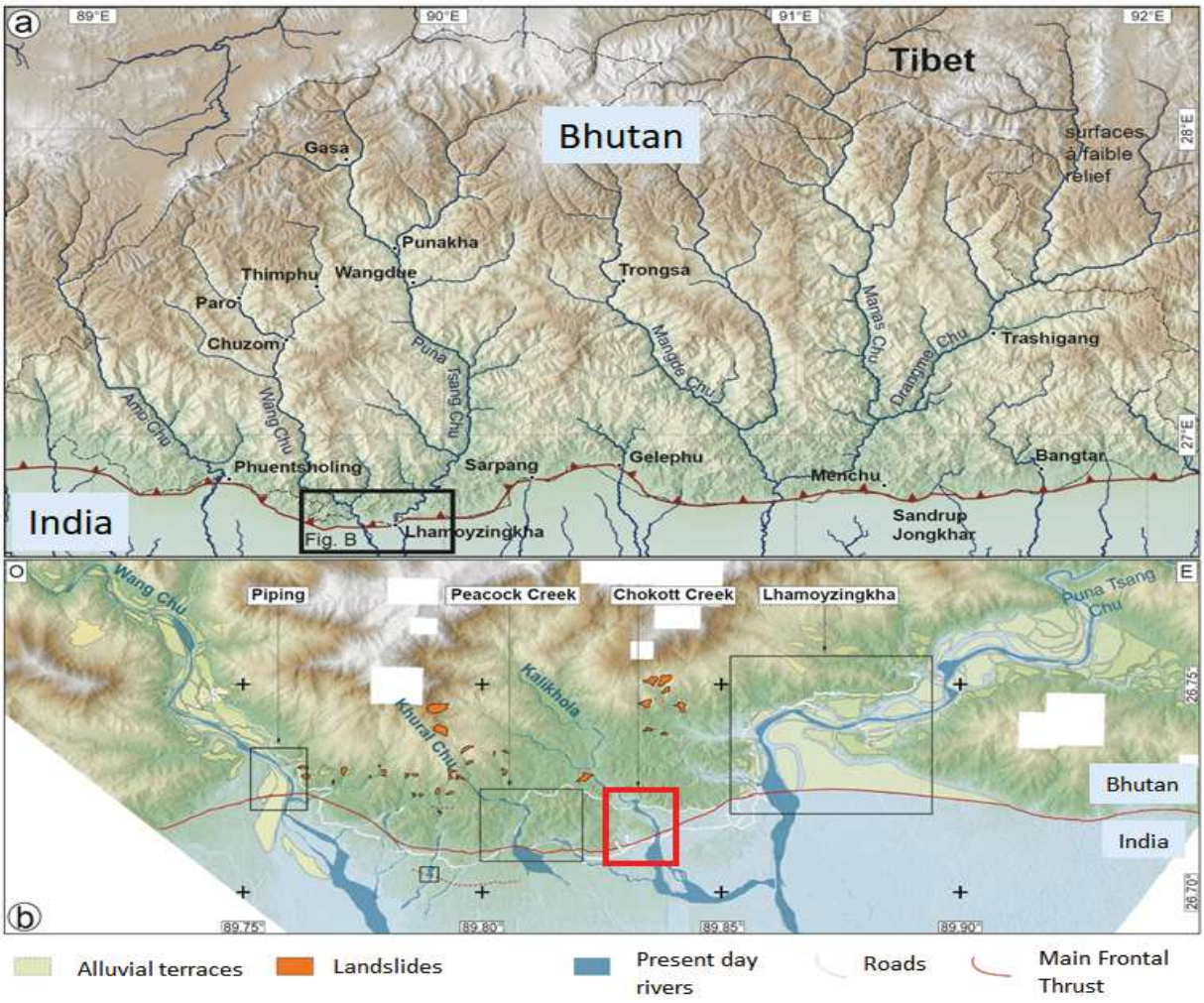

Figure 5.28: (a) Topographical map of Bhutan showing the location of the Lhamoizingkha region . (b) The Lhamoizingkha and vicinity areas show markers indicating intense tectonic activity: a system of perched alluvial terraces, landslides and evidences of surface rupture of the MFT. The black boxes show the location of the different paleoseismic study sites and red box at Chokott Creek is location where geophysical study was performed (Modified from Le Roux-Mallouf, 2016).

of Lhamoizingkha Chhu (Figure 5.28). This site is accessible with 4WD motor vehicle, at least during dry season. We performed electrical resistivity profile about 300m towards the west of Chokott Creek paleoseismic site. However, since the exact location of the MFT is not known at the geophysical profile site, we performed preliminary electrical resistivity study to verify the exact location of the MFT, and if present, conduct similar stochastic inversion approaches performed for Sarpang and Phuentsholing sites to constrain the fault geometry.

Figure 5.29: Location of the Piping paleoseismic trench on the left bank of Wang Chhu.

5.7.2 Geology of Piping-Lhamoizingkha area

The geology of Piping-Lhamoizingkha area (Figure 5.30) is dominated by undifferentiated Quaternary alluvial deposits that occupy the flat foothill sections belonging to the Indian-plate (Chaturvedi & Mishra, 1978; Long et al., 2011). The MFT is interpreted to separate this undifferentiated alluvium from the overlying sub-Himalayan Siwalik Group of Miocence-Pliocene age comprising mainly of medium to coarse grained conglomeratic sandstone; tan to gray, medium to coarse grained sandstone to pebble; gray to green massive weathering siltstone and shale, inter-bedded with lithic rich sandstone. The MBT divides the over-riding Lesser Himalaya from the sub-Himalayan Siwalik Group. Further north of the Siwalik Group, the geology is made of Buxa Group of the Lesser Himalaya zone. The Buxa Group is further divided into a) Phuntsholing Formation which is made of dark gray to black, finely laminated slate and phyllite inter-bedded with limestone, quartzite and dolostone, b) Manas Formation: comprising of medium to coarse grained conglomeratic quarzite exhibiting trough cross-bedding inter-bedded with thinly laminated phyllite and gray dolostone, c) Pangsari Formation: comprising of thinly laminated talcose phyllite inter-bedded with medium to thick bedded dolostone and marble, thin-bedded quartzite. The MCT separates the Lesser Himalaya zone from the over-riding Greater Himalaya sequence.

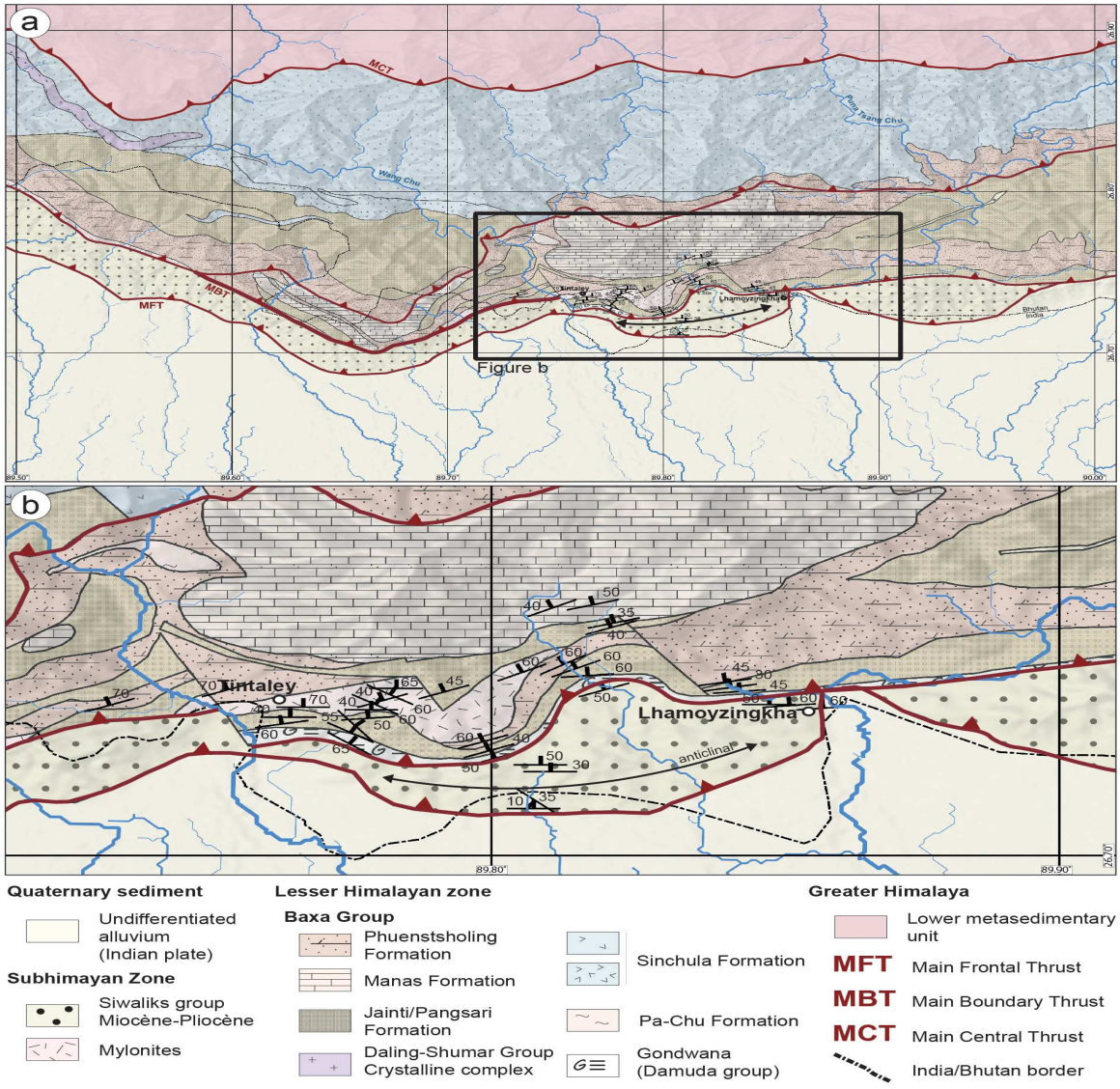

Figure 5.30: Geological map of the Piping-Lhamoizingkha area (After Le-Roux Mallouf, 2016).

Structural measurements in the area suggest high dip angle ranging from 30° to 70° (Figure 5.30). In general, the frontal areas along the Bhutanese Himalayas consistently show high dip angle of in-situ beddings/foliations, which may be correlated to high dip angle of the frontal thrust faults at shallow depth as observed in Sarpang and Phuentsholing. Le Roux-Mallouf (2016) estimated a vertical uplift rate of 9 mm/year in Lhamoizingkha area which is consistent with the uplift rates obtained in Sarpang (Berthet et al., 2014) and Piping (Le Roux-Mallouf et al., submitted).

5.7.3 Field equipment

We used ZZ FlashRes Universal 61 channels with 64 electrodes, belonging to the Department of Geology and Mines, to perform electrical resistivity tomography survey in Lhamoizingkha area. The FlashRes Universal equipment used for the survey is a comprehensive array-oriented resistivity equipment whereby it uses all 64 electrodes simultaneously, expect two current electrodes (A and B) used for current injection and another one as common reference electrode (M) to collect 61 potential data (N1, N2,...N61) as shown in Figure 5.31.

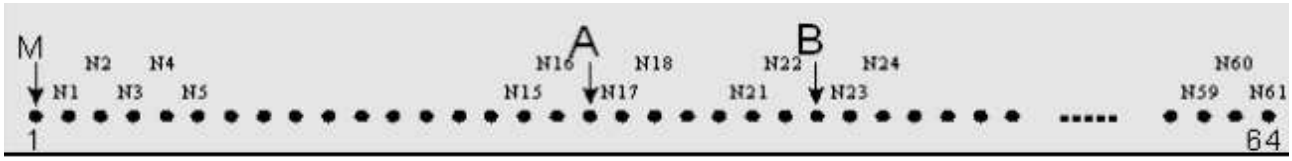

Figure 5.31: Diagram showing how ZZ FlashRes resistivity collects data compared to conventional resistivity equipment.

5.7.4 Electrical resistivity data

We conducted three electrical resistivity profiles with spacing interval of 1m, 2.5 m and 5 m corresponding to a total spread length of 63 m, 157.5 m and 315 m, respectively (Figure 5.32). The resistivity line is aligned almost in the north-south direction with electrode No.1 being located at the south end (Figure 5.32). Since there is no paleoseismic trench at the resistivity site, the exact location of the MFT is not known. We performed resistivity profile both to detect and image the fault based on the first location proposed by the geomorphological team where the MFT trace observed in the paleoseismic trench at Chokott Creek is inferred to extend almost at the center of the resistivity profile at around 155-160 m for the 5 m electrode interval as shown in Figure 5.32 and 5.33. The topography along the profile line is almost flat and therefore no detailed elevation data were collected. As seen in Figure 5.33, an electric power line passes through the resistivity profile. However, since the power line is perpendicular to our resistivity line, the electrical noise effect on the resistivity data is considered to be minimal. For data collection, we mainly employed combination of Wenner, Schlumberger and Dipole-Dipole array configuration.

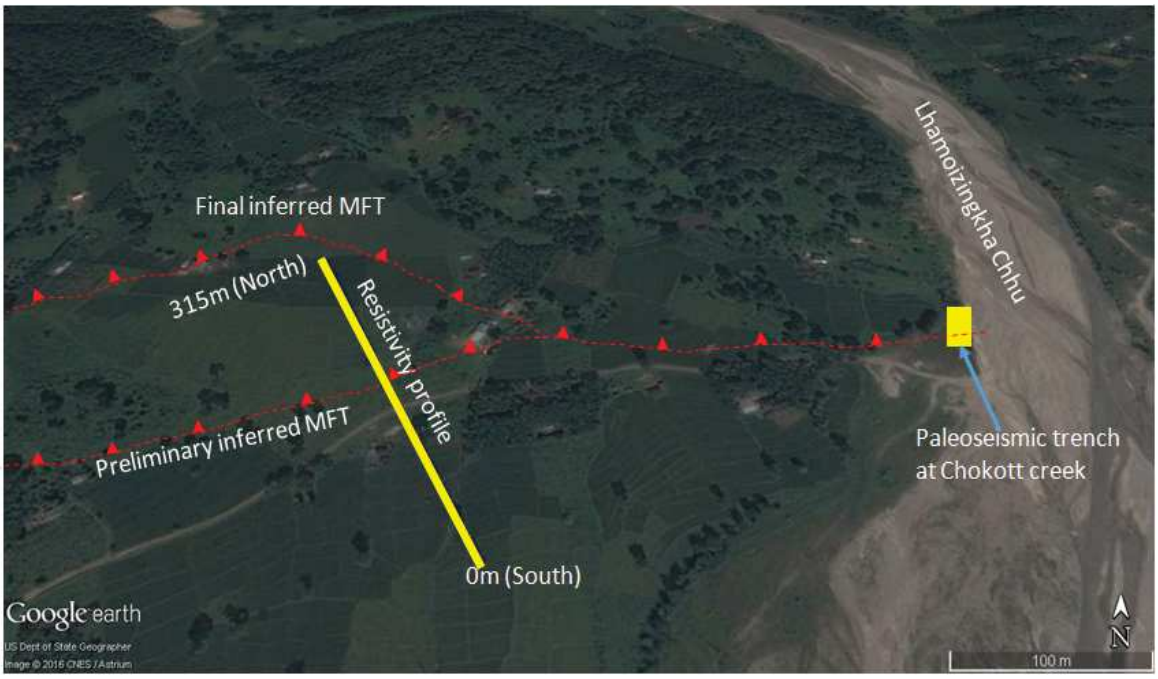

Figure 5.32: Geo-electrical resistivity line at Lhamoizingkha to the west of Chokott Creek.

Figure 5.33: Electrical resistivity profile line in relation to the inferred MFT and power line

5.7.4.1 ERT inversion results

To determine the subsurface resistivity distribution of the area with the aim to verify the location of the MFT and image the geometry of the fault, we performed inversion of the obtained resistivity data using res2dinv software. Employing a similar methods adopted for Sarpang area, the observed data were checked for any inconsistency and imported into the Res2dinv programme. In case of dipole-dipole geometric configuration, the inversion process returned high RMS error. The data point with large errors of above 100 percent were removed and inversion process was rerun which substantially reduced the misfit error between observed and calculated data. Since the topography of the study area is flat, no topographic correction is included in the inversion process.

The inverted resistivity pseudo-sections corresponding to different electrode spacing of 1m, 2.5 m and 5 m are shown in Figures 5.34, 5.35 and 5.36, respectively. Dipole-dipole and Wenner array was used for 1 m and 2.5 m electrode intervals, where as for 5 m electrode spacing, Schlumberger and Wenner geometric configuration was used. This is mainly because in case of 5m electrode spacing, the dipole-dipole geometric configuration resulted in poor data quality due to introduction of high noise level (or low signal), especially at higher "n" values. Notice in all the ERT pseudo-sections, consistent layered type resistivity distribution is depicted which may be correlated to subsurface with horizontal litho-strata devoid of any dipping structures. In general, all the resistivity sections show high resistivity (>2000 Ω.m) top layer (0-3.5 m) which could be representative of dry alluvium materials with multi-decimetric pebbles as observed by Le Roux-Mallouf (2016) in Chokott Creek paleoseismic trench. This is followed by a relatively low resistivity (100-500 Ω.m) between depths ranging from 3.5 m to 16 m which may be correlated to groundwater saturated zone in the area. By and large, the inverted resistivity sections suggest that the litho-strata may be representative of mainly Quaternary deposits on top of the Indian plate. Our investigation and related resistivity images do no show any fault trace. Thus it may be concluded that the fault is located further north. Our study, however, contribute to refine the location of the fault and also rule out possibility of secondary fault segment in the area. Following in-depth discussion with the geomorphological team, the MFT system in the area is later interpreted to be located further north of the profile (Figure 5.32 and 5.37). This emphasizes the importance of coordinated multi-disciplinary team approach to study complex near-surface characterization of fault geometry.

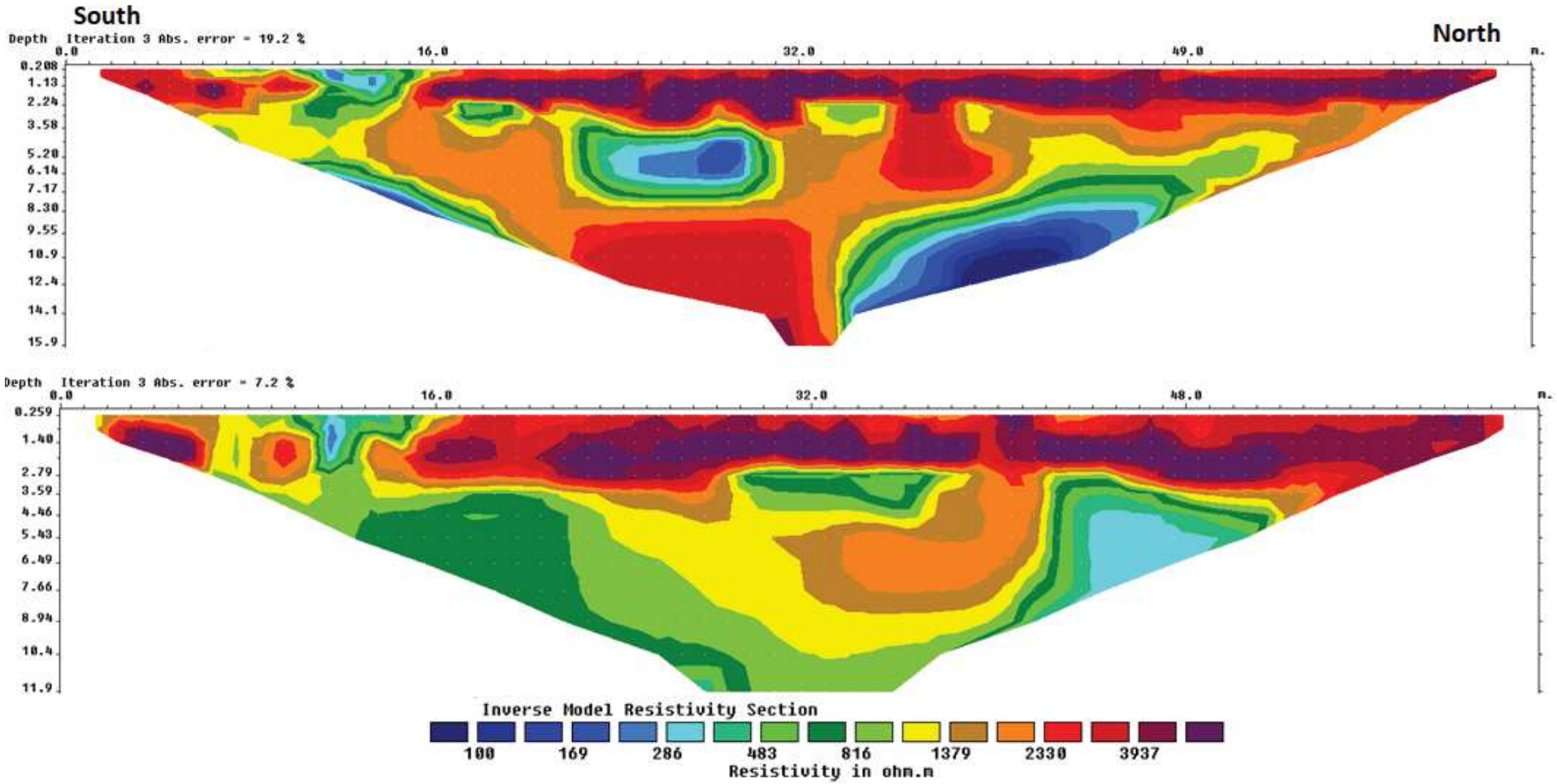

Figure 5.34: ERT section for 1m electrode spacing using Dipole-Dipole (top) and Wenner (bottom) geometric configuration

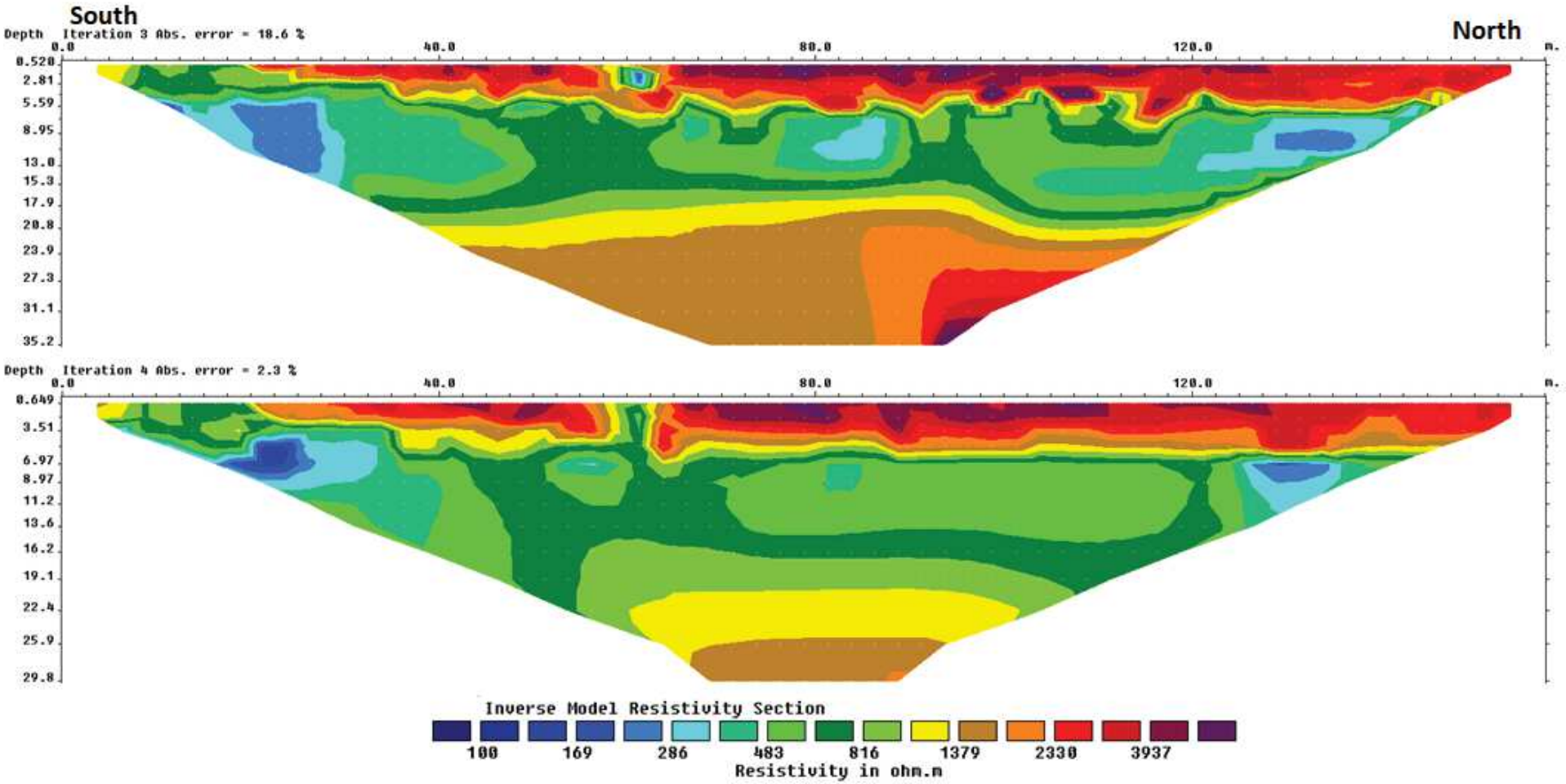

Figure 5.35: ERT section for 2.5 m electrode spacing using Dipole-Dipole (top) and Wenner (bottom) geometric configuration

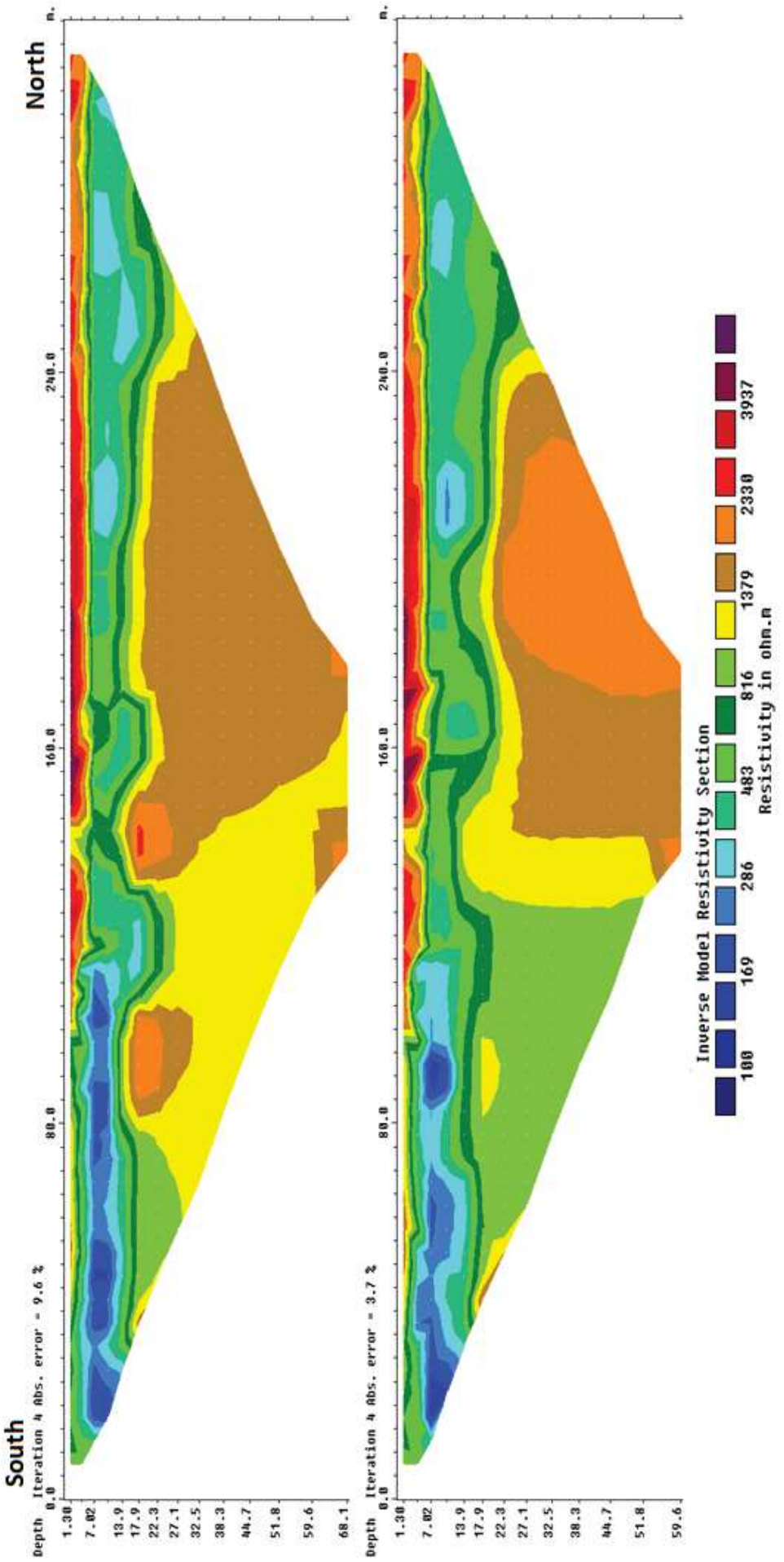

Figure 5.36: ERT section for 5 m electrode spacing using Schlumberger (top) and Wenner (bottom) geometric configuration

5.7.5 Conclusion

The electrical resistivity pseudo-sections do not exhibit any dipping structures that could be correlated to the MFT. This suggests that the MFT is located slightly north of our resistivity line. In view of absence of MFT along our profile, the stochastic inversion process was not performed for the resistivity data collected from Lhamoizingkha area. Thus the geometry of the MFT in Lhamoizingkha remains unresolved. However, based on geomorphological and paleoseismic studies, the vertical uplift rate in Lhamoizingkha is estimated to be around 9 mm/year, which is consistent with the uplift rates obtained in other frontal areas such as Sarpang and Piping. Moreover, structural measurements of bedrock outcrops along the Lhamoizingkha frontal areas show consistent steep dip angle in the range of 50°-60° as shown in Figure 5.31, which may suggest that the geometry of the MFT in Lhamoizingkha area is similar to geometry obtained in Sarpang and Phuentsholing. Nevertheless, in light of lack of definitive constraints on the shallow surface geometry of the MFT in the study area, future follow up studies using near-surface geophysics is highly recommended farther north of the present resistivity line as shown in Figure 5.33. By and large it is important to note that mapping surface trace of the MFT is difficult if one cannot follow a fault on a flat, open area on 3-400 m distance.

Possibility of conducting near-surface geophysics on the right bank of Wang Chhu (Figure 5.37), opposite to paleoseismic trench on the left side of river will be worthwhile. Firstly, in the Piping area, Le Roux-Mallouf (2016) and Le Roux-Mallouf et al. (submitted) showed clear evidences of at least six major historical seismic events having ruptured the MFT. This area, therefore, holds significant importance in terms of understanding seismic hazard in the region. Secondly, like in Sarpang, detailed surface information of MFT from the paleoseismic combined with flat topography along the right side of Wang Chhu river makes this area highly feasible to study the geometry of the MFT using near-surface geophysical methods.

Aside from the above sites, additional near-surface geophysical study about few 100 m on either side of the Sarpang site will be useful to discern lateral variation of the MFT. Moreover, given the important of Sarpang site, possibility of taking up 3D geophysical survey will be interesting. Towards east of Sarpang in Gelephu, geomorphological study (Berthet et al., 2014) show interesting topographic features which could be an interesting site for future near-surface geophysical investigation to study the MFT geometry at shallow depth.

Figure 5.37: Location of paleoseismic trench, MFT and proposed geophysical line in Piping area.

CHAPTER 6

LATERAL VARIATIONS ALONG THE HIMALAYAN ARC

6.1 Introduction

In the past, the Himalayas in general is understood as largely laterally uniform settings that stretches ca. 2500 km from the Hazara-Kashmir syntaxis in the west to the Namcha Barwa syntaxis in the east. However, evidences from decades of scientific studies in the Himalayan region (Grujic et al., 2002; Duncan et al., 2003; Bollinger et al., 2004; Drukpa et al., 2006; Robert et al., 2011; Gahalaut et al., 2011; Tobgay, 2011; Gahalaut & Arora, 2012; Burgess et al., 2012; Hammer et al., 2013; Coutand et al., 2014; Vernant et al., 2014; Hetényi et al., 2016) highlight significant along strike variations in terms of geological structures, topography, precipitation rate, convergence rates and low-temperature thermo-chronological ages. Within the Bhutan Himalaya region itself, occurrences of significant lateral variations have been observed (Grujic et al., 2006; Baillie & Norbu, 2004; Tobgay et al., 2012; Coutand et al., 2014; Vernant et al., 2014; Marechal et al., 2016; Singer et al., 2017; Singer et al., 2017; Diehl et al., 2017) that could play critical role for seismic hazard assessment. Here I describe some of the prominent lateral variations for the Himalayas in general, and the Bhutan Himalayas in particular. The findings from this thesis is also presented here with aim to further substantiate the current understanding of along strike variations along the Himalayan arc. Finally, summing up these lateral variations, the overall implications in terms of scientific understanding of the formation of the Bhutan Himalayas and its associated seismic hazard is presented with focus on better understanding of seismic hazard assessment in Bhutan.

6.2 Lateral variations: Bhutan Himalayas vs Nepal Himalayas

Duncan et al. (2003) studied the along strike topographic variations across Nepal and Bhutan Himalayas (Figure 6.1). They opined that the Bhutan Himalayas is characterized by two high-relief zones separated by a narrow, low-relief step in topographic and river profiles. The higher relief southern zones rises abruptly from the Main Frontal Thrust to Higher Himalayan peaks that rises >4000 m. The northern zone consists of low-relief, high elevation, plateau-like terrain cut by widely spaced, steeped-walled valleys. On the contrary, the Nepal Himalaya exhibits a narrow hinterland zone of extreme relief, steep slopes and channels, deep fluvial dissection and wide foreland zone of lower relief. In Nepal Himalayas, active shortening on the MFT occurs far deep into the sub-Himalayan foothills away from the steep topography of the Lesser Himalayas.

In terms of geology, the Bhutan Himalayas is significantly different from other parts of the Himalayas in two major ways (Grujic et al., 2002):

- low-grade sedimentary rocks overlay the Greater Himalayan Sequence as klippen
- an out-of-sequence thrust called the Kakhtang thrust, located above the klippen, and it doubles the thickness of the Greater Himalayan Sequence. This is especially so in case of western and central Bhutan where the Greater Himalayan Sequence is much widespread at the expense of the Lesser Himalaya

The geometry of the MHT is another important lateral variations reported in the Himalayas which plays important role in distribution of uneven micro-seismicity (Bollinger et al., 2004) and the kinematics and exhumation history of the region as demonstrated in the model proposed by Robert et al. (2011). The geometry of MHT is not laterally constant between western and central Nepal. In western Nepal the southern shallow flat part of the MHT is steeper than in central Nepal. In Bhutan, the MHT appears as continuous shallow dipping detachment with the mid-crustal ramp absent or possibly occurring further north than in the Nepal Himalayas (Le Roux-Mallouf et al., 2015).

Based on flexural geometry and rheology of the Indian plate beneath the Bhutan Himalayas, Hammer et al. (2013) and Hetényi et al. (2016) (see Annex-A.3) found that compared to Nepal, the observed Bouguer anamoly profiles across Bhutan show that the lithosphere bends down over a shorter distance, and the foreland basin is much narrow and shallower. Besides Hetényi et al. (2016) also noted that Arc Parallel Gravity Anomaly (APaGa)

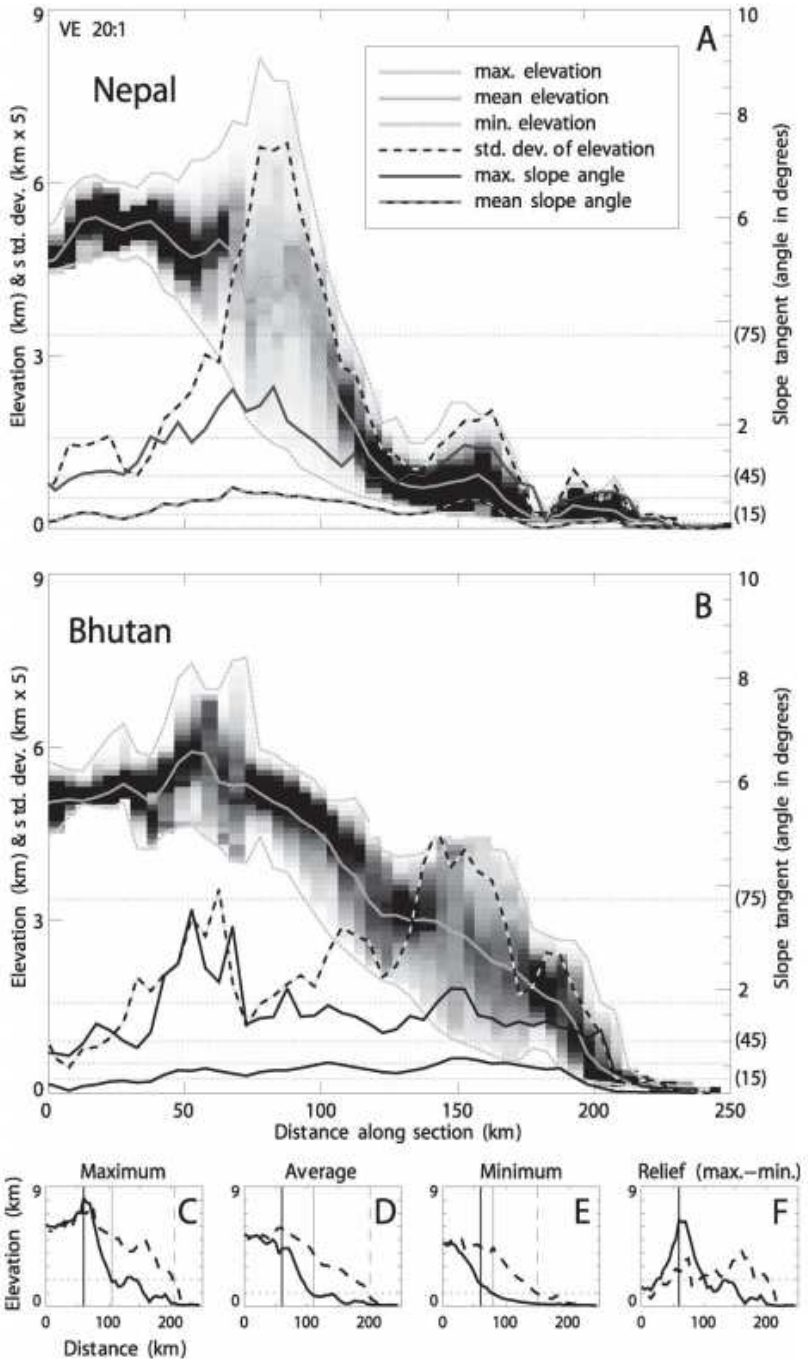

Figure 6.1: Profiles of elevation and slope for 50 km-wide swaths in Nepal (A) and Bhutan (B). Values sampled every 5 km along swath; maximum, minimum, and mean elevations and slopes are for each 5 $\times$ 50 km rectangle along swath. Relief computed as standard deviation of elevations. Gray scale shading between maximum and minimum swath elevations is density plot (histogram) of elevation samples (darker indicates greater concentration of terrain at that elevation). C-F: Comparison of Nepal and Bhutan profiles aligned at high peaks and Main Frontal thrust. Heavy vertical line at position of high peaks; thin solid (Nepal) and dashed (Bhutan) vertical lines are where profiles cross 2 km or 1 km elevations (dotted horizontal lines) (After Duncan et al., 2003).

reflects deep structure of the orogen and clearly shows existence of four lateral segmentation across the arc. The presence of Shillong Plateau to the south of the Bhutan Himalayas is another striking difference compared to other Himalayas. Vernant et al. (2014) found that because of clockwise rotation of the Brahmaputra valley with respect to India, GPS convergence rate east of Sikkim is reduced from ∼18 mm/year to ∼12 mm/year, while the convergence between Shillong Plateau and Bangladesh increase from 3 mm/year in the west to >8 mm/year towards the east. Similarly, many studies (Drukpa et al., 2006; Gahalaut et al., 2011; Gahalaut & Arora, 2012; Saric, 2014) have pointed the implication of reduced seismicity due to presence of Shillong Plateau and the resulting stress change induced by the Great Shillong earthquake of 1897 on the seismic hazard in eastern Himalayas. However, this apparent reduced seismicity in Bhutan region could be related to short observation period of seismicity vis-à-vis the full seismic cycle.

The deformation mechanism or type of faulting is another important difference between the Bhutan and Nepal Himalayas. Unlike in the Nepal Himalayas, which is dominated with thrust type faulting mechanism, the Bhutan Himalayas show predominantly show strike-slip faulting mechanism (Drukpa et al., 2006; Velasco et al., 2007; Diehl et al., 2017). Based on linear seismicity observed in south-west part of Bhutan, De & Kayal (2003) and Velasco et al. (2007) termed this obliquely striking dextral feature as the Goalpara lineament. Diehl et al. (2017) also observed similar linear seismicity but they however noted that seismicity associated with this structures is predominantly mid to lower crustal levels and proposed this mid-crustal zone of deformation, which extends from Chungthang in northeast Sikkim to Dhubri at the northwestern edge of Shillong Plateau in the foreland, as the Dhubri-Chungthang Fault Zone (DCF). They further proposed that the thickened crust and strike-slip seismicity associated with the DCF under western Bhutan could be expression of laterally changing stress regimes in Eastern Himalayas.

6.3 Lateral variations across the Bhutan Himalayas

6.3.1 Geology, topography & seismotectonics

Within the Bhutan Himalayas notable along strike variations have emerged as a result of decades of concerted scientific studies in the region. These variations are important for unraveling the uniqueness of the eastern Himalaya compared to other parts of the Himalayas

and also in enhancing the seismic hazard characterization of the region, by and large.

The rise of Shillong plateau in the Miocene-Pliocene transition, the only orographic barrier in the Himalayan foreland, plays an important role on the erosion, landscape and tectonics of the eastern Himalayas (Grujic et al., 2006; Coutand et al., 2016). Bilham & England (2001) noted that the Shillong plateau could account for one-third of the Indo-Eurasain convergence and consequently result in reduced fault slip rate and thus the uplift rate in eastern Himalaya compared to other frontal parts of the Himalayas. Grujic et al. (2006) observed that decreased precipitation along the front in eastern Bhutan due to rise of Shillong plateau has resulted in decrease in erosion rate in eastern Bhutan (Figure 6.2). They proposed that change in erosion rate is likely responsible for formation of second-order tectonic structures in Bhutan. For instance, apart from eastern Bhutan where the outliers of the Tethyan Sedimentary are still present, possibly due to low erosion rate as a result of Shillong plateau uplift, such structures that might have been extended throughout the Himalayan arc, is now been fully eroded back to the Himalayan crest (Grujic et al., 2002). Similarly, Coutand et al. (2014) observed significant differences in exhumation rates and patterns between western and eastern Bhutan. They noted that in western Bhutan, the slip rates and partitioning of deformation along the MHT has remained steady during the last 10 Ma, with long term exhumation rate of 3 mmm/year in the south to 0.7 mm/year at 27.25°N and up to 1-1.5 mm/year beyond 27.5°N. On the contrary, in eastern Bhutan, they predicted 40-50% decrease in overthrusting rate at 5-6 Ma with long term exhumation rate of 1-1.5 mm/year in the south to 0.7 mm/year along most of the transect and 1 mm/year north of 27.5°.

Using newly acquired GPS data across the Bhutan Himalayas, Marechal et al. (2016) observed significant interseismic coupling variations along the Bhutan Himalayan arc (Figure 6.3). They noted that in western and central Bhutan, the fully coupled segment is $\sim$ 145 km wide with an abrupt downdip transition, whereas in eastern Bhutan the fully coupled segment is $\sim$110 km wide with partially creeping updip and downdip segments. Moreover they observed that the MBT in eastern Bhutan is creeping and is part of the active thrusting front.

Based on receiver function imaging as part of GANSSER project outcome, Singer et al. (2017) observed significant lateral variations in the lithospheric structure beneath Bhutan (Figure 6.4). They found that in western Bhutan, the Moho geometry shows an increased dip south of the Higher Himalaya and reaching to a depth of $\sim$ 75 km beneath the Higher Himalaya. On the contrary, in eastern Bhutan, they observed sub-horizontal Moho at 50 km

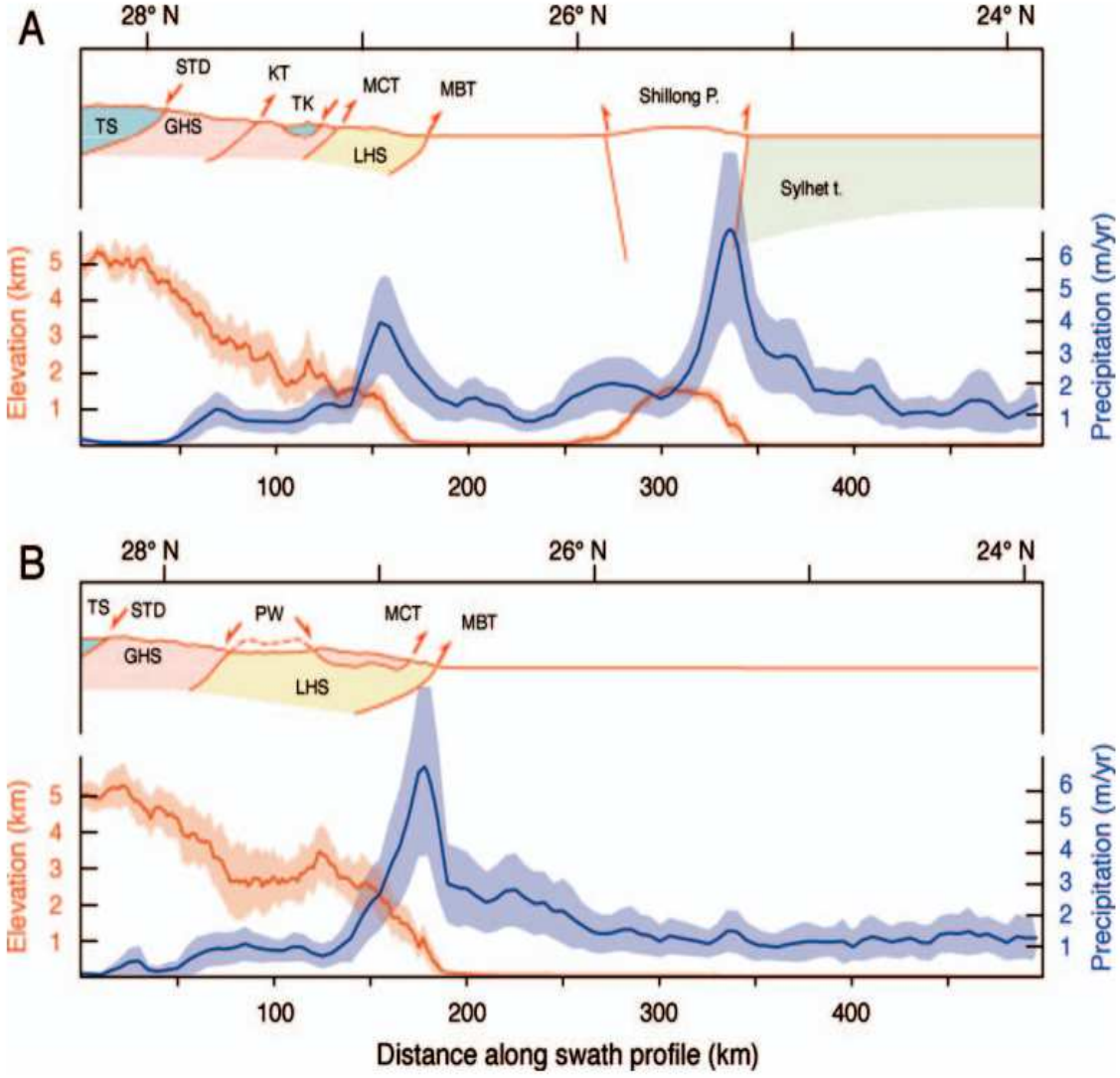

Figure 6.2: Topographic and precipitation profiles, in 40-km-wide swaths, across Bhutan Himalayas and Shillong plateau show that an orographic barrier of 1.5-2 km is sufficient to hinder moisture transport. A-eastern Bhutan; B-western Bhutan. Topography (orange) has been derived from Shuttle Radar Topography Mission data; precipitation (blue) is taken from the calibrated Tropical Rainfall Measuring Mission data. There is a strong E-W precipitation gradient: at $\sim$ 1-1.5 km elevation in the east it is $\sim$ 4 m/yr, while in the west it is $\sim$ 6 m/yr. MFT–Main Frontal thrust, MBT–Main Boundary thrust, MCT–Main Central thrust, KT–Kakhtang thrust, STD–South Tibetan detachment, LHS–Lesser Himalayan Sequence, GHS–Greater Himalayan Sequence, TK–Tethyan Klippen, PW–Paro window, TSS–Tethyan Sedimentary Sequence (After Grujic et al., 2006).

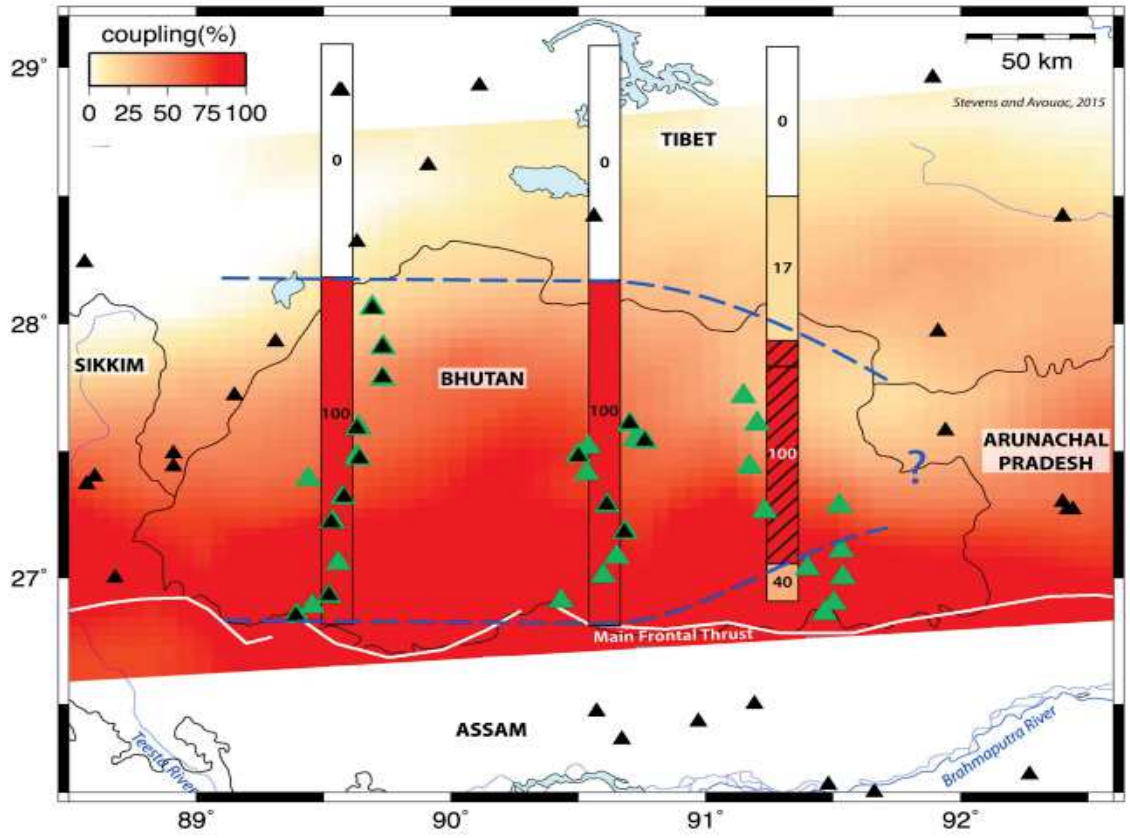

Figure 6.3: Interseismic coupling of the Main Himalayan Thrust in Bhutan. Rectangles show our estimates of interseismic coupling for the different fault segments. The hatched segment represents the flat part of the MHT constrained by the inversion. The colored base map representing seismic coupling estimates and black triangles representing GPS stations are from Stevens and Avouac (2015). Dashed blue lines show the possible limits of the fully coupled zone. Green triangles show the locations of our new GPS stations. (After Marechal et al., 2017).

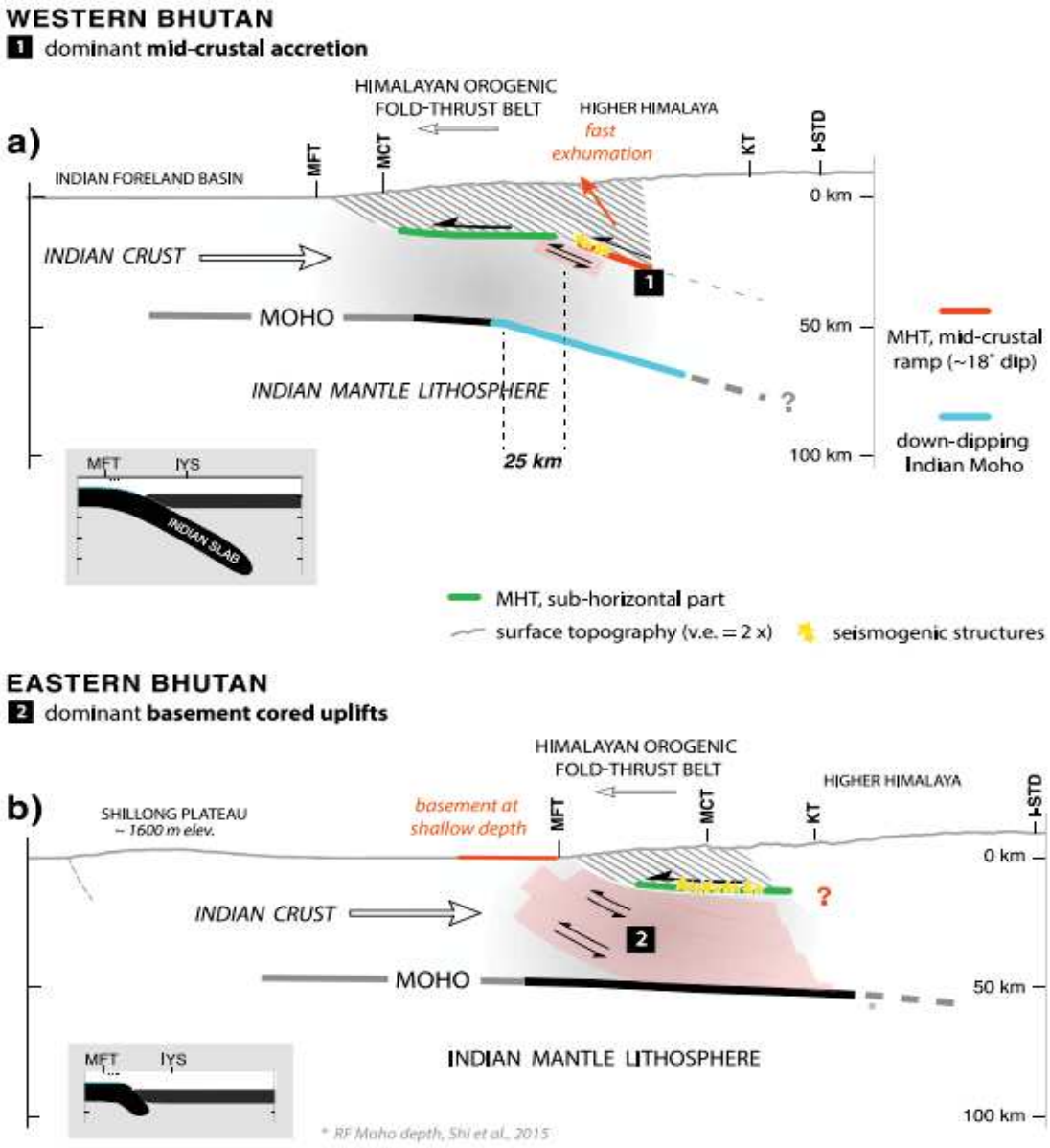

Figure 6.4: Tectonics models showing the role of Indian crust in collision dyanamics of western and eastern Bhutan (After Singer et al., 2017).

depth. They interpreted this to be due to distinct downbending of the underthrusting Indian plate in western Bhutan with an attached Indian mantle-slab subducting beneath the Lhasa block in the north. In eastern Bhutan, the influence of the mantle-slab disappears and the underthrusting plate is likely restricted to the Tethyan Himalaya resulting in a less pronounced crustal thickening beneath the Himalaya and a subhorizontal Moho geometry. Similarly, Singer et al. (2017) also found regional variation revealed by distinct high shear-wave velocity anomaly (>3.6 km/sec) corresponding to the along-strike variations in the upper crustal structure represented by the alternating tectonic window and klippen at the surface. They concluded that these lateral variations provide evidence for the formation and depth extent of localized duplexes at the base of the Himalayan orogenic wedge. Consistent with findings from Singer et al. (2017), Diehl et al. (2017) using high-resolution earthquake catalog and 3D crustal V_p model found that western Bhutan is characterized with thickened crust compared to eastern Bhutan (Figure 6.5). They also observed that seismicity in western Bhutan is

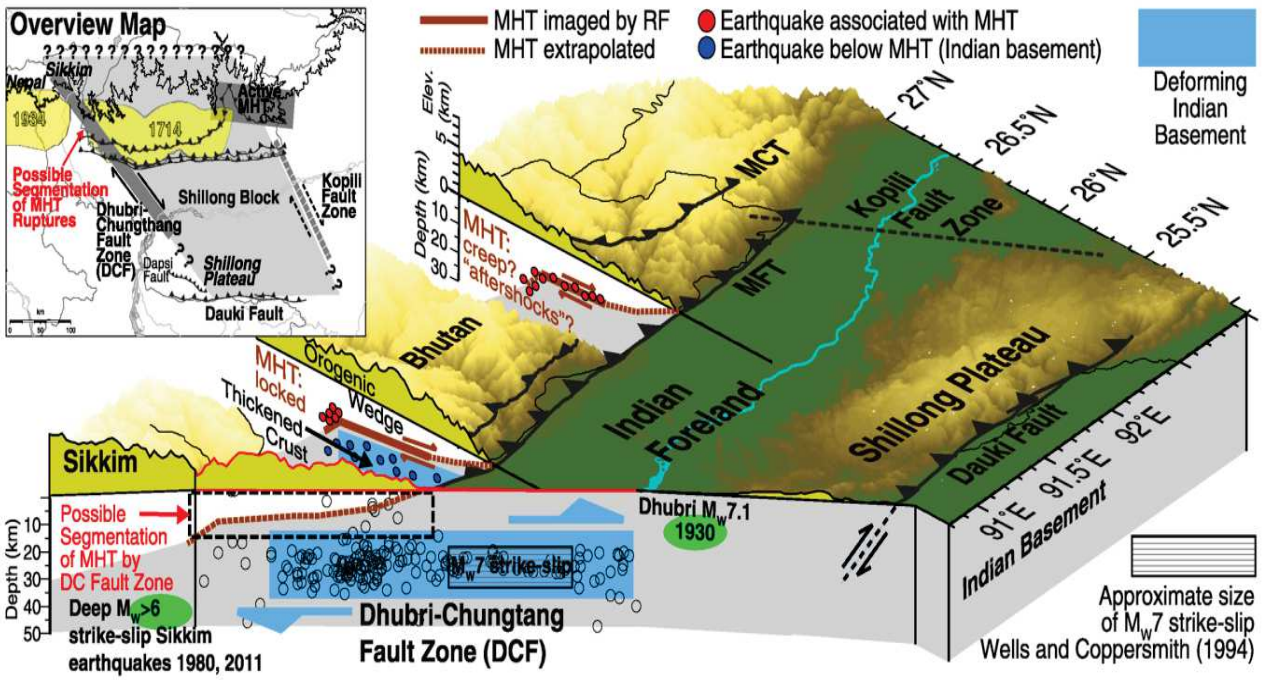

Figure 6.5: Seismotectonic model of the Bhutan Himalayas and its link to the foreland deformation. (After Diehl et al., 2016).

dominated by strike-slip in the Indian basement along the dextral Dhubri-Chungthang Fault Zone (DCFZ) which possibly causes segmentation of the MHT between western Bhutan and eastern Nepal. In eastern Bhutan, seismicity images a flat, seismogenic segment of the MHT,

which may be either related to the 2009 M_W 6.1 event, or representing a partially creeping fault segment.

6.3.2 Geometry of the MFT

The geometry of the MFT at shallow surface is a critical parameter for estimating overthrusting rate, unraveling lateral variations and consequently for improved seismic hazard assessment in the region. Based on geomorphological studies in Sarpang and Gelephu areas, Berthet et al. (2014) observed a consistent vertical slip rate of 8.8±2.1 mm/year. Following Long et al. (2011) which reported in-situ dip angle of ∼30° at the frontal area and TFT dip angle of ∼20° estimated by horizontal shift of the fault traces between the terraces in the study area, Berthet et al. (2014) used a TFT dip of 20° with vertical uplift rate of 8.8±2.1 mm/year to estimate a Holocene slip rate of 20.8±8.8 mm/year in Sarpang and Gelephu areas. Subsequent paleoseismic study in Sarpang (Le Roux-Mallouf et al., 2016) further refined the dip angle of TFT to be 17°-24° based on the dip angle of fault trace observed in the paleoseismic trench. Approximately 50 km east of Sarpang in Piping area, Le Roux-Mallouf et al. (submitted) observed a gentle dipping MFT dip angle of ∼10°N in the paleoseismic trench. They, however, noted that the dip of the MFT seems to be steeping at shallow depth.

The current effort in this thesis adopted near-surface geophysical techniques to constrain the geometry of the MFT at shallow surface and study lateral variations of the frontal system. Three sites namely at Sarpang, Phuentsholing and Lhaimoizingkha were investigated as part of this dissertation. Following are some of the significant observations from the geophysical investigation pertaining geometry and along-strike variation of the MFT in the Bhutanese frontal area:

- In Sarpang area we constrain a TFT with a flat and listric-ramp geometry with a low dip angle of 20°-30° at shallow depth, steeply dipping in the middle and gradually flattening with shallower dip angle of 30°-40° in its deeper part. The TFT geometry thus constrained is different from the assumed simple shallow dipping TFT geometry based on dip angle measured on the fault trace at the surface in the paleoseismic trench.

- The preliminary results from Phuenstholing area suggest a MFT with flat and listric-ramp geometry similar to the ones observed in Sarpang. The structure measurements of bedrock outcrops in Phuentsholing and vicinity areas also show steep dip angle indicating that there may not be significant along-strike variations in the geometry of the

frontal fault between the two studied area. In absence of terrace dating information for the Phuentsholing site, assessment of deformation partitioning along other active faults in the area was not possible. However, unlike in Sarpang, no active structures have been reported south of the present study area. Whether deformation partitioning exists, for instance along the MBT, needs further detailed investigations.

– In Lhamoizingkha area, since the MFT was not imaged by the geophysical study, we could not make any deduction on the geometry of the MFT. Similar to Sarpang and Phuentsholing, the in-situ structural measurement in Lhamoizingkha and Piping area show steeply dipping dip angles which may indicate that there is not much lateral variations in terms of the MFT geometry. From the paleoseismic investigation, the dip of the MFT is observed to be low at the surface and likely steeply dipping at depth which is similar to the geometry observed in other two areas. Like in Phuentsholing, no active structures have been reported to exist south of Lhamoizingkha area.

6.4 Conclusion

As discussed in the aforementioned sections, significant lateral variations exists in terms of topography, geology and seismo-tectonic characteristics between the Bhutan Himalayas and the Nepal Himalayas as well as within the geographic extent of the Bhutan Himalayas. Recent studies combining seismology, geodetic, gravity, geomorphological and paleo-seismological approaches conducted in the Bhutan Himalayas, unravels prevalence of significant lateral variations along the Bhutanese frontal area. For instance, as proposed in Marechal et al. (2016) (see Annex A.1), notable lateral variation seem to exists in the coupling behavior of the MHT between western and eastern Bhutan. While the MHT in western Bhutan appears fully coupled, in eastern Bhutan the MHT is observed to be partially coupled with possibility of aseismically creeping behavior. Le Roux-Mallouf et al. (2016)(see Annex A.2) and Drukpa et al. (2017) noted possibility of slip partitioning in Sarpang area between the TFT and the Frontal Back Thrust (FBT) reported by Dasgupta et al. (2013). Unlike in Sarpang area, the MFT appears to be the most frontal structure in the Lhamoizingkha, Piping and Phuentsholing area. This clearly indicates occurrences of lateral variations along the Bhutanese frontal region. Whether lateral variations exists in the geometry of MFT cannot be ascertained from the present study since results from Phuentsholing and Lhamoizinkgha are preliminary and not conclusive. However, from the detailed geophysical assessment of MFT geometry in

Sarpang, we conclude that slip partitioning seems to exist whereby only 60% of the far-field GPS convergence rate of $\sim$ 17 mm/year is accommodated along the TFT, while the remaining slip is apparently being accommodated along other active frontal faults such as the FBT and MBT. Further detailed studies combining near-surface geophysics and geomorphological approaches will be crucial in determining lateral variations in the geometry of frontal thrust system which is also important for proper seismic hazard assessment. Based on observations at sites in Sarpang, Phuentsholing and Lhamoizingkha, we observed that structural measurements along the frontal region in the studied areas consistently show higher dip angle of in-situ beddings/foliations, which may correspond to steeper dip angle of the MFT at shallow depth as confirmed in case of Sarpang and possibly for Phuentsholing area too.

CHAPTER 7

CONCLUSIONS

7.1 Main results

This thesis presents, to our knowledge, the first ever constraints on the shallow surface geometry of active thrust faults along the Bhutanese frontal system using high-resolution near-surface geophysical techniques. Constraining the geometry of the MFT is critical to 1) estimate the overthrusting slip rate along the frontal thrust system, 2) discerning along-strike variation across the frontal areas in the Bhutan Himalayas, and 3) improving seismic hazard assessment in the Kingdom of Bhutan. Lack of information on historical catalogs and instrumentally recorded seismicity data poses significant challenges to characterize active faults and understand seismic hazard assessment in the Bhutan Himalayas. However, over the past years, we employed multi-disciplinary approaches involving geomorphology, paleoseismic, and geophysical methods to study fault geometry and rupture mechanisms that help us to understand the characteristics of major seismic events dating back to several hundreds of years in the past.

Following detailed geomorphological and paleoseismic investigations at three sites along frontal areas of the Bhutan Himalayas, namely: Sarpang, Phuentsholing and Lhamoizingkha, geophysical studies were taken up as part of this thesis. The major contributions of this thesis and key results obtained are summarized below:

– Unlike commonly used method based on search for the simplest model, the main advantage of the stochastic inversion approach used in this thesis includes the ability (1) to assess the fault geometry because no smoothing is applied, (2) to provide a mea-

surement of the uncertainties on the obtained dip angle and (3) to allow the study of trade-off between geometric and either electrical resistivity, velocity or density properties.

– Our results, notably from Sarpang, strongly emphasizes the importance of studying the shallow surface fault geometry using near-surface geophysical methods. Assuming simplified geometry of the fault at depth based on dip angle measured at the surface leads to erroneous calculation of the fault geometry. Moreover, the stochastic inversion results strongly indicate that uplift rate estimated using terrace dating data at single location near the front may significantly introduce bias on the overthrusting slip rate estimates.

– The stochastic inversion approach applied to geophysical data from Sarpang favors a flat and listric-ramp fault geometry that is dipping northward with a shallow angle at the top (0-5 m), steeply dipping in the middle (5-40 m) and flattening at deeper depths (>40 m). Together, our new constraints on the fault geometry allow us to estimate a minimum overthrusting slip rate of ca. 10 mm/yr, which is only a part of the ca. 17 mm/yr GPS convergence. This suggests that, in the study area, significant deformation partitioning on several faults including the TFT, the Main Boundary Thrust or fault branches cannot be ruled out.

– The geometry of the MFT in Phuentsholing site is not well resolved compared to Sarpang area. This is mainly due to lack of sufficient a priori information and relatively thick alluvium deposit at the site in Phuentsholing. The stochastic inversion process outputs a probability distribution function which favors MFT geometry with dip angle in the range of $40°$-$70°$, especially at moderate depth. Non-prevalence of resistivity contrast between layers at the shallow surface hinders estimation of the MFT geometry. The geometry of the MFT estimated from gravity method shows two possible model sets: one model set with lower dip angle of ca. $20°$ and the other model set with high dip angle of ca. $70°$. Overall, the geometry of MFT in Phuentsholing area remains poorly constrained.

– In Lhamoizingkha site, due to uncertainty in the inferred location of the MFT at the time of taking up the geophysical investigation, the geometry of MFT remains unresolved. In fact, later following discussion with the geomorphology team, the MFT is interpreted

to be located slightly north of our geophysical line. Thus, electrical resistivity data acquired from Lhamoizingkha were subjected to common inversion method based on search for simplest model and no stochastic inversion processes were performed. As consequence, the geometry of MFT in Lhamoizingkha appears more complex as previously suggested.

– Based on field investigation at these sites, we assessed the capability and deficiency of each geophysical methods. While the resistivity and seismic method, with use of appropriate geometrical spacing, provides high resolution shallow depth information, the gravity performs better at assessing the geometry of the fault at deeper depths. By and large, in spite of different geophysical methods adopted, prevalence of physical parameter contrast together with robust a-priori knowledge is of critical importance for succinct correlation and interpretation of fault geometry and characterization of the subsurface geology.

– The steep dip angle of the MFT as revealed from the near-surface geophysical methods is consistent with high dip angle measured on the in-situ exposures and high rate of terrace uplift along the frontal areas. Both these surface observations can be only be explained with introduction of steep dip angle of the MFT at shallow depth.

– Based on surface observations and geometry of the frontal thrust constrained using near-surface geophysical methods, it is possible that that along-strike variations exists in terms of deformation partitioning along the Bhutanese frontal system. In Sarpang area, since there exists other active faults south of the TFT such as the FBT and moreover, the slip rate along the TFT is 60 % of the GPS convergence rate, deformation distribution along other faults such as the MBT and FBT cannot be ruled out. Accordingly, it can be deduced that return period between coseismic events require longer period for the stress accumulation to reach to the rupture threshhold. In other frontal areas in Phuentsholing and Lhamoizingkha, no prominent active structures exist south of the mapped active fault indicating that the imaged structure is the MFT and as per our observation, this is also the southern most active structure. Tentatively we interpret that no slip partitioning exist at these two places and thus, all the convergence is being accommodated along the MFT or partially along the MBT as deduced from Sarpang (Drukpa et al., 2017) and in eastern Bhutan from GPS observations (Marechal et al., 2016).

7.2 Discussions

Both geomorphological and paleoseismic approaches provide quantitative constraints on mechanism of deformation due to convergence of India and Eurasia continental plate and thus help us in estimating the vertical uplift rate and overthrusting slip rate along the fault. Such techniques are widely used for studying the characteristics of large historical events, which greatly contribute to improving seismic catalog for disaster risk assessment. However, as established from our study, the shallow depth fault geometry deduced through methodologies based only on surface observations are not entirely reliable. Therefore, to accurately constrain the overthrusting slip rate, which is critical parameter for studying lateral variation and seismic hazard assessment, the geometry of the fault at shallow depth must be properly evaluated. We discuss below the detailed account of near-surface geometry of the MFT and its implication in terms of constraining the overthrusting slip rate and assessing the deformation pattern at the front in the Bhutan Himalayas.

7.2.1 Overthrusting slip rate estimation

Based on dating of uplifted river terraces in Sarpang, Berthet et al. (2014) estimated a Holocene vertical uplift rate of 8.8±2.1 mm/year. Applying this estimated uplift rate along with MFT dip angle of 20°-30° inferred from structural measurements on outcrops at the front, they proposed a overthrusting slip rate of 20.8±8.8 mm/year, which is consistent with the far-field GPS convergence rate of 17 mm/year estimated across central Bhutan (Marechal et al., 2016). They finally concluded that the Himalayan convergence is mostly accommodated along the TFT. On the contrary, our findings from near-surface geophysical investigations allow us to propose a more complex TFT geometry which has significant bearing on the overthrusting slip rate calculation and determining the characteristic of deformation mechanism in the area.

Following Okada (1985), a vertical velocity profile is calculated from the above estimated vertical uplift rate assuming a constant overthrusting slip rate along the TFT. Notice in Figure 7.1a the calculated velocity profile depends on geometry of the TFT (i.e higher dip angle corresponds to higher uplift rate and vice-versa). Another notable observation is that it also depends on the distance between the TFT and location of terrace dating samples. As shown in Figure 7.1a, a distance of 5 m from the TFT yields two very different vertical velocity profiles associated with two end-member fault geometry models. On the other hand, if the

uplift rate is calculated based on dating sample collected ∼10 m north of the TFT, the uplift rate significantly reduces (Figure 7.1b). This, in other words, indicate that owing to the flat and listric-ramp geometry of the TFT, the uplift rate measured on the top of the river terraces are spatially variable and thus cannot be constant. Our results strongly questions the validity of commonly used approaches wherein mean uplift rate is estimated by combining several uplifted terraces at different locations with respect to the front. Moreover, assuming that the far-field GPS convergence rate corresponds to a upper limit for the uplift rate, our calculation shows that part of the model corresponding to green curve in Figure 7.1d is unrealistic. This suggests that both the convergence rate derived from GPS measurements and uplift rate estimated from terrace dating can be used to reduce the a priori geometric parameter ranges tested in our stochastic approach.

If we assume no prior information on the location of uplift rate measurements, the overthrusting rate can be calculated from the TFT geometry (Figure 7(c)). The slip rate associated to a rigid block model with a constant dip angle, α, can be estimated using the relationship

$$slip\ rate = \frac{uplift\ rate}{sin(\alpha)} \tag{7.1}$$

Berthet et al. (2014) proposed that based on the above assumption which provides a minimum TFT dip angle of 30°, the convergence along central Bhutan is mostly accommodated along the TFT. However, as determined from our study, the steeper dip angle would lead to greater possibility of slip partitioning along others faults in the region. In case of a constant uplift rate of 8.8±2.1 mm/year that correlates with the hypothesis of no information on the sampling location, the overthrusting slip rate can be estimated from a less straight forward modeling based on the obtained geometry. Adopting dislocations embedded in a homogeneous half-space (Okada, 1985), the calculated slip rate exhibits high variations along the profile (Figure 7.1c). The overthrusting slip rate will range from 20-40 mm/year above the very shallow part of the fault to 10-20 mm/year in the northern side of the profile. By using the GPS convergence rate as the maximum value for the slip rate, we estimate threshhold minimum distance of 8m for steepening of the TFT and slip accommodation of at least 10±2 mm/year of the 17 mm/year GPS convergence along the TFT. The resulting uncertainties associated with the slip rate estimation mainly comes from the location of samples for terrace dating and fault geometry estimated from the stochastic inversion method.

In Phuentsholing and Lhamoizingkha, since no detailed studies to assess the uplift rate has been carried, a reliable estimate of the slip rate cannot be performed for these two sites. However, in contrary to the site in Sarpang, where active faults have been mapped south

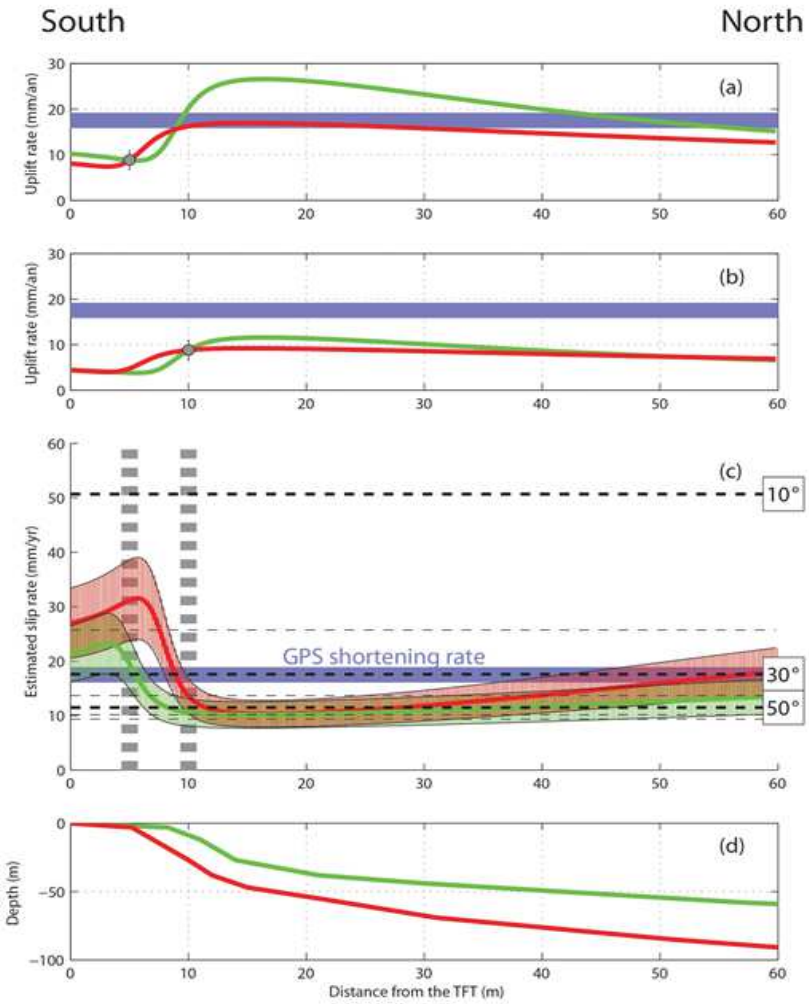

Figure 7.1: Estimated slip rate inferred from both fault geometry and observed uplift rate. (a) Uplift rate along the study profile. Red and green curves are show two end-member models obtained for fault geometry. Thick blue line denotes the far-field shortening rate estimated from GPS measurements (Marechal et al., 2016). It corresponds to the upper limit of uplift rate, which can be associated with a theoretical vertical fault. Gray circle is the observed uplift rate assuming a northward distance of 5 m from the TFT as reported by Berthet et al., 2014. (b) Same as (a) except a northward distance of 10 m is assumed. (c) Estimated slip along the TFT at depth assuming a constant uplift rate along the study profile for the two-end member models denoted by red and green curves. Hatched area around the curves is associated with uplift rate uncertainties. The thick grey dashed lines point out the area of uplift rate assuming a northward distance from the TFT of 5 m and 10 m, respectively. Note that within this area, the uncertainties in the uplift rate spikes up close to the TFT and decreases away from the front towards the north. Thick blue line denotes the far-field shortening rate estimated from GPS measurements (Marechal et al., 2016), which is the upper limit of slip rate. The slip obtained from rigid blocks model with a constant dip angles ranging from 10° to 60° is given by black dashed lines. (d) Fault geometry used.

of our site (Dasgupta et al., 2013), no such active structures have been reported south of our sites in Phuentsholing and Lhamoizingkha. Moreover, field observations and review of satellite images show no prominent elevated topographic features exist south of study sites in Phuentsholing and Lhamoizingkha, which may be interpreted that in these areas the MFT is the southern most active frontal thrust. Further, if there exists any slip partitioning in these areas, it could most likely be along the MBT, located towards north of the MFT. However, Marechal et al. (2016) proposed that only in eastern Bhutan the MBT is creeping and is part of the active thrusting front.

7.2.2 Tectonic deformation at the front

Our new constraints on the geometry of the TFT and resulting slip rate estimate at Sarpang permit us to propose that at least 60% of the convergence between India and the Himalayas in central Bhutan is accommodated along the TFT. This entails that besides the TFT there exists other active faults in the area. Similar observations of slip partitioning have been reported in the Kangra section of the Himalayas where out-of-sequence sequence fault such as the Jwalamukhi Thrust (JMT) accommodates a part of the sub-Himalayan shortening (Dey et al., 2016). At Sarpang site, the most likely active faults, besides the TFT, include the north-propagating active Frontal Back Thrust (FBT) documented by Dasgupta et al. (2013) in Brahmaputra plain and the Main Boundary Thrust (MBT), which accommodates present day deformation in eastern Bhutan (Marechal et al., 2016).

Based on detailed geomorphological and paleoseismic study, Le Roux-Mallouf (2016) and Le Roux-Mallouf et al. (submitted) observed that the cumulative vertical slip in Piping and Lhamoizingkha corresponds to a uplift rate of 9.5 mm/year which is consistent with the uplift rate of 8.8±2.1 mm/year proposed by Berthet et al. (2014) for the Sarpang frontal section. In absence of additional reported active faults south of MFT in Piping and Lhamoizingkha, it may suggests that the Himalayan convergence is mostly accommodated along the MFT. However, information on the geometry of MFT at shallow depth is necessary to accurately assess coupling in these areas.

In Phuentsholing frontal area, due to lack of terrace dating information and its corresponding uplift rate assessment, the deformation mechanism in this area cannot be ascertained. However, based on preliminary geometry of the MFT obtained from the geophysical investigation together with absence of active tectonic features south of the study area, it can be deduced that most of the convergence in the Phuentsholing area is being accommodated

along the MFT, which is in agreement with GPS observation (Marechal et al., 2016).

In terms of historical events rupturing the Bhutanese frontal areas, at least two major events have taken place along the TFT in the south central Bhutan in Sarpang–the latest event occurred in 1714 (Berthet et al., 2014; Le Roux-Mallouf et al., 2016; Hetényi et al., 2016). Further, in Piping area, the longest continuous record of paleo-earthquakes along the Himalayan arc have been uncovered from the detailed study of 18 m thick sedimentary sequence dated from 16 radiocarbon samples (Le Roux-Mallouf, 2016; Le Roux-Mallouf et al., submitted). They found that at least 6 surface-rupturing events occurred along this section in south western Bhutan during the last 3500 years with an average earthquake recurrence interval of 550±300 years for the MFT in Bhutan.

Based on results obtained from this thesis, we conclude that at least 60 % of the far-field GPS convergence of ca. 17 mm/year is being accommodated on the MFT in southern Bhutan suggesting high seismic hazard potential of this fault. Moreover, this also mean that the remaining convergence is being accommodated on other faults such as the MBT and FBT, which could be potential sources of future large events. Since no geomorphology and paleoseismic works have been performed on the MBT or FBT to document paleo-earthquakes, it may be important to study and assess any evidences of past large earthquakes on these faults. Another important implication could be due to the possible slip distribution on different faults, the recurrence interval between coseismic events would require longer time period for the stress buildup to attain the rupture threshold.

7.3 Future works

This thesis presented the results of the near-surface geophysical methods conducted at three sites in Sarpang, Phuentsholing and Lhamoizingkha to constrain the geometry of active thrust system that stretches along the approximately 320 km long Bhutanese frontal area. Prior to the start of cooperation research study with the University of Montpellier (France) and ETH Zürich, way back in 2010, no detailed information existed on the large scale historical earthquakes and the deformation characteristics of frontal thrust system in the Bhutan Himalaya, which is key for assessing seismic hazard in the region. Following the start of the cooperation research study, several studies have been conducted by combing approaches such as GPS, gravity, geomorphology, paleoseismic and near-surface geophysics. This has greatly improved our understanding of the Himalayan geodynamics and more importantly, in determining the

key parameters such as the uplift rate and geometry of the shallow surface MFT which is crucial for estimating the overthrusting slip rates along the frontal thrust faults for proper seismic hazard assessment in the region. However, more such multi-disciplinary approaches combining seismology, geomorphology, paleoseismology and near-surface geophysics needs to be pursued to document large historical events along the MFT and to determine lateral variations along the front. Based on the studies conducted so far, we outline some of the important follow up research works that deserve special consideration and prioritization. This effort will undoubtedly affirm the findings from this study which indicate that the common method of random sample dating at the front to estimate the uplift rate and projection of fault geometry based on dip angle of the MFT observed on the surface to constraint the fault geometry at shallow depth is not sufficient to characterize the deformation pattern and slip rate determination at the front.

- To assess local variability of the TFT, near-surface geophysical studies may be conducted few 100s of metres east and west of the Sarpang study area. Moreover, taking up combined geomorphology and geophysical investigation along the front in eastern Bhutan would be important to study lateral variation in the geometry of the MFT and determine its implication in the present-day strain partitioning.

- The geometry of the MFT in Phuentsholing site remains poorly constrained due to site conditions and limited a priori information. Moreover, the overthrusting slip rate in this area is unknown since no dating of terraces were done. Therefore, terrace carbon-dating could be conducted to determine the uplift rate in the area. However, conduct of additional near-surface geophysical investigation in and around the site in Phuentsholing area is rather challenging due to thick cover of alluvial deposits.

- To the west of Chokott Creek paleoseismic site in Lhamoizingkha, the present geophysical study couldn't image the geometry of the MFT mainly because the geophysical line selected based on the tentative inferred location of the MFT was apparently not the correct location. The actual location of the MFT is later interpreted to be slightly north of our geophysical profile. Since we have adequate information on the uplift rate estimated from the terrace dating in Lhamoizingkha area, it is highly recommended to perform near-surface geophysical line due north of the present line with reference to the MFT inferred by Le Roux-Mallouf (2016).

– The most interesting and significant area studied so far in the frontal areas in Bhutan is located on the left bank of the Wang Chhu in Piping. From the spectacular geomorphological features exposure in Piping, Le Roux-Mallouf et al. (submitted) documented the longest continuous record of paleo-earthquakes along the Himalayan arc showing at least 6 surface-rupturing events having occurred along this section in south western Bhutan during the last 3500 years. However, our effort to perform geophysical lines at this section was not realized due to unfavorable site conditions for geophysical study at the paleoseismic trench; the ideal site for performing geophysical study located on the right side of Wang Chhu was not accessible at the time of our field work. Nevertheless, given the significance of this site, future near-surface geophysical survey on the right side of the Wang Chhu opposite to the paleoseismic trench site will be extremely important to constraint the geometry of the MFT and the corresponding overthrusting slip rate in this area.

REFERENCES

Ader, T., Avouac, J. P., Liu-Zeng, J., Lyon-Caen, H., Bollinger, L., Galetzka, J., Genrich, J., Thomas, M., Chanard, K., Sapkota, S. N., Rajaure, S., Shrestha, P., Ding, L., & Flouzat, M. (2012). Convergence rate across the Nepal Himalaya and interseismic coupling on the Main Himalayan Thrust: Implications for seismic hazard. *Journal of Geophysical Research: Solid Earth*, *117*(4), 1–16.

Agnew, D. C., et al. (2002). History of seismology. *International handbook of earthquake and engineering seismology*, *81*, 3–11.

Airy, G. B. (1855). On the computation of the effect of the attraction of mountain-masses, as disturbing the apparent astronomical latitude of stations in geodetic surveys. *Philosophical Transactions of the Royal Society of London*, *145*, 101–104.

Ambraseys, N., & Jackson, D. (2003). A note on early earthquakes in northern India and southern Tibet. *Current Science*, *84*(4), 570–582.

Ansari, M. A., Khan, P. K., Tiwari, V. M., & Banerjee, J. (2014). Gravity anomalies, flexure, and deformation of the converging Indian lithosphere in Nepal and Sikkim-Darjeeling Himalayas. *International Journal of Earth Sciences*, *103*(6), 1681–1697.

Avouac, J.-P. (2008). Dynamic processes in extensional and compressional settings-mountain building: from earthquakes to geological deformation. *Treatise on Geophysics*, *6*, 377–439.

Avouac, J.-P. (2015). Mountain Building: From earthquakes to geological deformation. In *Treatise on geophysics* (Vol. 6, pp. 381–432).

Backus, G., & Gilbert, F. (1970). Uniqueness in the inversion of inaccurate gross earth data. *Philosophical Transactions of the Royal Society of London A: Mathematical, Physical and Engineering Sciences*, *266*(1173), 123–192.

Backus, G. E., & Gilbert, J. F. (1967). Numerical Applications of a Formalism for Geophysical Inverse Problems. *Geophysical Journal International*, *13*(1-3), 247–276.

Baillie, I., & Norbu, C. (2004). Climate and other factors in the development of river and interfluve profiles in Bhutan, Eastern Himalayas. *Journal of Asian Earth Sciences*, *22*(5), 539–553.

Ben-Menahem, A. (1995). Review A Concise History of Mainstream Seismology : Origins , Legacy , and Perspectives. *Bulletin of the Seismological Society of America*, *85*(4), 1202–1225.

Berge, M. A. (2014). Electrical resistivity tomography investigations on a paleoseismological trenching study. *Journal of Applied Geophysics*, *109*, 162–174.

Berthet, T., Hetényi, G., Cattin, R., Sapkota, S. N., Champollion, C., Kandel, T., Doerflinger, E., Drukpa, D., Lechmann, S., & Bonnin, M. (2013). Lateral uniformity of India Plate strength over central and eastern Nepal. *Geophysical Journal International*, *195*(3), 1481–1493.

Berthet, T., Ritz, J. F., Ferry, M., Pelgay, P., Cattin, R., Drukpa, D., Braucher, R., & Hetényi, G. (2014). Active tectonics of the eastern Himalaya: New constraints from the first tectonic geomorphology study in southern Bhutan. *Geology*, *42*(5), 427–430.

Besse, J., Courtillot, V., Pozzi, J. P., Westphal, M., & Zhou, Y. X. (1984). Palaeomagnetic estimates of crustal shortening in the Himalayan thrusts and Zangbo suture. *Nature*, *311*(5987), 621–626.

Bettinelli, P., Avouac, J. P., Flouzat, M., Jouanne, F., Bollinger, L., Willis, P., & Chitrakar, G. R. (2006). Plate motion of India and interseismic strain in the Nepal Himalaya from GPS and DORIS measurements. *Journal of Geodesy*, *80*(8-11), 567–589.

Bilham, R. (2004). Earthquakes in India and the Himalaya: Tectonics, geodesy and history. *Annals of Geophysics*, *47*(2-3), 839–858.

Bilham, R., & England, P. (2001). Plateau “pop-up” in the great 1897 Assam earthquake. *Nature*, *410*(6830), 806–809.

Bilham, R., Gaur, V. K., & Molnar, P. (2001). Himalayan seismic hazard. *Science*, *293*(5534), 1442–1444.

Bilham, R., Larson, K., & Freymueller, J. (1997). GPS measurements of present-day convergence across the Nepal Himalaya. *Nature*, *386*(6620), 61–64.

Binley, A. (2015). *Tools and Techniques: Electrical Methods* (Vol. 11). Elsevier B.V.

Binley, A., & Kemna, A. (2005). Electrical Methods, p. 129-156. In Hubbard, S., Rubin,Y. (eds.). *Hydrogeophysics. Springer*.

Bollinger, L., Avouac, J., Cattin, R., & Pandey, M. (2004). Stress buildup in the Himalaya. *Journal of Geophysical Research: Solid Earth*, *109*(B11).

Boness, N. L., & Zoback, M. D. (2004). Stress-induced seismic velocity anisotropy and physical properties in the SAFOD Pilot Hole in Parkfield, CA. *Geophysical Research Letters*, *31*(15).

Bouilhol, P., Jagoutz, O., Hanchar, J. M., & Dudas, F. O. (2013). Dating the India-Eurasia collision through arc magmatic records. *Earth and Planetary Science Letters*, *366*, 163–175.

Brown, L., Zhao, W., Nelson, K., Hauck, M., et al. (1996). Bright spots, structure, and magmatism in southern Tibet from INDEPTH seismic reflection profiling. *Science*, *274*(5293), 1688.

Burgess, W. P., Yin, A., Dubey, C. S., Shen, Z.-K., & Kelty, T. K. (2012). Holocene shortening across the Main Frontal Thrust zone in the eastern Himalaya. *Earth and Planetary Science Letters*, *357*, 152–167.

Butler, D. K. (2005). *Near-surface geophysics*. Society of Exploration Geophysicists.

Cattin, R., & Avouac, J. P. (2000). Modeling mountain building and the seismic cycle in the Himalaya of Nepal. *Journal of Geophysical Research*, *105*(B6), 13389.

Cattin, R., Martelet, G., Henry, P., Avouac, J. P., Diament, M., & Shakya, T. R. (2001). Gravity anomalies, crustal structure and thermo-mechanical support of the Himalayas of Central Nepal. *Geophys. j. int.*, *147*, 381–392.

Cattin, R., Mazzotti, S., & Baratin, L. M. (2015). GravProcess: An easy-to-use MATLAB software to process campaign gravity data and evaluate the associated uncertainties. *Computers and Geosciences*, *81*, 20–27.

Chaturvedi, R., & Mishra, S. (1978). Geological map of Sinchula-Sami khola area, Phuntsholing, Chirang and Gaylegphug Districts, Bhutan. *Geological Survey of India*.

Clark, M. K., & Bilham, R. (2008). Miocene rise of the Shillong Plateau and the beginning of the end for the Eastern Himalaya. *Earth and Planetary Science Letters*, *269*(3), 337–351.

Coutand, I., Barrier, L., Govin, G., Grujic, D., Hoorn, C., Dupont-Nivet, G., & Najman, Y. (2016). Late Miocene-Pleistocene evolution of India-Eurasia convergence partitioning between the Bhutan Himalaya and the Shillong plateau: New evidences from foreland basin deposits along the Dungsam Chu section, Eastern Bhutan. *Tectonics*.

Coutand, I., Whipp, D. M., Grujic, D., Bernet, M., Fellin, M. G., Bookhagen, B., Landry, K. R., Ghalley, S., & Duncan, C. (2014). Geometry and kinematics of the Main Himalayan Thrust and Neogene crustal exhumation in the Bhutanese Himalaya derived from inversion of multithermochronologic data. *Journal of Geophysical Research: Solid Earth*, *119*(2), 1446–1481.

Dahlin, T., & Zhou, B. (2004). A numerical comparison of 2D resistivity imaging with 10 electrode arrays. *Geophysical Prospecting*, *52*(5), 379–398.

Dasgupta, S., Mazumdar, K., Moirangcha, L. H., Gupta, T. D., & Mukhopadhyay, B. (2013). Seismic landscape from Sarpang re-entrant, Bhutan Himalaya foredeep, Assam, India: Constraints from geomorphology and geology. *Tectonophysics*, *592*, 130–140.

De, R., & Kayal, J. (2003). Seismotectonic model of the Sikkim Himalaya: Constraint from microearthquake surveys. *Bulletin of the Seismological Society of America*, *93*(3), 1395–1400.

DeCelles, P. G., Robinson, D. M., & Zandt, G. (2002). Implications of shortening in the Himalayan fold-thrust belt for uplift of the Tibetan Plateau. *Tectonics*, *21*(6).

deGroot Hedlin, C., & Constable, S. (1990). Occam's inversion to generate smooth, two-dimensional models from magnetotelluric data. *Geophysics*, *55*(12), 1613–1624.

de Lima, O. A., & Sharma, M. M. (1990). A grain conductivity approach to shaly sandstones. *Geophysics*, *55*(10), 1347–1356.

Demanet, D., Pirard, E., Renardy, F., & Jongmans, D. (2001). Application and processing of geophysical images for mapping faults. *Computers and Geosciences*, *27*(9), 1031–1037.

DeMets, C., Gordon, R. G., Argus, D. F., & Stein, S. (1994). Effect of recent revisions to the geomagnetic reversal time scale on estimates of current plate motions. *Geophysical research letters*, *21*(20), 2191–2194.

Dewey, J., & Byerly, P. (1969). The early history of seismometry (to 1900). *Bulletin of the Seismological Society of America*, *59*(1), 183–227.

Dewey, J. F., & Bird, J. M. (1970). Mountain Belts and the New Global Tectonics. *Journal of Geophysical Research*, *75*(14), 2625–2647.

Dey, S., Thiede, R. C., Schildgen, T. F., Wittmann, H., Bookhagen, B., Scherler, D., & Strecker, M. R. (2016). Holocene internal shortening within the northwest Sub-Himalaya: Out-of-sequence faulting of the Jwalamukhi Thrust, India. *Tectonics*.

Diebold, J. B., & Stoffa, P. L. (1981). The traveltime equation, tau-p mapping, and inversion of common midpoint data. *Geophysics*, *46*(3), 238–254.

Diehl, T., Singer, J., Hetényi, G., Grujic, D., Clinton, J., Giardini, D., Kissling, E., Group, G. W., et al. (2017). Seismotectonics of Bhutan: Evidence for segmentation of the Eastern Himalayas and link to foreland deformation. *Earth and Planetary Science Letters*, *471*, 54–64.

Dix, C. H. (1955). Seismic velocities from surface measurements. *Geophysics*, *20*(1), 68–86.

Drukpa, D., Stephanie, G., Rodolphe, C., Kinley, N., & Nicolas, L. M. (2017). Impact of near-surface fault geometry on secular slip rate assessment derived from uplifted river terraces: Implications for convergence accommodation across the frontal thrust in southern Central Bhutan. *Geophysical Journal International*.

Drukpa, D., Velasco, A. A., & Doser, D. I. (2006). Seismicity in the Kingdom of Bhutan (1937-2003): Evidence for crustal transcurrent deformation. *Journal of Geophysical Research: Solid Earth*, *111*(6), 6301.

Duncan, C., Masek, J., & Fielding, E. (2003). How steep are the Himalaya? Characteristics and implications of along-strike topographic variations. *Geology*, *31*(1), 75–78.

Gabo, J. A. S., Dimalanta, C. B., Yumul Jr., G. P., Faustino-Eslava, D. V., & Imai, A. (2015). Terrane Boundary Geophysical Signatures in Northwest Panay, Philippines: Results from Gravity, Seismic Refraction and Electrical Resistivity Investigations. *Terrestrial, Atmospheric and Oceanic Sciences*, *26*(6), 663.

Gahalaut, V. K., & Arora, B. R. (2012). Segmentation of Seismicity Along the Himalayan Arc Due to Structural Heterogeneities in the Under-Thrusting Indian Plate and Overriding Himalayan Wedge. *Episodes*, *35*(4), 493–500.

Gahalaut, V. K., Rajput, S., & Kundu, B. (2011). Low seismicity in the Bhutan Himalaya and the stress shadow of the 1897 Shillong Plateau earthquake. *Physics of the Earth and Planetary Interiors*, *186*(3-4), 97–102.

Gansser, A. (1981). The geodynamic history of the Himalaya. *Zagros Hindu Kush Himalaya Geodynamic Evolution*, 111–121.

Grujic, D., Coutand, I., Bookhagen, B., Bonnet, S., Blythe, A., & Duncan, C. (2006). Climatic forcing of erosion, landscape, and tectonics in the Bhutan Himalayas. *Geology*, *34*(10), 801–804.

Grujic, D., Hollister, L. S., & Parrish, R. R. (2002). Himalayan metamorphic sequence as an orogenic channel: insight from Bhutan. *Earth and Planetary Science Letters*, *198*(1), 177–191.

Hadamard, M. (1902). On problems in partial derivatives, and their physical significance. *Princeton University Bulletin*, *13*, 82–88.

Hammer, P., Berthet, T., Hetényi, G., Cattin, R., Drukpa, D., Chophel, J., Lechmann, S., Moigne, N. L., Champollion, C., & Doerflinger, E. (2013). Flexure of the India plate underneath the Bhutan Himalaya. *Geophysical Research Letters*, *40*(16), 4225–4230.

Hetényi, G., Cattin, R., Berthet, T., Le Moigne, N., Chophel, J., Lechmann, S., Hammer, P., Drukpa, D., Sapkota, S. N., Gautier, S., et al. (2016). Segmentation of the Himalayas as revealed by arc-parallel gravity anomalies. *Scientific Reports*, *6*.

Hetényi, G., Cattin, R., Brunet, F., Bollinger, L., Vergne, J., Nábělek, J. L., & Diament, M. (2007). Density distribution of the India plate beneath the Tibetan plateau: Geophysical and petrological constraints on the kinetics of lower-crustal eclogitization. *Earth and Planetary Science Letters*, *264*(1-2), 226–244.

Hetényi, G., Roux-Mallouf, L., Berthet, T., Cattin, R., Cauzzi, C., Phuntsho, K., Grolimund, R., et al. (2016). Joint approach combining damage and paleoseismology observations constrains the 1714 AD Bhutan earthquake at magnitude 8±0.5. *Geophysical Research Letters*, *43*(20).

Hirn, A., Lepine, J.-C., Jobert, G., Sapin, M., Wittlinger, G., Zhong Xin, X., En Yuan, G., Xiang Jing, W., Ji Wen, T., Shao Bai, X., Pandey, M. R., & Tater, J. M. (1984). *Crustal structure and variability of the Himalayan border of Tibet* (Vol. 307) (No. 5946).

Hung, J.-H., Ma, K.-F., Wang, C.-Y., Ito, H., Lin, W., & Yeh, E.-C. (2009). Subsurface structure, physical properties, fault-zone characteristics and stress state in scientific drill holes of Taiwan Chelungpu Fault Drilling Project. *Tectonophysics*, *466*(3), 307–321.

Isacks, B., J. O., & Sykes, L. R. (1968). Seismology and the New Global Tectonics. *Journal of Geophysical Research*, *73*(18).

Jackson, M., & Bilham, R. (1994). Constraints on Himalayan deformation inferred from vertical velocity fields in Nepal and Tibet. *Journal of Geophysical Research: Solid Earth*, *99*(B7), 13897–13912.

Jeppson, T. N., Bradbury, K. K., & Evans, J. P. (2010). Geophysical properties within the San Andreas Fault Zone at the San Andreas Fault Observatory at Depth and their relationships to rock properties and fault zone structure. *Journal of Geophysical Research: Solid Earth*, *115*(B12).

Jouanne, F., Mugnier, J.-L., Gamond, J., Le Fort, P., Pandey, M., Bollinger, L., Flouzat, M., & Avouac, J. (2004). Current shortening across the Himalayas of Nepal. *Geophysical Journal International*, *157*(1), 1–14.

Kaiser, A. E., Green, A. G., Campbell, F. M., Horstmeyer, H., Manukyan, E., Langridge, R. M., McClymont, A. F., Mancktelow, N., Finnemore, M., & Nobes, D. C. (2009). Ultrahigh-resolution seismic reflection imaging of the Alpine Fault, New Zealand. *Journal of Geophysical Research: Solid Earth*, *114*(11), 1–15.

Kayal, J. (2008). *Microearthquake seismology and seismotectonics of South Asia*. Springer Science & Business Media.

Kayal, J., Arefiev, S. S., Baruah, S., Tatevossian, R., Gogoi, N., Sanoujam, M., Gautam, J., Hazarika, D., & Borah, D. (2010). The 2009 Bhutan and Assam felt earthquakes (Mw 6.3 and 5.1) at the Kopili fault in the northeast Himalaya region. *Geomatics, Natural Hazards and Risk*, *1*(3), 273–281.

Kayal, J. R., Arefiev, S. S., Baruah, S., Tatevossian, R., Gogoi, N., Sanoujam, M., Gautam, J. L., Hazarika, D., & Borah, D. (2010). The 2009 Bhutan and Assam felt earthquakes (Mw 6.3 and 5.1) at the Kopili fault in the northeast Himalaya region. *Geomatics, Natural Hazards and Risk*, *1*(3), 273–281.

Kearey, P., Brooks, M., & Hill, I. (2013). *An introduction to geophysical exploration*. John Wiley & Sons.

Keller, G. V., & Frischknecht, F. C. (1966). *Electrical methods in geophysical prospecting*. Pergamon.

Khattri, K. (1987). Great earthquakes, seismicity gaps and potential for earthquake disaster along the Himalaya plate boundary. *Tectonophysics*, *138*(1), 79–92.

Klein, J. D., & Sill, W. R. (1982). Electrical properties of artificial clay bearing sandstone. *Geophysics*, *47*(11), 1593–1605.

Knopf, A. (1948). The geosynclinal theory. *Geological Society of America Bulletin*, *59*(7), 649–670.

Lavé, J., & Avouac, J. P. (2000). Active folding of fluvial terraces across the Siwaliks Hills, Himalayas of central Nepal. *Journal of Geophysical Research*, *105*(B3), 5735.

Le Fort, P. (1986). Metamorphism and magmatism during the Himalayan collision. *Collision Tectonics*, *19*(19), 159–172.

Le Roux-Mallouf, R., Ferry, M., Ritz, J., Cattin, R., & Drukpa, D. (submitted). A 3500-yr-long paleoseismic record for the Himalayan Main Frontal Thrust (Western Bhutan). *Journal of Geophysical Research*.

Le Roux-Mallouf, R., Ferry, M., Ritz, J.-f., Berthet, T., Cattin, R., & Drukpa, D. (2016). First paleoseismic evidence for great surface-rupturing earthquakes in the Bhutan Himalayas. *Journal of Geophysical Research: Solid Earth*, 1–13.

Le Fort, P. (1975). Himalayas: the collided range. Present knowledge of the continental arc. *American Journal of Science*, *275*(1), 1–44.

Le Roux-Mallouf, R. (2016). Holocene deformation in the Bhutan Himalaya through geomorphological and paleoseismological approaches. *Geosciences Montpellier, University of Montpellier*, *Doctorate*(November), 300.

Le Roux-Mallouf, R., Godard, V., Cattin, R., Ferry, M., Gyeltshen, J., Ritz, J.-F., Drupka, D., Guillou, V., Arnold, M., Aumaître, G., et al. (2015). Evidence for a wide and gently dipping Main Himalayan Thrust in western Bhutan. *Geophysical Research Letters*, *42*(9), 3257–3265.

Loke, M. (1999). Electrical imaging surveys for environmental and engineering studies. *A practical guide to*, *2*.

Loke, M., & Barker, R. D. (1996). Rapid least-squared inversion of apparent resisitivity pseudosections by a quasi-Newton method. *Geophysical prospecting*, *44*(1), 131–152.

Loke, M. H. (2015). Tutorial : 2-D and 3-D electrical imaging surveys. *Geotomo Software Malaysia*(July), 176.

Long , McQuarrie, N., Tobgay, T., Grujic, D., & Hollister, L. (2011). Geologic map of Bhutan. *Journal of Maps*, *7*(1), 184–192.

Long, McQuarrie, N., Tobgay, T., & Grujic, D. (2011). Geometry and crustal shortening of the Himalayan fold-thrust belt, eastern and central Bhutan. *Geological Society of America Bulletin*, B30203–1.

Loris, I., Douma, H., Nolet, G., Daubechies, I., & Regone, C. (2010). Nonlinear regularization techniques for seismic tomography. *Journal of Computational Physics*, *229*(3), 890–905.

Louis, I. F., Raftopoulos, D., Goulis, I., & Louis, F. I. (2002). Geophysical imaging of faults and fault zones in the urban complex of Ano Liosia neogene basin, Greece: synthetic simulation approach and field investigation. *International Conference on Earth Sciences and Electronics*, *2002*(October), 269–285.

Lyon-Caen, H., & Molnar, P. (1983). Constraints on the structure of the Himalaya from an analysis of gravity anomalies and a flexural model of the lithosphere. *Journal of Geophysical Research: Solid Earth*, *88*(B10), 8171–8191.

Lyon-Caen, H., & Molnar, P. (1985). Gravity anomalies, flexure of the Indian Plate, and the structure, support and evolution of the Himalaya and Ganga Basin. *Tectonics*, *4*(6), 513.

Marechal, A., Mazzotti, S., Cattin, R., Cazes, G., Vernant, P., Drukpa, D., Thinley, K., Tarayoun, A., Roux-Mallouf, L., Thapa, B. B., et al. (2016). Evidence of interseismic coupling variations along the bhutan himalayan arc from new gps data. *Geophysical Research Letters*.

Menke, W. (1989). Discrete inverse theory. *Geophysical Data Analysis*, *289*.

Milsom, J. (2007). *Field geophysics* (Vol. 25). John Wiley and Sons.

Molnar, P., & Stock, J. M. (2009). Slowing of India's convergence with Eurasia since 20 Ma and its implications for Tibetan mantle dynamics. *Tectonics*, *28*(3), 1–11.

Molnar, P., & Tapponnier, P. (1975). Cenozoic Tectonics of Asia: Effects of a Continental Collision: Features of recent continental tectonics in Asia can be interpreted as results of the India-Eurasia collision. *Science*, *189*(4201), 419–426.

Morandi, S., & Ceragioli, E. (2002). Integrated interpretation of seismic and resistivity images across the «Val d'Agri» graben (Italy). *Annals of Geophysics*, *45*(2).

Morey, D., & Schuster, G. T. (1999). Palaeoseismicity of the Oquirrh Fault, Utah from shallow seismic tomography. *Geophysical Journal International*, *138*(1), 25–35.

Mosegaard, K., & Tarantola, A. (1995). Monte Carlo sampling of solutions to inverse problems. *Journal of Geophysical Research: Solid Earth*, *100*(B7), 12431–12447.

Murphy, M., & Yin, A. (2003). Structural evolution and sequence of thrusting in the Tethyan fold-thrust belt and Indus-Yalu suture zone, southwest Tibet. *Geological Society of America Bulletin*, *115*(1), 21–34.

Nábělek, J., Hetényi, G., Vergne, J., Sapkota, S., Kafle, B., Jiang, M., Su, H., Chen, J., Huang, B.-S., et al. (2009). Underplating in the Himalaya-Tibet collision zone revealed by the Hi-CLIMB experiment. *Science*, *325*(5946), 1371–1374.

Nelson, K. D., Zhao, W., Brown, L., Kuo, J., Che, J., Liu, X., Klemperer, S., Makovsky, Y., Meissner, R., Mechie, J., et al. (1996). Partially molten middle crust beneath southern Tibet: synthesis of project INDEPTH results. *Science*, *274*(5293), 1684–1688.

Nguyen, F. (2005). Near-surface Geophysical Imaging and Detection of Slow Active Faults. *Department of Georessources, Geotechnologies and Construction Materials*, *Doctorate*(May), 359.

Nguyen, F., Garambois, S., Chardon, D., Hermitte, D., Bellier, O., & Jongmans, D. (2007). Subsurface electrical imaging of anisotropic formations affected by a slow active reverse fault, Provence, France. *Journal of Applied Geophysics*, *62*(4), 338–353.

Nguyen, F., Garambois, S., Jongmans, D., Pirard, E., & Loke, M. H. (2005). Image processing of 2D resistivity data for imaging faults. *Journal of Applied Geophysics*, *57*(4), 260–277.

Ni, J., & Barazangi, M. (1984). Seismotectonics of the Himalayan collision zone: Geometry of the underthrusting Indian plate beneath the Himalaya. *Journal of Geophysical Research: Solid Earth*, *89*(B2), 1147–1163.

Okada, Y. (1985). Surface deformation due to shear and tensile faults in a half-space. *Bulletin of the seismological society of America*, *75*(4), 1135–1154.

Okpoli, C. C. (2013). Sensitivity and resolution capacity of electrode configurations. *International Journal of Geophysics*, *2013*(Dic).

Palmer, D. (1981). An introduction to the generalized reciprocal method of seismic refraction interpretation. *Geophysics*, *46*(11), 1508–1518.

Pandey, M., Tandukar, R., Avouac, J., Lave, J., & Massot, J. (1995). Interseismic strain accumulation on the Himalayan crustal ramp (Nepal). *Geophysical Research Letters*, *22*(7), 751–754.

Pandey, M., Tandukar, R., Avouac, J., Vergne, J., & Heritier, T. (1999). Seismotectonics of the nepal himalaya from a local seismic network. *Journal of Asian Earth Sciences*, *17*(5), 703–712.

Patriat, P., & Achache, J. (1984). India–Eurasia collision chronology has implications for crustal shortening and driving mechanisms of plates. *Nature*, *311*(18), 615–621.

Powell, C. M., & Conaghan, P. (1973). Plate tectonics and the Himalayas. *Earth and Planetary Science Letters*, *20*(1), 1–12.

Pratt, J. H. (1855). On the attraction of the Himalaya Mountains, and of the elevated regions beyond them, upon the plumb-line in India. *Philosophical Transactions of the Royal Society of London*, *145*, 53–100.

Ramirez, A. L., Nitao, J. J., Hanley, W. G., Aines, R., Glaser, R. E., Sengupta, S. K., Dyer, K. M., Hickling, T. L., & Daily, W. D. (2005). Stochastic inversion of electrical resistivity changes using a Markov Chain Monte Carlo approach. *Journal of Geophysical Research: Solid Earth*, *110*(B2).

Robain, H., Albouy, Y., Dabas, M., Descloitres, M., Camerlynck, C., Mechler, P., & Tabbagh, A. (1999). The location of infinite electrodes in pole-pole electrical surveys: Consequences for 2D imaging. *Journal of Applied Geophysics*, *41*(4), 313–333.

Robert, X., Van Der Beek, P., Braun, J., Perry, C., & Mugnier, J.-L. (2011). Control of detachment geometry on lateral variations in exhumation rates in the Himalaya: Insights from low-temperature thermochronology and numerical modeling. *Journal of Geophysical Research: Solid Earth*, *116*(B5).

Rohdewald, S. (1999). *Rayfract manual.*

Saric, A. (2014). Stress Changes in the Shillong Plateau and the cause of the Seismic Gap in the Eastern Himalaya. *Department of Earth Science, Dalhousie University, Halifax, Nova Scotia*(March), 125.

Sasaki, Y. (1992). Resolution of resistivity tomography inferred from numerical simulation. *Geophysical prospecting*, *40*(4), 453–463.

Scales, J. A., & Smith, M. L. (2000). *Introductory geophysical inverse theory (draft)*. Samizdat Press.

Schelling, D., & Arita, K. (1991). Trust tectonics , crust shortening , and the structure of the far-eastern Nepal Himalaya. *Tectonics*, *10*(5), 851–862.

Schrott, L., & Sass, O. (2008). Application of field geophysics in geomorphology: Advances and limitations exemplified by case studies. *Geomorphology*, *93*(1-2), 55–73.

Schulte-Pelkum, V., Monsalve, G., Sheehan, A., Pandey, M., Sapkota, S., Bilham, R., & Wu, F. (2005). Imaging the Indian subcontinent beneath the Himalaya. *Nature*, *435*(7046), 1222–1225.

Searle, M., Windley, B., Coward, M., Cooper, D., Rex, A., Rex, D., Tingdong, L., Xuchang, X., Jan, M., Thakur, V., et al. (1987). The closing of Tethys and the tectonics of the Himalaya. *Geological Society of America Bulletin*, *98*(6), 678–701.

Seaton, W. J., & Burbey, T. J. (2002). Evaluation of two-dimensional resistivity methods in a fractured crystalline-rock terrane. *Journal of Applied Geophysics*, *51*(1), 21–41.

Seeber, L., & Armbruster, J. G. (1981). Great Detachment Earthquakes Along the Himalayan Arc and Long-Term Forecasting. *Earthquake Prediction*, *4*, 259–277.

Sengor, A. M. C. (1990). Plate-Tectonics and Orogenic Research after 25 Years - a Tethyan Perspective. *Earth-Science Reviews*, *27*(1-2), 1–201.

Sharma, R. S. (2009). The young and old fold belts. In *Cratons and Fold Belts of India* (pp. 117–141). Springer.

Singer, J., Kissling, E., Diehl, T., & Hetényi, G. (2017). The underthrusting Indian crust and its role in collision dynamics of the Eastern Himalaya in Bhutan: Insights from receiver function imaging. *Journal of Geophysical Research: Solid Earth*, *122*(2), 1152–1178.

Singer, J., Obermann, A., Kissling, E., Fang, H., Hetényi, G., & Grujic, D. (2017). Along-strike variations in the Himalayan orogenic wedge structure in Bhutan from ambient seismic noise tomography. *Geochemistry, Geophysics, Geosystems*, *18*(4), 1483–1498.

Snieder, R. (1998). The role of nonlinearity in inverse problems. *Inverse Problems*, *14*(3), 387–404.

Song, T.-R. A., & Simons, M. (2003). Large trench-parallel gravity variations predict seismogenic behavior in subduction zones. *Science*, *301*(5633), 630–633.

Stevens, V., & Avouac, J.-P. (2015). Coupling on the Main Himalayan Thrust. *Geophys. Res. Lett.*, *42*, 5828–5837.

Suzuki, K., Toda, S., Kusunoki, K., Fujimitsu, Y., Mogi, T., & Jomori, A. (2000). Case studies of electrical and electromagnetic methods applied to mapping active faults beneath the thick quaternary. *Engineering Geology*, *56*(1), 29–45.

Szeliga, W., Hough, S., Martin, S., & Bilham, R. (2010). Intensity, magnitude, location, and attenuation in India for felt earthquakes since 1762. *Bulletin of the Seismological Society of America*, *100*(2), 570–584.

Tang, R. (2013). Sensitivity analysis and application in exploration geophysics. In *AGU Fall Meeting Abstracts* (Vol. 1, p. 2456).

Tapponnier, P., & Molnar, P. (1979). Active faulting and cenozoic tectonics of the tien shan, mongolia, and baykal regions. *Journal of Geophysical Research: Solid Earth*, *84*(B7), 3425–3459.

Tarantola, A. (1987). *Inverse problem theory: Methods for data fitting and parameter estimation*. Elsevier, Amsterdam.

Tarantola, A. (2005). *Inverse problem theory and methods for model parameter estimation*. Society for Industrial and Applied Mathematics.

Telford, W. M., Geldart, L. P., & Sheriff, R. E. (1990). *Applied geophysics* (Vol. 1). Cambridge university press.

Tiwari, V., Rao, M. V., Mishra, D., & Singh, B. (2006). Crustal structure across Sikkim, NE Himalaya from new gravity and magnetic data. *Earth and Planetary Science Letters*, *247*(1), 61–69.

Tobgay, T. (2011). *Tectonics, structure, and metamorphic evolution of the Himalayan fold-thrust belt, western Bhutan* (Unpublished doctoral dissertation). Princeton University.

Tobgay, T., McQuarrie, N., Long, S., Kohn, M. J., & Corrie, S. L. (2012). The age and rate of displacement along the Main Central Thrust in the western Bhutan Himalaya. *Earth and Planetary Science Letters*, *319*, 146–158.

Velasco, A., Gee, V., Rowe, C., Grujic, D., Hollister, L., Hernandez, D., Miller, K., Tobgay, T., Fort, M., & Harder, S. (2007). Using small, temporary seismic networks for investigating tectonic deformation: Brittle deformation and evidence for strike-slip faulting in Bhutan. *Seismological Research Letters*, *78*(4), 446–453.

Vernant, P., Bilham, R., Szeliga, W., Drupka, D., Kalita, S., Bhattacharyya, a. K., Gaur, V. K., Pelgay, P., Cattin, R., & Berthet, T. (2014). Clockwise rotation of the Brahmaputra valley

relative to India: Tectonic convergence in the eastern Himalaya, Naga Hills, and Shillong Plateau. *Journal of Geophysical Research: Solid Earth*(Figure 1), 6558–6571.

Villani, F., Tulliani, V., Sapia, V., Fierro, E., Civico, R., & Pantosti, D. (2015). Shallow subsurface imaging of the Piano di Pezza active normal fault (central Italy) by high-resolution refraction and electrical resistivity tomography coupled with time-domain electromagnetic data. *Geophysical Journal International*, *203*(3), 1482–1494.

Ward, S. H. (1990). Resistivity and induced polarization methods. *Geotechnical and environmental geophysics*, *1*, 147–189.

White, D. (1989). Two-dimensional seismic refraction tomography. *Geophysical Journal International*, *97*(2), 223–245.

Wilson, J. T. (1965). A new class of faults and their bearing on continental drift. *Nature*, *207*, 343–347.

Wise, D. J., Cassidy, J., & Locke, C. A. (2003). Geophysical imaging of the Quaternary Wairoa North Fault, New Zealand: A case study. *Journal of Applied Geophysics*, *53*(1), 1–16.

Yagi, H., Higaki, D., Dorji, Y., & Koike, T. (2002). Active faulting along mout foot of the Bhutan Himalayas near Phuentsholing, south-western Bhutan. *Bhutan Geology*(6), 19-24.

Yin, A., & Harrison, T. M. (2000). Geologic evolution of the Himalayan-Tibetan orogen. *Annual Review of Earth and Planetary Sciences*, *28*(1), 211–280.

Zelt, C., & Smith, R. (1992). Seismic traveltime inversion for 2-D crustal velocity structure. *Geophysical journal international*, *108*(1), 16–34.

Zhang, J., & Ding, L. (2003). East–west extension in Tibetan Plateau and its significance to tectonic evolution. *Chin. J. Geol*, *38*, 179–189.

Zhang, P.-Z., Shen, Z., Wang, M., Gan, W., Bürgmann, R., Molnar, P., Wang, Q., Niu, Z., Sun, J., Wu, J., et al. (2004). Continuous deformation of the Tibetan Plateau from global positioning system data. *Geology*, *32*(9), 809–812.

Zhao, W., Nelson, K., Che, J., Quo, J., Lu, D., Wu, C., & Liu, X. (1993). Deep seismic reflection evidence for continental underthrusting beneath southern Tibet. *Nature*, *366*(6455), 557–559.

Zoback, M. L. (2006). The 1906 earthquake and a century of progress in understanding earthquakes and their hazards. *GSA Today*, *16*(4-5), 4–11.

APPENDIX A

ANNEXES

A.1 First paleoseismic evidence for great surface-rupturing earthquakes in the Bhutan Himalayas

AGU PUBLICATIONS

JGR

Journal of Geophysical Research: Solid Earth

RESEARCH ARTICLE
10.1002/2015JB012733

Key Points:
- Bhutan has been struck by at least two great earthquakes over the last millennium
- The present-day low-seismicity rate observed in Bhutan is not representative of the seismic activity at a longer timescale
- A M_w 9 earthquake from central Nepal to Assam between A.D. 1090 and A.D. 1145 may satisfy all observations

Supporting Information:
- Supporting Information S1

Correspondence to:
R. Le Roux-Mallouf,
lerouxmallouf@gm.univ-montp2.fr

Citation:
Le Roux-Mallouf, R., M. Ferry, J.-F. Ritz, T. Berthet, R. Cattin, and D. Drukpa (2016), First paleoseismic evidence for great surface-rupturing earthquakes in the Bhutan Himalayas, *J. Geophys. Res. Solid Earth*, *121*, doi:10.1002/2015JB012733.

Received 11 DEC 2015
Accepted 14 SEP 2016

First paleoseismic evidence for great surface-rupturing earthquakes in the Bhutan Himalayas

Romain Le Roux-Mallouf[1], Matthieu Ferry[1], Jean-François Ritz[1], Théo Berthet[2], Rodolphe Cattin[1], and Dowchu Drukpa[3]

[1]Géosciences Montpellier, CNRS, UMR5243, Université de Montpellier, Montpellier, France, [2]Department of Earth Sciences, Uppsala University, Uppsala, Sweden, [3]Seismology and Geophysics Division, Department of Geology and Mines, Thimphu, Bhutan

Abstract The seismic behavior of the Himalayan arc between central Nepal and Arunachal Pradesh remains poorly understood due to the lack of observations concerning the timing and size of past major and great earthquakes in Bhutan. We present here the first paleoseismic study along the Himalayan topographic front conducted at two sites in southern central Bhutan. Paleoseismological excavations and related OxCal modeling reveal that Bhutan experienced at least two great earthquakes in the last millennium: one between the seventeenth and eighteenth century and one during medieval times, producing a total cumulative vertical offset greater than 10 m. Along with previous studies that reported similar medieval events in Central Nepal, Sikkim, and Assam, our investigations support the occurrence of either (i) a series of great earthquakes between A.D. 1025 and A.D. 1520 or (ii) a single giant earthquake between A.D. 1090 and A.D. 1145. In the latter case, the surface rupture may have reached a total length of ~800 km and could be associated with an earthquake of magnitude $M_w = 8.7–9.1$.

1. Introduction

The Himalayan belt forms the boundary between the India Plate and the Tibetan plateau and is well known for its recent destructive earthquakes and elevated seismic hazard. However, the timing and size of major earthquakes that have struck this area over the last millennium remain poorly constrained. This is mostly due to uncertainties associated with the chronology, location, and magnitude of pretwentieth century Himalayan earthquakes, which allow a number of possible rupture scenarios.

In spite of an increasing number of paleoseismic studies carried out over the last decade [e.g., *Lavé et al*., 2005; *Yule et al*., 2006; *Kumar et al*., 2010; *Mugnier et al*., 2013; *Bollinger et al*., 2014; *Rajendran et al*., 2015], several areas remain poorly studied. This includes Bhutan, where the lack of observations leads to inconclusive results regarding the seismic behavior for this part of the Himalayas. Hence, the probability of occurrence of a $M_w = 9$ earthquake in this region remains debated [*Kumar et al*., 2010; *Mugnier et al*., 2013; *Srivastava et al*., 2013; *Stevens and Avouac*, 2016]. On the one hand, *Gahalaut et al*. [2011] consider the Bhutan Himalaya as a zone of low seismic activity on the basis of the present-day seismicity. On the other hand, *Kumar et al*. [2010] infer the occurrence of a large medieval earthquake in Bhutan from paleoseismic investigations in Sikkim and Assam.

Here in order to test the possibility of such a great earthquake, we present paleoseismic investigations at two sites along the Himalayan front in Bhutan. After describing the Bhutan Himalaya setting, we summarize historical and geological observations of past major earthquakes in and nearby Bhutan. We then present the results of our paleoseismic investigation carried out in Central Bhutan. Our results, combined with previous studies, allow us to discuss the occurrence of major events in Bhutan and to propose two end-member scenarios for medieval earthquake rupture(s) along the Himalayan arc from central Nepal to Arunachal Pradesh.

2. Seismotectonic Setting of Bhutan Himalaya

2.1. Geological Setting

As is typical along the whole Himalayan arc, Bhutan can be divided into four distinct tectonic units in our study area [*Gansser*, 1964; *Le Fort*, 1975; *McQuarrie et al*., 2008; *Long et al*., 2011]: from north to south, the

Table 1. Great Earthquakes Occurring Between Central Nepal and Arunachal Pradesh Over the Last Millennium

Event	Location	Estimated Magnitude	Reference
2015 Gorkha[a]	28.23°N–84.731°E	M_w 7.8	*Avouac et al.* [2015], *Grandin et al.* [2015], and *Wang and Fialko* [2015]
1950 Assam[a,b,c]	28.38°N–96.68°E	M_w 8.6	*Ben-Menahem et al.* [1974], *Chen and Molnar* [1977], *Triep and Sykes* [1997], and *Kumar et al.* [2010]
1934 Bihar[b,c]	26.86°N–86.59°E	$M_w \sim 8.0$	*Chen and Molnar* [1977], *Ambraseys and Douglas* [2004], and *Sapkota et al.* [2013]
1833–1866 Kathmandu[b]	27.7°N–85.7°E	$M_w \sim 7.5$	*Bilham* [1995], *Rajendran and Rajendran* [2005], and *Szeliga et al.* [2010]
1713 Bhutan[b]	East Bhutan-Arunachal Pradesh	?	*Jackson* [2002], *Ambraseys and Jackson* [2003], and *Berthet et al.* [2014]
1255 Kathmandu[b,c]	East Nepal	?	*Pant* [2002], *Mugnier et al.* [2013], *Sapkota et al.* [2013], and *Bollinger et al.* [2014]
1100 Medieval earthquake(s)[c]	Central Nepal-East Nepal-Sikkim-Assam	Unique event or sequence of ruptures?	*Nakata et al.* [1998], *Upreti et al.* [2000], *Lavé et al.* [2005], and *Kumar et al.* [2010]

[a]Instrumentally recorded.
[b]Historically recorded.
[c]Paleoseismology study.

Tethyan Sedimentary Series (TSS), the Higher Himalaya (HH), the lesser Himalaya (LH), and the Siwaliks. The width of these units varies from Nepal to Bhutan. For instance, the LH is only a few kilometers wide in central Nepal and western Bhutan whereas it is tens of kilometers wide in Sikkim and East Bhutan. All these units are bounded by major faults including the South Tibetan Detachment (STD) to the north, the Main Central Thrust (MCT), the Main Boundary Thrust (MBT), and the Main Frontal Thrust (MFT) to the south, which is the most recent expression of the thrust sequence. While the MFT is well defined in Nepal and coincides with the present-day Himalayan topographic front, its location in Bhutan is less straightforward. The thrust fault that runs along the Bhutan/India border generally corresponds to the MFT, except in the Sarpang area where a 10 km wide reentrant feature directly juxtaposes LH and Quaternary alluvium [*Long et al*., 2011] (Figure 2). There, the most frontal structure expressed in the geomorphology is an anticline (Frontal Back Thrust) that likely accommodates a limited—though undetermined—fraction of the shortening [*Dasgupta et al*., 2013]. Its relationship to the main structures is yet to be explored. Within the reentrant, the main topographic scarp studied here corresponds structurally to the MBT or one of its splays and will be referred to as the Topographic Frontal Thrust (TFT) of Bhutan (Figure 2). South of the TFT is the foreland basin with recent sedimentary infill. At depth, the TFT and the three major north dipping MCT, MBT, and MFT root along the Main Himalayan Thrust (MHT), which is a midcrustal decollement where the India plate is underthrusted beneath the Himalayas and Tibet. Several studies suggest a ramp-flat-ramp-flat geometry for the MHT [e.g., *Zhao et al*., 1993; *Nelson et al*., 1996; *Cattin and Avouac*, 2000; *Nábelek et al*., 2009, *Le Roux-Mallouf et al*., 2015].

In central and east Nepal, the present-day shortening rate of ~20 mm/yr is associated with interseismic coupling on the MHT [e.g., *Stevens and Avouac*, 2015]. At longer timescales, fluvial terrace analyses [e.g., *Lavé and Avouac*, 2000] and tectonostratigraphic studies give a consistent rate, suggesting that the Nepal Himalaya absorbs about 20 km/Myr by localized thrusting since the Middle Miocene. In Bhutan, the present-day localization of deformation is only constrained by sparse GPS measurements in western Bhutan [*Vernant et al*., 2014] and a single estimate of Holocene uplift rate along the TFT in central Bhutan [*Berthet et al*., 2014].

Strain budget from past earthquakes reveals a deficit of seismic moment compared to the moment derived from geodetic measurements [e.g., *Bilham et al*., 2001; *Stevens and Avouac*, 2016]. This suggests the potential occurrence of several $M_w \geq 8.5$ earthquakes along the arc in the next few hundred years or a potential subduction-type $M_w = 9$ earthquake [*Kumar et al*., 2010; *Srivastava et al*., 2013; *Stevens and Avouac*, 2016].

2.2. Large Past Earthquakes

Many large historical earthquakes have been documented along the Himalayan arc (Table 1). However, for Bhutan and regions nearby, information remains limited and partial. In the following, we will focus on the major earthquakes that have been documented within the study area between longitude 88°N and 93°N (Figure 1).

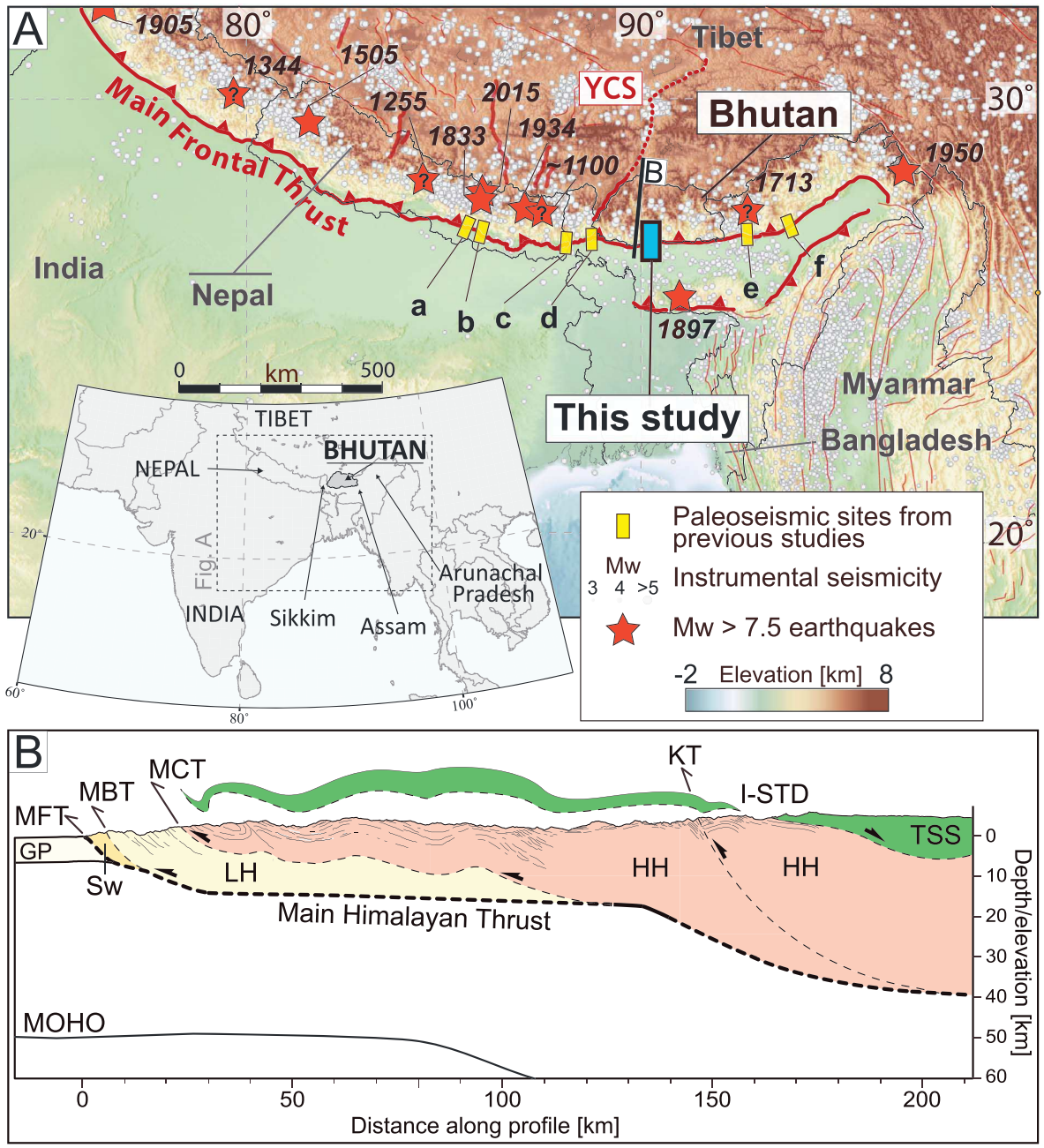

Figure 1. Location of the study area and regional context. (A) Inset shows the location of Bhutan along the Himalayan arc. Instrumental earthquakes of the Himalayan Arc are shown by open circles that show the instrumental seismicity (M_w >3) between 1950 and 2015. Red stars are epicenters of great and large earthquakes from instrumental data, surface damage, and paleoseismological investigations, queried where epicenter location is uncertain. Yellow rectangles are previous paleoseismological studies (a) Marha Khola [Lavé *et al.*, 2005]; (b) Sir Khola [Sapkota *et al.*, 2013]; (c) Hokse [*Nakata et al.*, 1998; *Upreti et al.*, 2000]; (d) Chalsa [*Kumar et al.*, 2010]; (e) Nameri [*Kumar et al.*, 2010]; (f) Harmutty [*Kumar et al.*, 2010]. The blue rectangle is the location of this study. YCS = Yadong Cross Structure. (B) North-south simplified geological cross section across western Bhutan (modified after *Grujic et al.* [2011]). See Figure 1A for location, line B. Abbreviations are as follows: TSS, Tethyan Sedimentary Sequence; HH, Higher Himalayan; LH, Lesser Himalayan; Sw, Siwaliks sediments; GP, Ganga Plain; I-STD, Inner South Tibetan Detachment; KT, Kakhtang Thrust; MCT, Main Central Thrust; MBT, Main Boundary Thrust; TFT, Topographic Frontal Thrust; MFT, Main Frontal Thrust.

From instrumental and historical records, it appears that Bhutan has experienced no major earthquake in the past 200 years [*Gahalaut et al.*, 2011]. The last major historical earthquake occurred in A.D. 1713, but its magnitude and location are poorly known. Described by a single Tibetan eyewitness traveling Bhutan, the event "destroyed all houses in all districts" and was reported in numerous contemporary Bhutanese sources

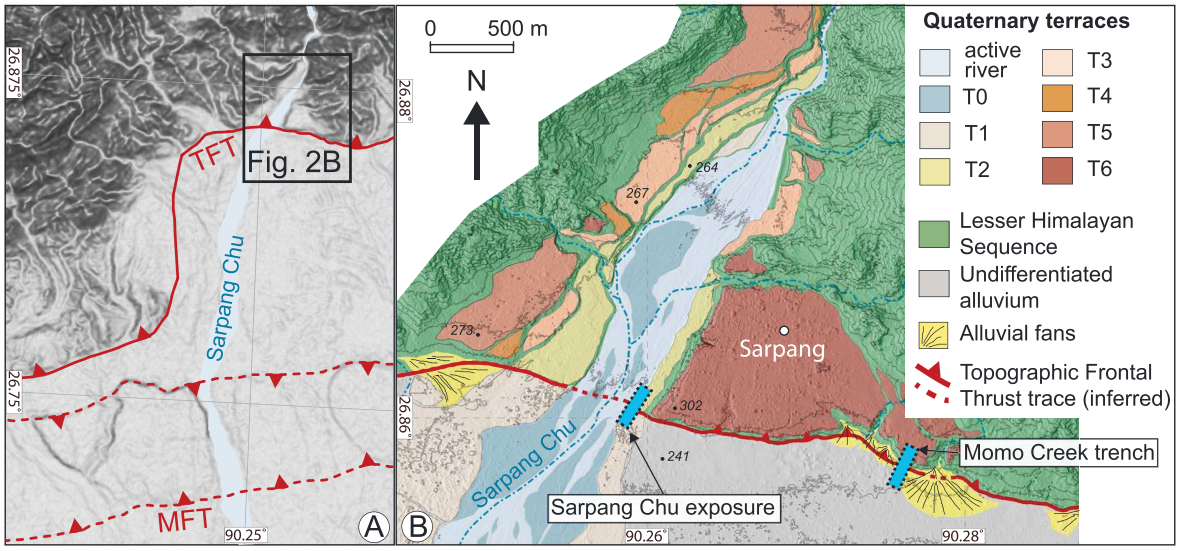

Figure 2. Geomorphological map of the Sarpang area. (a) Shaded map showing the position of the MFT and the TFT in the Sarpang area (DEM from SRTM 90 m). Black rectangle shows the position of the geomorphological study. (b) Geomorphological map of the Topographic Frontal Thrust, near the village of Sarpang, superimposed on 2 m resolution Pleiades Digital Elevation Model. Alluvial terraces are labeled from T0 (active channel) to T6 (oldest). Blue rectangles indicate the locations of the two trench sites (not to scale). Spacing of elevation contours is 20 m. Black points indicate elevation values based on Pleiades DEM.

[*Jackson*, 2002]. On the basis of such "significance," *Ambraseys and Jackson* [2003] suggest a magnitude "probably approaching M_S~7." In nearby Arunachal Pradesh, an earthquake is also reported between A.D. 1696 and A.D. 1714, and the same authors propose that both accounts could reflect a single event in A.D. 1713. In light of the 2015 Gorkha earthquake sequence [*Avouac et al.*, 2015], we consider it likely that the Bhutan and Arunachal Pradesh earthquakes are distinct events. Furthermore, since the A.D. 1713 earthquake is characterized by intense and widespread destruction over the territory of Bhutan, we conclude that its magnitude is greater than $M_S = 7$ and its epicenter likely within the borders of Bhutan.

In Sikkim and Assam (i.e., immediately west and east of Bhutan), two trench sites reveal large-displacement events reaching as much as 18 m that occurred around A.D. 1100 [*Kumar et al.*, 2010]. This event—or sequence of events—is also known at other paleoseismic sites. In the Marha Khola region of east central Nepal, *Lavé et al.* [2005] conclude that a large earthquake ruptured the MFT around A.D. 1100, with an estimated component of vertical offset of 7–7.5 m (and an inferred total coseismic displacement of 14–22 m). A prior trenching study at the border between Nepal and Sikkim suggests a coseismic displacement larger than 4 m associated with an event radiocarbon-dated to A.D. 1100–A.D. 1200 [*Nakata et al.*, 1998, *Upreti et al.*, 2000]. Assuming they are due to the same event, these paleoseimic observations suggest the occurrence of a great medieval earthquake, which had to affect Bhutan.

As previously mentioned, the information above is clearly insufficient to properly characterize past seismic ruptures in Bhutan. In the following, we present our approach to fill this data gap from paleoseismic investigations conducted in central Bhutan.

3. Paleoseismological Analysis in Bhutan

Following the study of *Berthet et al.* [2014], we focus our effort on two sites located in south central Bhutan, near the village of Sarpang, where the TFT cuts through Holocene deposits and uplifts a well-developed flight of fluvial terraces up to ~50 m (T6 in Figure 2). Deformed Holocene features at this site include the following: (1) fluvial Holocene terraces associated with the Sarpang Chu (or Sarpang River) and (2) an alluvial fan deposited over the foot of the main tectonic scarp at Momo Creek. At both sites, we observed fault scarps several meters in height that indicate recent displacement across the TFT.

In order to define a chronostratigraphic framework, we collected 19 charcoal samples from the two sites. They were processed by the Poznan Radiocarbon Laboratory and resulting radiocarbon ages were calibrated using

Table 2. ^{14}C Dating From the Two Bhutanese Sites (Sarpang Chu and Momo Creek)

Unit[a]	Sample Name[b]	Lab. No. B[c]	Measured Radiocarbon Age[d]	Calibrated Ages (Calendric, 2σ)[e]
		Sarpang Chu		
C	SC-02	Poz-64699	940 ± 30 B.P.	Cal A.D. 1030–1160
C	SC-03	Poz-64700	1105 ± 30 B.P.	Cal A.D. 890–1010
C	SC-07	Poz-64701	1000 ± 80 B.P.	Cal A.D. 890–1120
B	SC-10	Poz-64702	105 ± 30 B.P.	Cal A.D. 1680–1930
B	SC-12	Poz-64703	85 ± 30 B.P.	Cal A.D. 1690–1930
B	SC-13	Poz-64704	50 ± 30 B.P.	Cal A.D. 1690–1960
B	SC-14	Poz-64706	100 ± 30 B.P.	Cal A.D. 1680–1930
C	SC-15	Poz-64707	870 ± 30 B.P.	Cal A.D. 1050–1250
C	SC-16	Poz-64708	870 ± 40 B.P.	Cal A.D. 1040–1250
B	P4-C06	From *Berthet et al.* [2014]		Cal A.D. 1490–1650
B	P4-C07	From *Berthet et al.* [2014]		Cal A.D. 1420–1620
		Momo Creek		
E	MO-01	Poz-64709	880 ± 30 B.P.	Cal A.D. 1040–1220
E	MO-02	Poz-64710	880 ± 30 B.P.	Cal A.D. 1040–1220
C	MO-04	Poz-64711	225 ± 30 B.P.	Cal A.D. 1530–1800
C	MO-05	Poz-64712	320 ± 35 B.P.	Cal A.D. 1480–1650
E	MO-06	Poz-64713	1165 ± 30 B.P.	Cal A.D. 770–970
E	MO-07	Poz-64755	880 ± 30 B.P.	Cal A.D. 1040–1220
E	MO-10	Poz-64756	1430 ± 80 B.P.	Cal A.D. 430–770
E	MO-11	Poz-64757	3050 ± 30 B.P.	Cal B.C. 1400–1220
B	MO-13	Poz-64758	145 ± 30 B.P.	Cal A.D. 1680–1950
C	MO-16	Poz-64759	360 ± 40 B.P.	Cal A.D. 1450–1640

[a]See trench logs for stratigraphic unit designations.
[b]The two sites are indicated by SC for Sarpang Chu and MO for Momo Creek.
[c]Laboratory sample codes. All samples have been dated by the Poznan Radiocarbon Laboratory.
[d]Radiocarbon years B.P. relative to 1950 A.D. (with 1σ counting error).
[e]Calendric dates were calibrated using OxCal and the atmospheric calibration curve IntCal13. Calendric ages have been rounded to the nearest ½ decade assuming the 5 years accuracy of the IntCal13 curve.

OxCal 4.2 [*Bronk Ramsey*, 2009] with the IntCal13 calibration curve [*Reimer et al.*, 2013] (Table 2). Charcoal samples yield radiocarbon ages older than that of the sediment in which they deposited (reflecting fluvial transport and sample location within the original tree section) and therefore maximum ages for the host layer. We account for potential inheritance of up to 200 years by building into our OxCal model an outlier model [*Bronk Ramsey*, 2009; *Barnett et al.*, 2015]. Inheritance sensitivity tests result in a marginal variation in the range of 10 years; hence, we prefer relying on the original age distributions that are directly comparable to nearby paleoseismic sites for which inheritance was not implemented. Additionally, we attempt to limit the effect of inheritance by favoring study sites with geomorphological contexts indicative of short transport time (i.e., scarp-controlled watershed basins), consider charcoal-derived ages as a lower bound for the associated deposit and assess variability by processing as many as three distinct samples per unit, wherever possible.

3.1. Sarpang Chu

The Sarpang Chu site (26.860893°N, 90.258855°E) is a ~6 m high topographic scarp where a river-cut cliff exposes a shallow north dipping thrust fault zone between an abandoned fluvial terrace and modern alluvium (Figure 3a). We extended the natural exposure to a depth of 1.5 m below the water level. The scarp influences local drainages and guides a lateral tributary toward the Sarpang Chu (Figure 3a).

The photomosaic and associated trench log (Figures 3b and 3c) document the main lithological units that we defined in the field: in the hanging wall (northern side) the deepest exposed unit G is a highly deformed, massive, pale purple phyllite that corresponds to the Paleozoic Baxa formation (Lesser Himalayan sequence in *Long et al.* [2011]). It is only exposed near the northern end of the outcrop and is overlain by a 3 m thick openwork, clast-supported alluvial gravel unit D, which comprises well-rounded pebbles and cobbles in a sandy matrix. Unit D is overlain by a distinct fine sand to silt unit that we interpret as an overbank deposit (unit B). Unit D is exposed near the base of the trench on the footwall (southern side), and we interpret it as a fluvial deposit from the Sarpang Chu. There, it is overlain by the 2.5 m thick fine-grained sand unit C, typical of a low-energy alluvial deposit. In cross section, unit C reveals sand channels associated with the

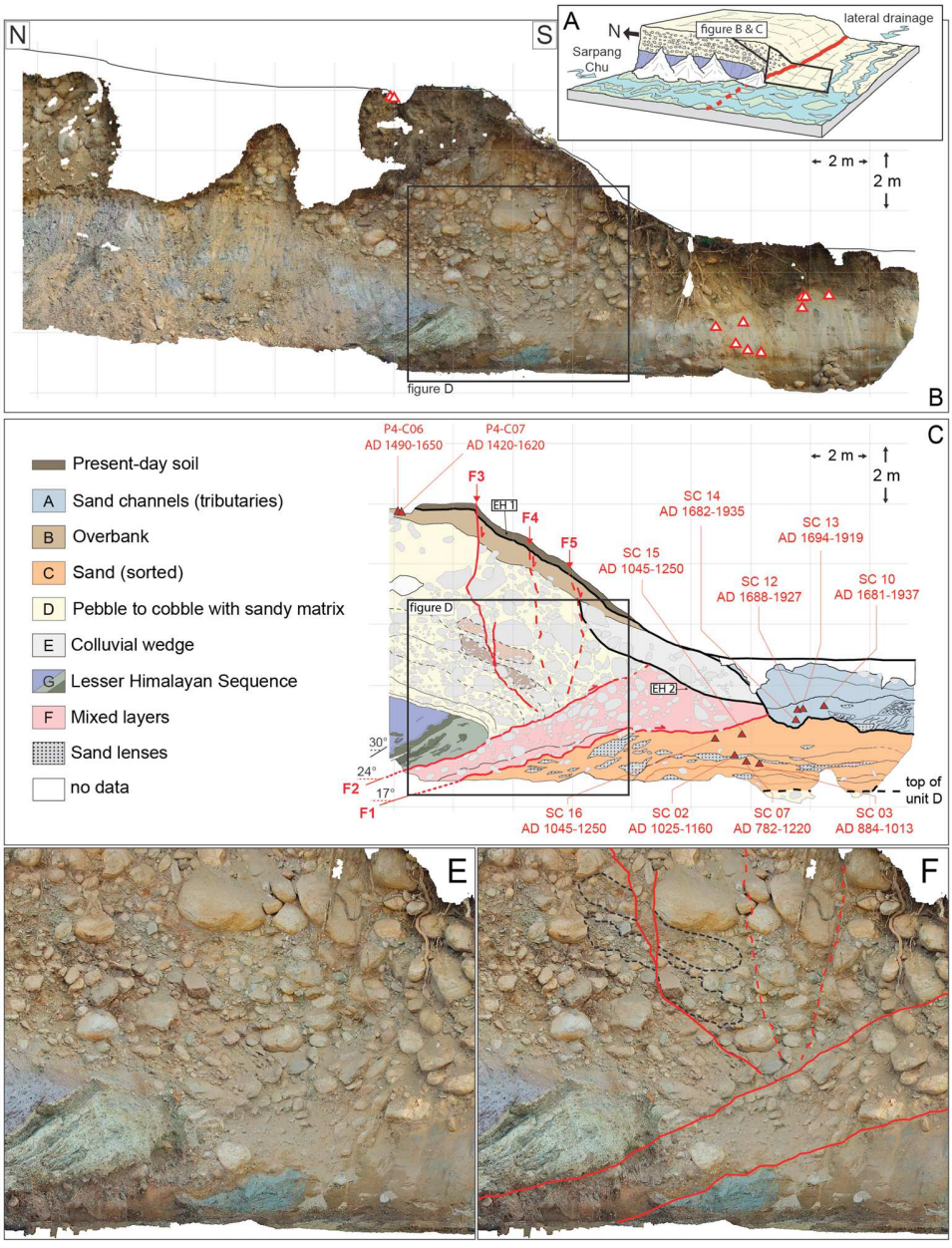

Figure 3. Sarpang Chu paleoseismic site. (a) Block diagram showing geomorphic context of the Sarpang Chu site. Black Q7 polygon shows the area that we logged in detail. (b) Orthorectified photomosaic of the left bank of the Sarpang Chu. Triangles indicate the locations and 2σ-calibrated calendar ages of 11 detrital charcoal samples (including P4-C06 and P4-C07 from *Berthet et al.* [2014]). (c) Detailed log over a 2m grid. Solid and dashed red lines are main faults (respectively certain and suspected). Thick black lines labeled "EH 1" and "EH 2" are the event horizons. (d) Enlarged orthophotography of the deformation zone showing sheared sediments within the fault zone. (e) Interpretation of the enlarged orthophotography of the deformation zone.

tributary drainage controlled by the topographic scarp. Large-scale observations show a shear zone that juxtaposes units G and D on the northern side against units D and C on the southern side along a 1 m wide deformation zone composed of sheared sand and gravel (unit F). It is limited by faults F2 and F1 dipping 24°N and 17°N, respectively (Figure 3c). This shear zone is truncated within its upper part (notably within the F2 strand) and sealed by unit E, which we interpret as scarp-derived colluvium from unit D. This feature corresponds to a fault termination criteria sealed by a colluvial wedge unit [e.g., *Kumar et al.*, 2010; *Sapkota et al.*, 2013]

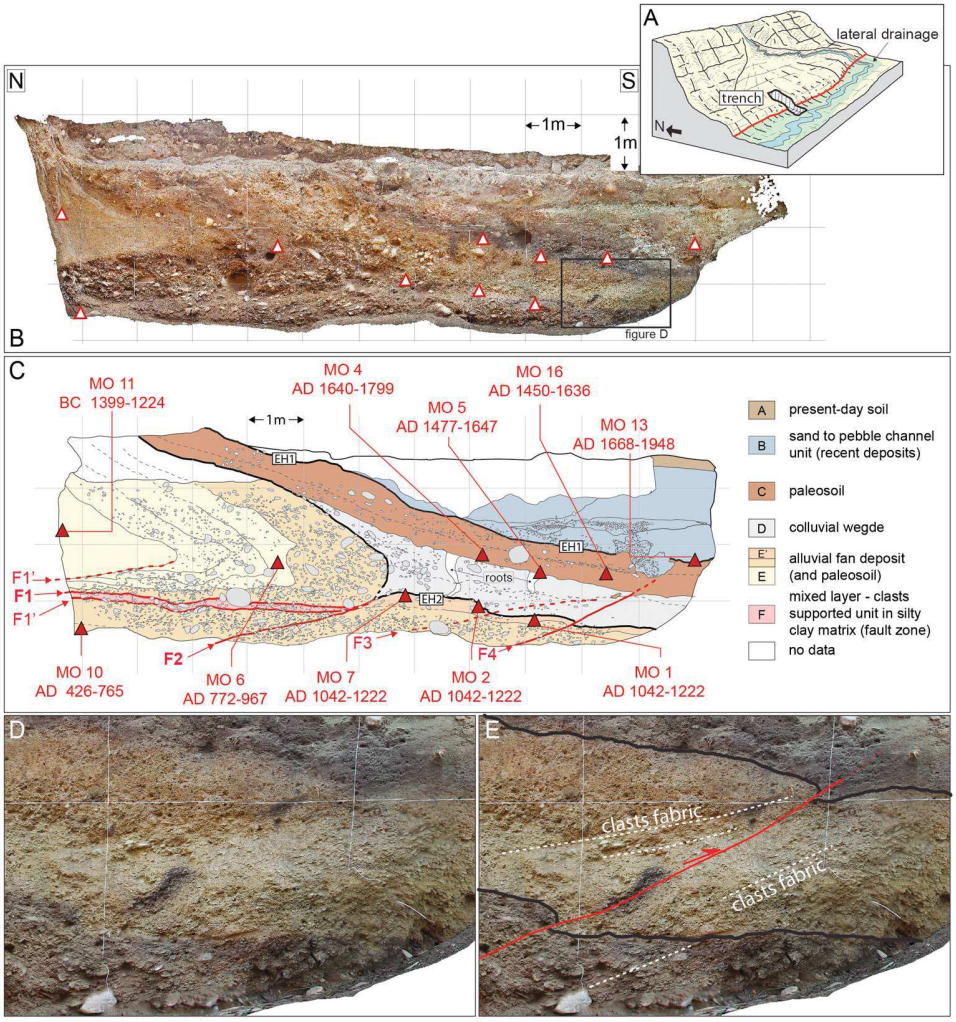

Figure 4. Momo Creek paleoseismic site. (a) Block diagram showing geomorphic context of the Momo Creek site. Black polygon shows the area that we logged in detail. (b) Orthorectified photomosaic of the eastern wall of the trench. Triangles indicate the locations and 2σ-calibrated calendar ages of 10 detrital charcoals samples. (c) Detailed log of the eastern wall over a 1m grid. Solid and dashed red lines are main faults. Heavy black lines labeled "EH 1" and "EH 2" are the event horizons. (d) Enlarged orthophotography showing (i) the deformation of units E, E', D, and C across F3 and (ii) the Q8 shear texture within the unit D. (e) Interpretation of the enlarged orthophotography of the deformation zone.

indicating that a surface-rupturing earthquake occurred between the time of deposition of Units C and D (see event horizon EH2 in Figure 3c).

Within the hanging wall, near-vertical normal fault strand F3 offsets units D and B vertically by about 0.5 m and connects to the main fault zone. Unit G forms a competent indenter driven along F2 and into the unconsolidated unit D. We propose that slip along F2 induces uplift above the tip of the indenter and collapse ahead of it. Hence, F3 limits such collapse zone that may be associated to either a small coseismic displacement along the upper F2 (event 1) or a small-scale mass movement induced by the development of the free face. The deformation event is predated by unit B and postdated by unit A.

We collected charcoal samples from units A, B [from *Berthet et al.*, 2014], and C for radiocarbon dating that yielded ages between A.D. 782 and A.D. 1937 (Table 2). Considering that (1) a small catchment implies short transport for charcoals sampled in units A and C (Figure 2) and (2) charcoal samples within the same stratigraphic unit yield similar radiocarbon ages (Table 2), we assume the charcoals are not significantly older than the depositional age. Using the methodology proposed by *Lienkaemper and Bronk Ramsey* [2009] for

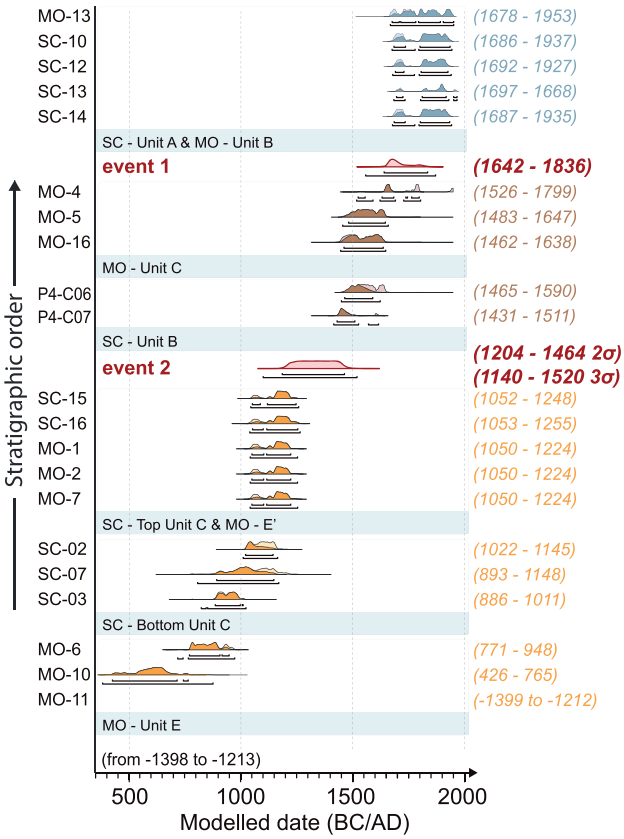

Figure 5. OxCal chronostratigraphic model for surface-rupturing events 1 and 2 inferred from the two paleoseismic sites. The model is built from (1) the stratigraphic information on associated faulted and unfaulted layers and (2) 20 detrital charcoal samples (including P4-C06 and P4-C07 from *Berthet et al.* [2014]). The different colors indicate charcoals within the same phase: orange dates predate the event 2; brown postdate the event 2 and predate the event 1; blue postdate the event 1.

paleoseismic studies, we built an OxCal stratigraphic model [*Bronk Ramsey*, 2009; *Reimer et al.*, 2013] to derive the best age constraints for the occurrence of events 1 and 2. This model indicates that event 2 occurred between A.D. 1167 and A.D. 1487 and that event 1 occurred between A.D. 1524 and A.D. 1815 (Table S1 in the supporting information).

The vertical offset of the main terrace (unit D) reaches ~9 m. The vertical displacement across F3—and to a lesser extent F4 and F5—suggests that the vertical displacement for event 1 is on the order of 0.5 m. This implies that event 2 would have produced the remaining ~8.5 m of vertical offset.

3.2. Momo Creek

Two kilometers east of the Sarpang Chu site, the Momo Creek trench site (26.857049°N, 90.275234°E) (Figure 2) is located on a small alluvial fan associated with a gully draining the top of the T6 terrace. The fan is displaced across a 4.4 ± 0.5 m high scarp [*Berthet et al.*, 2014] that we trenched for this study (Figure 4a).

The photomosaic and trench log document the stratigraphy exposed in the trench, which is composed of alluvial and colluvial units, similar to what we observed at the Sarpang Chu site but with smaller angular clasts consistent with a nearby source (Figures 4b and 4c). The occurrence of rare boulders show that the watershed basin of Momo Creek includes material eroded from alluvial terrace T6 (Figure 2). The oldest exposed unit (E) is a massive sequence of matrix-supported, poorly sorted, and poorly rounded cobble to pebble layers associated with alluvial fan deposition. Over the southern side of the trench, the unit is capped by a thin (~10 cm) paleosol (unit E'). The whole unit is folded and offset along faults F1 and F2. Faults F1 and F2 are overlain by a wedge-shaped unit (D) composed of silty sand with rare gravel layers. Units E and D form a topographic scarp that is covered by an organic-rich 70 cm thick paleosol, unit (C). At the base of the scarp, Unit C is buried by unit B that is composed of small gravel and sand channels deposited by a tributary stream that drains along the scarp (Figures 4a and 4c). The uppermost unit A is the 20 cm thick modern soil.

The trench exposes (Figure 4c) a fault propagation fold developed in unit E by motion along fault F1. The upper part of the fold forms a 4.4 ± 0.5 m high topographic scarp, which is buried by colluvial wedge Unit D, derived from unit E. This indicates that a surface-rupturing earthquake (event 2) occurred after unit E/E' formed and prior to the deposition of colluvial wedge unit D. Considering the geometry and lithology of unit E, we propose (i) a minimum of 6 m of relative displacement of the fold nose, including the thickening of the nose fold and the shearing and thinning of the base of the unit. Because the northern termination of the fold is not visible in the trench, we propose the total of 6 m as a minimum value of coseismic slip for event 2 (Figure S8).

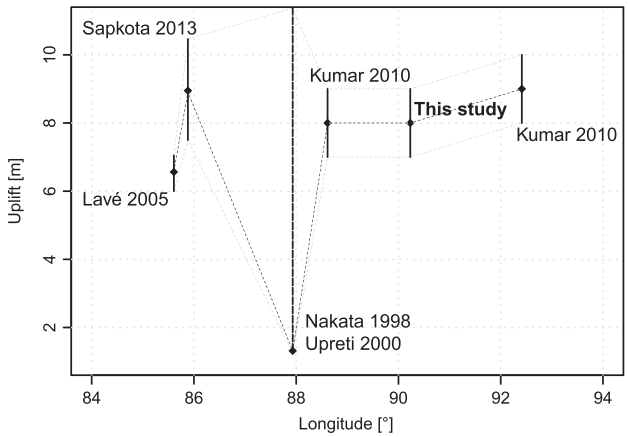

Figure 6. Distribution of coseismic uplift for medieval surface ruptures from *Nakata et al.* [1998], *Upreti et al.* [2000], *Lavé et al.* [2005], *Kumar et al.* [2010], and *Sapkota et al.* [2013] along the Himalayan arc. Coseismic uplift estimated from paleoseimic studies and scarp heights. Upreti et al.'s uplift (heavy dashed line) is calculated using (1) a minimum of 4 m of coseismic slip and (2) an average of dip angle derived from the other trenches used in this study. Black and grey dashed lines connecting to the points correspond to the coseismic slip value and associated uncertainties envelopes.

South of F2, unit E/E′ exhibits a step-like geometry and is affected by F3 and F4. Fault F3 is attested by warping of the stratigraphic contact between units E/E′ and D prolonged by a diffuse shear zone within unit D. At the southern end of the exposed section, F4 is more clearly expressed by shearing within units E/E′ and ~10 cm offset of the base and top of unit D (Figure 4). Overall, these relatively subtle features define a significantly smaller second event (event 1), which occurred after or during the development of unit C and before unit B was deposited. At this site, the rupture associated with this first event may not have fully reached the surface or with minimal geomorphic expression.

We collected 10 charcoal samples from units E, C, and B to constrain the ages of the units (Table 2). Considering that (1) units E, C, and B derive from a small catchment (Figure 2), (2) samples collected within the same stratigraphic unit yield similar radiocarbon ages (Table 2), and (3) the relationships between samples chronology, stratigraphy, and events closely reflects observations from the Sarpang site, we assume negligible inheritance in the radiocarbon ages. The OxCal stratigraphic model for the Momo Creek trench suggests that the second event occurred between A.D. 1179 and A.D. 1547 and that the tentative first event occurred between A.D. 1650 and A.D. 1910 (Table 2). The total vertical offset recorded by unit E between the undeformed bottom layer at 3.5 m depth inside the trench and the top of the scarp at 4.4 ± 0.5 m is about 8 m. Because the first event appears to contribute little to this cumulative value, we consider that 8 m approximates the vertical displacement associated with event 2.

The two events identified at Momo Creek are consistent with the two events identified at Sarpang Chu in terms of timing and coseismic slip. Though evidence for event 1 is subtle and its tectonic origin may not be fully attested at Sarpang Chu, its occurrence is supported by similar observations within a different stratigraphic setting at Momo Creek. Hence, we propose that event 1 may correspond to a relatively smaller surface-rupturing earthquake along the TFT. Consequently, we build an OxCal stratigraphic model (Figure 5) combining stratigraphy and age constraints and abutting relationships from both trench exposures. This allows bracketing the occurrence of event 2 between A.D. 1140 and A.D. 1520 (3σ) and the occurrence of possible event 1 between A.D. 1642 and A.D. 1836 (2σ).

4. Discussion

Paleoseismological investigations conducted at two different sites along the TFT in the Sarpang area yield consistent results for both age and vertical offset associated with at least one major earthquake that occurred in Bhutan over the last millennium. Our observations suggest that a great earthquake occurred between A.D. 1140 and A.D. 1520 with ~8 m of vertical offset. A second event may have occurred between A.D. 1642 and A.D. 1836 and was associated with up to 0.5 m of vertical offset. Thirty kilometers to the east, *Berthet et al.* [2014] find comparable values for an alluvial terrace dated to A.D. 1150 ± 100 and uplifted by 7.9 ± 0.5 m.

4.1. The Seventeenth to Eighteenth Century Earthquake

Our study suggests that the most recent event (event 1) along the TFT in Bhutan may have occurred between A.D. 1642 and A.D. 1836 with a weak surface expression suggestive of a relatively low magnitude or a distant hypocenter. Based on the historical record, the only known earthquake that could correspond to this event is

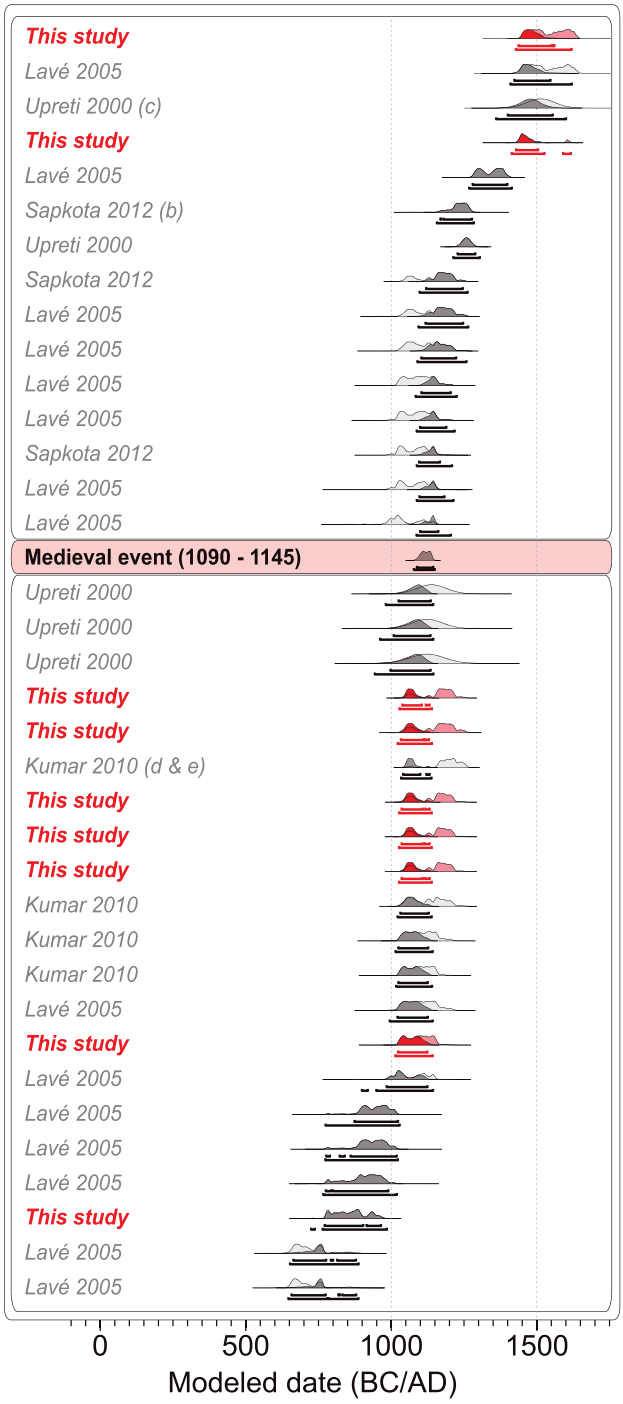

Figure 7. OxCal chronostratigraphic model for a single surface-rupturing event along the Himalayan arc yields a 2σ of occurrence between A.D. 1090 and A.D. 1145. Grey and pink distributions correspond to the probability of ages for each sample. Black and red distributions correspond to modeled ages that take into account the stratigraphic constraints. The calibrated ages and the stratigraphical model are built from (1) radiocarbon age data from *Nakata et al.* [1998], *Upreti et al.* [2000], *Lavé et al.* [2005], *Kumar et al.* [2010], and *Sapkota et al.* [2013] and (2) abutting relationships regarding faulted (older than the medieval event) and unfaulted (younger than the medieval event) layers.

the A.D. 1713 earthquake that "destroyed all houses in all districts" and occurred "somewhere in Bhutan or in Arunachal Pradesh" [*Jackson*, 2002; *Ambraseys and Jackson*, 2003].

We consider three possibilities. First, assuming that this event is a $M_s \sim 7$ earthquake as proposed by *Ambraseys and Jackson* [2003], this suggests that the actual epicenter is probably farther west in central Bhutan, closer to our study sites. Second, if the epicenter is reasonably well located ~200 km east of our study sites, the magnitude of this event may have been significantly underestimated. Lastly, neither the magnitude nor the location is adequately determined by historical data. Presently, the scarcity of data available on that earthquake does not allow discriminating between these scenarios. However, the small coseismic slip measured for event 1 is consistent with the relatively low magnitude proposed for the A.D. 1713 earthquake.

4.2. The Medieval Earthquake in Bhutan

The penultimate event (event 2) occurred during a period for which historical records are scarce. The only known historical earthquake that occurred during this period is the A.D. 1255 earthquake in central Nepal (see section 2). In parallel, on the basis of a paleoseismic study aimed at complementing historical records, *Lavé et al.* [2005] propose another great earthquake may have occurred along the MFT at ~A.D. 1100. Uncertainties associated with radiocarbon dating do not allow us to determine to which earthquake our event 2 should be associated.

Our study suggests a coseismic vertical offset of ~8 m for event 2. According to the fault bend folding model proposed by *Lavé and Avouac* [2000] and a dip of 40° to 60° for the TFT deduced from dip measurements from the nearby Baxa formation [*Long et al.*, 2011b], this would result from 9 m to 13 m of coseismic dip slip at depth. In the Sarpang Chu exposure, where the fault juxtaposes

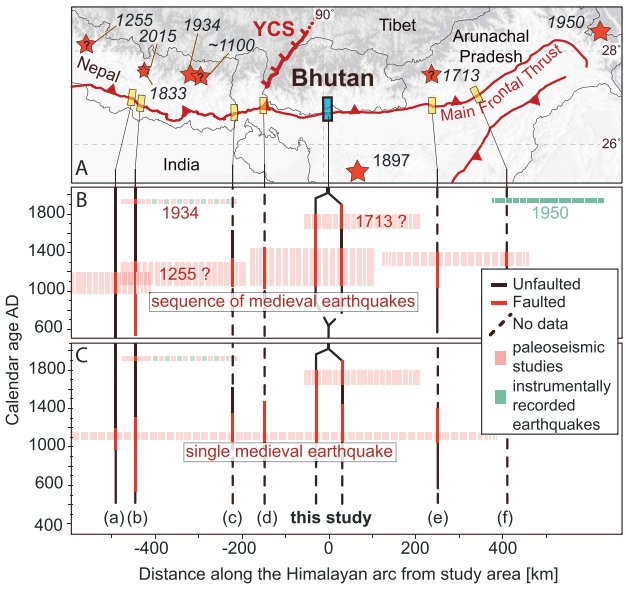

Figure 8. Summary of paleoseismic investigations. (a) Map showing estimated locations of great earthquakes (red stars) and paleoseismological investigations along the MFT/TFT in the Nepal-Sikkim-Bhutan area. Yellow rectangles are the locations of previous paleoseismological studies [*Lavé et al.*, 2005; *Sapkota et al.*, 2013; *Nakata et al.*, 1998; *Upreti et al.*, 2000; *Kumar et al.*, 2010]. Blue rectangle indicates location of sites studied here (Sarpang Chu and Momo Creek). YCS = Yadong Cross Structure. (b) Space-time diagram showing modeled constraints on the timing of occurrence of surface-rupturing earthquakes for a sequence of medieval great earthquakes. Vertical axis is time in calendar years A.D., horizontal axis is kilometers from our study area. Red and green approximate constraints in terms of length and timing from paleoseismological and instrumental studies, respectively. Faulted and unfaulted segments come from paleoseismic data developed by a range of different authors. (c) Space-time diagram showing radiocarbon-modeled constraints on timing of occurrence for the scenario of a single regional event between A.D. 1090 and A.D. 1145 with a 95.4% probability.

the Baxa formation and Holocene alluvium, observed dips of 20° to 30° yield 16 to 23 m of coseismic dip slip at the surface. This would represent some of the largest values observed along continental faults worldwide and may only be compared to subduction-type earthquakes [*Blaser et al.*, 2010]. They are, however, observed systematically in the Central Himalaya, the Indian Sikkim and Assam [*Lavé et al.*, 2005; *Kumar et al.*, 2010; *Bollinger et al.*, 2014]. Figure 6 shows measured coseismic uplift for medieval surface-rupturing events along that section of the arc with values ranging consistently between 4 m and 12 m. Uplift to dip-slip conversion relies either (1) on trench observations where the free surface induces fault refraction and the dip often is extremely small or (2) on nearby structural measurements reflecting the dip values at a lower depth. Hence, uncertainties on dip-slip values are noticeably larger and yield coseismic slip values ranging from 10 m to 30 m.

Determining an associated magnitude may as well involve uncertainties as such amounts of coseismic slip are rarely documented in databases used to derive scaling laws [e.g., *Wells and Coppersmith*, 1994; *Shaw and Scholz*, 2001, and references therein]. For instance, Dmax – L functions proposed by *Manighetti et al.* [2007] for mature faults saturate above ~8 m and an associated ~500 km long rupture. According to *Leonard* [2010], the 16–23 m of coseismic slip derived at Sarpang Chu corresponds to M_w ~ 8.7 (for the maximum value). Since coseismic slip and age constraints are consistent across several contiguous paleoseismic studies along the Himalayas, we propose two end-member hypotheses: (1) the large estimate of vertical offset is a local phenomenon and the rupture zone of this earthquake is limited to one segment of the MFT, likely part of a sequence or (2) event 2 is part of the same earthquake rupture that is documented elsewhere along the Himalayan arc during this time period. We test and further discuss these two end-member hypotheses in light of previous paleoseismic studies along the Himalayan Arc between central Nepal and eastern Bhutan.

4.3. Scenarios for Medieval Earthquake(s) Sequence

We revisit original data from trench studies by *Nakata et al.* [1998], *Upreti et al.* [2000], *Lavé et al.* [2005], *Kumar et al.* [2010], and *Sapkota et al.* [2013]. We build OxCal stratigraphic models for each section to update calibrated dates and provide consistent radiocarbon age calibration and event identification (Figures 7, S3–S7, and Tables S1–S9).

Our calculations demonstrate that both the single great earthquake hypothesis and the multiple earthquake hypothesis are consistent with the whole data set (Figure 7). Using age constraints from all published paleoseismological trenches, and regardless of favored values and historical a priori, we show that the single-event model implies the occurrence of a great earthquake between A.D. 1090 and A.D. 1145 with a 95.4% probability with respect to the data set (Figures 7 and 8). We note that this model yields a single

age distribution and rejects the A.D. 1255 earthquake as a potential candidate in favor of the ~A.D. 1100 event. Following relationships from *Leonard* [2010] with (i) an average coseismic slip of 10–20 m [*Nakata et al.*, 1998; *Upreti et al.*, 2000; *Lavé et al.*, 2005; *Kumar et al.*, 2010; *Sapkota et al.*, 2013], (ii) a locked zone of ~100 km in width [*Vernant et al.*, 2014], and (iii) a full rupture with a surface length ranging from 500 km (Bhutan to West Arunachal Pradesh) to 800 km (Central Nepal to Assam), this great medieval earthquake may have reached $M_w = 8.7–9.1$.

5. Conclusions

Our results demonstrate that Bhutan has experienced at least one great earthquake over the last millennium. This points out that the present-day low seismicity rate observed in Bhutan is not representative of the seismic activity at a longer timescale.

First, we conclude that a large earthquake may have occurred in Central Bhutan in the seventeenth to eighteenth century. Assuming that the event is the A.D. 1713 earthquake and considering historical accounts, it may be associated with a 200 to 300 km long rupture from Bhutan to Arunachal Pradesh. Such events, comparable to the 2015 $M_w = 7.8$ Gorka earthquake in Nepal [*Avouac et al.*, 2015], contribute little to the deformation budget and exhibit subtle—if any—expression in surface exposures [*Angster et al.*, 2015]. However, their large magnitude and shallow depth yield intense ground motion and a concerning potential for destruction that calls for extensive studies [*Grandin et al.*, 2015].

Second, we identify an older far larger earthquake that would have produced ~8 m of coseismic uplift (16–23 m of coseismic surface slip) in medieval times with an inferred $M_w \sim 8.7$. A comparable event is observed at numerous trench sites in Central Nepal, Sikkim, and Assam and may be part either of a series of great single-segment earthquakes between A.D. 1025 and A.D. 1520 or of one even greater multisegment earthquake that ruptured from central Nepal to Assam between A.D. 1090 and A.D. 1145 with $M_w = 8.7–9.1$.

In a densely populated region exposed to intense natural disasters, these results point out the necessity to document past large to great earthquakes in terms of chronology, coseismic slip, and rupture extent to properly assess seismic hazard for the whole Himalayan Arc.

Acknowledgments
This project is funded by the French Agence Nationale de la Recherche (ANR-13-BS06-0006-01), the CNES/ISIS program, and the CNES/TOSCA program. R.L.M. PhD is supported by a fellowship from the French Ministry for Higher education and Research. We would like to thank all the people who helped in the fieldwork, particularly our drivers Phajo Kinley and Tsheten from the Department of Geology and Mines. We would like to thank Stéphane Mazzotti who helped us improve and clarify the manuscript. We also thank Serge Lallemand for constructive comments and three anonymous reviewers for detailed and constructive comments that improved the quality of this contribution. Supporting data are included in an SI file. Correspondence and requests for materials should be addressed to lerouxmallouf@gm.univ-montp2.fr

References

Ambraseys, N., and D. Jackson (2003), A note on early earthquakes in northern India and southern Tibet, *Curr. Sci.*, *84*, 570–582.
Ambraseys, N. N., and J. Douglas (2004), Magnitude calibration of north earthquakes, *Geophys. J. Int.*, *159*, 165–206.
Angster, S., E. J. Fielding, S. Wesnousky, I. Pierce, D. Chamlagain, D. Gautam, B.-N. Upreti, Y. Kumahara, and T. Nakata (2015), Field reconnaissance after the 25 April 2015 *M* 7.8 Gorkha earthquake, *Seismol. Res. Lett.*, *86*(6), 1506–1513.
Avouac, J.-P., L. Meng, S. Wei, T. Wang, and J.-P. Ampuero (2015), Lower edge of locked Main Himalayan Thrust unzipped by the 2015 Gorkha earthquake, *Nat. Geosci.*, *8*(9), 708–711, doi:10.1038/ngeo2518.
Barnett, E. A., B. L. Sherrod, J. F. Hughes, H. M. Kelsey, J. L. Czajkowski, T. J. Walsh, T. A. Contreras, E. R. Schermer, and R. J. Carson (2015), Paleoseismic evidence for late Holocene tectonic deformation along the Saddle Mountain fault zone, southeastern Olympic peninsula, Washington, *Bull. Seismol. Soc. Am.*, *105*, 38–71, doi:10.1785/0120140086.
Ben-Menahem, A., E. Aboodi, and R. Schild (1974), The source of the great Assam earthquake—An interplate wedge motion, *Phys. Earth Planet. Inter.*, *9*(4), 265–289, doi:10.1016/0031-9201(74)90056-9.
Berthet, T., J. F. Ritz, M. Ferry, P. Pelgay, R. Cattin, D. Drukpa, R. Braucher, and G. Hetényi (2014), Active tectonics of the eastern Himalaya: New constraints from the first tectonic geomorphology study in southern Bhutan, *Geology*, *42*(5), 427–430, doi:10.1130/G35162.1.
Blaser, L., F. Krüger, M. Ohrnberger, and F. Scherbaum (2010), Scaling relations of earthquake source parameter estimates with special focus on subduction environment, *Bull. Seismol. Soc. Am.*, *100*(6), 2914–2926, doi:10.1785/0120100111.
Bilham, R. (1995), Location and magnitude of the 1833 Nepal earthquake and its relation to the rupture zones of contiguous great Himalayan earthquakes, *Curr. Sci.*, *69*(2), 101–128.
Bilham, R., V. K. Gaur, and P. Molnar (2001), Himalayan seismic hazard, *Science*, *293*(5534), 1442–1444.
Bollinger, L., S. N. Sapkota, P. Tapponnier, Y. Klinger, M. Rizza, J. Van der Woerd, D. R. Tiwari, R. Pandey, A. Bitri, and S. Bes de Berc (2014), Estimating the return times of great Himalayan earthquakes in eastern Nepal: Evidence from the Patu and Bardibas strands of the Main Frontal Thrust, *J. Geophys. Res. Solid Earth*, *119*, 7123–7163, doi:10.1002/2014JB010970.
Bronk Ramsey, C. (2009), Bayesian analysis of radiocarbon dates, *Radiocarbon*, *51*(1), 337–360.
Cattin, R., and J. P. Avouac (2000), Modeling mountain building and the seismic cycle in the Himalaya of Nepal, *J. Geophys. Res.*, *105*(B6), 13,389–13,407, doi:10.1029/2000JB900032.
Chen, W. P., and P. Molnar (1977), Seismic moments of major earthquakes and the average rate of slip in central Asia, *J. Geophys. Res.*, *82*(20), 2945–2969, doi:10.1029/JB082i020p02945.
Dasgupta, S., K. Mazumdar, L. H. Moirangcha, T. D. Gupta, and B. Mukhopadhyay (2013), Seismic landscape from Sarpang re-entrant, Bhutan Himalaya foredeep, Assam, India: Constraints from geomorphology and geology, *Tectonophysics*, *592*, 130–140.
Gahalaut, V. K., S. Rajput, and B. Kundu (2011), Low seismicity in the Bhutan Himalaya and the stress shadow of the 1897 Shillong Plateau earthquake, *Phys. Earth Planet. Inter.*, *186*(3), 97–102.
Gansser, A. (1964), Geology of the Himalaya(s), *Geol. Mag.*, *104*(01), 86, doi:10.1017/S0016756800040450.

Grandin, R., M. Vallée, C. Satriano, R. Lacassin, Y. Klinger, M. Simoes, and L. Bollinger (2015), Rupture process of the $M_w = 7.9$ 2015 Gorkha earthquake (Nepal): Insights into Himalayan megathrust segmentation, *Geophys. Res. Lett.*, *42*, 8373–8382, doi:10.1002/2015GL066044.

Grujic, D., C. J. Warren, and J. L. Wooden (2011), Rapid synconvergent exhumation of Miocene-aged lower orogenic crust in the eastern Himalaya, *Lithosphere*, *3*(5), 346–366, doi:10.1130/L154.1.

Jackson, D. (2002), *The Great Western-Himalayan Earthquake of 1505: A Rupture of the Central Himalayan Gap?* pp. 147–159, Brill's Tibetan Studies Library I, Leiden.

Kumar, S., S. G. Wesnousky, R. Jayangondaperumal, T. Nakata, Y. Kumahara, and V. Singh (2010), Paleoseismological evidence of surface faulting along the northeastern Himalayan front, India: Timing, size, and spatial extent of great earthquakes, *J. Geophys. Res.*, *115*, B12422, doi:10.1029/2009JB006789.

Lavé, J., and J. P. Avouac (2000), Active folding of fluvial terraces across the Siwaliks Hills, Himalayas of central Nepal, *J. Geophys. Res.*, *105*(B3), 5735–5770.

Lavé, J., D. Yule, S. Sapkota, K. Basant, C. Madden, M. Attal, and R. Pandey (2005), Evidence for a great medieval earthquake (~1100 A.D.) in the central Himalayas, Nepal, *Science*, *307*(5713), 1302–1305, doi:10.1126/science.1104804.

Le Fort, P. (1975), Himalaya: The collided range. Present knowledge of the continental arc, *Am. J. Sci.*, *275*, 1–44.

Leonard, M. (2010), Earthquake fault scaling: Self-consistent relating of rupture length, width, average displacement, and moment release, *Bull. Seismol. Soc. Am.*, *100*(5A), 1971–1988.

Le Roux-Mallouf, R., et al. (2015), Evidence for a wide and gently dipping Main Himalayan Thrust in western Bhutan, *Geophys. Res. Lett.*, *42*, 3257–3265, doi:10.1002/2015GL063767.

Lienkaemper, J. J., and C. Bronk Ramsey (2009), OxCal: Versatile tool for developing paleoearthquake chronologies—A primer, *Seismol. Res. Lett.*, *80*(3), 431–434, doi:10.1785/gssrl.80.3.431.

Long, S., N. McQuarrie, T. Tobgay, D. Grujic, and L. Hollister (2011), Geologic map of Bhutan, *J. Maps*, *7*(1), 184–192, doi:10.4113/jom.2011.1159.

Long, S., N. McQuarrie, T. Tobgay, and D. Grujic (2011b), Geometry and crustal shortening of the Himalayan fold-thrust belt, eastern and central Bhutan, *Geol. Soc. Am. Bull.*, *123*, B30203-1.

Manighetti, I., M. Campillo, S. Bouley, and F. Cotton (2007), Earthquake scaling, fault segmentation, and structural maturity, *Earth Planet. Sci. Lett.*, *253*(3), 429–438.

McQuarrie, N., D. Robinson, S. Long, T. Tobgay, D. Grujic, G. Gehrels, and M. Ducea (2008), Preliminary stratigraphic and structural architecture of Bhutan: Implications for the along strike architecture of the Himalayan system, *Earth Planet. Sci. Lett.*, *272*(1), 105–117, doi:10.1016/j.epsl.2008.04.030.

Mugnier, J.-L., A. Gajurel, P. Huyghe, R. Jayangandaperumal, F. Jouanne, and B. Upreti (2013), Structural interpretation of the great earthquakes of the last millennium in the central Himalaya, *Earth Sci. Rev.*, *127*, 30–47, doi:10.1016/j.earscirev.2013.09.003.

Nábelek, J., G. Hetényi, J. Vergne, S. Sapkota, B. Kafle, M. Jiang, H. Su, J. Chen, B.-S. Huang, and H.-C. Team (2009), Underplating in the Himalaya-Tibet collision zone revealed by the Hi-CLIMB experiment, *Science*, *325*(5946), 1371–1374, doi:10.1126/science.1167719.

Nakata, T., K. Kumura, and T. Rockwell (1998), First successful paleoseismic trench study on active faults in the Himalaya, *Eos Trans. AGU*, *79*, 45.

Nelson, K. D., et al. (1996), Partially molten middle crust beneath southern Tibet: Synthesis of project INDEPTH results, *Science*, *274*(5293), 1684–1688.

Pant, M. R. (2002), A step toward a historical seismicity of Nepal, *Adarsa*, *2*, 29–60.

Rajendran, C. P., and K. Rajendran (2005), The status of central seismic gap: A perspective based on the spatial and temporal aspects of the large Himalayan earthquakes, *Tectonophysics*, *395*(1), 19–39, doi:10.1016/j.tecto.2004.09.009.

Rajendran, C. P., B. John, and K. Rajendran (2015), Medieval pulse of great earthquakes in the central Himalaya: Viewing past activities on the frontal thrust, *J. Geophys. Res. Solid Earth*, *120*, 1623–1641, doi:10.1002/2014JB011015.

Reimer, P. J., et al. (2013), IntCal13 and Marine13 radiocarbon age calibration curves 0–50,000 years cal BP, *Radiocarbon*, *55*, 1869–1887, doi:10.2458/azu_js_rc.55.16947.

Sapkota, S. N., L. Bollinger, Y. Klinger, P. Tapponnier, Y. Gaudemer, and D. Tiwari (2013), Primary surface ruptures of the great Himalayan earthquakes in 1934 and 1255, *Nat. Geosci.*, *6*(2), 71–76, doi:10.1038/ngeo1669.

Shaw, B. E., and C. H. Scholz (2001), Slip-length scaling in large earthquakes: Observations and theory and implications for earthquake physics, *Geophys. Res. Lett.*, *28*(15), 2995–2998, doi:10.1029/2000GL012762.

Srivastava, H. N., B. K. Bansal, and M. Verma (2013), Largest earthquake in Himalaya: An appraisal, *J. Geol. Soc. India*, *82*(1), 15–22.

Stevens, V. L., and J. P. Avouac (2015), Interseismic coupling on the main Himalayan thrust, *Geophys. Res. Lett.*, *42*, 5828–5837, doi:10.1002/2015GL064845.

Stevens, V. L., and J.-P. Avouac (2016), Millenary $M_w > 9.0$ earthquakes required by geodetic strain in the Himalaya, *Geophys. Res. Lett.*, *43*, 1118–1123, doi:10.1002/2015GL067336.

Szeliga, W., S. Hough, S. Martin, and R. Bilham (2010), Intensity, magnitude, location and attenuation in India for felt earthquakes since 1762, *Bull. Seism. Soc. Amer.*, *100*(2), 570–584, doi:10.1785/0120080329.

Triep, E. G., and L. R. Sykes (1997), Frequency of occurrence of moderate to great earthquakes in intracontinental regions: Implications for changes in stress, earthquake prediction, and hazards assessments, *J. Geophys. Res.*, *102*(B5), 9923–9948, doi:10.1029/96JB03900.

Upreti, B. N., T. Nakata, Y. Kumahara, H. Yagi, K. Okumura, T. K. Rockwell, N. S. Virdi, and H. Maemoku (2000), The latest active faulting in southeast Nepal, in *Proceedings of the Hokudan International Symposium and School in Active Faulting*, pp. 533–536.

Vernant, P., R. Bilham, W. Szeliga, D. Drupka, S. Kalita, A. K. Bhattacharyya, V. K. Gaur, P. Pelgay, R. Cattin, and T. Berthet (2014), Clockwise rotation of the Brahmaputra Valley relative to India: Tectonic convergence in the eastern Himalaya, Naga Hills, and Shillong Plateau, *J. Geophys. Res. Solid Earth*, *119*, 6558–6571.

Wang, K., and Y. Fialko (2015), Slip model of the 2015 M_w 7.8 Gorkha (Nepal) earthquake from inversions of ALOS-2 and GPS data, *Geophys. Res. Lett.*, *42*, 7452–7458, doi:10.1002/2015GL065201.

Wells, D. L., and K. J. Coppersmith (1994), New empirical relationships among magnitude, rupture length, rupture width, rupture area, and surface displacement, *Bull. Seismol. Soc. Am.*, *84*(4), 974–1002.

Yule, D., J. Lave, S. N. Sapkota, D. Tiwari, B. Kafle, M. R. Pandey, S. Dawson, C. Madden, and M. Attal (2006), Large surface rupture of the Main Frontal Thrust in east-central and western Nepal—Evidence for an unprecedented type of Himalayan earthquake, Proceedings on the International Workshop on Seismology, seismotectonics and seismic hazard in the Himalayan region, Kathmandu, 28–29 November, 2006, 13–14.534.

Zhao, W., K. D. Nelson, J. Che, J. Quo, D. Lu, C. Wu, and X. Liu (1993), Deep seismic reflection evidence for continental underthrusting beneath southern Tibet, *Nature*, *366*(6455), 557–559.

A.2 Evidence of interseismic coupling variations along the Bhutan Himalayan arc from new GPS data

AGU PUBLICATIONS

Geophysical Research Letters

RESEARCH LETTER
10.1002/2016GL071163

Key Points:
- New detailed GPS velocity field in Bhutan showing lateral variations of interseismic coupling
- Decoupled upper ramp of the Main Himalayan Thrust in eastern Bhutan
- Potential first evidence of transient events on the Main Himalayan Thrust

Supporting Information:
- Supporting Information S1

Correspondence to:
A. Marechal,
marechal@gm.univ-montp2.fr

Citation:
Marechal, A., et al. (2016), Evidence of interseismic coupling variations along the Bhutan Himalayan arc from new GPS data, *Geophys. Res. Lett.*, *43*, doi:10.1002/2016GL071163.

Received 9 SEP 2016
Accepted 5 DEC 2016
Accepted article online 9 DEC 2016

Evidence of interseismic coupling variations along the Bhutan Himalayan arc from new GPS data

Anais Marechal[1], Stephane Mazzotti[1], Rodolphe Cattin[1], Gael Cazes[2], Philippe Vernant[1], Dowchu Drukpa[3], Kinzang Thinley[4], Alizia Tarayoun[1], Romain Le Roux-Mallouf[1], Bal Bahadur Thapa[4], Phuntsho Pelgay[3], Jampel Gyeltshen[3], Erik Doerflinger[1], and Stéphanie Gautier[1]

[1]Geosciences Montpellier, UMR5243, Université de Montpellier, Montpellier, France, [2]School of Earth and Environmental Sciences, University of Wollongong, Wollongong, New South Wales, Australia, [3]Seismology and Geophysics Division, Department of Geology and Mines, Ministry of Economic Affairs, Thimphu, Bhutan, [4]National Land Commission, Royal Government of Bhutan, Thimphu, Bhutan

Abstract Although the first-order pattern of present-day deformation is relatively well resolved across the Himalayas, irregular data coverage limits detailed analyses of spatial variations of interseismic coupling. We provide the first GPS velocity field for the Bhutan Himalaya. Combined with published data, these observations show strong east-west variations in coupling between central and eastern Bhutan. In contrast with previous estimations of first-order uniform interseismic coupling along the Himalayan arc, we identify significant lateral variations: In western and central Bhutan, the fully coupled segment is 135–155 km wide with an abrupt downdip transition, whereas in eastern Bhutan the fully coupled segment is 100–120 km wide and is limited updip and downdip by partially creeping segments. This is the first observation of decoupling on the upper ramp along the Himalayan arc, with important implications for large earthquake surface rupture and seismic hazard.

1. Introduction

In the Himalayas, as in all active tectonic regions, strain budget on the main seismogenic faults during large earthquakes and over interseismic periods is a key element to improve seismic hazard assessment. The first-order present-day crustal deformation along the Himalayan arc is now relatively well constrained from leveling data [*Jackson and Bilham*, 1994], interferometric synthetic aperture radar observations [*Grandin et al.,* 2012], and GPS measurements [e.g., *Bettinelli et al.,* 2006; *Jade et al.,* 2011; *Vernant et al.,* 2014]. Altogether, these observations show that nearly all of the present-day convergence is accommodated along the Main Himalayan Thrust (MHT), which reaches the surface at the Main Boundary Thrust (MBT) and Main Frontal Thrust (MFT). However, data coverage remains irregular, and areas such as Bhutan Himalaya are poorly constrained. This lack of data results in significant limitations in the interseismic strain analysis. Although the MHT is considered as fully locked along its entire length without any aseismic barrier [*Stevens and Avouac*, 2015], small-scale decoupled or aseismic region might exist in regions such as Bhutan, where the geodetic data are, up to now, limited to a few stations [*Vernant et al.,* 2014].

Here we provide the first detailed GPS velocity solution for the region of Bhutan Himalaya, consisting in (1) north-south profiles composed of nineteen campaign stations installed and surveyed in western, central, and eastern Bhutan since 2003, (2) nine new campaign stations deployed in central and eastern Bhutan in 2012, and (3) eight permanent stations distributed across the country and operating since 2011 (except for two older stations that operated from 2003 to 2008). Combined with published data, these new GPS observations are used to improve the assessments of interseismic coupling along the MHT and of the first-order geometry of the unlocked portions of the fault at depth. After a brief presentation of the GPS data, we describe the modeling approach and discuss its results and implications in terms of east-west lateral variations of present-day interseismic strain buildup.

2. Methodology

2.1. GPS Data

We extend the GPS data published for the Kingdom of Bhutan by *Vernant et al.* [2014] with (1) nine new campaign sites installed in 2013 and 2014 in central and eastern Bhutan, surveyed between 2013 and

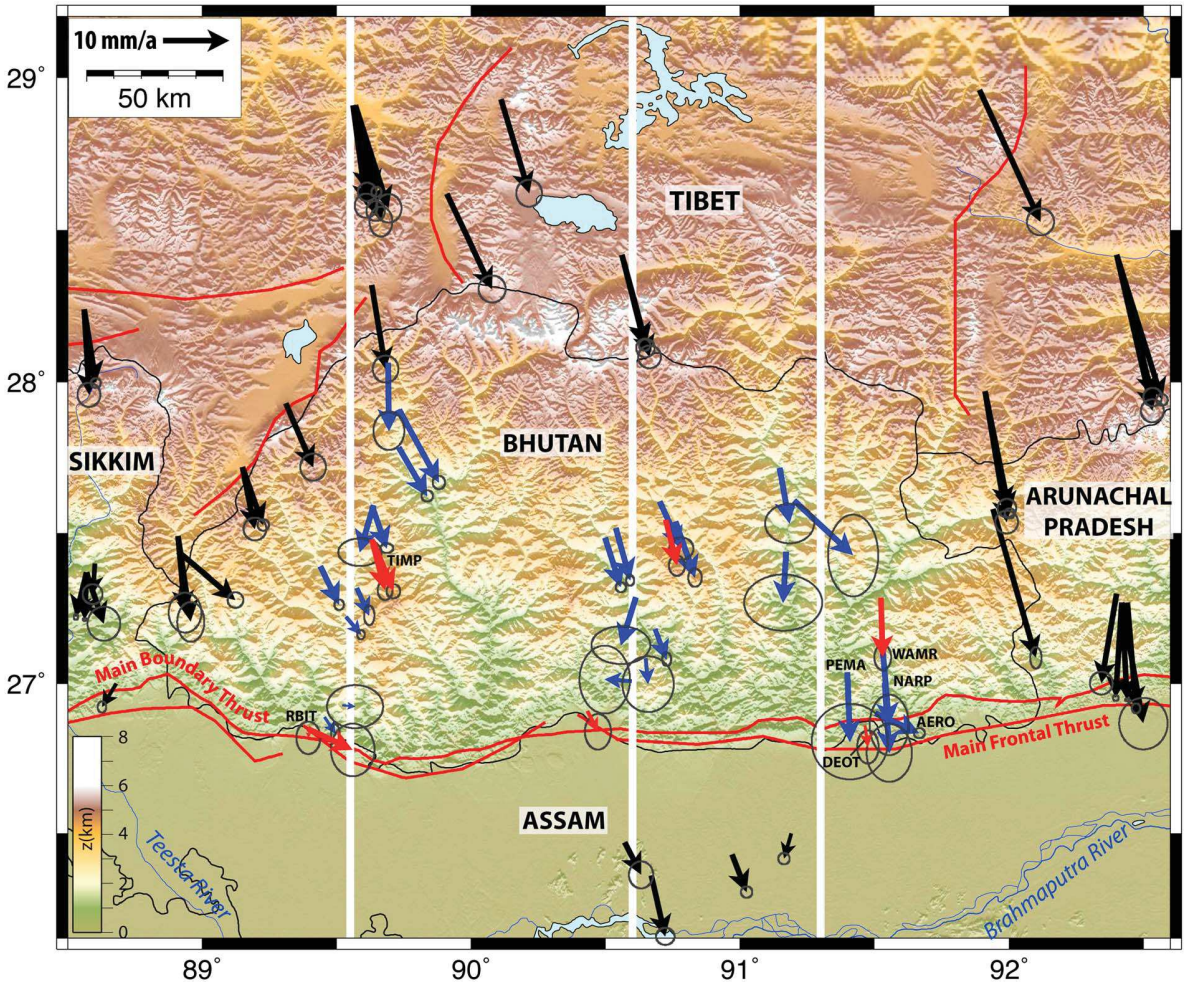

Figure 1. New GPS velocity field for Bhutan Himalaya relative to stable India (as defined by *Ader et al.* [2012]). Blue and red vectors show campaign and permanent GPS data from this study, respectively. Black vectors are from *Banerjee et al.* [2008], *Bettinelli et al.* [2006], *Gahalaut et al.* [2013], *Gan et al.* [2007], *Jade* [2004], *Jade et al.* [2007], *Jade et al.* [2014], *Liang et al.* [2013], *Mahesh et al.* [2012], *Mukul et al.* [2010], *Tang et al.* [2010], and *Vernant et al.* [2014]. Ellipses indicate 1σ confidence regions.

2016, (2) four campaign sites installed and surveyed in 2003 and reoccupied between 2013 and 2016, and (3) six permanent sites installed in 2011 and 2012 by the National Land Commission (NLC) of Bhutan. The full network comprises 28 campaign stations and 8 permanent sites (Figure 1). The continuous site data span 2003–2008 (TIMP and RBIT) and 2011–2016 (new NLC sites). Data for the campaign sites range between 2003 and 2016, with a minimum of two surveys over 2 years for the newest sites (Table S1 in the supporting information). Campaign and permanent sites are instrumented with geodetic-grade receivers and antennas, and campaign sites were surveyed at the same period (March-April) for at least 24 h (commonly over 48 h) for each campaign.

GPS daily positions in the International GNSS Service reference frame IGb08 are calculated with the CSRS-Precise Point Positioning v1.5 software [*Héroux and Kouba*, 2001] using the approach described in *Marechal et al.* [2015]. Velocities are estimated by a least squares inversion weighted by the position formal uncertainties. The inverted model comprises a linear term (velocity) and, for the permanent stations, an annual sinusoid to account for seasonal effects, mostly related to the load variations of the Brahmaputra River alluvial plain. The final velocities (Table S1) are expressed relative to stable India using the India/International Terrestrial Reference Frame rotation defined by *Ader et al.* [2012]. We do not apply corrections for transient events such as coseismic displacements, which are not significant in Bhutan [*Vernant et al.*, 2014].

Velocity uncertainties are calculated using the formulation of *Mao et al.* [1999] assuming that the campaign and permanent data are characterized by a "white + flicker" colored noise model. Long gaps in the Bhutan permanent time series preclude a robust noise analysis of the local data. Thus, we use analyses of permanent data with similar PPP processing in western Europe and North America [*Marechal et al.,* 2015; *Nguyen et al.,* 2016] to define average noise model parameters. We derive scaling coefficients between the time series root-mean-square dispersion and white and flicker noise amplitudes for these data sets, which are then applied to the Bhutan permanent and campaign data. This approach puts an emphasis on both the length and number of data points of the time series, with mean horizontal velocity standard errors of 3.5–4.5 mm/yr for data spanning 2–3 years versus 1.0–1.5 mm/yr for longer data sets (Table S1).

2.2. Modeling Approach

The most conventional approach used to reproduce interseismic GPS velocities and assess interseismic coupling is the back slip dislocation model [*Savage*, 1983], which considers virtual normal faulting along the seismogenic portion of the MHT [e.g., *Stevens and Avouac,* 2015]. However, the back slip formulation is only rigorously correct for a purely planar fault or a fully locked fault [*Vergne et al.,* 2001]. Hence, although back slip models can provide a good fit to geodetic data, it cannot be used to assess potential partial coupling along the Bhutanese MHT, which is well known for its flat and ramp geometry [e.g., *Long et al.,* 2011; *Coutand et al.,* 2014; *Le Roux-Mallouf et al.,* 2015].

Here we favor the use of a dislocation model of buried reverse faults associated with aseismic slip, allowing us to assess simultaneously the convergence rate, potential partial coupling, and the geometry of the unlocked portions of the MHT [e.g., *Vergne et al.,* 2001; *Kanda and Simons,* 2010]. Because the three-dimensional geometry of the MHT remains poorly constrained in our study region, we use a two-dimensional approach along three north-south profiles, orthogonal to the regional MFT direction, in western, central, and eastern Bhutan (Figure 1). We project the GPS velocities along the profiles and only consider the component of coupling parallel to the profile directions, thus neglecting the small oblique component of the regional convergence.

For each profile, the geometry of the MHT is defined by the coordinates of six breakpoints that allow to model a complex ramp-flat system and to take into account slip rate variations with depth (Figure 2a and Table S2). Assuming that the depth of the MHT increases northward, these coordinates are treated as dependent parameters. Furthermore, available geological and geophysical data along our study profiles are used as a priori knowledge of these coordinates [*Coutand et al.,* 2014; *Le Roux-Mallouf et al.,* 2015]. This includes (1) the location of the emergence of the MHT at the surface with a maximum dip angle of 50° [*Long et al.,* 2011], (2) a subhorizontal section at a depth of 10–15 km [*Bhattacharyya and Mitra*, 2009; *Acton et al.,* 2011; *Long et al.,* 2011; *Tobgay et al.,* 2012], (3) a maximum dip angle of 30° for crustal ramp(s) as imaged by seismic experiments in Garhwal, Nepal, and Sikkim [*Nábělek et al.,* 2009; *Acton et al.,* 2011; *Caldwell et al.,* 2013], and (4) a depth of ~ 40 km of the southernmost point imaged beneath southern Tibet from the INDEPTH experiment (International Deep Profiling of Tibet and the Himalaya) [*Hauck et al.,* 1998]. We also assume a convergence of 15 to 25 mm/yr for the three profiles, consistent with the estimate across western Bhutan from GPS observations [*Vernant et al.,* 2014].

In order to solve the nonlinear equations linking surface displacements with fault slip rate and geometry at depth [e.g., *Okada*, 1985], data inversion is performed using a pseudorandom walk through the parameter space, which consists of 14 parameters including the slip rates for the five fault segments (u_1 to u_5) as well as the depth and distance along the profile of the six breakpoints (Figure 2a and Table S2). Following *Mosegaard and Tarantola* [1995], a Markov Chain Monte Carlo technique is used to generate a large collection of 10^8 models with stochastic sampling that depends on the posterior probability of the model likelihood. This pseudorandom walk is controlled by the following rules for the transition from model m_i to model m_j:

1. If $L(m_j) \geq L(m_i)$ then accept the proposed transition from i to j,
2. If $L(m_j) < L(m_i)$ then the proposed transition from i to j has a probability $L(m_j)/L(m_i)$,

where $L(m_i)$ and $L(m_j)$ are the likelihood of the old and the new models, respectively. We define the likelihood function L of a model m as

$$L(m) = \exp\left(-\frac{1}{n}\sum_{i=1}^{n}\left(\frac{\mathrm{Ucalc}_i - \mathrm{Uobs}_i}{\sigma_i}\right)^2\right),$$

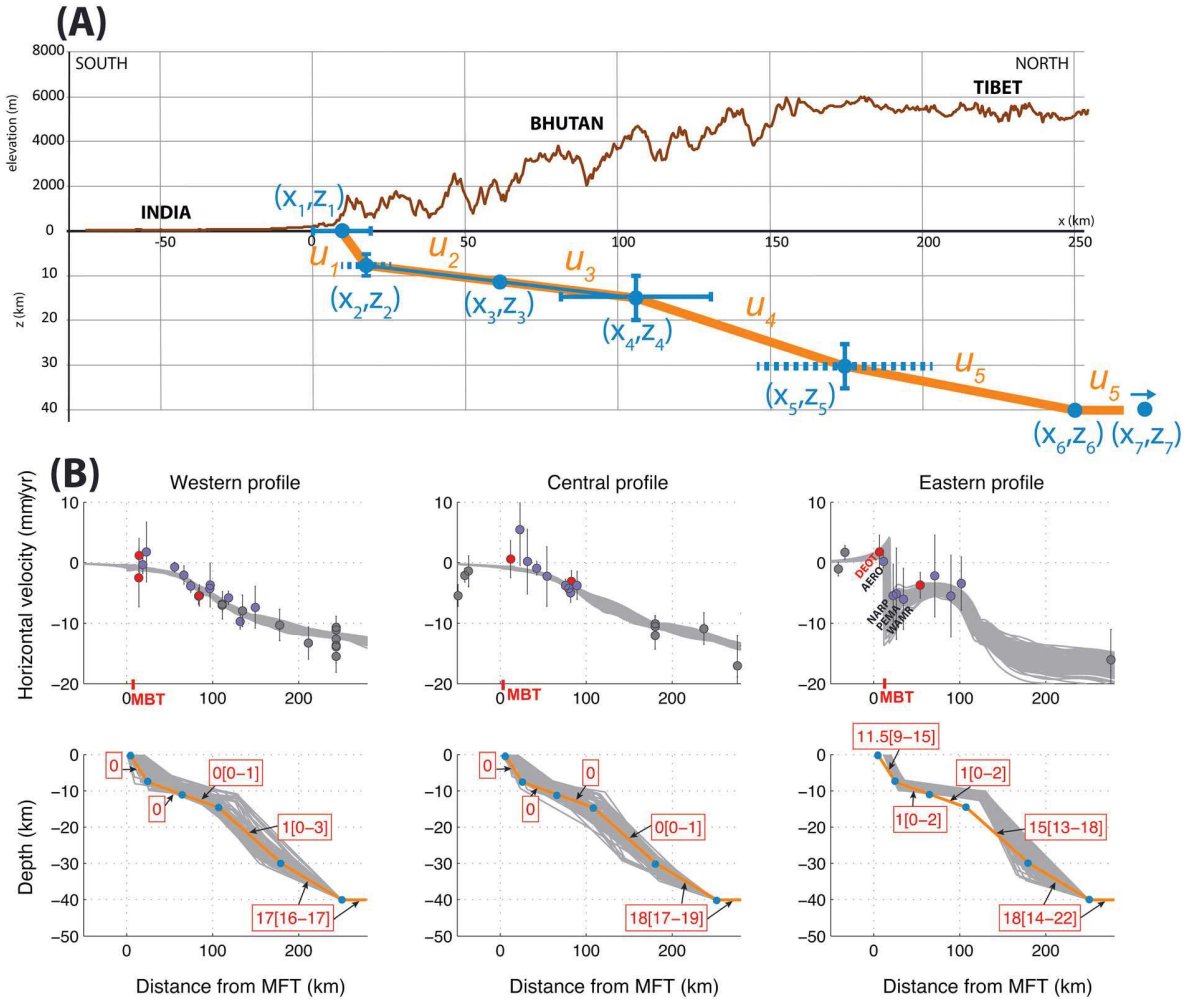

Figure 2. Model geometry and fault slip rates. (a) Geometry used in the inversion. Orange: a priori geometry. The ranges of the fault breakpoints (blue dots and segments) and allowed slip rates are detailed in Table S2. Dashed blue segments represent the angle constraint for points 2 and 5. Note that vertical scales are different for the topography and at depth. (b) Horizontal velocity profiles across western, central, and eastern Bhutan (see Figure 1 for locations). Gray lines are associated with the 100 best models. (top) GPS (circles, cf. Figure 1 for color legend) and calculated (lines) velocities. Note that GPS horizontal velocities are projected along the profile. (bottom) Obtained fault geometry (gray lines) and overthrusting slip rates (in red rectangles). Numbers in bracket corresponds to the slip rate uncertainties. Orange lines show the a priori model.

where n is the number of data points, $U\text{obs}_i$ is the observed GPS velocity and σ_i is the velocity uncertainty, and $U\text{calc}_i$ is the velocity calculated from the analytical solution given by *Singh and Rani* [1993] assuming a two-dimensional dip-slip fault embedded in a homogeneous half-space.

We only use the horizontal components of the GPS velocity vectors, projected along the profile direction, due to the limited availability of good-quality vertical velocities (see section 4 for a comparison of the models with vertical data). The posterior probability of each model parameter is obtained from the final collection of the sampled models (Figures 2, 3, and S1). In the following, the results of the inversion are presented in terms of highest density probability value (preferred value) and full width at half maximum (uncertainty).

3. Results

Our results indicate a present-day far-field convergence rate ~ 16.5–17.5 mm/a, without significant lateral variations along the Bhutan Himalaya arc (Figures 2b and 3), consistent with estimates of 17.6 ± 0.9 mm/a [*Stevens and Avouac*, 2015] and 15.5 ± 1.5 mm/a [*Vernant et al.*, 2014]. In contrast with this uniform convergence rate, we highlight lateral variations of interseismic slip pattern at depth (cf. Figures 2b and 3).

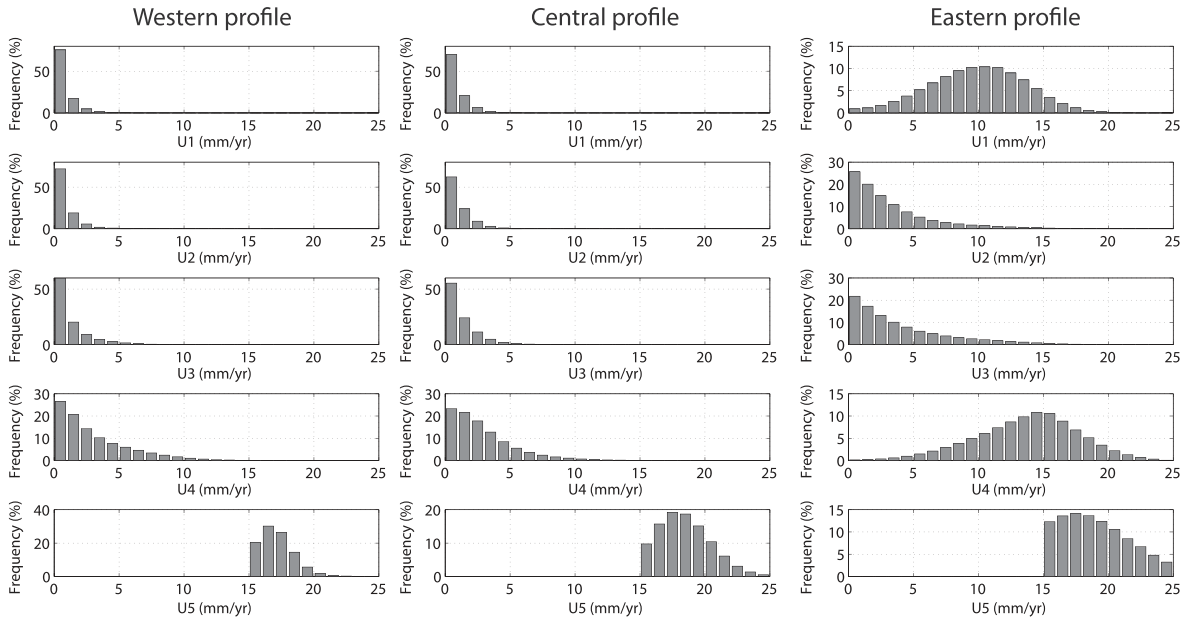

Figure 3. Slip rate posterior distributions on fault segments. u_1 to u_5 are the slip rates along the fault (from south to north, cf. Figure 2a) on the western, central, and eastern profiles.

1. Along the western and central Bhutan profiles, slip pattern is mostly bimodal, with an abrupt decrease on the crustal ramp from full convergence on the lower segment of the ramp (u_5) to near-zero slip rate on the upper segments (u_1 to u_4). The dense GPS coverage along these profiles (less than 30 km between sites) allows a good definition of this abrupt transition, as shown by the tight constraints on its location ($\pm$10 km) and on the slip rates of the various segments (Table S2).
2. In contrast with the western and central profiles, the interseismic slip pattern on the eastern profile shows a smoother transition on the deepest ramp with u_4 = 10–18 mm/a (illustrating the capacity of our analysis to resolve a gradual downdip transition). However, because of the lack of GPS coverage between 100 and 260 km north of the MFT, the precise location of this transition is poorly resolved (breakpoint 5, Figure S1d).
3. Whereas the slip rate on the flat segment of the MHT is similar for the three profiles (u_2 and u_3~ 0 mm/a), the shallow upper ramp of the eastern profile exhibits a higher slip rate with u_1 = 5.5–14.5 mm/a. This aseismic slip on the upper ramp is well constrained owing to very good data coverage within the $\pm$50 km of the MFT: Specifically, the three sites located north of the MBT (NARP, PEMA, and WAMR, above segment u_1) have the same velocity and present an abrupt change of ~6 mm/a compare to the sites directly south of the MBT (DEOT and AERO, see Figure 2b).

In our modeling approach, a fault segment with a null velocity is similar to no fault and its geometry cannot be constrained by the inversion. However, we can obtain information on the MHT geometry for the creeping segments, albeit with variable sensitivity on the different parameters (i.e., spread of the 100 best models, Figure 2b). This sensitivity can be assessed from the posterior probability distributions that show near-uniform probabilities for segments with near-zero slip rates in contrast with sharp probability clusters for faster creeping segments (cf. Figure S1). On this basis, new constraints on the MHT geometry can be derived for the creeping segments (Table S2).

1. The deepest and northernmost limit of the fully coupled section is located 135–155 km north of the MFT on the western and central profiles (breakpoint 5—Figures S1b and S1c) but only 120–130 km for the eastern profile (breakpoint 4—Figure S1d).
2. The deep flat-ramp transition is located 120–130 km north of the MFT in eastern Bhutan (breakpoint 4—Figure S1d).
3. The depth of the flat segment is constrained to 9–12 km in eastern Bhutan (breakpoints 2, 3, and 4—Figure S1d).

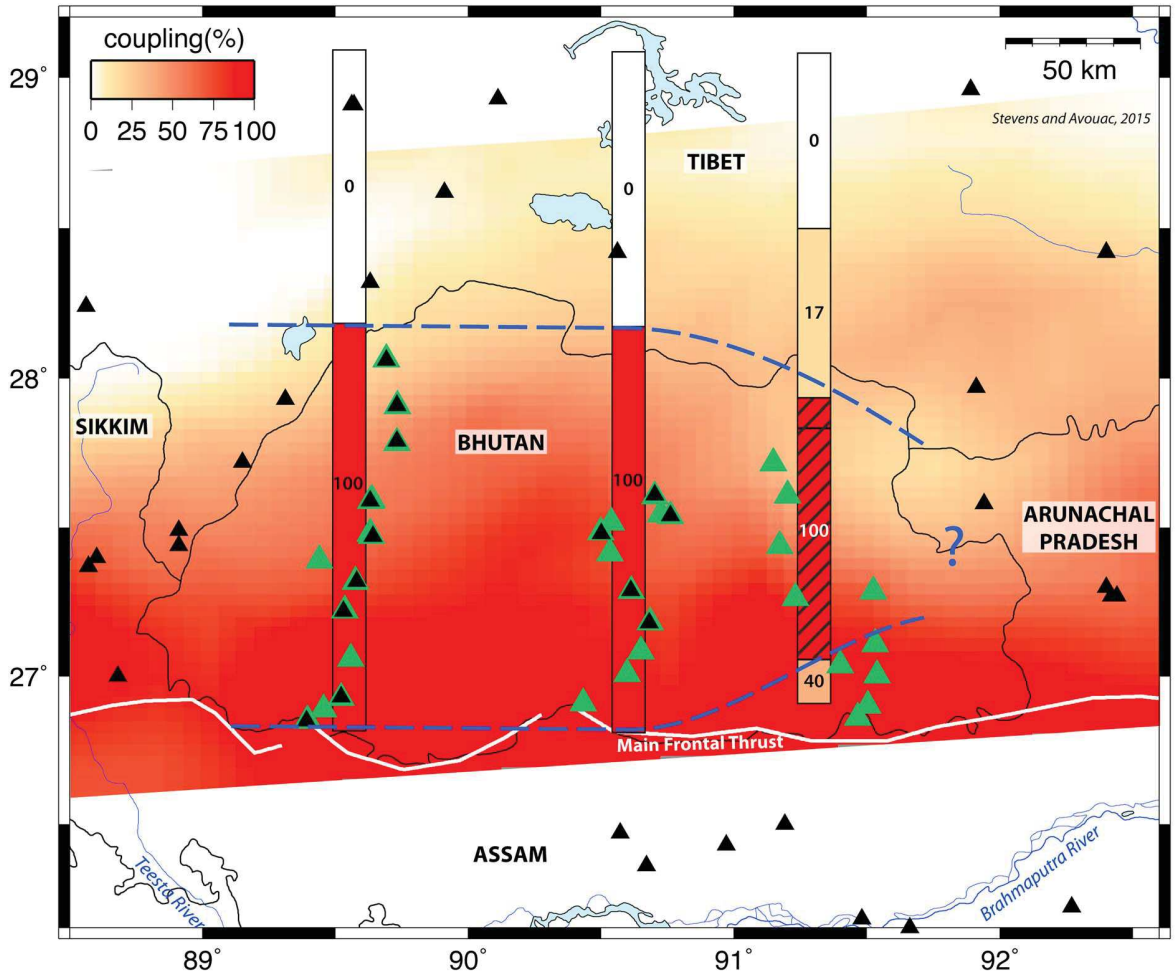

Figure 4. Interseismic coupling of the Main Himalayan Thrust in Bhutan. Rectangles show our estimates of interseismic coupling for the different fault segments. The hatched segment represents the flat part of the MHT constrained by the inversion. The colored base map represents the estimates of *Stevens and Avouac* [2015]. Dashed blue lines show the possible limits of the fully coupled zone. Green triangles show the locations of our new GPS stations. Black triangles are GPS stations used in the solution of *Stevens and Avouac* [2015].

4. On the eastern profile, active faulting takes place on the MBT, i.e., 13–20 km north of the MFT (breakpoint 1—Figure S1d). On both sides and nearby the surface expression of the upper fault segment, the GPS coverage is dense: DEOT and AERO, located between the MFT and MBT, have similar velocities to those south of the MFT, and we measure an abrupt change of ~ 6 mm/yr across the MBT (Figure 2b). These results indicate that the MBT in eastern Bhutan is currently active and that it accommodates part of the convergence by aseismic creep.

4. Discussion

In order to compare our results with other studies, we describe the interseismic state of the MHT in terms of coupling, defined as the ratio between the fault interseismic slip rate and the present-day far-field convergence rate ($u_5 = 17 \pm 2$ mm/a). On the basis of a smooth back slip model, *Stevens and Avouac* [2015] conclude that a frontal ~ 100 km large portion of the MHT is fully locked in Bhutan (coupling $> 50\%$). They argue for an abrupt transition to a decoupled segment along the downdip ramp, although their smoothed large-scale coupling map does not clearly resolve this transition pattern (Figure 4). The addition of new GPS data in western and central Bhutan allows us to better define this transition and its location. Our slip rate posterior distribution (Figure 3) shows that the interseismic coupling decreases northward from 100% to 0% along the deep ramp

segment, about 145 km north of the MFT in western and central Bhutan (Figure 4 and Table S2). Our results also indicate a significant change in the coupling pattern between central and eastern Bhutan, with a smoother transition (17% of coupling on the deeper ramp) and a slightly less wide coupled zone (100–120 km versus 135–155 km) along the eastern profile. We show for the first time in the Himalayas that the upper ramp is partially decoupled (40% (17–70%) of coupling), suggesting that the long-term convergence may not be fully expressed in large earthquakes in this particular region.

The current resolution of the vertical GPS velocities remains too low to provide significant constraints to our slip rate analysis. However, a first-order comparison of uplift rates from our campaign stations (with other 10 years of data) versus other geological indicators shows the potential importance of these data sets for short-and long-term uplift constraints. In western Bhutan, our vertical GPS velocities suggest a peak of 2–3.5 mm/a about 100 km north of the MFT (Figure S2), whereas Holocene denudation rates indicate a sharp peak of ~2 mm/a 130–150 km north of the MFT with near-zero rates between 40 and 110 km [*Le Roux-Mallouf et al.,* 2015; *Portenga et al*., 2014; *Adams et al.,* 2016]. This difference in patterns likely reflects the difference in measurement time scales: GPS data cover a decadal interseismic period and are mostly sensitive to the coupled-decoupled transition; denudation data are representative of several thousand years over several seismic cycles and are primarily sensitive to the fault geometry. A few additional years of campaign GPS data combined with longer-term denudation and incision data may thus provide important constraints on the geometry and seismic behavior of the MHT.

Our analysis of new GPS data in Bhutan provide three major constraints to the interseismic state of the MHT: (1) An abrupt downdip termination of the fully coupled segment, about 145 km north of the MFT in western and central Bhutan; (2) a less wide fully coupled segment in eastern Bhutan (~110 km), with a partially unlocked deeper crustal ramp; (3) in this eastern region, the MBT is creeping and is part of the active thrusting front. These observations raise questions regarding the seismic and interseismic behavior of the MHT. We infer creep on the eastern Bhutan MBT on the basis of velocity measurements over 3 years (2013–2016); hence, we cannot resolve whether this represents long-term creep or could potentially correspond to a transient slip episode on the upper part of the MHT, which would contribute to release part of the interseismic stress buildup. Similarly, our observation of partial creep on the MBT suggests that an event similar to the recent 2015 Gorkha earthquake occurring on the MHT could potentially not reach the surface in eastern Bhutan.

Acknowledgments
This project is funded by the French Agence Nationale de la Recherche (ANR-13-BS06-0006-01). We are grateful to the Department of Geology and Mines, M. Chokila and the National Land Commission of Bhutan for their major contributions to the field campaigns. The 2013–2016 surveys benefited from the support of the French RESIF-GPSMob Research Infrastructure (http://www.resif.fr). The discussion greatly benefited from talks with J.-P. Avouac whom we warmly thank. The manuscript has been greatly improved by helpful suggestions by Editor A.V. Newman and two anonymous reviewers. Data availability: Campaign GPS data for the 2003 survey are from R. Bilham project (NSF Cooperative Agreement EAR-0735156) and are available on the UNAVCO archive (https://www.unavco.org/data/gps-gnss/gps-gnss.html). Campaign GPS data for the 2013–2016 surveys are available on the RESIF-GPSMob archive (https://gpsmob.resif.fr) and by request to the authors for other periods. Permanent GPS data are available by request to the National Land Commission of Bhutan. GPS data processing was done with CSRS-PPP v1.5 provided by Natural Resources Canada (https://webapp.geod.nrcan.gc.ca/geod/tools-outils/ppp.php), using the International GNSS Service precise products (http://www.igs.org/products). GPS time series analysis was done with R software (https://www.r-project.org) with codes available by request to the authors. The slip rate and geometry inversion software is available by request to the authors.

References

Acton, C. E., K. Priestley, S. Mitra, and V. K. Gaur (2011), Crustal structure of the Darjeeling—Sikkim Himalaya and southern Tibet, *Geophys. J. Int.*, *184*(2), 829–852.

Adams, B. A., K. X. Whipple, K. V. Hodges, and A. M. Heimsath (2016), In situ development of high-elevation, low-relief landscapes via duplex deformation in the Eastern Himalayan hinterland, Bhutan, *J. Geophys. Res. Earth Surf.*, *121*, 294–319, doi:10.1002/2015JF003508.

Ader, T., et al. (2012), Convergence rate across the Nepal Himalaya and interseismic coupling on the Main Himalayan Thrust: Implications for seismic hazard, *J. Geophys. Res.*, *117*, B04403, doi:10.1029/2011JB009071.

Banerjee, P., R. Bürgmann, B. Nagarajan, and E. Apel (2008), Intraplate deformation of the Indian subcontinent, *Geophys. Res. Lett.*, *35*, L18301, doi:10.1029/2008GL035468.

Bettinelli, P., J. P. Avouac, M. Flouzat, F. Jouanne, L. Bollinger, P. Willis, and G. R. Chitrakar (2006), Plate motion of India and interseismic strain in the Nepal Himalaya from GPS and DORIS measurements, *J. Geod.*, *80*(8–11), 567–589.

Bhattacharyya, K., and G. Mitra (2009), A new kinematic evolutionary model for the growth of a duplex—An example from the Rangit duplex, Sikkim Himalaya, India, *Gondwana Res.*, *16*(3), 697–715.

Caldwell, W. B., S. L. Klemperer, J. F. Lawrence, S. S. Rai, and Ashish (2013), Characterizing the Main Himalayan Thrust in the Garhwal Himalaya, India with receiver function CCP stacking, *Earth Planet. Sci. Lett.*, *367*, 15–27, doi:10.1016/j.epsl.2013.02.009.

Coutand, I., D. M. Whipp Jr., D. Grujic, M. Bernet, M. G. Fellin, B. Bookhagen, K. R. Landry, S. K. Ghalley, and C. Duncan (2014), Geometry and kinematics of the Main Himalayan Thrust and Neogene crustal exhumation in the Bhutanese Himalaya derived from inversion of multi-thermochronologic data, *J. Geophys. Res. Solid Earth*, *119*, 1446–1481, doi:10.1002/2013JB010891.

Gahalaut, V. K., et al. (2013), Aseismic plate boundary in the Indo-Burmese wedge, northwest Sunda Arc, *Geology*, *41*(2), 235–238.

Gan, W., P. Zhang, Z.-K. Shen, Z. Niu, M. Wang, Y. Wan, D. Zhou, and J. Cheng (2007), Present-day crustal motion within the Tibetan Plateau inferred from GPS measurements, *J. Geophys. Res.*, *112*, B08416, doi:10.1029/2005JB004120.

Grandin, R., M. P. Doin, L. Bollinger, B. Pinel-Puysségur, G. Ducret, R. Jolivet, and S. N. Sapkota (2012), Long-term growth of the Himalaya inferred from interseismic InSAR measurement, *Geology*, *40*(12), 1059–1062.

Hauck, M. L., K. D. Nelson, L. D. Brown, W. Zhao, and A. R. Ross (1998), Crustal structure of the Himalayan orogen at ~90 east longitude from Project INDEPTH deep reflection profiles, *Tectonics*, *17*, 481–500, doi:10.1029/98TC01314.

Héroux, P., and J. Kouba (2001), GPS precise point positioning using IGS orbit products, *Phys. Chem. Earth, Part A*, *26*(6), 573–578.

Jackson, M., and R. Bilham (1994), Constraints on Himalayan deformation inferred from vertical velocity fields in Nepal and Tibet, *J. Geophys. Res.*, *99*, 13–897, doi:10.1029/94JB00714.

Jade, S. (2004), Estimates of plate velocity and crustal deformation in the Indian subcontinent using GPS geodesy, *Curr. Sci.*, *86*, 1443–1448.

Jade, S., et al. (2007), Estimates of interseismic deformation in northeast India from GPS measurements, *Earth Planet. Sci. Lett.*, *263*(3), 221–234.

Jade, S., H. R. Rao, M. S. M. Vijayan, V. K. Gaur, B. C. Bhatt, K. Kumar, S. Jaganathan, M. B. Ananda, and P. D. Kumar (2011), GPS-derived deformation rates in northwestern Himalaya and Ladakh, *Int. J. Earth Sci.*, *100*(6), 1293–1301.

Jade, S., et al. (2014), Contemporary deformation in the Kashmir–Himachal, Garhwal and Kumaon Himalaya: Significant insights from 1995–2008 GPS time series, *J. Geod.*, *88*(6), 539–557.

Kanda, R. V. S., and M. Simons (2010), An elastic plate model for interseismic deformation in subduction zones, *J. Geophys. Res.*, *115*, B03405, doi:10.1029/2009JB006611.

Le Roux-Mallouf, R., et al. (2015), Evidence for a wide and gently dipping Main Himalayan Thrust in western Bhutan, *Geophys. Res. Lett.*, *42*, 3257–3265, doi:10.1002/2015GL063767.

Liang, S., W. Gan, C. Shen, G. Xiao, J. Liu, W. Chen, X. Ding, and D. Zhou (2013), Three-dimensional velocity field of present-day crustal motion of the Tibetan Plateau derived from GPS measurements, *J. Geophys. Res. Solid Earth*, *118*, 5722–5732, doi:10.1002/2013JB010503.

Long, S., N. McQuarrie, T. Tobgay, and D. Grujic (2011), Geometry and crustal shortening of the Himalayan fold-thrust belt, eastern and central Bhutan, *Geol. Soc. Am. Bull.*, *123*(7/8), 1427–1447, doi:10.1130/B30203.1.

Mahesh, P., et al. (2012), Rigid Indian plate: Constraints from GPS measurements, *Gondwana Res.*, *22*(3), 1068–1072.

Mao, A., C. G. Harrison, and T. H. Dixon (1999), Noise in GPS coordinate time series, *J. Geophys. Res.*, *104*, 2797–2816, doi:10.1029/1998JB900033.

Marechal, A., S. Mazzotti, J. L. Elliott, J. T. Freymueller, and M. Schmidt (2015), Indentor-corner tectonics in the Yakutat-St. Elias collision constrained by GPS, *J. Geophys. Res. Solid Earth*, *120*, 3897–3908, doi:10.1002/2014JB011842.

Mosegaard, K., and A. Tarantola (1995), Monte Carlo sampling of solutions to inverse problems, *J. Geophys. Res.*, *100*, 12,431–12,447, doi:10.1029/94JB03097.

Mukul, M., S. Jade, A. Bhattacharyya, and K. Bhusan (2010), Crustal shortening in convergent orogens: Insights from Global Positioning System (GPS) measurements in northeast India, *J. Geol. Soc. India*, *75*(1), 302–312, doi:10.1007/s12594-010-0017-9.

Nábělek, J., G. Hetényi, J. Vergne, S. Sapkota, B. Kafle, M. Jiang, H. Su, J. Chen, B. S. Huang, and the Hi-CLIMB Team (2009), Underplating in the Himalaya-Tibet collision zone revealed by the Hi-CLIMB experiment, *Science*, *325*(5946), 1371–1374, doi:10.1126/science.1167719.

Nguyen, H. N., P. Vernant, S. Mazzotti, G. Khazaradze, and E. Asensio (2016), 3D GPS velocity field and its implications on the present-day post-orogenic deformation of the Western Alps and Pyrenees, *Solid Earth*, *7*, 1349–1363.

Okada, Y. (1985), Surface deformation due to shear and tensile faults in a half-space, *Bull. Seismol. Soc. Am.*, *75*(4), 1135–1154.

Portenga, E. W., P. R. Bierman, C. Duncan, L. B. Corbett, N. M. Kehrwald, and D. H. Rood (2014), Erosion rates of the Bhutanese Himalaya determined using in situ-produced ^{10}Be, *Geomorphology*, *233*, 112–126.

Savage, J. C. (1983), A dislocation model of strain accumulation and release at a subduction zone, *J. Geophys. Res.*, *88*, 4984–4996, doi:10.1029/JB088iB06p04984.

Singh, S. J., and S. Rani (1993), Crustal deformation associated with two-dimensional thrust faulting, *J. Phys. Earth*, *41*, 87–101.

Stevens, V. L., and J. P. Avouac (2015), Interseismic coupling on the main Himalayan thrust, *Geophys. Res. Lett.*, *42*, 5828–5837, doi:10.1002/2015GL064845.

Tang, L., C. Li, J. Zhang, X. Shl, and P. Wei (2010), Precise monitoring technique for regional surface deformation using GPS/CORS observation, *Bull. Surv. Mapp.*, *5*, 6–9.

Tobgay, T., N. McQuarrie, S. Long, M. J. Kohn, and S. L. Corrie (2012), The age and rate of displacement along the Main Central Thrust in the western Bhutan Himalaya, *Earth Planet. Sci. Lett.*, *319*, 146–158.

Vergne, J., R. Cattin, and J. P. Avouac (2001), On the use of dislocations to model interseismic strain and stress build-up at intracontinental thrust faults, *Geophys. J. Int.*, *147*, 155–162.

Vernant, P., R. Bilham, W. Szeliga, D. Drupka, S. Kalita, A. K. Bhattacharyya, V. K. Gaur, P. Pelgay, R. Cattin, and T. Berthet (2014), Clockwise rotation of the Brahmaputra Valley relative to India: Tectonic convergence in the eastern Himalaya, Naga Hills, and Shillong Plateau, *J. Geophys. Res. Solid Earth*, *119*, 6558–6571, doi:10.1002/2014JB011196.

Geophysical Research Letters

Supporting Information for

Evidence of interseismic coupling variations along the Bhutan Himalayan arc from new GPS data

Anais Marechal[1], Stephane Mazzotti[1], Rodolphe Cattin[1], Gael Cazes[2], Philippe Vernant[1], Dowchu Drukpa[3], Kinzang Thinley[4], Alizia Tarayoun[1], Romain Le Roux-Mallouf[1], Bal Bahadur Thapa[4], Phuntsho Pelgay[3], Jampel Gyeltshen[3], Erik Doerflinger[1], Stéphanie Gautier[1]

[1] Geosciences Montpellier, UMR5243, Université de Montpellier, Place E. Bataillon, 34 095 Montpellier, France

[2] School of Earth and Environmental Sciences, University of Wollongong, Wollongong, NSW, Australia

[3] Seismology and Geophysics Division, Department of Geology and Mines, Ministry of Economic Affairs, Post Box 173, Thimphu, Bhutan

[4] National Land Commission, Royal Government of Bhutan, Post Box 142, Thimphu, Bhutan

Contents of this file

Tables S1 to S2

Figures S1 to S2

Introduction

This supporting information contains (1) GPS velocities and (2) inversions results, prior and posterior ranges and likelihood probability distributions of the model parameters (fault segment geometries and slip rates).

Table S1. GPS velocities and associated standard errors (1σ uncertainty) in North, East and Up components. Length: duration of the time series used to calculate the velocities (in year). Nobs: number of surveys for the campaign sites or percentage of days of observations for the time series duration for the permanent sites.

			Velocity relative to stable India (Ader et al., 2012) (mm/a)			Velocity in ITRF2008 (mm/a)			1σ uncertainty (mm/a)				
station	lat. (°)	lon. (°)	North	East	Up	North	East	Up	North	East	Up	length (a)	Nobs
AERO	26.90	91.50	-3.0	6.6	-7.2	31.84	46.38	-7.19	0.7	0.8	1.3	12.4	4
AUTS	27.44	91.17	-7.7	-0.5	5.5	27.18	39.02	5.51	3.9	5.5	13.6	2.0	2
BHUM	27.54	90.72	-6.9	1.7	-1.1	27.92	41.05	-1.12	1.4	1.1	1.9	3.5	47.9%
CHUC	27.48	90.50	-7.4	2.4	2.5	27.47	41.65	2.53	0.7	0.7	1.2	12.4	4
DEOT	26.86	91.46	-3.2	0.4	-2.2	31.61	40.18	-2.2	2.3	1.5	2.8	3.5	61.2%
DGON	27.52	90.54	-7.9	2.2	0.3	26.96	41.48	0.34	0.7	0.6	1.4	12.4	3
DODI	27.59	89.63	-6.4	2.2	4.2	28.51	41.19	4.2	0.7	0.9	2.7	12.4	5
GANG	27.22	89.53	-2.7	2.3	0.3	32.18	41.4	0.34	0.7	0.5	1.1	12.4	4
GASA	27.91	89.73	-10.9	6.0	0.1	23.95	44.9	0.07	0.9	0.9	3.1	8.6	3
GEDU	26.93	89.52	-0.2	2.0	-3.6	34.73	41.15	-3.64	3.0	3.9	6.4	3.0	2
GELE	26.91	90.43	-3.1	1.6	-1.8	31.76	41.05	-1.8	2.5	1.8	3.8	3.5	63.6%
GENE	27.32	89.57	-4.2	1.9	-1.0	30.71	40.95	-0.96	1.4	0.7	2.2	12.4	4
JAKR	27.54	90.76	-8.5	2.9	4.2	26.41	42.29	4.19	1.3	1.0	1.2	12.4	4
KABU	27.79	89.73	-7.4	4.3	3.1	27.52	43.25	3.06	0.8	0.8	2.8	12.5	4
KAMJ	26.89	89.45	-2.5	1.6	1.2	32.39	40.83	1.15	1.3	0.6	1.1	12.4	2
KANG	27.29	91.52	-9.1	0.3	-2.2	25.79	39.9	-2.2	1.8	1.2	2.1	4.1	20.9%
KHOS	27.29	90.61	-7.3	-2.3	3.8	27.62	37.12	3.81	2.7	4.1	3.3	3.0	2
KNGA	27.41	90.53	-28.6	2.1	-14.8	6.23	41.4	-14.76	0.9	0.7	0.6	3.0	2
KURJ	27.61	90.70	-7.1	3.3	1.3	27.76	42.56	1.28	1.6	1.7	4.9	12.4	4

LAYA	28.06	89.69	-10.3	0.1	-3.1	24.6	39	-3.12	2.7	2.2	3.3	3.0	2
LHUE	27.72	91.15	-8.4	1.5	-9.9	26.46	40.88	-9.94	2.8	3.4	7.9	3.1	3
MONG	27.26	91.23	-1.7	6.0	-12.3	33.19	45.6	-12.25	2.4	35.4	16.2	3.1	3
NARP	27.00	91.54	-10.7	0.7	20.8	24.18	40.45	20.84	4.0	3.2	5.0	2.0	2
PARO	27.39	89.44	-5.8	2.9	-1.4	29.09	41.88	-1.37	0.7	0.7	1.5	12.4	2
PEMA	27.04	91.40	-10.5	0.4	7.6	24.37	40.08	7.56	5.3	5.4	13.3	2.0	2
PHUN	26.85	89.39	-1.4	0.0	-0.6	33.5	39.18	-0.55	2.3	1.7	3.2	3.6	31.2%
RBIT	26.85	89.39	-3.2	6.8	-16.2	31.73	45.99	-16.21	3.7	3.1	6.1	2.2	75.2%
SAMK	27.01	90.60	0.3	-4.1	14.5	35.14	35.42	14.53	4.8	3.5	11.1	2.0	2
TAMA	27.08	90.65	-3.9	0.4	2.4	30.99	39.82	2.35	3.9	3.6	10.5	2.0	2
TAN2	27.61	91.20	-8.3	8.9	-24.2	26.57	48.36	-24.19	5.7	3.5	14.7	2.0	2
TANG	27.59	89.64	-7.1	-2.1	1.1	27.77	36.92	1.07	1.9	3.0	4.9	12.5	3
THIM	27.48	89.63	-7.7	2.0	-0.2	27.22	41.06	-0.2	1.4	1.0	1.9	4.6	55.8%
TIMP	27.47	89.63	-7.5	3.1	-3.9	27.43	42.12	-3.85	1.0	1.0	2.1	5.2	82.9%
WAMR	27.11	91.53	-11.2	1.0	-588.5	23.66	40.67	-588.53	4.2	2.8	4.6	3.1	2
WONK	27.06	89.56	3.5	14.4	-3.0	38.38	53.55	-3.01	0.1	2.2	0.2	3.0	2
ZHEM	27.18	90.68	-4.6	1.7	0.5	30.25	41.18	0.47	1.0	0.6	2.4	12.4	4

Table S2. Prior and posterior distributions of inversion parameters. Prior constraints (column 2): investigated range of the free parameters used in the inversion. Note that parameters are not independent. Posterior values (columns 3-5): parameter values associated with the most likely model and associated uncertainties (in parenthesis) for the western, central and eastern profiles. Uncertainties are given by the full width at half maximum of the posterior distributions (cf. text). Symbols "-" indicate parameters that are not constrained by the inversion. Cf. Fig. S1b-d for the posterior distributions.

Parameter	**Prior constraints**	**Posterior values**		
number of models	10^8	West	Central	East
x_1 (km)	from 0 to 20	-	-	13 (13-20)
z_1 (km)	0	0	0	0
x_2 (km)	from $x_1 + z_2$ /tan(50°) to $x_1 + z_2$ /tan(10°)	-	-	30 (30-35)
z_2 (km)	from 5 to 10	-	-	9 (9-10)
x_3 (km)	from x_2 to x_4	-	-	115 (100-125)
z_3 (km)	from z_2 to z_4 This point is on the line segment from (x_2,z_2) to (x_4,z_4)	-	-	10 (9-11)
x_4 (km)	from 80 to 130	-	-	125 (120-130)
z_4 (km)	from 10 to 20	-	-	11 (10-12)
x_5 (km)	from $x_4+(z_5-z_4)/\tan(\alpha_{min})$ to $x_4+(z_5-z_4)/\tan(30°)$	145 (135-145)	145 (135-155)	185 (170-205)
z_5 (km)	from 25 to 35 With α_{min} the lowest dip angle between the two line segments $[(x_2,z_2); (x_4,z_4)]$ and $[(x_4,z_4); (x_6,z_6)]$	26 (25-27)	29 (27-31)	26 (25-28)
x_6 (km)	250	250	250	250
z_6 (km)	40	40	40	40
x_7 (km)	1000	1000	1000	1000
z_7 (km)	40	40	40	40
U_1 (mm/yr)	from 0 to U_4	0	0	10.5 (5.5-14.5)
U_2 (mm/yr)	from 0 to U_4	0	0	0 (0-2)
U_3 (mm/yr)	from 0 to U_4	0	0	0 (0-3)
U_4 (mm/yr)	from 0 to U_5	0 (0-3)	0 (0-3)	14.5 (10-18)
U_5 (mm/yr)	from 15 to 25	16.5 (15-18)	17.5 (15-20)	17.5 (15-22)

Figure S1a. Bivariate frequency histograms showing the prior distribution of the fault breakpoint coordinates. Due to dependencies between parameters, these distributions are not homogeneous, especially for points 2 and 3. The position of point 1 is only given as the x coordinate as the depth z is fixed at 0 km. Cf. Table S2 for constraints on the prior parameter ranges and dependencies.

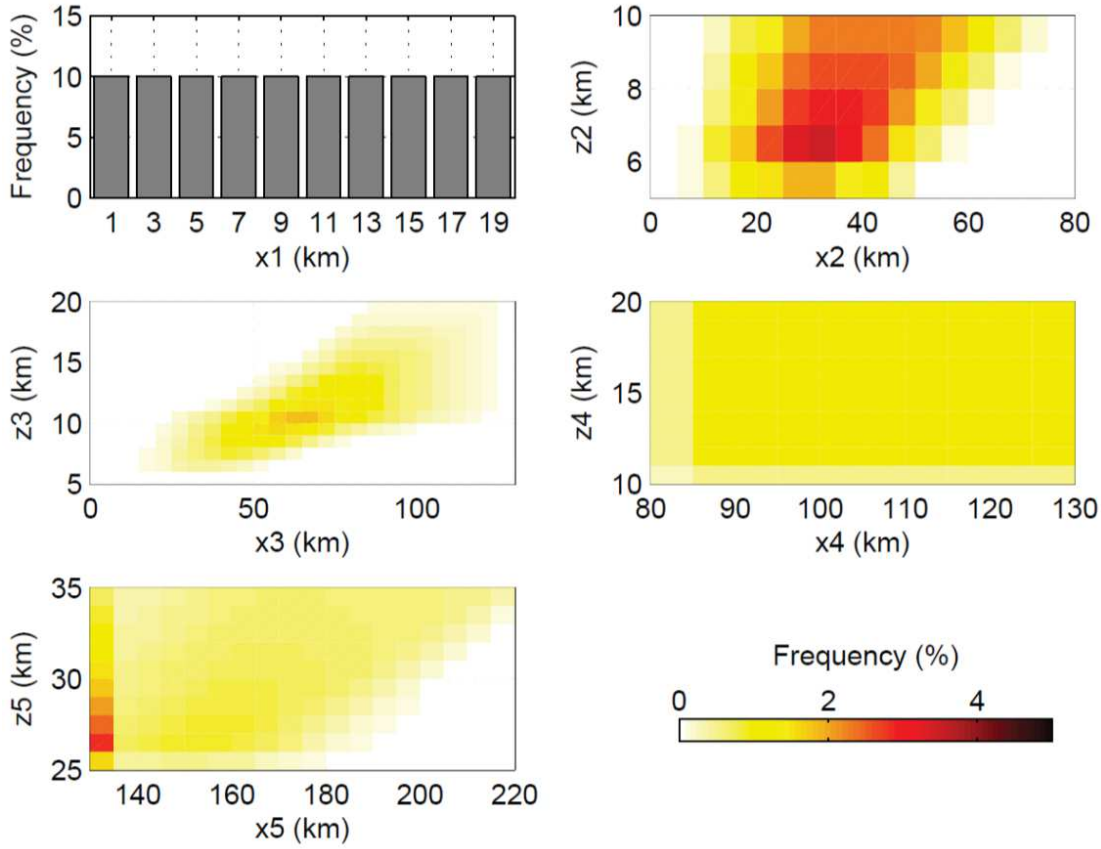

Figure S1b. Fault geometry obtained from inversion of horizontal GPS data for western Bhutan. The bivariate frequency histograms represent the parameter likelihood constrained by GPS data only. In order to correct for prior distribution biases due to parameter dependencies (cf. Fig. S1a), these posterior distributions correspond to the difference between the full frequency histograms obtained by the inversion and the prior histograms.

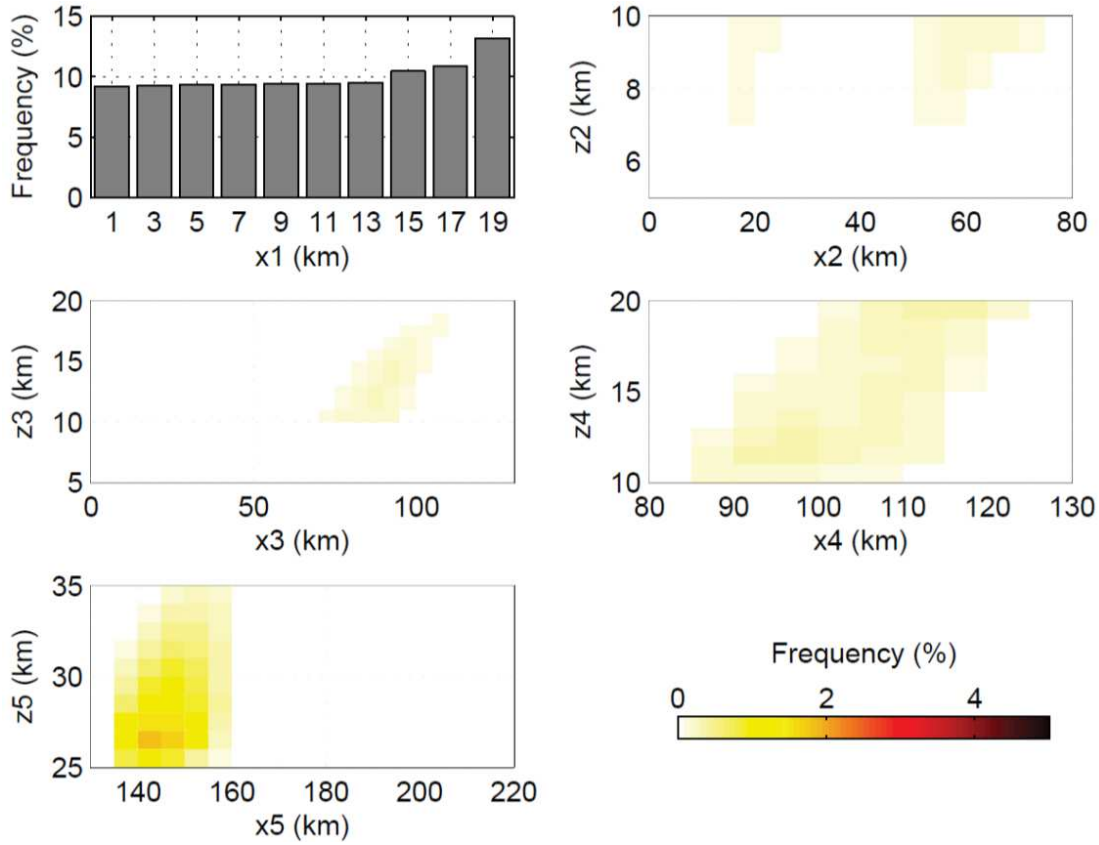

Figure S1c. Same as figure S1b for central Bhutan.

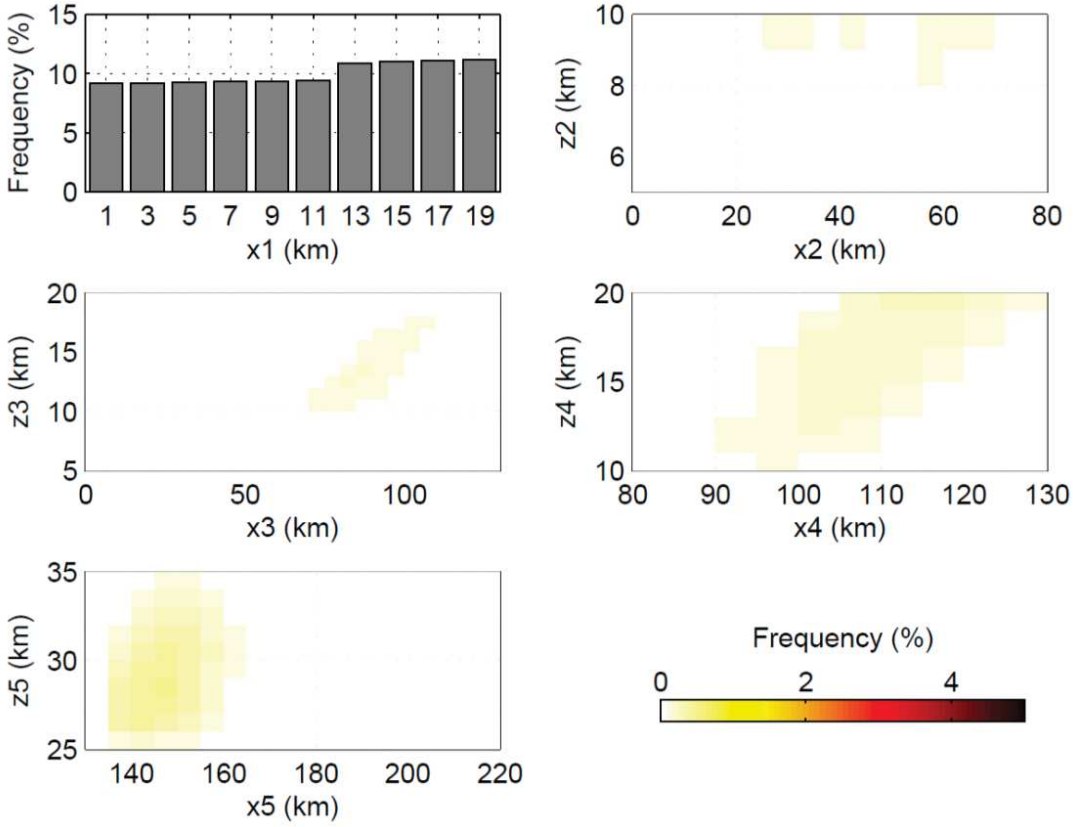

Figure S1d. Same as figure S1b for eastern Bhutan.

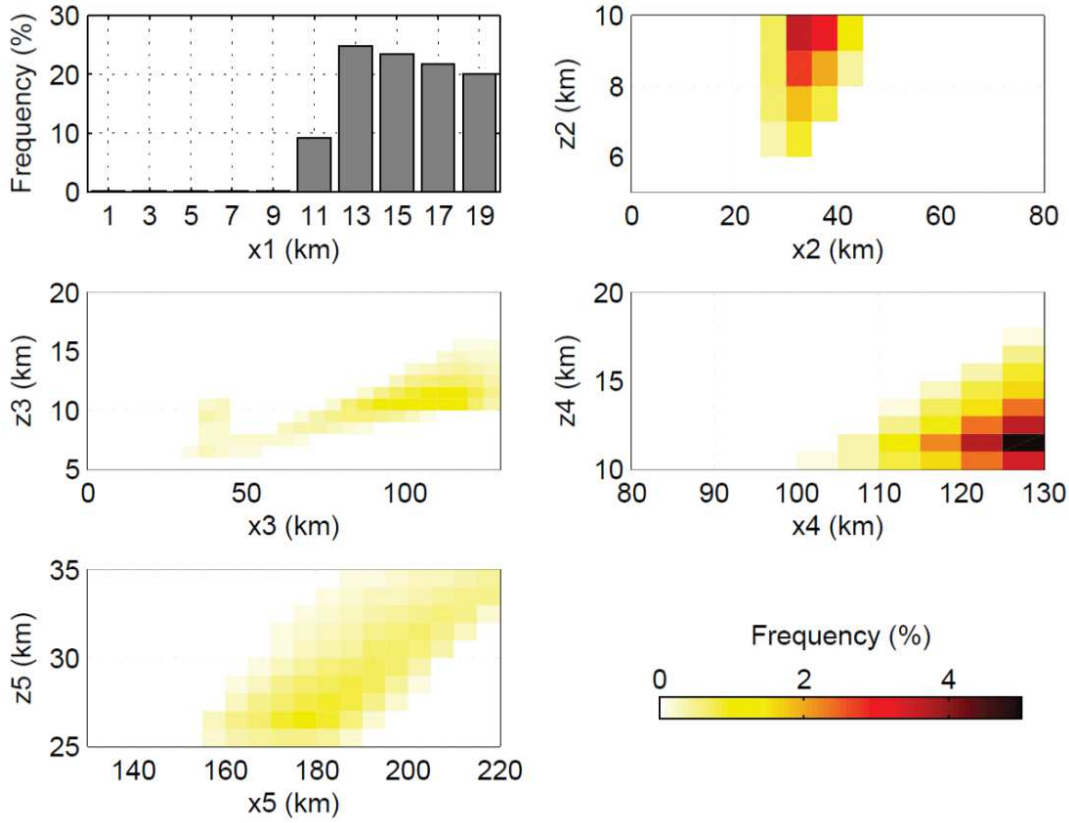

Figure S2. Observed and model-derived vertical velocities in western and central Bhutan. Gray lines are associated with the 100 best models. Blue circles show vertical GPS velocities for campaign stations with over 10 years of data. Green diamonds show the denudation rates derived from cosmogenic nuclides concentration in riverbed sediments (Le Roux-Mallouf *et al.*, 2015); Red squares from Adams et al. (2016); Orange triangles same from Portenga et al. (2014).

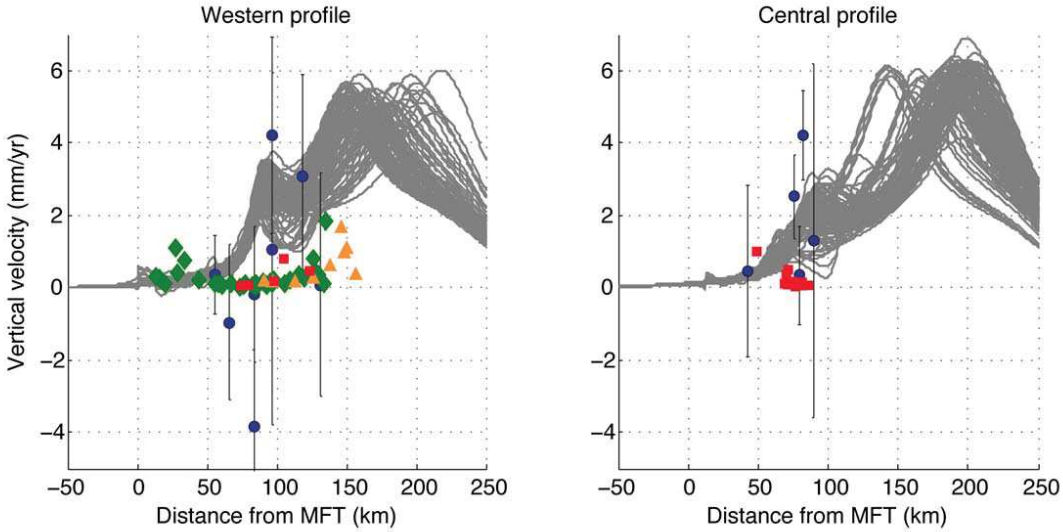

A.3 Segmentation of the Himalayas as revealed by arc-parallel gravity anomalies

SCIENTIFIC REPORTS

OPEN

Segmentation of the Himalayas as revealed by arc-parallel gravity anomalies

Received: 12 June 2016
Accepted: 02 September 2016
Published: 21 September 2016

György Hetényi[1,2,3], Rodolphe Cattin[3,4], Théo Berthet[5], Nicolas Le Moigne[4], Jamyang Chophel[6], Sarah Lechmann[2,7], Paul Hammer[2,8], Dowchu Drukpa[6], Soma Nath Sapkota[9], Stéphanie Gautier[4] & Kinzang Thinley[10]

Lateral variations along the Himalayan arc are suggested by an increasing number of studies and carry important information about the orogen's segmentation. Here we compile the hitherto most complete land gravity dataset in the region which enables the currently highest resolution plausible analysis. To study lateral variations in collisional structure we compute arc-parallel gravity anomalies (APaGA) by subtracting the average arc-perpendicular profile from our dataset; we compute likewise for topography (APaTA). We find no direct correlation between APaGA, APaTA and background seismicity, as suggested in oceanic subduction context. In the Himalayas APaTA mainly reflect relief and erosional effects, whereas APaGA reflect the deep structure of the orogen with clear lateral boundaries. Four segments are outlined and have disparate flexural geometry: NE India, Bhutan, Nepal & India until Dehradun, and NW India. The segment boundaries in the India plate are related to inherited structures, and the boundaries of the Shillong block are highlighted by seismic activity. We find that large earthquakes of the past millennium do not propagate across the segment boundaries defined by APaGA, therefore these seem to set limits for potential rupture of megathrust earthquakes.

Most of the largest earthquakes occur in subduction zones: on the Chile margin the 1960 Valdivia earthquake reached 9.5 on the Richter magnitude scale and more recently, in 2004 and 2011, magnitude 9 earthquakes have struck Sumatra and Japan. Major earthquakes also happen in the context of continental collision: in the Himalayas the 1950 Assam earthquake was estimated at magnitude Mw 8.6 (ref. 1). Several studies suggest that a historical event near 1100 AD could have reached magnitude 9 along the Himalayan front[2,3]. Such large events are also required in the Himalayas to balance the moment deficit derived from geodetic strain measurements[4].

The three key parameters controlling the magnitude of an event are the co-seismic slip, the width and the length of the ruptured zone. While slip is mainly dictated by convergence rate and inter-seismic coupling between the two plates, rupture width and length are geometrical properties that can be assessed from the structure of the subduction or collision zone. The more the plate interface is continuous and homogeneous along strike, the easier it will be for rupture to propagate and extend laterally. Therefore, assuming uniform coupling[5], segmentation of subduction and collision zones is primarily dependent on lateral variations in plate structure.

Although direct access to the plate interface is beyond reach, variations in its geometry can be reasonably assumed to be reflected in topography (e.g. ref. 6) and in the gravity field. The bending of the subducting plate determines the topographic signal through deformation of the upper plate and through the amount of sediments accumulating in the foreland basin and then entering the accretionary wedge. The gravity signal senses density

[1]Institute of Earth Sciences, University of Lausanne, Géopolis, Quartier UNIL-Mouline, 1015 Lausanne, Switzerland. [2]Department of Earth Sciences, ETH Zürich, Soneggstrasse 5, 8092 Zürich, Switzerland. [3]Laboratoire de Géologie, Ecole Normale Supérieure, CNRS - UMR 8538, 24 rue Lhomond, 75005 Paris, France. [4]Géosciences Montpellier, CNRS UMR5243, Université de Montpellier, Place E. Bataillon, 34095 Montpellier, France. [5]Department of Earth Sciences, Uppsala University, Villavägen 16, 75236 Uppsala, Sweden. [6]Department of Geology and Mines, Ministry of Economic Affairs, PO Box 173 Thimphu, Bhutan. [7]armasuisse, Science & Technology, Federal Department of Defence, Civil Protection and Sport, Feuerwerkerstrasse 39, 3602 Thun, Switzerland. [8]SwissRe, Mythenquai 50/60, 8022 Zürich, Switzerland. [9]Department of Mines and Geology, Lainchaur, Kathmandu, Nepal. [10]National Land Commission, Kawang Jagsa, PO Box 142 Thimphu, Bhutan. Correspondence and requests for materials should be addressed to G.H. (email: gyorgy.hetenyi@unil.ch)

contrasts at depth, and is therefore directly mapping the crust-mantle boundary geometry, as well as the thickness of the foreland basin sediments.

In oceanic subduction zones these two fields were analysed by Song and Simons[7]. Compared to the average topography and gravity (marine free-air anomaly from satellite) profile *across* the subduction zone they have computed trench-*parallel* topography and gravity anomalies (TPTA and TPGA, respectively – here renamed to TPaTA and TPaGA to avoid confusion with arc-perpendicular variations). Their findings around the Pacific plate have demonstrated that the largest earthquakes have mostly occurred in areas where both TPaTA and TPaGA are negative. In these areas the plate interface is located relatively deeper, and larger shear tractions accumulate on the down-dip part of the locked zone, resulting in larger stick-slip events[7]. The steeper flexural geometry is reflected in the ocean bottom bathymetry, which has a relatively deeper topography and especially lower gravity signal, even if sediments accumulate in the topographic low. Song and Simons speculate that the structure of the subduction zone, and therefore of TPaTA and TPaGA, should be stable over a million-year time scale.

As subduction velocity is larger than continental convergence rate (by a roughly estimated factor of 4–5 on average), and as the total length of subduction zones is longer than that of collision zones (by a roughly estimated factor of 4–5 as well), large subduction-zone earthquakes occur more frequently: out of 17 M8.5+ earthquakes since 1900 only 1 was in a collisional setting. This means that the two contexts, subduction and collision, are roughly equally active when comparing them by the area of subducted material. As oceanic plate structure is in general simpler (and therefore laterally more homogeneous) than continental, subduction zone earthquakes may reach extremely large magnitudes, for which we have no equivalent instrumentally recorded event in collision zones. However, in terms of seismic risk, collision zones are prone to much larger devastation and damage as population and infrastructure are located literally on and very close to the rupture zone. Therefore assessing seismic segmentation in a continental collision setting, especially in the Himalayas, is essential to evaluate seismic hazard.

In our study, motivated by the approach presented by Song and Simons[7], we compute arc-parallel topography and gravity anomalies (APaTA and APaGA) along the 2500-km long Himalayan orogen. Song and Simons' study used free-air anomalies, an appropriate choice as all of the topography is found beneath sea-level, and also because of complete free-air gravity data availability from satellites on sea. For studying a collisional orogen we opt for Bouguer anomaly data, on one hand to eliminate the effect of masses above sea-level to be able to focus on deep structural features, on the other hand because of practical reasons (see sections on Data and Methods). Especially: how the lateral variations of these relate to instrumental and historical seismicity, whether there is any causal link between them, and how the foreland basins reflect these variations?

Data and New Measurements

Gravity Data Compilation. Song and Simons[7] used ETOPO-5 digital elevation model for bathymetry/topography and marine satellite gravity data-derived free-air anomalies[8] to perform their study. Today, bathymetry as well as marine gravity field derived from satellite altimetry are available at a resolution of ~10 km and an accuracy of ~2 mGal (ref. 9). In a collisional setting high-resolution topography data is readily available from the SRTM mission[10], but contrary to subduction zones continental satellite gravity data remains to be low-resolution. Therefore the challenge of constituting a comprehensive dataset hinges on gravity data. Satellite gravity datasets from missions such as GRACE and GOCE have a resolution of ca. 100 km (ref. 11), which is similar to the width of the Himalayas (ca. 250 km) and the width of the seismically locked zone (ca. 100 km). Global gravity models such as EGM2008 (refs 12 and 13) claiming higher resolution are created using interpolation, therefore studies based on such models (e.g. ref. 14, with application to the Himalaya) cannot resolve features smaller than 100 km wavelength. We hence aim to build an as complete as possible land gravity dataset to carry out the highest resolution plausible analysis.

We start from our previous compilation of gravity data[15], based on data from the International Gravimetric Bureau (BGI, http://bgi.omp.obs-mip.fr/), and refs 16–18. This dataset has a good coverage on either side of the Himalayas, but only a few profiles across the orogen. Therefore we carried out targeted field campaigns to complete this dataset with new field measurements in Nepal[19] and Bhutan[20]. Finally, we include gravity anomaly data from further three sources. Data by ref. 21 were digitized from projected profiles of the publication. Data reported in ref. 22 were kindly made available by the authors. Unpublished data by G. Poretti was also made available for our study (personal communication). The distribution of the source of gravity data is shown in Fig. 1a.

The consistency of the eight different datasets was verified by producing a series of profiles across the orogen. The relative gravity anomaly dataset of ref. 21 was shifted by −210 mGal to fit the earlier compilation (see details in ref. 15), and two out of five profiles were discarded as found inconsistent with neighbouring datasets. The gravity data from ref. 22 and Poretti (pers. comm.) have been reprocessed in the same manner as our own new data in Bhutan and Nepal. Finally, our hitherto relative gravity anomaly dataset in Bhutan[20] was calibrated by three absolute gravity bases (see description below) and fully reprocessed using the GravProcess software[23], resulting in a ca. −20 mGal shift (-19.9 ± 1.7 (1σ) mGal) compared to ref. 20.

Absolute Gravity Measurement in Bhutan. In March 2015, we have established the first three absolute gravity measurements in Bhutan, two in Thimphu and one in Gelephu, a small city in south central Bhutan (Table 1, Fig. 1a). We have used a Micro-g LaCoste FG5 absolute gravimeter[24], which has an accuracy of 2 μGal.

To ensure high-quality absolute measurements, gravity has been recorded during 24 hours, with one set of measurement every 30 minutes, and 100 drops per sets at the two stations in Thimphu. In Gelephu the series have been terminated after 7.5 hours of recording due to a too elevated ambient temperature; this should not affect our measurements as the two measurements in Thimphu have demonstrated that tidal effects are very well corrected for by the selected synthetic model. During the calculation of absolute gravity, the recorded data have been corrected for polar motion, pressure variations, Earth tides (ETGTAB[25]) and ocean load (FES2004[26]).

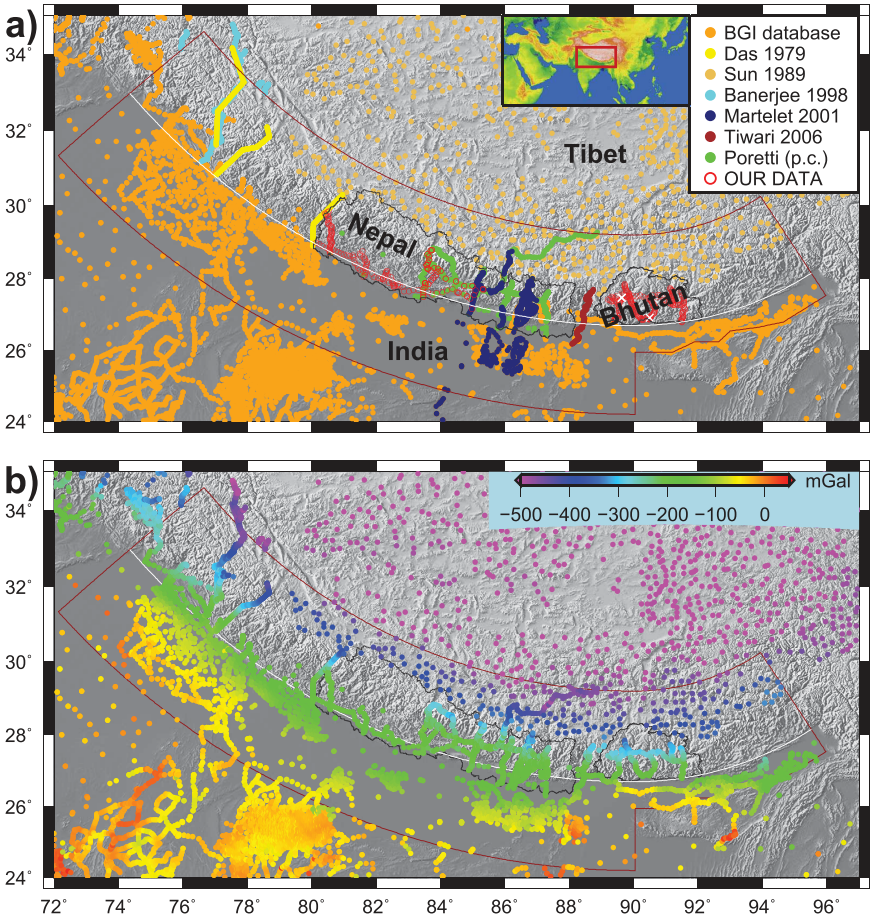

Figure 1. Gravity data. (**a**) Sources of our gravity data compilation (11470 points on map), including new absolute gravity points in Bhutan (white crosses). See main text for description and references. Inset: location of maps in this study. (**b**) Bouguer anomaly map of the Himalayas and surrounding region, referenced to sea-level and using 2670 kg/m^3 reduction density. Brown contour is the limit of our study area. White arc approximates the topographic front (mostly the Main Frontal Thrust). Boundaries of Nepal and Bhutan are shown in black as reference. Map created with GMT software[39] version 4 (http://gmt.soest.hawaii.edu/).

Station code	AGTDGM	AGTLS	AGGDGM
Location	Thimphu, DGM	Thimphu, LS	Gelephu, DGM
Longitude (°E)	89.635	89.630	90.504
Latitude (°N)	27.474	27.481	26.924
Altitude (m a.s.l.)	2350	2409	284
Vertical gradient (mGal/m)	−0.2639 ± 0.0048	−0.2668 ± 0.0051	−0.2544 ± 0.003
Gravity at the benchmark (μGal)	978′367′276.63	978′357′349.94	978′837′282.28
Date of measurement	11-12.03.2015	13-14.03.2015	16.03.2015

Table 1. Absolute gravity data at the three benchmark stations established in Bhutan. DGM: Department of Geology and Mines. LS: Land Survey.

The FG5 instrument provides an absolute gravity value at about 120 cm height above ground. We transfer this to the benchmark on the floor by estimating the vertical gravity gradient in a series of relative gravity (Scintrex CG5 instrument) measurement loops between the floor and 120 cm height[27]. A similar protocol has been used to connect the absolute gravity value with the relative gravity network: gravity ties have been done between the absolute benchmarks and the reference stations of the relative gravity surveys[23].

Our final new gravity dataset in Nepal and Bhutan is available from the authors and will be available through BGI (http://bgi.omp.obs-mip.fr/). In summary, we constructed an unprecedented gravity dataset in the Himalayan region (Fig. 1a), which is presented in terms of Bouguer anomalies (Fig. 1b). The gravity as well as topography data are processed as described in the Methods section to obtain the respective arc-parallel anomalies (Fig. 2).

Results

Arc-Parallel Topography Anomaly. The variation of raw APaTA exceeds 1000 m north of the topographic front, in the high range of the Himalayas. Lower values (not saturated colours) are only present north of the range itself, mostly in the central part of the arc. Along the southern part of the Himalaya there are a number of alternating negative and positive patches in the West, while in the East APaTA is mostly positive with a number of narrow negative features.

While these narrow negative APaTA features correspond to deeply eroded valleys in Eastern Nepal, Sikkim and Bhutan, the larger patches can be explained with arc-normal variations. It is simply local relief between the Lesser Himalaya and the Higher Himalaya formations. The Main Central Thrust, which marks the boundary between two formations (Fig. 2a; ref. 28) correlates visually well with this change of APaTA polarity. The sedimentary basin in NW India extending further north than our central arc explains the large negative patch there.

The smoothed APaTA map (Fig. 2b) clearly shows the same features: the topographic relief and the re-entrant in NW India are clearly visible. However, the narrow valleys are filtered out.

South of the topographic front the APaTA values are roughly an order of magnitude smaller (100 m range). Beyond a few topographic features clearly present, there is an overall trend in the Ganges Basin going from high values in the West to low values in the East, showing the long-wavelength topographic dip of the sedimentary basin.

Arc-Parallel Gravity Anomaly. The variation of APaGA exceeds 100 mGal. There are distinct along-arc segments when one looks at the variation of gravity from the foreland into the orogen:

- In northwesternmost India APaGA is positive in the foreland and negative in the orogen;
- There is a change around 77°E, gradual in the foreland, the sharpness in the orogen is not well constrained;
- All of Nepal is the opposite: negative-to-positive from foreland to orogen;
- There is a change around ca. 88°E, sharp in the foreland and little more gradual in the orogen;
- Bhutan is again positive-to-negative from foreland to orogen;
- There is a change around 93°E, visible in the foreland (there is no data within the Himalayas, but there is also a change further north near 94°E);
- APaGA is negative in the Assam foreland, with a few positive data points north of the Himalayas.

At the current level of data coverage, the foreland-to-orogen variation of APaGA is negative-to-positive at the area of Nepal and NE India, and is positive-to-negative near Bhutan and NW India. This is also represented on Fig. 3a as an anti-correlation of APaGA values south and north of the topographic front along the arc. Despite some spread in the gravity data in Nepal due to merging various datasets, the APaGA averages with 1σ deviation are distinct on either side of the orogen front. The two curves cross each other at ca. 350, ca. 1500 and ca. 2100 km along-arc distance (respective longitudes at the topographic front: ca. 77°E, 88°E and 93°E, with ca. ±1° when considering the 1σ zones).

Seismicity Data. To compare our results with Himalayan seismicity in the discussion (see next section) we show the pattern of both instrumental and historical events along the orogen (Fig. 3b,c).

Figure 3b shows the energy (cumulative moment) released by instrumentally recorded earthquakes. We take the USGS catalogue as events smaller than M4 that are detected by local networks do not contribute to this picture significantly. We aim to choose the maximum magnitude for this graph so that the along-arc comparison makes sense, i.e. the catalogue is complete for events of that magnitude. Irrespective of taking M6.0 (likely complete), M6.5 or M7.0 (likely incomplete) as higher bound, the pattern is the same: there are clear lows at ca. 250, ca. 900 and ca. 1700 km along-arc distance (resp. 76°E near Kangra, 81–83°E in West Nepal and 90°E in Bhutan). With the equivalent Mw-scale on the right it is clear that these zones have not only never produced an instrumental M6 event, but also that the cumulated effect of all smaller events does not reach that of a single M6 event. At these zones either (1) aseismic slip accommodates more of the convergence than in other parts of the orogen, or (2) more strain has accumulated than elsewhere, or (3) the instrumental record is not representative of the long-term seismic cycle.

Figure 3b complements this picture by showing the major and great earthquakes along the Himalayan arc, following ref. 29: three events (2015, 1950, 1934) with relatively well-defined rupture zones, and earlier events with more uncertain bounds. Note that at the longitude of Bhutan (1) the 1897 event occurred at the Shillong Plateau and not in the Himalayas; (2) the 1714 is speculative both in magnitude and location[30]; and (3) the 1180–1490 earthquake has been documented in two paleoseismological sites in south central Bhutan only[3,31].

Discussion

Comparison To Subduction Zones. While the respective ranges of arc-parallel topography and gravity anomalies in the Himalayas are the same as in oceanic subduction zones (few 100 to 1000 m, few 10 to 100 mGal), they are far from being correlated (Fig. S1). Therefore zones where both anomalies are negative cannot be used to discuss the location of large earthquakes in the Himalayas. Major events also do not clearly correlate with the low values of either of the anomalies: large earthquakes are known all along the Himalayas, and areas with relatively smaller events (Western Nepal, Bhutan) do show neither the same APaTA nor APaGA pattern. We therefore conclude that Song and Simons' approach is not directly applicable to continental collision.

The explanation lies, on one hand, in the nature of APaTA: it is primarily controlled by erosion (locally incised valleys) and the geological structure of the Himalayas (relief between Lesser and Higher Himalaya formations). Submarine erosion is slower and spatially more homogeneous than subaerial, resulting in different topography signals for an oceanic (simple) and an orogenic (complex) prism. On the other hand, the intrinsic relationship between bathymetry and free-air gravity on sea is not present in our study, as with Bouguer anomalies we have removed the effect of masses above sea-level, on purpose, to be able to focus on the deep structure of the orogen.

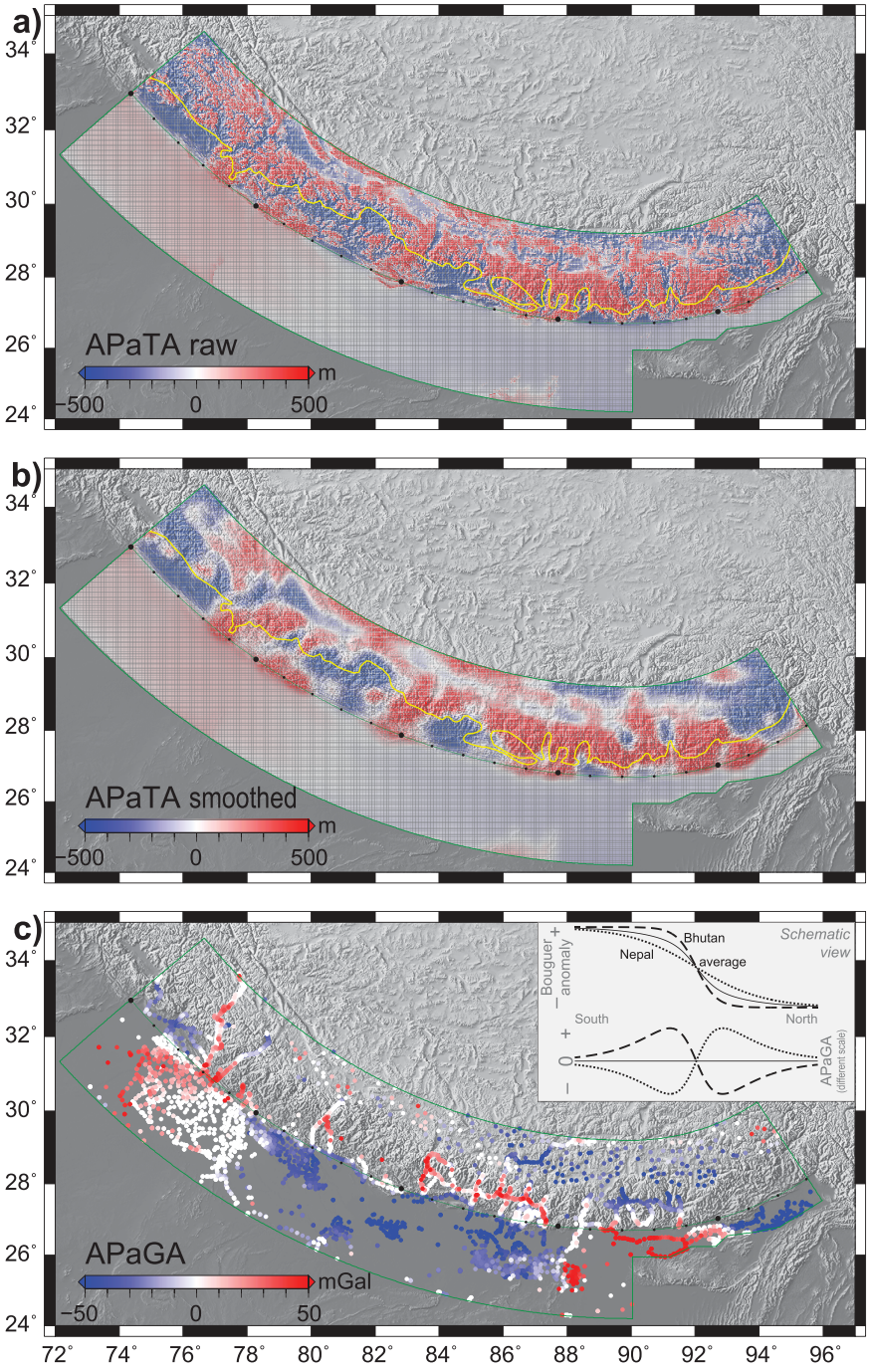

Figure 2. Arc-Parallel Topography and Gravity Anomalies (APaTA and APaGA). Red and blue values represent respectively higher and lower values of topography and gravity compared to the average profile perpendicular to the Himalayan arc. (**a**) APaTA in its raw format. Yellow line marks the Main Central Thrust, the boundary between the Lesser and Higher Himalaya formations (digitised from ref. 28). (**b**) APaTA after smoothing with a 30-km radius circle. (**c**) APaGa in the study area. Inset schematically shows how APaGA is determined: it is the residual anomaly (dashed and dotted lines are examples) compared to the cross-orogen gravity anomaly profile averaged along the orogen (solid line). Black dots on arc approximating the topographic front are placed every 100 km (every 5th larger) as reference for Fig. 3. Map created with GMT software[39] version 4 (http://gmt.soest.hawaii.edu/).

Interpretation. The arc-parallel gravity anomalies presented here do not correlate with instrumental seismicity (Fig. 3a,b). The low seismic moment release zone at ca. 250 km distance has near-zero APaGA both north and south of the topographic front. The second zone at ca. 900 km has low/high APaGA south/north of the topographic front. The third zone at ca. 1700 km is the opposite.

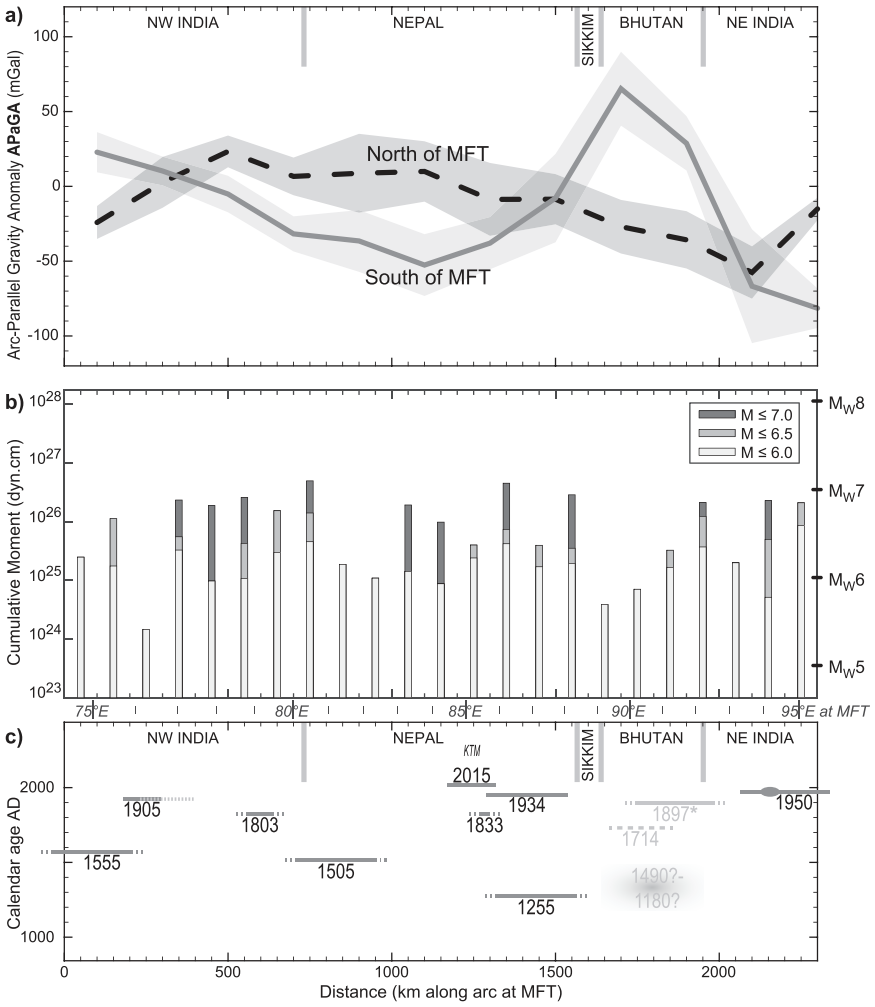

Figure 3. Variations of gravity and seismicity along the Himalayan arc. Horizontal distance is measured along the arc approximation of the topographic front within the study area (see maps on other figures); reciprocally, longitudes at the arc approximating the topographic front are indicated between panels (b,c) as reference. (**a**) Arc-Parallel Gravity Anomaly (APaGA) on either side of the topographic front. Lines represent the averages to at least 25 km to the South, and between 25 and 145 km to the North; shaded areas represent the 1σ deviation of values within each 200-km long bin. Approximate country boundaries are indicated as reference. (**b**) Amount of energy released by moderate to strong (but neither major nor great) earthquakes. Cumulative moment is in dyn.cm, equivalent moment magnitude is shown on right axis. (**c**) Known major and great earthquakes in the Himalaya. Base figure is from ref. 29. Star notes that the 1897 earthquake occurred outside of the Himalaya, at the Shillong Plateau. The 1714 earthquake location is speculative. The medieval event in Bhutan is after refs 3 and 31. The 1905 Kangra earthquake rupture extent is from ref. 40, dotted line is reported from ref. 29. The epicentre was on the western end of the segment and rupture propagated eastwards (see Fig. 4). The knot on the 1950 Assam earthquake represents the 1947 M7.3 event. Other instrumentally recorded events on this diagram are the 1905 M7.9 Kangra earthquake, the 1934 M8.0 Bihar earthquakes, and the 2015 M7.8 and M7.3 events in the Kathmandu (KTM) region. Magnitudes as of the USGS catalogue (http://earthquake.usgs.gov/earthquakes/search/).

However, there is a correlation between APaGA and large earthquakes (Fig. 3a,c). Locations where there is a flip of APaGA polarity north and south of the topographic front (Fig. 3a, ca. 350–1500–2100 km, resp. ca. 77–87–93°E) mark out boundaries across which major seismic events do not rupture laterally. The eastern segment boundary sees the 1950 Assam earthquake rupture stopping east of it, with no or uncertain rupture zones in Bhutan. The middle segment boundary near Sikkim also sees the 1255 earthquake rupture zone stop west of it. Finally, the western segment boundary in NW India is near the 1905 Kangra earthquake: this event has initiated at the western end of its rupture area, clearly west of this boundary, and rupture propagated eastward until or into this boundary zone (discussion of this continues below).

APaGA variations suggest a primary structural segmentation at depth. The four segments defined by flipping foreland-to-orogen APaGA described above (Figs 2c and 3a) clearly point to different flexural geometry and behaviour of the underthrusting India plate. Homogeneity of the India plate flexure within Nepal was already demonstrated by ref. 31 using thermo-mechanical modelling, the same as the difference between Nepal (long

flexural wavelength) and Bhutan (short flexural wavelength) by ref. 20. Here we spatially constraint the location of the transition, which is possible thanks to the use of land gravity data. Furthermore, we here document two further segments of the Himalayas by APaGA variations, to obtain a total of four (Fig. 4a): NE India, Bhutan, Nepal (plus India until Dehradun), NW India. From the APaGA pattern we infer that Nepal and NE India start to bend farther south of the topographic front, and disappear beneath the Himalaya at a relatively lower angle, while NW India and especially Bhutan begin to bend closer to the topographic front (farther north) and dip at a steeper angle. Segment boundaries where APaGA indicate major changes are first drawn in yellow on Fig. 4a, and then reported to Fig. 4b,c.

Lateral variation in structure is also reflected in the depth of the sedimentary basin (Fig. 4c). The Ganges Basin south of Nepal is broad and deep, in line with a longer flexural wavelength. The Brahmaputra Basin south of Bhutan is narrow and shallow, flexure occurs on a shorter wavelength. Note that APaGA values south of the topographic front cannot be the effect of the sedimentary basin only, as in NW India there are high APaGa values above a ca. 4 km deep basin.

We therefore conclude that APaGA primarily reflects the lateral variations in the deep structure of the India plate and of the Himalayan collision zone. The western boundary near 77°E, aligned with the Mahendragar-Dehradun Fault[32] (also referred to as Delhi-Haridwar Ridge), is also visible in the topography. The middle boundary near 88°E, aligned with the eastern end of the Munger-Saharsa Ridge[32], is also visible in the topography and is the clear termination of the deep foreland basin. This is certainly a major boundary in (or of) the India plate. Whether it has any relationship to the Yadong-Gulu Rift cannot be established here, APaGA values do not vary across the rift, and the Yadong Cross Structure[33] has not been documented to reach deep in the crust. The eastern boundary near 93°E, east of Bhutan in Arunachal Pradesh, connects to the dextral Kopili Fracture Zone in the foreland (e.g. ref. 34).

The continuation of these boundaries into the orogen in map view (Fig. 4a) is clear for the middle one (at 88°E) and speculative for the two others (although certainly present, see Fig. 3a). The gravity data coverage in NW India does not allow a clear statement, moreover the topographic re-entrant and the presence of Siwalik sediments west of 76°E causes low APaGA values. In NE India (Arunachal Pradesh) there is also a lack of data, however one can could connect the boundary in the foreland with that in the orogen (dotted line on Fig. 4).

The argument to do so is supported by the pattern of seismicity: east of Bhutan, in Arunachal Pradesh, there is a clear, seismically active band that extends across the foreland into the orogen. On the western end of Bhutan, a similar but much more localized, seismically active line was suggested[35] in the SW corner of the Kingdom, and recently confirmed on a much longer extent[36]. This transfer (and potentially transform) fault zone extends from the north of Sikkim to the northwestern corner of the Shillong Plateau[36]. Thus the Shillong block appears to be cut from both the India plate and the Arunachal Pradesh block, and may behave separately in terms of deformation and flexure. GPS observations also point towards such micro-blocks in NE India[37]. Their boundaries, at depth and at surface, will need to be defined with denser geophysical field campaigns in the future, and block rotations made compatible with the observed pattern and sense of seismicity. New gravity points in Arunachal Pradesh and around the surface trace of the aforementioned transfer fault zone will refine our APaGA analysis in these areas.

While the boundary between the India plate and the Shillong block appears to strike NW-SE, the APaGA pattern reveals a sharp structural boundary within the India plate at 88°E in the N-S direction. The zone East of this area, roughly triangular in shape starting in Sikkim and between ca. 88°E and 90°E in the foreland, produces a few earthquakes (more than the foreland of Nepal), however little can be said about its nature from available data. Since the extents of large earthquakes' rupture areas in and south of Bhutan are not well constrained (Fig. 3c), we cannot define this segment boundary of the Himalayas more precisely. This segment boundary cuts the presumed rupture zone of the eventual M9 event in 1100 AD suggested by paleoseismology. However, neither this super-earthquake nor its inability to rupture through a segment boundary have been hitherto documented.

Finally, the western segment boundary in NW India also produces a few small earthquakes in the foreland (Fig. 4b). The 1905 Kangra earthquake respects this boundary as the full rupture area is located west of it (Fig. 4b). Instrumental seismicity is misleading in the sense that the "gap" of lower activity is located where the 1905 Kangra event has ruptured, which is further west than the segment boundary. It seems that the instrumental seismicity pattern is not representative of the lateral segmentation of the orogen. Note, however, the cluster of seismicity extending into the Himalayan orogen, turning northwards as a continuation of the Mahendragar-Dehradun Fault.

Figures 3c and 4b highlight that known M7+ earthquakes in the Himalayas occur away from the segment boundaries identified with APaGA. This implies that the structurally different segments also put limits on the lateral propagation of rupture during megathrust earthquakes. From our results two segment lengths can be quantified: the Nepal block is over 1000 km at the topographic front, the Bhutan block is 250–500 km long (depending on the block boundaries being at the transfer fault zone or at 88°E in the west, and on what is selected in the seismicity cluster in the east). While large co-seismic slips on relatively shorter segments can still produce large magnitude events (e.g. ref. 38), we consider that the long-term seismic hazard in Nepal is higher than in Bhutan, especially that part of the accumulated strain may be released at the Shillong Plateau, and not in Bhutan itself, as presumably during the 12 June 1897 M8.3 (USGS) earthquake.

Conclusions

We have compiled the to-date most comprehensive field-based gravity anomaly database for the Himalayan orogen and investigated arc-parallel topography and gravity anomalies (APaTA and APaGA). While APaTA mainly reflect relief and erosional effects within the Himalayas, APaGA reflect the deep structure of the orogen and its clear lateral segmentation. Four blocks are outlined: NE India, Bhutan, Nepal & India until Dehradun, and NW India. The segment boundaries in the India plate are related to inherited structure (Mahendragar-Dehradun Fault, Munger-Saharsa Ridge), while in the Eastern Himalayas the Shillong block boundaries are highlighted by focused seismic activity. The segmentation of the orogen into these blocks is also reflected in the mean features of the sedimentary foreland basin. We found that the cumulated seismic moment of instrumental seismicity does not highlight

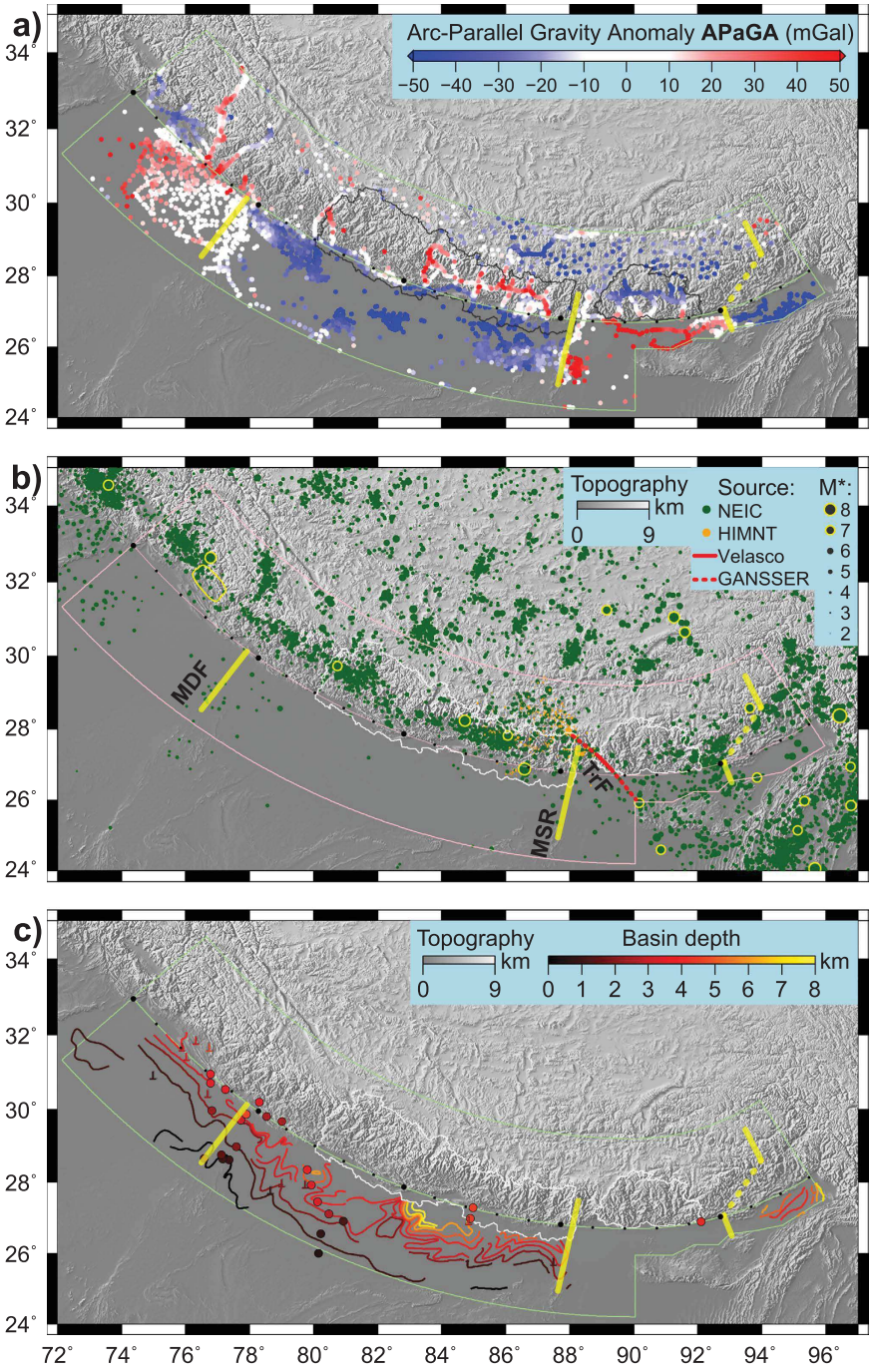

Figure 4. Spatial comparison of APaGA, seismicity and foreland basin depth. Study area and central arc as in Fig. 1, black dots on arc approximating the topographic front are placed every 100 km (every 5th larger) as a reference for Fig. 3. (**a**) Arc-Parallel Gravity Anomaly (from Fig. 2c). Red and blue values represent respectively higher and lower values of gravity compared to the average profile perpendicular to the Himalayan arc. Yellow lines highlight along-arc changes in APaGA, which are then reported on the two subsequent figures. (**b**) Distribution of seismicity. Colour code refers to the source of the data: NEIC is the ANSS Comprehensive Catalogue maintained by the USGS (http://earthquake.usgs.gov/earthquakes/search/), HIMNT project data ref. 41. TrF is the transfer (or transform) fault zone as suggested by seismicity based on ref. 35 and GANSSER project data[36]. Star indicates that magnitude scales are not homogeneous across the three catalogues. Earthquakes with magnitude larger than 7 are highlighted with yellow contour. The 1905 Kangra earthquake rupture contour[40] is shown in yellow. MDF: Mahendragar-Dehradun Fault. MSR: Munger-Saharsa Ridge. (**c**) Foreland basin depth. Isopach contours are from ref. 32. Inverted T symbols denote borehole data[42–45]. Circles are estimates from receiver functions[46–49]. Map created with GMT software[39] version 4 (http://gmt.soest.hawaii.edu/).

the boundaries found by APaGA, likely because the observation time is not representative of the full seismic cycle. However, large earthquakes of the past millennium do not propagate across the segment boundaries defined by lower plate inherited structure. Therefore the here identified segments are not only disparate in terms of flexural behaviour, but also seem to set an upper limit for the lateral extent of potential megathrust earthquakes. Further geophysical and paleoseismological measurements are needed to constrain the rupture extent of past events along the Himalayas, and to better characterize the nature of transition between the here defined segments.

Methods

We define our study along the Himalayan orogen. As the curvature of the mountain belt is different west and east of longitude 90°E, we approximate the arc with two small circles centred at latitudes 42°N and 35°N respectively, joining each other at longitude 90°E (Fig. 1). The central arc approximating the topographic front of the Himalayas (mostly coincident with the Main Frontal Thrust) is drawn with radii of 15.3° and 8.3° respectively, connecting at latitude 26.7°N at 90°E. On either side of this line a band of 2.5° width is considered[7], the low-lying India plate to the South, and the deformed orogen to the North. In the South we omit the area of the Shillong Plateau with much higher topography, which cannot be considered when estimating the average topographic profile. The thus defined curved area extends between azimuths 144° and 239° (clockwise from North), spanning from the state of Assam in NE India to NW India, respectively (Fig. 1).

Topography data was taken from the SRTM mission[10] at 1 arc-minute resolution. This is averaged using 8 km-wide radial bins to compute the mean arc-perpendicular topography profile. For gravity anomaly profile a similar averaging is performed with further binning into 1°-wide azimuthal elements, to avoid artefacts from the uneven distribution of data points. The thus obtained average arc-perpendicular profiles are then subtracted from the original datasets to result in Arc-Parallel Topography and Gravity Anomalies, APaTA and APaGa (Fig. 2a,c). APaTA is also presented in a smoothed version with spatial averaging within a 30 km radius circle (Fig. 2b) to filter out short wavelength variations related to fluvial and glacial erosion.

References

1. Triep, E. G. & Sykes, L. R. Frequency of occurrence of moderate to great earthquakes in intracontinental regions: Implications for changes in stress, earthquake prediction, and hazards assessments. *J. Geophys. Res.* **102,** 9923–9948 (1997).
2. Kumar, S. *et al.* Paleoseismological evidence of surface faulting along the northeastern Himalayan front, India: Timing, size, and spatial extent of great earthquakes. *J. Geophys. Res.* **115,** B12422 (2010).
3. Le Roux-Mallouf, R. *et al.* Paleoseismic evidence for two major historical earthquakes in Bhutan: new insight for rupture segmentation along the Himalayan arc. *Geophys. Res. Abs.* **18,** EGU2016–EGU7105 (2016).
4. Stevens, V. L. & Avouac, J.-P. Millenary Mw >=9.0 earthquakes required by geodetic strain in the Himalaya. *Geophys. Res. Lett.* **43,** 1118–1123 (2016).
5. Stevens, V. L. & Avouac, J.-P. Interseismic coupling on the main Himalayan thrust. *Geophys. Res. Lett.* **42,** 5828–5837 (2015).
6. Davis, D., Suppe, J. & Dahlen F. A. Mechanics of fold-and-thrust belts and accretionary wedges. *J. Geophys. Res.* **88,** 1153–1172 (1983).
7. Song, T.-R. A. & Simons, M. Large Trench-Parallel Gravity Variations Predict Seismogenic Behavior in Subduction Zones. *Science* **301,** 630–633 (2003).
8. Sandwell, D. T. & Smith, W. H. F. Marine gravity anomaly from Geosat and ERS-1 satellite altimetry. *J. Geophys. Res.* **102,** 10,039–10,054 (1997).
9. Sandwell, D. T., Müller, R. D., Smith, W. H., Garcia, E. & Francis, R. New global marine gravity model from CryoSat-2 and Jason-1 reveals buried tectonic structure. *Science* **346,** 65–67 (2014).
10. Farr, T. G. *et al.* The Shuttle Radar Topography Mission. *Rev. Geophys.* **45,** RG2004 (2007).
11. Panet, I. *et al.* Mapping the mass distribution of Earth's mantle using satellite-derived gravity gradients. *Nature Geoscience* **7,** 131–135 (2014).
12. Pavlis, N. K., Holmes, S. A. & Kenyon, S. C. & Factor, J. K. The development and evaluation of the Earth Gravitational Model 2008 (EGM2008). *J. Geophys. Res.* **117,** B04406 (2012).
13. Pavlis, N. K., Holmes, S. A., Kenyon, S. C. & Factor, J. K. An Earth Gravitational Model to Degree 2160: EGM2008. EGU General Assembly Abs. A-01891, Vienna, Austria (2008).
14. Godin, L. & Harris, L. B. Tracking basement cross-strike discontinuities in the Indian crust beneath the Himalayan orogen using gravity data – relationship to upper crustal faults. *Geophys. J. Int.* **198,** 198–215 (2014).
15. Hetényi, G. *et al.* Density distribution of the India plate beneath the Tibetan Plateau: geophysical and petrological constraints on the kinetics of lower-crustal eclogitization. *Earth Planet Sci. Lett.* **264,** 226–244 (2007).
16. Sun, W. Bouguer Gravity Anomaly Map of the People's Republic of China. Chin. Acad. Geoexploration, Beijing (1989).
17. Martelet, G., Sailhac, P., Moreau, F. & Diament, M. Characterization of geological boundaries using 1-D wavelet transform on gravity data: theory and application to the Himalayas. *Geophysics* **66,** 1116–1129 (2001).
18. Tiwari, V. M., Vyghreswara, R., Mishra, D. C. & Singh, B. Crustal structure across Sikkim, NE Himalaya from new gravity and magnetic data. *Earth Planet. Sci. Lett.* **247,** 61–69 (2006).
19. Berthet, T. *et al.* Lateral uniformity of India plate strength over Central and Eastern Nepal. *Geophys. J. Int.* **195,** 1481–1493 (2013).
20. Hammer, P. *et al.* Flexure of the India plate underneath the Bhutan Himalaya. *Geophys. Res. Lett.* **40,** 4225–4230 (2013).
21. Das, D., Mehra, G., Rao, K. G. C., Roy, A. L. & Narayana, M. S. Bouguer, free-air and magnetic anomalies over northwestern Himalaya. Himalayan Geology seminar, Section III, Oil and Natural Gas Resources. *Geol. Surv. India Misc. Publ.* **41,** 141–148 (1979).
22. Banerjee, P. Gravity measurements and terrain corrections using a digital terrain model in the NW Himalaya. *Comp. Geosci.* **24,** 1009–1020 (1998).
23. Cattin, R., Mazzotti, S. & Baratin, L. M. GravProcess: An easy-to-use MATLAB software to process campaign gravity data and evaluate the associated uncertainties. *Comp. Geosci.* **81,** 20–27 (2015).
24. Niebauer, T. M., Sasagawa, G. S., Faller, J. E., Hilt, R. & Klopping, F. A new generation of absolute gravimeters. *Metrologia* **32,** 159–180 (1995).
25. Timmen, L. & Wenzel, H.-G. Worldwide synthetic gravity tide parameters. In: *Gravity and Geoid* (eds Sünkel, H. & Marson, I.) IAGS **113**, 92–101 (1995).
26. Lyard, F., Lefevre, F., Letellier, T. & Francis, O. Modelling the global ocean tides: modern insights from FES2004. *Ocean Dynamics* **56,** 394–415 (2006).
27. Jacob, T., Bayer, R., Chery, J. & Le Moigne, N. Time-lapse microgravity surveys reveal water storage heterogeneity of a karts aquifer. *J. Geophys. Res.* **115,** B06402 (2010).

28. Yin, A. Cenozoic tectonic evolution of the Himalayan orogen as constrained by along-strike variation of structural geometry, exhumation history, and foreland sedimentation. *Earth Sci. Rev.* **76,** 1–131 (2006).
29. Bollinger, L. *et al.* Estimating the return times of great Himalayan earthquakes in eastern Nepal: Evidence from the Patu and Bardibas strands of the Main Frontal Thrust. *J. Geophys. Res.* **119,** 7123–7163 (2014).
30. Jackson, D. The great Western-Himalayan earthquake of 1505: A rupture of the central Himalayan gap? In Tibet, Past and Present (ed. Blezer, H.) 147–159 (Brill's Tibetan Studies Library I, Leiden, 2002).
31. Berthet, T. *et al.* Active tectonics of the eastern Himalaya: new constraints from the first tectonic geomorphology study in southern Bhutan. *Geology* **42,** 427–430 (2014).
32. Dasgupta, S. *et al. Seismotectonic Atlas of India and its environs* (eds Narula, P. L., Acharyya, S. K. & Banerjee J.) 87 pp (Geological Survey of India, Calcutta, India, 2000).
33. Burchfiel, B. C. *et al.* The South Tibetan Detachment System, Himalayan Orogen: Extension Contemporaneous With and Parallel to Shortening in a Collisional Mountain Belt. *Geol. Soc. Am. Spec. Pap.* **269** (1992).
34. Kumar, A., Mitra, S. & Suresh, G. Seismotectonics of the eastern Himalayan and indo-burman plate boundary systems. *Tectonics* **34,** 2279–2295 (2015).
35. Velasco, A. A. *et al.* Using Small, Temporary Seismic Networks for Investigating Tectonic Deformation: Brittle Deformation and Evidence for Strike-Slip Faulting in Bhutan. *Seismo. Res. Lett.* **78,** 446–453 (2007).
36. Diehl, T., Singer, J., Hetényi, G., Kissling, E. & Clinton, J. Seismicity and Seismotectonics in the Himalaya of Bhutan: Insights from the GANSSER Seismic Network. *AGU Fall Meeting, Abs.* T11E–03 (2014).
37. Vernant, P. *et al.* Clockwise rotation of the Brahmaputra Valley relative to India: Tectonic convergence in the eastern Himalaya, Naga Hills, and Shillong Plateau. *J. Geophys. Res.* **119,** 6558–6571 (2014).
38. Bassett, D., Sandwell, D. T., Gialko, Y. & Watts, A. B. Upper-plate controls on co-seismic slip in the 2011 magnitude 9.0 Tohoku-oki earthquake. *Nature* **531,** 92–96 (2016).
39. Wessel, P. & Smith, W. H. F. New, improved version of the Generic Mapping Tools released. *EOS Trans. AGU* **79,** 579 (1998).
40. Wallace, K., Bilham, R., Blume, F., Gaur, V. K. & Gahalaut, V. Surface deformation in the region of the 1905 Kangra Mw = 7.8 earthquake in the period 1846–2001. *Geophys. Res. Lett.* **32,** L15307 (2005).
41. Monsalve, G. *et al.* Seismicity and one-dimensional velocity-structure of the Himalayan collision zone: earthquakes in the crust an upper mantle. *J. Geophys. Res.* **111,** B10301 (2006).
42. Mathur, L. P. & Evans, P. Oil in India. *Proc. 22nd Int Geol Congs*, New Delhi, 86 pp (1964).
43. Sastri, V. V., Bhandari, L. L., Raju, A. T. R. & Datta, A. K. Tectonic framework and subsurface stratigraphy of the Ganga basin. *J. Geol. Soc. India* **12,** 222–233 (1971).
44. Karunakaran, C. & Ranga Rao, A. Status of exploration for hydrocarbons in the Himalayan region—Contributions to stratigraphy and structure. *Geol. Surv. India Misc. Publ.* **41,** 1–66 (1976).
45. Raiverman, V., Kunte, S. V. & Mukherjea, A. Basin geometry, Cenozoic sedimentation and hydrocarbon peospects in north western Himalaya and Indo-Gangetic Plains. Petroleum *Asia Journ.* **11,** 67–92 (1983).
46. Hetényi, G., Cattin, R., Vergne, J. & Nábělek, J. L. The effective elastic thickness of the India Plate from receiver function imaging, gravity anomalies and thermomechanical modelling. *Geophys. J. Int.* **167,** 1106–1118 (2006).
47. Srinivas, D., Srinagesh, D., Chadha, R. K. & Ravi Kumar, M. Sedimentary Thickness Variations in the Indo-Gangetic Foredeep from Inversion of Receiver Functions. *Bull. Seismo. Soc. Am.* **103,** 2257–2265 (2013).
48. Bora, D. K., Hazarika, D., Borah, K., Rai, S. S. & Baruah, S. Crustal shear-wave velocity structure beneath northeast India from teleseismic receiver function analysis. *J. Asian Earth Sci.* **90,** 1–14 (2014).
49. Borah, K., Kanna, N., Rai, S. S. & Prakasam, K. S. Sediment thickness beneath the Indo-Gangetic Plain and Siwalik Himalaya inferred from receiver function modelling. *J. Asian Earth Sci.* **99,** 41–56 (2015).

Acknowledgements

We are grateful to people and institutions who have made fieldwork possible in Nepal and Bhutan, namely the Department of Mines and Geology (Kathmandu), Department of Geology and Mines (Thimphu), HELVETAS Swiss Intercooperation Thimphu Office, and all the local drivers. We greatly acknowledge the RESIF-Gmob facilities for making gravimeter Micro-g LaCoste FG5 #228 and Scintrex CG5 instruments available. We are indebted to colleagues who have provided gravity data: Giorgio Poretti (Trieste), Paramesh Banerjee (Singapore), as well as the Bureau Gravimétrique International. We thank a large number of colleagues for help and discussions over the past 10 years at ENS Paris, at Géosciences Montpellier, at ETH Zürich, and in Nepal and Bhutan. This study was financed by North-South Centre at ETH Zürich, ETH Zürich, CNES TOSCA, CNRS-INSU, ANR, and Swiss National Science Foundation (Grant PP00P2_157627).

Author Contributions

G.H., R.C. and T.B. designed the study, performed the calculations and wrote the manuscript. N.L.M. orchestrated the absolute gravity measurements. All authors (G.H., R.C., T.B., N.L.M., J.C., S.L., P.H., D.D., S.N.S., S.G. and K.T.) collected data and reviewed the manuscript.

Additional Information

Supplementary information accompanies this paper at http://www.nature.com/srep

Competing financial interests: The authors declare no competing financial interests.

How to cite this article: Hetényi, G. *et al.* Segmentation of the Himalayas as revealed by arc-parallel gravity anomalies. *Sci. Rep.* **6**, 33866; doi: 10.1038/srep33866 (2016).

A.4 Abstract: HKT 2016

ABSTRACT

Imaging the Main Frontal Thrust (MFT) system in Southern Bhutan using high resolution near surface geophysical techniques. Implications for tectonic morphology and seismic hazard assessment

Dowchu Drukpa[1,2], Stephanie Gautier[1], Rodolphe Cattin[1], Kinley Namgay[2], Nicolas Le Moigne[1].

[1] Geosciences Montpellier, Universitè de Montpellier, Place Eugène Bataillon, 34090 Montpellier, France
[2] Department of Geology and Mines, Ministry of Economic Affairs, Thimphu, Bhutan
*Email: dawchu@gmail.com

Seismic potentials of the eastern Himalayan region, particularly in the Kingdom of Bhutan, is poorly understood primarily due to lack of historical documentation and limited scientific studies conducted so far (Drukpa, 2006). Recently, first ever detailed geomorphological and paleo-seismological studies in 2013 and 2014 have documented vertical displacements on the Main Frontal Thrust (MFT) in Sarpang district located in south-central part of Bhutan. They propose a vertical uplift of 8.8 +/- 2 mm/yr over Holocene (Berthet et al, 2014) and reveals that at least two large historical events have occurred over the last millennium in this area (Roux-Mallouf et. al., submitted). Following these studies, additional information on the geometry of the MFT are now needed to assess the over thrusting slip rate, which is a key parameter to study the dynamics of this fault system and to improve seismic hazard assessment and disaster risk mitigation in the region.

Here we present our preliminary results associated with a high resolution near surface geophysical investigation conducted in 2015 in the same area. Preliminary results highlight that geophysical data are influenced by the presence and the geometry of the fault. Electrical Resistivity Tomography (ERT) images clearly show that we are able to image the MFT up to a maximum depth of approximately 40m (Fig.1). Based on res2dmod forward modeling, our preliminary analysis suggests a preferred MFT dip angle of 35-45° to the north. We also present the new micro-gravity measurements and seismic refraction data that we have obtained along the same profile. Together, these data sets are combined to propose a first image of near surface geological strata and to constrain the geometry of the MFT at depth.

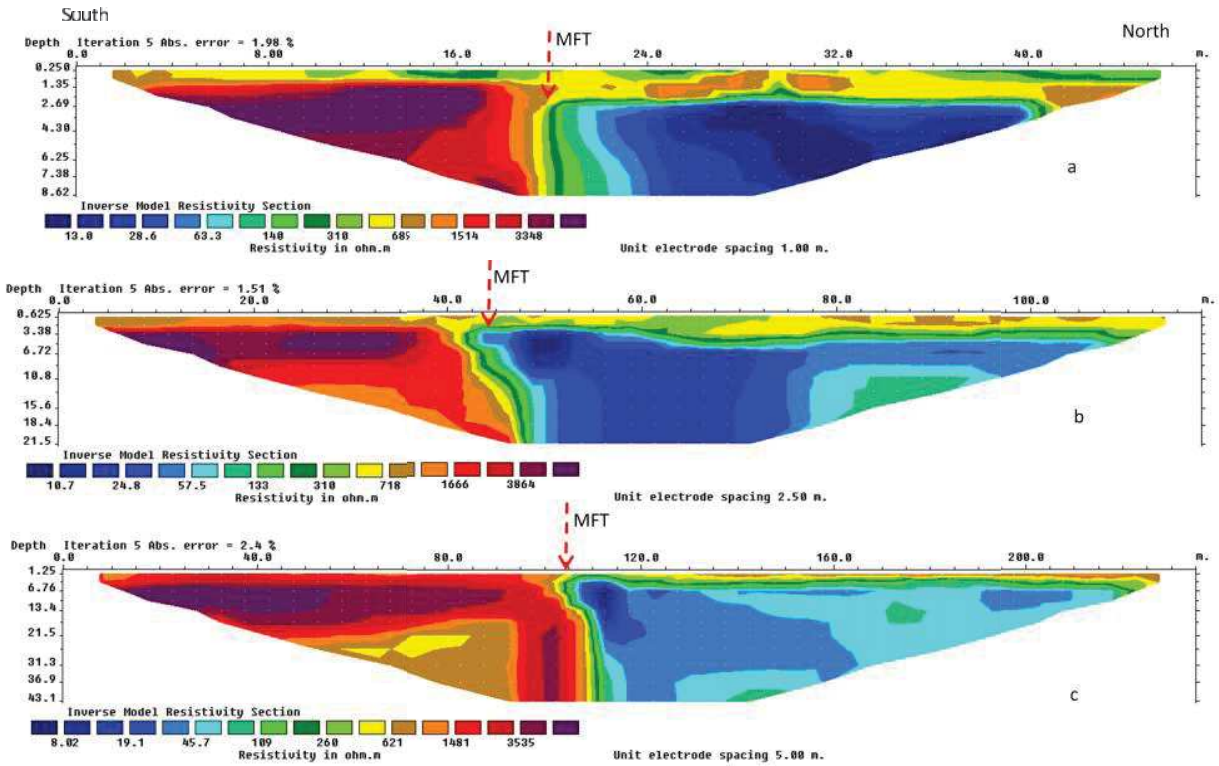

Fig.1 Wenner-Schlumberger ERT section with electrode spacing of 1m, 2.5m and 5m, respectively for a, b, and c sections above. All profiles in south-north direction and perpendicular to MFT trace observed in the paleo-trench.

References

Berthet, T., Ritz, J.F., Ferry, M., Pelgay, P., Cattin, R., Drukpa, D., Braucher, R. and Hetényi, G., 2014, Active tectonics in eastern Himalaya : new constraints from the first morphotectonic study in southern Bhutan, Geology, 42 (5), 427-430.

Drukpa, Dowchu, Aaron A. Velasco, and Diane I. Doser. "Seismicity in the Kingdom of Bhutan (1937–2003): Evidence for crustal transcurrent deformation." *Journal of Geophysical Research: Solid Earth (1978–2012)*111.B6 (2006).

Roux-Mallouf, L., Matthieu, F., Ritz, J.F.,Berthet T., CattinR.,,Drukpa, D., 2015. Segmentation and earthquake magnitudes along the Himalayan Arc: effect of the Yadong cross structure (submitted to JGR)

Imaging the Topographic Frontal Thrust (TFT) system in southern Bhutan using high resolution near surface geophysical techniques: implications for tectonic geomorphology and seismic hazard assessment

Drukpa Dowchu, Gautier Stephanie and Cattin Rodolphe
Geosciences Montpellier, University of Montpellier, France

Abstract

Seismic potentials of the eastern Himalayan region, particularly in the Kingdom of Bhutan, is poorly understood (*Drukpa et al., 2006*). Recent studies in south-central part of Bhutan on the Topographic Frontal Thrust (TFT) system proposed a vertical uplift of 8.8 ± 2 mm/yr over Holocene (*Berthet et al., 2014*) and reveals that at least two large historical events have occurred over the last millennium in this area (*Roux-Mallouf et al., 2015*). Following these studies, additional information on the geometry of the TFT are now needed to assess the over thrusting slip rate for improved seismic hazard assessment in this region.

Here we present our preliminary results of high resolution near surface geophysical investigations conducted in 2015 and 2016 in the same area. Results show that geophysical data are influenced both by the presence and the geometry of the fault. Electrical Resistivity Tomography (ERT) clearly highlights the fault up to a depth of ~40m and suggests that the dip angle increases with depth. We also present the new micro-gravity measurements and seismic refraction data obtained along the same profile. Together, these data sets are combined to propose a first image of near surface geometry of the TFT.

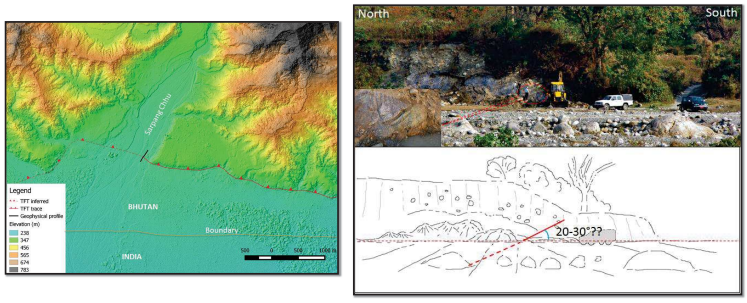

Fig.1 On the left side: Pleiades DEM image of the study area in Sarpang (south-central part of Bhutan) with the TFT fault trace and geophysical profile line indicated. On the right side: picture of excavated site in Sarpang with inset in the bottom left corner showing the TFT trace at the surface and a sketch of the outcrop showing the estimated dip angle of the fault as observed in the trench.

Electrical Resistivity Tomography

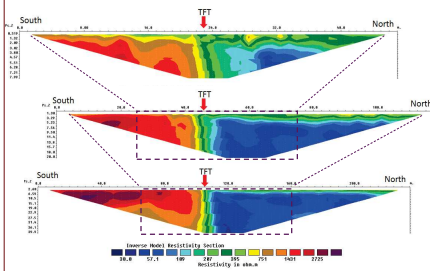

Fig.2 ERT sections (Wenner-Schlumberger array) along the profile for electrode spacing of 1m (top), 2.5m (middle) and 5m (bottom).

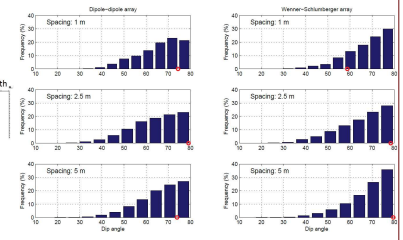

Fig.3 Probability density of distribution for the TFT dip angle obtained from ERT sections using both Dipole-dipole and Wenner-Schlumberger arrays. Electrode spacing ranges from 1 m (top) to 5 m (bottom).

Seismic Refraction Tomography

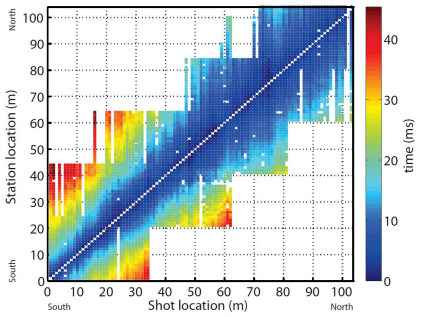

Fig.7 Shot location along the geophysical line; color scale indicates first arrival travel-time from each shot location to the geophone positions along the profile.

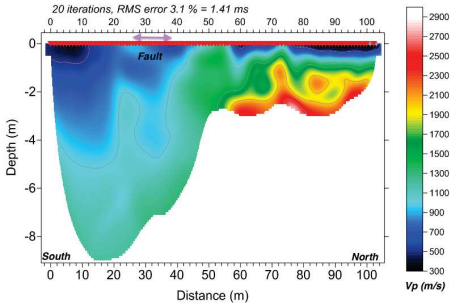

Fig. 8 Tomographic image showing the location of fault .

Gravimetry measurements

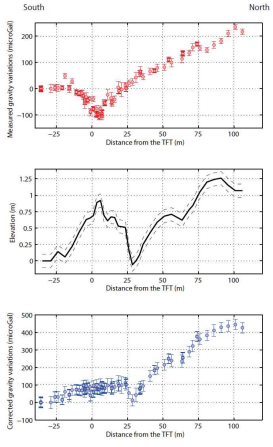

Fig.4 Measured gravity (top) and elevation (middle) variations along the profile; gravity variation along the profile after removal of topographic effect (bottom).

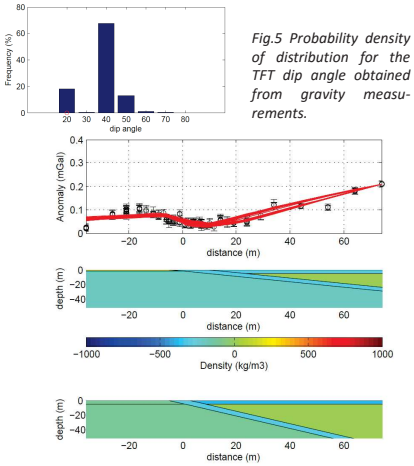

Fig.5 Probability density of distribution for the TFT dip angle obtained from gravity measurements.

Fig.6 Comparison between calculated (red lines) and observed (black circles) gravity anomalies. Density models infer from the inversion of gravity measurements (bottom)

Geometry of the TFT based on geophysical results

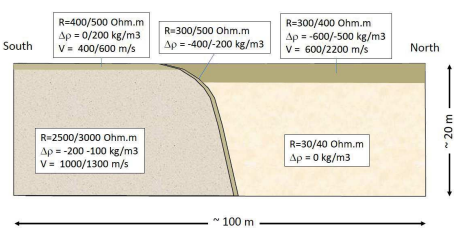

Fig. 9 Schematic cross section showing the main geophysical results obtained from electrical resistivity tomography, gravity measurements and seismic refraction. Together these results suggest a TFT that steepens with depth with a dip angle ranging from ~20° at the surface to ~70° at 30 m depth.

References

Drukpa, D., Velasco, A. A., & Doser, D. I. (2006). Seismicity in the Kingdom of Bhutan (1937–2003): Evidence for crustal transcurrent deformation.*Journal of Geophysical Research: Solid Earth*, *111*(B6).

Berthet, T., Ritz, J. F., Ferry, M., Pelgay, P., Cattin, R., Drukpa, D., ... & Hetényi, G. (2014). Active tectonics of the eastern Himalaya: New constraints from the first tectonic geomorphology study in southern Bhutan.*Geology*, *42*(5), 427-430.

Roux-Mallouf, L. (2015, December). Segmentation And Earthquake Magnitudes Along The Himalayan Arc: Effect Of The Yadong Cross Structure. In *2015 AGU Fall Meeting*. Agu.